

Crystal structure, electron density and
chemical bonding in inorganic compounds
studied by the
Electric Field Gradient

DISSERTATION

zur Erlangung des akademischen Grades

Doktor rerum naturalium
(Dr. rer. nat.)

vorgelegt

der Fakultät Mathematik und Naturwissenschaften
der Technischen Universität Dresden

von

DIPL. PHYS. KATRIN KOCH

geboren am 19.7.1979 in Bergisch Gladbach

Eingereicht am 26.6.2009

Die Dissertation wurde in der Zeit von Oktober 2005 bis Juni 2009 im
Max-Planck-Institut für chemische Physik fester Stoffe angefertigt.

Tag der Verteidigung: 18.9.2009

Gutachter: Prof. Juri Grin
Prof. Dr. Peter Blaha

Contents

List of abbreviations	III
List of figures	V
List of tables	VII
1 Introduction	1
2 Density functional theory	3
2.1 The quantum mechanical description of a solid	3
2.2 Density functional theory	4
2.2.1 The exchange-correlation functionals LDA and GGA	5
2.2.2 The exchange-correlation functional LSDA+ U	6
2.3 Band structure codes	7
2.3.1 The linearised augmented plane wave code WIEN2k	8
2.3.2 The full-potential local-orbital code FPLO	9
3 The electric field gradient: EFG	14
3.1 Why is it interesting to study the EFG?	14
3.2 What is the EFG?	14
3.3 Where does the EFG play a role in physics?	16
3.4 How can the EFG be measured?	16
3.5 How can the EFG be calculated?	19
4 Implementation of the EFG	21
4.1 Implementation in FPLO	21
4.1.1 Orbital contributions to the EFG	23
4.1.2 Remark about the potential	24
4.2 Implementation tests	25
5 Application of the EFG: studied compounds	28
5.1 The di- and tetragallides $M\text{Ga}_2$ and $M\text{Ga}_4$ ($M = \text{Na}, \text{Ca}, \text{Sr}, \text{Ba}$)	28
5.1.1 Introduction	28
5.1.2 Methods	29
5.1.3 Results	30
5.1.4 Summary and conclusion	40
5.2 Aluminium diboride $\text{Al}_{1-x}\text{B}_2$	42
5.2.1 Introduction	42
5.2.2 Methods	42
5.2.3 Results	44
5.2.4 Summary and conclusion	52
5.3 The perovskites SrTiO_3 and BaTiO_3	53
5.3.1 Introduction	53
5.3.2 Motivation	54
5.3.3 Methods	54

5.3.4	Results	54
5.3.5	Discussion	57
5.3.6	Summary and Conclusion	62
5.4	Strongly correlated low-dimensional cuprates	63
5.4.1	Introduction	63
5.4.2	The relation of J and U	63
5.4.3	Methods	64
5.4.4	La_2CuO_4	65
5.4.5	CuGeO_3	67
5.4.6	Sr_2CuO_3	67
5.4.7	SrCuO_2	69
5.4.8	$\text{Cu}_2(\text{PO}_3)_2\text{CH}_2$	70
5.4.9	Summary and conclusion	70
5.5	The recently emerged high T_c superconductors	72
5.5.1	Introduction	72
5.5.2	Structural similarities of AFe_2As_2 and REFeAsO	72
5.5.3	The EFG as a tool to study the Fe-As interaction	73
5.5.4	The iron arsenides AFe_2As_2	74
5.5.5	The iron oxypnictides REFeAsO	79
5.5.6	Summary and conclusion	85
6	Beyond the EFG: electron penetration in the nucleus – its effect on the quadrupole interaction	87
6.1	Formalism	87
6.1.1	Classical interaction energy without charge-charge overlap	87
6.1.2	Overlap corrections	88
6.1.3	Quantum formulation	91
6.1.4	Zooming in on E_2	93
6.2	Observable consequences	93
6.3	Computational aspects	95
6.3.1	Formulation in spherical notation	95
6.3.2	Relativity and the role of a finite nucleus	95
6.3.3	Comparison with the PCNQM method	96
6.4	Numbers and trends	97
6.4.1	Trends in \tilde{Q}	97
6.4.2	Trends in n_{zz}	98
6.4.3	Trends in the quadrupole shift	98
6.5	Experimental and computational accuracies	100
6.5.1	Accuracy of quadrupole interaction experiments	100
6.5.2	Accuracy of EFG calculations	102
6.5.3	Other small perturbations to the quadrupole interaction	103
6.6	Experimental implications of the quadrupole shift	103
6.6.1	Determination of Q and \tilde{Q}	103
6.6.2	Quadrupole moment ratios: the quadrupole anomaly	104
6.7	Summary and conclusions	107
7	Summary and outlook	109
A	Nuclear multipole moments	111

B	Spherical notation of the EFG tensor	113
C	Derivation of the quadrupole Hamiltonian	116
D	Contributions to the interaction energy from the 4th order Taylor expansion	119
E	Derivation of the quadrupole shift Hamiltonian	123
F	EFG implementation	126
G	Model Hamiltonian results for perovskites	131
H	Data sets and elaborated results for the quadrupole shift	134
H.1	Trends in n_{zz}	134
H.2	Models for the nuclear charge density, Q and \tilde{Q}	137
H.2.1	Axially symmetric ellipsoid	137
H.2.2	Nuclear model	138
H.2.3	Trends for Q and R	142
	Bibliography	145
	List of scientific contributions	154
	Acknowledgments	158

List of abbreviations

1(2,3)D	one (two, three)-dimensional
AFM	antiferromagnetic
AMF	around mean field
AL	atomic limit
a.u.	atomic units
ASA	atomic sphere approximation
BEB	Blackman-Esterling-Berk
bct	body-centred tetragonal
CAS	crystal axis system
CF	crystal field
CPA	coherent potential approximation
DFT	density functional theory
DMFT	dynamical mean field theory
DOS	density of states
EFG	electric field gradient
FPLO	full-potential local-orbital (minimum-basis)
FREL	full relativistic
FM	ferromagnetic
fn	finite nucleus
f.u.	formula unit
GGA	generalised gradient approximation
HDI	hexadecapole interaction
HDS	hexadecapole shift
hcp	hexagonal close-packed
HTSC	high-temperature superconductivity
IBZ	irreducible (part of the) Brillouin zone
(L)APW	(linearised) augmented plane wave
L(S)DA	local (spin) density approximation
LO (lo)	local orbital
MBS	molecular beam spectroscopy
MI	monopole interaction
MS	monopole shift
MT	muffin tin
NMR	nuclear magnetic resonance
NM	nonmagnetic
NN-AFM	chequerboard nearest neighbour AFM
NREL	non-relativistic
NQCC	nuclear quadrupole coupling constant
NQR	nuclear quadrupole resonance
PAC	perturbed angular correlation
PAS	principle axis system
PCM	point charge model
PCNQM	point charge nuclear quadrupole moment
pn	point nucleus

QI	quadrupole interaction
QS	quadrupole shift
rf	radio frequency
RMS	root-mean-square (of the nuclear radius)
SI	Le Système International d'Unités
SDW	spin density wave (columnar/stripe-type AFM order)
SREL	scalar relativistic
VCA	virtual crystal approximation
WP	Wyckoff position
xc	exchange and correlation

Physical constants and units used in this work

a_0	=	$0.529177249 \cdot 10^{-28}$ m	Bohr radius
b	=	10^{-28} m ²	barn
e	=	$1.6021773 \cdot 10^{-19}$ C	elementary charge
ϵ_0	=	$8.8541878 \cdot 10^{-12}$ As/(Vm)	permittivity of free space
h	=	$6.6260755 \cdot 10^{-34}$ Js	Planck's constant
Ha	=	27.2113845 eV	Hartree
m_e	=	$9.1093897 \cdot 10^{-31}$ kg	electron rest mass
m_p	=	$1.6726231 \cdot 10^{-27}$ kg	proton rest mass
μ_B	=	$9.2740154 \cdot 10^{-24}$ Am ²	Bohr magneton
N_A	=	$6.022045 \cdot 10^{23}$ mol ⁻¹	Avogadro constant

The physical constants are taken from Ref. [221].

List of Figures

3.1	Schematic pictures of V_{zz}	15
3.2	Nuclear energy levels (NQR experiments)	17
3.3	The coordinate systems Σ and Σ'	17
3.4	Nuclear energy levels (NMR experiments)	18
3.5	NQR and NMR spectra	19
4.1	Hcp metal comparison of V_{zz} for different methods	26
4.2	Basis dependence of V_{zz} for FPLO 5	27
5.1	Unit cells of MGa_2 and $CaGa_2$	28
5.2	Unit cells of MGa_4 and $CaGa_4$	29
5.3	Density of states of MGa_2	30
5.4	Measured and calculated V_{zz} of Ga in MGa_2	31
5.5	Energy dependence of Ga displacement in $BaGa_2$ and $CaGa_2$	32
5.6	The quadrupole coupling in dependence of the EFG for ^{71}Ga in MGa_2 and MGa_4	33
5.7	Fermi surfaces of MGa_2	34
5.8	Density of states of MGa_4	36
5.9	Fermi surfaces of MGa_4	38
5.10	Anisotropy ratio in dependence of V_{zz} for MGa_2 and MGa_4	39
5.11	Unit cell of AlB_2	42
5.12	Unit cells of $Al_{0.75}B_2$ and $Al_{0.875}B_2$	43
5.13	Equilibrium of $Al_{1-x}B_2$	45
5.14	Optimised lattice parameters of $Al_{1-x}B_2$	45
5.15	Density of states of $Al_{1-x}B_2$	47
5.16	Band structure of $Al_{1-x}B_2$	47
5.17	Band characters of $Al_{1-x}B_2$	48
5.18	Energy dependence of the boron displacement	50
5.19	Charge density pictures of $Al_{0.75}B_2$ and $Al_{0.875}B_2$	50
5.20	V_{zz} of boron in $Al_{1-x}B_2$	51
5.21	Unit cell of $SrTiO_3$ and $BaTiO_3$	53
5.22	Calculated V_{zz} in dependence of the lattice parameter	55
5.23	Occupation of p_x and p_z states in dependence of the lattice parameter	57
5.24	Band structure of $SrTiO_3$	58
5.25	Calculated exchange integrals J in dependence of U compared with measured J 's	64
5.26	CuO_4 plaquettes and V_{zz} of Cu in La_2CuO_4	66
5.27	Comparison of V_{zz} and U_J in La_2CuO_4 between FPLO and WIEN2k	66
5.28	CuO_4 plaquettes and V_{zz} of Cu in $CuGeO_3$	67
5.29	CuO_4 plaquettes and V_{zz} of Cu in Sr_2CuO_3	68
5.30	CuO_4 plaquettes and V_{zz} of Cu in $SrCuO_2$	68
5.31	CuO_4 plaquettes and V_{zz} of Cu in $Cu_2(PO_3)_2CH_2$	69
5.32	Comparison of $U_{V_{zz}}$ for the calculated cuprates	70
5.33	Unit cells of $REFeAsO$ and AFe_2As_2	73
5.34	Density of states of $LaFeAsO$ and $SrFe_2As_2$	74
5.35	Dependence of the magnetic moment on the As z position in $SrFe_2As_2$	75

5.36	Dependence of the EFG of As on the As z position in AFe_2As_2	76
5.37	V_{xx} , V_{yy} and V_{zz} of As in dependence of the As z position in $SrFe_2As_2$ and $BaFe_2As_2$	78
5.38	Temperature dependence of the EFG of As in $CaFe_2As_2$ and $BaFe_2As_2$	79
5.39	The influence of doping and pressure on the EFG of As in AFe_2As_2	80
5.40	Dependence of V_{zz} of As on the As z position in $LaFeAsO$ and $NdFeAsO$	82
5.41	The influence of doping on the EFG of As in $LaFeAsO$	84
5.42	The influence of doping on the EFG of As in $NdFeAsO$	85
6.1	Nuclear energy levels for the quadrupole shift	94
6.2	The density component $n_{2m}(r)$ for a point and finite nucleus	96
6.3	The ratio of the quadrupole interaction and quadrupole shift frequency in dependence on the mass number A	99
6.4	The quadrupole anomaly in dependence of the mass number A	105
F.1	On-site and off-site atom, separated by \vec{R}	126
G.1	Lattice parameter dependence of the model parameters (Γ point energies) of $SrTiO_3$	133
H.1	The investigated elements	134
H.2	The electronic quantity n_{zz} in dependence of the nuclear charge Z	135
H.3	Schematic pictures of a nucleus (nuclear model with varying parameters)	139
H.4	Schematic pictures of a nucleus (nuclear model with varying parameters)	139
H.5	The nuclear quadrupole moment and the nuclear radius in dependence of the mass number A	142

List of Tables

4.1	Hcp metal comparison of V_{zz} for different methods	25
5.1	Lattice parameters of $M\text{Ga}_2$	30
5.2	Plasma frequencies of $M\text{Ga}_2$	34
5.3	Lattice parameters of $M\text{Ga}_4$	36
5.4	Measured and calculated V_{zz} of Ga in $M\text{Ga}_4$	37
5.5	Plasma frequencies of $M\text{Ga}_4$	38
5.6	Structural data of the $\text{Al}_{1-x}\text{B}_2$ super cells	43
5.7	Lattice parameters of AlB_2 and Al	44
5.8	Measured and calculated V_{zz} of O in SrTiO_3 and BaTiO_3	54
5.9	Structural data of the calculated cuprates	65
5.10	V_{zz} of As in AFe_2As_2	77
5.11	Calculated V_{zz} of As in LaFeAsO and NdFeAsO	83
6.1	Systematic overview of nuclear multipole moments and electric multipole fields . .	90
6.2	Nuclear parameters/quantities of some hcp metals	97
6.3	Quadrupole interaction and quadrupole shift frequencies of several hcp metals . . .	98
6.4	Ratios of experimental quadrupole coupling constants	107
G.1	Model parameters (Γ and X point energies) of SrTiO_3	132
G.2	Model parameters (transfer integrals) of SrTiO_3	133
H.1	The electronic quantity n_{zz} of several (artificial) hcp metals	136
H.2	The electronic quantity n_{zz} of several (artificial) bct metals	144

1 Introduction

The goal of solid state physics and chemistry is to gain a deeper understanding of the basic principles of condensed matter. This ongoing process is achieved by the combination of experimental methods and theoretical models. In particular, many-body phenomena like magnetism, superconductivity or ferroelectricity are investigated, not only from a conceptual point of view in describing collective phenomena but also because of their high relevance concerning technological applications. Furthermore, a prerequisite for the development of new applications is the understanding of the underlying microscopic principles for such effects. Large progress has been made in the last decades as a result of a strong interplay of experimental and theoretical studies. This has been enabled by a continuous improvement of experimental techniques as well as a sophisticated development of the first-principles methods, additionally boosted by the rapidly increasing computational power. Consequently, electronic structure calculations have developed into a standard tool to study even very complex systems.

Most first-principles calculations are based on the concept of density functional theory (DFT). Since a solid typically contains around 10^{23} atoms, it is described by a many-particle wave function. The corresponding Schrödinger equation can be solved neither analytically nor numerically, due to the huge number of degrees of freedom. In the 1960s, Hohenberg, Kohn and Sham derived two theorems, which made the approximate numerical treatment of solids possible. These theorems and their implementation in the DFT based band structure codes WIEN [1] and FPLO [2], as well as remaining open questions (*e.g.*, that of correlations), will be explained in the second chapter.

In order to test the reliability of a band structure calculation, its results have to be compared with experiments. Since the electron density, the main constituent of DFT codes, cannot be directly determined experimentally with sufficient accuracy (*e.g.*, by X-ray diffraction), other experimentally available properties are needed for the comparison with the calculation.

A quantity that can be measured with high accuracy and that can provide indirect information about the electron density is the electric field gradient (EFG). The EFG reflects local structural symmetry properties of the charge distribution surrounding a nucleus: the EFG is nonzero if the density deviates from cubic symmetry and therefore generates an inhomogeneous electric field at the nucleus. Since the EFG is highly sensitive to structural parameters and to disorder, it is a valuable tool to extract structural information. Furthermore, the evaluation of the EFG can provide valuable insight into the chemical bonding.

Since the EFG is responsible for the quadrupole interaction, it can be measured via the quadrupole frequency by nuclear resonance methods, for instance, such as nuclear quadrupole resonance (NQR) or nuclear magnetic resonance (NMR). As the quadrupole interaction is well described by the quadrupole Hamiltonian, no additional model has to be applied to interpret the experimental data. From band structure codes, all components of the EFG tensor can be calculated. It is therefore straightforward to compare experiment and theory. In the third chapter, the definition and the properties of the EFG tensor and its experimental and theoretical determination will be described in detail.

Whereas the experimental determination of the quadrupole frequency, and therefore in principle the EFG, has been possible since 1939 [3], reliable values for calculated EFGs could not be obtained before 1985 [4], when an EFG module was implemented in the full-potential, linearised augmented plane wave code WIEN. One goal of this work was to implement an EFG module in the full-potential local-orbital minimum-basis scheme FPLO. FPLO provides an accuracy similar to

that of WIEN but is numerically more efficient due to its use of a minimal basis set. Furthermore, the local-orbital scheme allows an easy analysis of the different contributions to the EFG. The implementation of the EFG module in the FPLO code will be presented in the fourth chapter.

In the fifth chapter, we discuss the application of the newly implemented EFG module on different systems: starting from simple metals, then approaching more complex systems and finally tackling strongly correlated oxides. Parallel to the calculations, the EFGs for the studied compounds were also determined experimentally by NMR spectroscopists. This close collaboration enables the comparison of the calculated EFGs with the experimental observations, which provides a deeper understanding of *e.g.*, distortion, the chemical bonding or the relevance of electron correlation.

First, we calculate the EFG for binary metals with simple crystal structures: the digallides $M\text{Ga}_2$ with $M = \text{Ca}, \text{Sr}$ and Ba and the tetragallides $M\text{Ga}_4$ with $M = \text{Na}, \text{Ca}, \text{Sr}$ and Ba . Here, the comparison of experiment and theory reveals an until now overlooked deviation of the AlB_2 -type structure for SrGa_2 and BaGa_2 . Furthermore, by means of the EFG, the flexibility of the Ga atoms with respect to the chemical bonding is investigated.

Then, we apply the EFG module to a more complex metal: the hexagonal aluminium diboride. AlB_2 has been examined intensely in the last few years by different experimental methods, all of them indicating deficiencies on the Al sites. In order to understand the experimental findings, we investigate in a first-principles study the vacancies in the Al sublattice.

We subsequently employ the EFG module to study electronically weakly correlated oxides: the perovskites SrTiO_3 and BaTiO_3 . A counter-intuitive dependence of the EFG on the lattice parameter is observed, which can not be explained by the standard model Hamiltonian for perovskites. The analysis provides an improved description of the perovskites by an extended model Hamiltonian that captures the observed behaviour.

Finally, we use the EFG module for strongly correlated oxides: a few selected members of the cuprates. DFT calculations based on the linear density approximation (LDA) strongly underestimate the correlation in these systems. Better results are obtained by applying the LSDA+ U method, where the correlations are treated in a mean field-like approach. The parameter U is usually determined from the comparison of measured and calculated properties like for instance the exchange integral J or the gap size. We will study the influence of the Coulomb parameter U on the EFG and how this influence can be used to determine U .

In the course of this work (2008), a second class of high-temperature superconductors was discovered: the iron oxypnictides $R\text{FeAsO}$ and the iron arsenides AFe_2As_2 , respectively. As these systems are in the focus of present scientific interest, and the mechanism of the superconductivity is still unknown, they will be presented in this manuscript as well. One of the key features for the understanding of the superconductivity in these systems is the Fe-As interaction, which is reflected by the Fe-As distance. Furthermore, doping leads to the onset of superconductivity in these systems. This makes the EFG an ideal tool to study the Fe-As interplay.

After the application of the EFG, a methodological development beyond the EFG is presented. In the sixth chapter, corrections to the multipole interactions due to electron penetration into the nucleus will be discussed. The correction to the monopole interaction is well-known and experimentally observed since 1960 [5]: the penetration of s electrons in the nucleus results in the isomer shift and is measurable with Mössbauer spectroscopy. From the corrections to higher multipole interactions, we focus on the correction to the quadrupole interaction (the “quadrupole shift”) and discuss how it modifies the experimental spectra, as well as possible ways in which it could be exploited to improve the accuracy of experimentally determined quadrupole moments.

The thesis closes with a summary and an outlook. Several appendices contain explicit derivations of the shown results and additional details of the calculations presented in this work.

2 Density functional theory

The challenge of computational solid state physics is to describe the observable, macroscopic properties of a solid based on its crystal structure. The solid is described by a many-particle wave function, which could be obtained by solving the Schrödinger equation for this many-particle problem. However, this problem can neither be solved analytically nor can it be treated numerically, due to the huge number of degrees of freedom. In the 1960s, Hohenberg, Kohn and Sham came up with a powerful tool for the calculation of the quantum states of many-electron systems: density functional theory (DFT). They showed that the electron density is sufficient to describe the macroscopic properties of the solid in its ground state or in thermal equilibrium [6]. Furthermore, they reduced the many-particle problem to a set of coupled single-particle equations. Two theorems made the numerical treatment of solids (and molecules) possible. These theorems and their implementation in DFT band structure codes (focusing on FPLO and WIEN2k) will be explained in this chapter.

2.1 The quantum mechanical description of a solid

In quantum mechanics, a solid with N_e electrons and N_n nuclei is described by a many-particle wave function $|\psi\rangle$. In the Schrödinger representation the wave function is given by $\langle \vec{r}_1, \dots, \vec{r}_{N_e}, \vec{R}_1, \dots, \vec{R}_{N_n} | \psi \rangle = \psi(\vec{r}_1, \dots, \vec{r}_{N_e}, \vec{R}_1, \dots, \vec{R}_{N_n})$ and the Hamilton operator by

$$\mathcal{H} = \mathcal{H}_e + \mathcal{H}_n + \mathcal{H}_{en}. \quad (2.1)$$

Both the electronic and the nuclear part are described by a kinetic energy and a Coulomb interaction term

$$\begin{aligned} \mathcal{H}_e &= -\hbar^2 \sum_{i=1}^{N_e} \frac{\nabla_{\vec{r}_i}^2}{2m_e} + \frac{1}{2} \frac{e^2}{4\pi\epsilon_0} \sum_{i \neq j}^{N_e} \frac{1}{|\vec{r}_i - \vec{r}_j|} \\ \mathcal{H}_n &= -\hbar^2 \sum_{i=1}^{N_n} \frac{\nabla_{\vec{R}_i}^2}{2M_i} + \frac{1}{2} \frac{e^2}{4\pi\epsilon_0} \sum_{i \neq j}^{N_n} \frac{Z_i Z_j}{|\vec{R}_i - \vec{R}_j|}. \end{aligned}$$

The Coulomb interaction between the electrons and the positively charged nuclei is described by

$$\mathcal{H}_{en} = -\frac{e^2}{4\pi\epsilon_0} \sum_{i,j}^{N_e, N_n} \frac{Z_j}{|\vec{r}_i - \vec{R}_j|}.$$

It is impossible to solve the time independent (stationary) Schrödinger equation, $\mathcal{H}|\psi\rangle = E|\psi\rangle$, exactly with the wave function and the Hamilton operator given above. This is due to the large number of degrees of freedoms, which is in the order of the Avogadro constant N_A . Thus, approximations are needed. Since the proton mass is three orders of magnitude larger than the electron mass, $\frac{m_e}{m_p} \simeq \frac{1}{2000}$, the nuclei have a much larger inertia. Therefore, the electrons will move much faster and can be considered in an instantaneous equilibrium with respect to the motion of the nuclei. This is the so called adiabatic (or Born-Oppenheimer) approximation [7], which reduces the nuclei to a given arrangement of positive point charges (which the electrons feel as external potential)¹. Therefore, the first term in the nuclear operator \mathcal{H}_n disappears and

¹The adiabatic approximation becomes invalid for strong electron-phonon coupling and high phonon energies (especially for light nuclei).

the second term reduces to a (charge neutralising) constant C and the Hamiltonian becomes

$$\hat{H} = \hat{T} + \hat{V} + \hat{V}_{ext}, \quad (2.2)$$

with

$$\begin{aligned} \hat{T} &= -\hbar^2 \sum_{i=1}^{N_e} \frac{\nabla_{\vec{r}_i}^2}{2m_e}, & \hat{V} &= \frac{1}{2} \frac{1}{4\pi\epsilon_0} \sum_{i \neq j}^{N_e} \frac{e^2}{|\vec{r}_i - \vec{r}_j|}, \\ \hat{V}_{ext} &= \sum_i^{N_e} v_{ext}(\vec{r}_i) + C = -\frac{1}{4\pi\epsilon_0} \sum_{i,j}^{N_e, N_n} \frac{e^2 Z_j}{|\vec{r}_i - \vec{R}_j|} + C. \end{aligned}$$

Also the wave function $|\psi\rangle$ is reduced to describe the many-electron system only, $\langle \vec{r}_1, \dots, \vec{r}_{N_e} | \psi \rangle = \psi(\vec{r}_1, \dots, \vec{r}_{N_e})$. Even though this approximation eliminates many degrees of freedom, the remaining degrees of freedom are still too large to allow an exact solution.

2.2 Density functional theory

One way out of the many particle problem is density functional theory². DFT was formally established in 1964 by two theorems of Hohenberg and Kohn. In order to apply these theorems [8], we define $|\psi_G\rangle$ as the ground state wave function, yielding the ground state energy $E_G = \langle \psi_G | \hat{H} | \psi_G \rangle$ and the ground state density $n_G = \langle \psi_G | \psi^* \psi | \psi_G \rangle$. The first theorem proves that for a non-degenerate³ ground state, the external potential v_{ext} is (apart from an additive constant) a unique functional of the ground state density n_G . Since v_{ext} enters the Hamiltonian \hat{H} in Eq. (2.2), the full (non-degenerate) many-particle ground state $|\psi_G\rangle$ is a unique functional of n_G [8]. This means that the dependence of a functional on v_{ext} is transferred into a dependence of a functional on $n_G \rightarrow v_{ext}[n_G]$. For the second theorem, Hohenberg and Kohn define the universal (valid for any number of particles and any external potential) functional $F_{HK}[n] \equiv \langle \psi | \hat{T} + \hat{U} | \psi \rangle$, and for a given external potential the energy functional $E[v_{ext}] \equiv F_{HK}[n] + \int v_{ext}(\vec{r}) n(\vec{r}) d\vec{r}$. Now, the second theorem states that the ground state energy for a given potential v_{ext} is found by minimising the functional of the density under the constraint of a fixed particle number N_e (Hohenberg-Kohn variational principle)

$$E_G[v_{ext}] = \min_n \left\{ F_{HK}[n] + \int v_{ext}(\vec{r}) n(\vec{r}) d\vec{r} \quad \left| \quad \int n(\vec{r}) d\vec{r} = N_e \right. \right\}.$$

However, the Hohenberg-Kohn functional $F_{HK}[n]$ is not known but can be rewritten as $F_{HK}[n] = T_0[n] + V_H[n] + E_{xc}[n]$ and yields for the ground state energy

$$E_G[v_{ext}] = \min_n \left\{ T_0[n] + V_H[n] + E_{xc}[n] + V_{ext}[n] \quad \left| \quad \int n(\vec{r}) d\vec{r} = N_e \right. \right\}. \quad (2.3)$$

Here, T_0 describes the kinetic energy of a non-interacting electron gas, V_H describes the mean-field electron-electron interaction (including self-interaction) and E_{xc} describes the effects beyond mean field: the kinematic exchange (kinetic energy) and the dynamic correlation of the electron-electron interaction.

In 1965, Kohn and Sham [10] used the fact that the ground state density $n(\vec{r})$ of an N_e electron system can be written by single-particle wave functions $\phi_i(\vec{r})$: $n(\vec{r}) = \sum_i^{N_e} \phi_i^*(\vec{r}) \cdot \phi_i(\vec{r})$ with

²At least for the ground state energy and the electron density.

³In the work of Hohenberg and Kohn in 1964, the theorem was proven for a non-degenerate ground state. However, the theorem can also be proven for a degenerated ground state [9].

$\langle \phi_i | \phi_j \rangle = \delta_{ij}$. This simplifies Eq. (2.3), T_0 , V_H and V_{ext} can now be expressed as

$$\begin{aligned} T_0[n] &= \min_{\phi_i, \phi_i^*} \left\{ -\hbar^2 \sum_i^{N_e} \int \phi_i^*(\vec{r}) \nabla^2 \phi_i(\vec{r}) d\vec{r} \right\} \\ V_H[n] &= \min_{\phi_i, \phi_i^*, \phi_j, \phi_j^*} \left\{ \frac{1}{2} \frac{e^2}{4\pi\epsilon_0} \sum_{i,j} \int \int \frac{|\phi_i(\vec{r})|^2 |\phi_j(\vec{r}')|^2}{|\vec{r} - \vec{r}'|} d\vec{r} d\vec{r}' \right\} \\ V_{ext}[n] &= \min_{\phi_i, \phi_i^*} \left\{ \sum_i \int v_{ext}(\vec{r}) |\phi_i(\vec{r})|^2 d\vec{r} \right\}. \end{aligned}$$

The functional derivative using the Lagrange multipliers ε_i to ensure normalised wave functions ϕ_i

$$\frac{\delta}{\delta \phi_j^*} \left[T_0[n] + V_H[n] + E_{xc}[n] + V_{ext}[n] \right] \stackrel{!}{=} \sum_i \varepsilon_i \frac{\delta(\int |\phi_i(\vec{r})|^2 d\vec{r} - 1)}{\delta \phi_j^*}$$

leads finally to the Kohn-Sham equation

$$[\nabla_i^2 + v_{eff}] \phi_i(\vec{r}) = \varepsilon_i \phi_i(\vec{r}), \quad (2.4)$$

with

$$v_{eff} = \frac{e^2}{4\pi\epsilon_0} \int \frac{n(\vec{r}')}{|\vec{r} - \vec{r}'|} d\vec{r}' + \frac{\delta E_{xc}[n(\vec{r})]}{\delta n(\vec{r})} + v_{ext}(\vec{r}).$$

Note that the single-particle wave functions ϕ_i describe mathematical quantities without direct physical meaning. Yet, the overall density $n = \sum_i \phi_i^* \phi_i$ has physical meaning and is the electron density. The Lagrange multipliers ε_i are the so-called Kohn-Sham energies.

The Kohn-Sham equation (2.4) poses a self-consistency problem: the solutions ϕ_i determine the original equation (the Hartree and the exchange-correlation potential in v_{eff}). The equation can be solved iteratively, with a guessed starting density until convergence is reached.

2.2.1 The exchange-correlation functionals LDA and GGA

Within the Born-Oppenheimer approximation, the Kohn-Sham equation is exact. But since the exchange-correlation functional is not known, it has to be modelled. For weakly correlated systems, there are two widely used approximation for the exchange-correlation functional – the local density approximation (LDA) and the generalised gradient approximation (GGA). At this point, we point out that due to these approximations, all results obtained with codes based on DFT are model results. Since some of the models (*e.g.*, LDA) do not need adjustable parameters, they are often called *ab initio*. A better term, however, is first-principles method⁴.

LDA is based on the theory of the homogeneous electron gas, which is one of the most important model systems. Here, the electrons are exposed to a constant external potential, *i.e.*, the nuclei are replaced by a homogeneous positive charge density. The ground state density of the electrons is constant. For this model, the exchange and correlation energy ε_{xc}^{homo} can be obtained with Monte Carlo calculations with very high precision [11, 12]. Note that there are different parametrisations to obtain ε_{xc}^{homo} , *e.g.*, by Barth and Hedin [13], by Perdew and Zunger [14] and by Perdew and

⁴It is a convention that *ab initio* stands for parameter free methods, like the Hartree-Fock method. Since LDA and GGA are not parameter free (although the parameters are element independent, see below), DFT calculations are better described by the word first-principles.

Wang [15]⁵. The last one contains the most precise fit [9] and is used in most calculations reported in Chapter 5.

Kohn and Sham [10] used the exchange and correlation energy $\varepsilon_{xc}^{homo}(n(\vec{r}))$ of the homogeneous electron gas to describe the exchange and correlation energy E_{xc} for an inhomogeneous system

$$E_{xc}[n(\vec{r})] = \int n(\vec{r})\varepsilon_{xc}^{homo}(n(\vec{r}))d\vec{r}. \quad (2.5)$$

Since ε_{xc}^{homo} describes the exchange and correlation energy per particle and n the particles per unit volume, the integral over these two quantities yields an energy. Eq. (2.5) is the so-called local density approximation. It works surprisingly well also for strongly inhomogeneous systems (*e.g.*, atoms, molecules and solids)⁶.

In GGA, also the densities of the surrounding infinitesimal volumes are considered, which means the gradient of the density plays a role. Since the straightforward gradient would violate relationships of the true (and the LDA) exchange-correlation functional, a proper function of the density gradient (hence, the name “generalised” gradient) has to be chosen [16]. Unlike LDA, there is no unique way to express ε_{xc} in GGA and several GGA functionals exist⁷. Furthermore, many GGA functionals are fitted to a set of experimental parameters, what deprives these functionals of their first-principles status. Like LDA, GGA fails in correctly describing the strongly-correlated system, see *e.g.*, Ref. [9] or Section 5.4.

If the spin degree of freedom σ of the electrons is taken into account and the density is replaced by a spin density matrix $n_{\sigma\sigma'}$ with $n = \sum_{\sigma\sigma'} n_{\sigma\sigma'} = n_{\uparrow} + n_{\downarrow}$ and the states (ε_i, ϕ_i) are replaced by the corresponding spinors $(\varepsilon_{i,\sigma}, \phi_{i,\sigma})$ the theory still holds [13]. In case of LDA, this is often called local spin density approximation (LSDA).

2.2.2 The exchange-correlation functional LSDA+U

For strongly correlated systems, *e.g.*, transition metal oxides (like cuprates with localised 3d electrons) or rare earth compounds (localised *f* electrons), both LDA and GGA fail. These systems exhibit phenomena like metal-insulator transitions, heavy fermion behaviour [17] and high-temperature superconductivity (see Section 5.4). However, these compounds can be treated with a certain success with the LSDA+*U* approach. Here, LDA (or GGA) type calculations are coupled with an additional orbital-dependent interaction. This interaction is described by a functional, which adds a Coulomb repulsion energy *U*, whenever two electrons with opposite spin occupy a correlated orbital, and subtracts the “double counting correction” term (the correlation already included in LDA). The effect of the added *U* is to first split the “correlated” orbitals and then to shift the occupied orbitals in direction of lower and the unoccupied orbitals in direction of higher energy. The obtained distance in energy (which is the total shift) has roughly the value of *U*. This mean field-like treatment of correlations influences, *e.g.*, the hybridisation or localisation and tries to correct the errors known to be large in the usual LDA (GGA) calculations. In LSDA+*U*, the dynamical character of the correlation is treated imperfectly. This is improved in dynamical mean field theory (DMFT) [18, 19]. *U* is an additional, free parameter, which is not known per se and needs to be evaluated. This can be done by a comparison of calculated properties with experimental measurements (see Section 5.4) or by constrained LDA calculations [20]. The other quantity, which is involved in a LSDA+*U* calculation is the on-site exchange integral J_t ⁸,

⁵These parametrisations are the reason why LDA calculations are described as first-principles and not *ab initio* method.

⁶This can be understood (isotropy of the Coulomb interaction $\propto 1/|\vec{r}-\vec{r}'|$) and is presented in detail in Chapter 7.2 of Ref. [9].

⁷Though there is a unique E_{xc} in LDA, there are also several LDA functionals due to the different parametrisations, see text before.

⁸Be aware not to confuse this “intra-atomic” J_t with the “inter-site” exchange integral J , will comes into play in the LSDA+*U* calculations in Section 5.4.

which describes the exchange interaction within the correlated orbital. U and J_t are obtained from the Slater integrals: $U = F_0$ and $J_t = (F_2 + F_4)/14$ for d orbitals, $J_t = (286F_2 + 195F_4 + 250F_6)/6435$ for f orbitals.

There are two frequently used versions of double-counting correction schemes in LDA+ U : the around-mean-field (AMF) and atomic limit (AL). The AMF functional was introduced by Czyżyk and Sawatzky in 1994 [21]. This functional assumes that LDA works well for the case without orbital polarisation of the correlated shell, *i.e.*, if the shell is fully occupied and fully spin polarised. It may be understood as an orbital polarisation functional, since it corrects the correlated shell, if it is orbital polarised. It gives nearly nothing for a half filled shell. Clearly, the AMF functional depends on the shell occupation. Also the AL functional was introduced by Czyżyk and Sawatzky [21]. Contrary to the AMF functional, this one is independent of the shell occupation. If the correlated shell is isolated, it moves all occupied states by $(U - J)/2$ downward in energy and all unoccupied states by $(U - J)/2$ upward in energy [9].

Details on the implementation of LSDA+ U method into the FPLO code (see Section 2.3.2) can be found in Ref. [22].

2.3 Band structure codes

In order to solve the Kohn-Sham equation (2.4), we expand the single-particle orbitals $|\phi_i\rangle$ in a given basis set $|\phi_n^B\rangle$

$$|\phi_i\rangle = \sum_n^N c_n^i |\phi_n^B\rangle. \quad (2.6)$$

The remaining task is to find the coefficients c_n^i . This is done by inserting the basis expansion Eq. (2.6) in the Kohn-Sham equation $\hat{H}_{KS}|\phi_i\rangle - \varepsilon_i|\phi_i\rangle = 0$ (with $\hat{H}_{KS} = \nabla_i^2 + v_{eff}$) and then multiplying this equation from the left with $\langle\phi_m|$, yielding for $m = 1, \dots, N$

$$\sum_n \left(\langle\phi_m^B|\hat{H}_{KS}|\phi_n^B\rangle - \varepsilon_i\langle\phi_m^B|\phi_n^B\rangle \right) c_n^i = 0. \quad (2.7)$$

Diagonalising the matrix $\left[\langle\phi_m^B|\hat{H}_{KS}|\phi_n^B\rangle - \varepsilon_i\langle\phi_m^B|\phi_n^B\rangle \right]$ finally gives the coefficients c_n^i .

The larger the basis set (N) the better the single-particle wave function is described. But it comes with a price: the larger the basis, the larger the matrix and the larger the computational effort: since diagonalising a matrix scales with N^3 (the cube of the size of the matrix), it is more time consuming to choose a large basis set. Therefore, a compromise of efficiency and accuracy must be found.

There are four categories to characterise band structure codes.

- The basis set: in general there are two possibilities for the basis set, local orbitals (as used by the FPLO code, see Section 2.3.2) or (linearised augmented) plane waves (as used in combination with local orbitals by the WIEN2k code, see Section 2.3.1).
- The potential representation: also here, there are two possibilities, depending on if there are approximations done to the potential, or not. “Non full-potential” codes are muffin-tin (MT) or atomic sphere approximation (ASA) codes. In MT codes, there is a constant potential between the non-overlapping spheres (MT). In ASA codes, there is no interstitial region because the atomic spheres are allowed to overlap. In both cases, the interstitial region is treated only approximately, contrary to WIEN2k, see below. On the other side, in “full-potential” codes, no shape approximation for the potential is made, like in FPLO

and WIEN2k. (There are also mixtures of these two representations, where different parts of the potential (Hartree, exchange) are treated partially “full-” or non-“full-potential”.)

- The treatment of core electrons: there are again two possibilities. Either the core electrons are taken properly into account, which is the case for an “all-electron” code, or not, which is the case for a “pseudo-potential” code. In the latter case, the strong Coulomb potential of the nucleus and the effects of the tightly bound core electrons are replaced by an effective ionic potential acting on the valence electrons only. This allows pseudo-potential codes to calculate systems with a larger number of atoms than all-electron codes. Examples for pseudo-potential codes are ABINIT, SIESTA and VASP. Examples for all-electron codes, which are by way of comparison slower but therefore more accurate, are FPLO and WIEN2k.
- The numerical treatment: also here, there are in principle two possibilities. The first method is the one discussed above, the (full) diagonalization, which scales with N^3 (true for FPLO and WIEN2k). The second possibility is the so-called “order N ” method, which scales linearly with the size of the system. This method is based on a different algorithm, due to different approaches to describe the solid. Order N methods are still under development and there are still problems in actual practice. Since this is not topic of this thesis, it will not be discussed further. For more information see Ref. [23].

2.3.1 The linearised augmented plane wave code WIEN2k

The WIEN2k code is a full-potential, all-electron and full diagonalization code, with basis functions that are nonzero over the entire unit cell. In the linearised augmented plane wave (LAPW) method, the crystal is divided into two regions: non-overlapping atomic spheres (centred at the atomic sites) (called muffin tin spheres) and an interstitial region. In the interstitial region, the wave functions are rather flat and can therefore be described by plane waves

$$\phi_{\vec{k}_n} = \frac{1}{\sqrt{\omega}} e^{i\vec{k}_n \cdot \vec{r}}. \quad (2.8)$$

With $\vec{k}_n = \vec{k} + \vec{K}_n$, where \vec{K}_n are the reciprocal lattice vectors and \vec{k} the wave vectors inside the first Brillouin zone.

In the atomic sphere, the wave function oscillates and is better described by a set of atomic-like orbitals. These orbitals are a linear combination of radial functions and spherical harmonics

$$\phi_{\vec{k}_n} = \sum_{lm} \left[A_{lm, \vec{k}_n} u_l(r, E_l) + B_{lm, \vec{k}_n} \dot{u}_l(r, E_l) \right] Y_{lm}(\hat{r}). \quad (2.9)$$

Here, $u_l(r, E_l)$ is the solution of the radial Schrödinger equation for the energy E_l and $\dot{u}_l(r, E_l)$ is the energy derivative of $u_l(r, E_l)$ at E_l . Taking into account the energy derivative of $u_l(r, E_l)$ (the linear term in a Taylor expansion) improves⁹ this method from the augmented plane wave (APW) to the *linearised* augmented plane wave (LAPW) method. The coefficients A_{lm, \vec{k}_n} and B_{lm, \vec{k}_n} are obtained from the boundary conditions that the plane waves and the atomic-like orbitals match in value and slope at the sphere border. A plane wave, Eq. (2.8), and atomic-like functions, Eq. (2.9), then form a single LAPW basis function.

We choose the LAPW’s as given above as basis for the solution of the Kohn-Sham equation, see Eq. (2.6)

$$\psi_{\vec{k}} = \sum_n c_n \phi_{\vec{k}_n}. \quad (2.10)$$

⁹In principle, APW is much more accurate than LAPW. But it is hopelessly slow, because its basis functions are energy-dependent. By linearising this energy dependence a bit of accuracy is lost, but a huge amount of speed is gained.

Here, the coefficients c_n are determined by the Rayleigh-Ritz variational principle. The cutoff parameter $R_{mt}K_{max}$ (usually between 6 and 9) controls the convergence of the basis set: R_{mt} is the smallest atomic sphere radius in the unit cell and K_{max} the magnitude of the largest \vec{K} vector in Eq. (2.10).

This method distinguishes between three different types of electronic states. Core states are confined inside the corresponding atomic sphere and are very deep in energy (more than 90 eV below the Fermi energy). Semi-core states are not entirely confined inside the sphere – a few percent of the charge are outside of the corresponding sphere – and their energy well below the Fermi energy, but much higher compared to the core states (between 13.6 and 90 eV below the Fermi energy). The valence states have a significant amount of charge outside the sphere and are the highest (occupied) states.

In order to treat the semi-core states more accurately, additional basis functions, so-called “local orbitals” (LO) can be added

$$\phi_{lm}^{LO} = \sum_{lm} [A_{lm}u_l(r, E_{1,l}) + B_{lm}\dot{u}_l(r, E_{1,l}) + C_{lm}u_l(r, E_{2,l})] Y_{lm}(\hat{r}). \quad (2.11)$$

Since this orbital is only nonzero inside the atomic sphere under consideration, it is called *local orbital*. This way, semi-core and valence states with same l value, but different n value (*e.g.*, $3p$ and $4p$ states) can be treated more adequately. Here, $u_l(r, E_{1,l})$ and $\dot{u}_l(r, E_{1,l})$ are taken from the LAPW basis for the high lying states (*e.g.*, the $4p$ states) and a single radial function at the low lying energy $E_{2,l}$ is sufficient to describe $u_l(r, E_{2,l})$ for the low lying states (*e.g.*, the $3p$ states). Since the local orbitals are not connected to the interstitial plane waves, no \vec{k} dependence is needed. The coefficients A_{lm} , B_{lm} and C_{lm} are determined from the conditions that the local orbital is normalised and has zero value and slope at the sphere boundary.

Nowadays, WIEN2k can be used with an APW+lo or with a LAPW basis set as well, where the APW+lo basis functions follow the same general idea as LAPW but in a somewhat different mathematical formulation. They turn out to provide a more efficient (*i.e.* smaller) basis [24].

See the WIEN2k user guide [1] or the WIEN2k based LAPW documentation [25] for more details.

2.3.2 The full-potential local-orbital code FPLO

Since most calculations were performed with the FPLO code and also the implementation of the electric field gradient in the FPLO code will be shown (Section 4), this code is presented in more detail. The following sections are based on the FPLO version 5, since this version was mainly used in this work. Differences to the new versions are given at the end of this section.

The FPLO code is a full-potential band structure scheme and based on linear combinations of overlapping non-orthogonal atom-centred orbitals. The core relaxation is properly taken into account (so called all-electron method). The crystal potential and density are represented as a lattice sum of local overlapping non-spherical contributions. FPLO is numerically very efficient, because it uses a self-adjusting minimal basis set. The eigenvalue problem is reduced to the dimension of a minimum valence orbital basis only. The valence basis is completed by a few semicore states and polarisation states. The total energy calculated by FPLO agrees with the total energy obtained by the WIEN code within the chemical accuracy (order of mHa per atom) [26]. In addition, the DOS, the band structure and differences in energy, which are more relevant, agree very well between these two codes [27, 28, 29].

Minimal basis

The eigen functions of the Kohn-Sham Hamiltonian \hat{H}_{KS} are given by Bloch states $\psi_{\vec{k},n}$ (due to the periodicity of the crystal)

$$\psi_{\vec{k},n}(\vec{r}) = \sum_{\vec{R},\vec{s},L} c_{\vec{s}L}^{\vec{k},n} \varphi_{\vec{s},L}(\vec{r} - \vec{R} - \vec{s}) e^{i\vec{k}(\vec{R} + \vec{s})}. \quad (2.12)$$

Here, the index L describes a complete set of atomic quantum numbers $L = \{n, l, m\}$. The basis states $\varphi_{\vec{s},L}$ (which are $|\phi_n^B\rangle$ in the simple notation of Eq. (2.6)) are local orbitals centred at the site \vec{s} in the elementary cell defined by the lattice vector \vec{R} . They are expanded in terms of localised atomic-like orbitals consisting of radial functions $\phi_{\vec{s}}^l$ (solutions of the radial Schrödinger or Dirac equation) and spherical harmonics

$$\varphi_{\vec{s},L}(\vec{r} - \vec{R} - \vec{s}) \equiv \phi_{\vec{s}}^l(|\vec{r} - \vec{R} - \vec{s}|) Y_L(\vec{r} - \vec{R} - \vec{s}). \quad (2.13)$$

The basis states are divided into core and valence states. Core states (denoted by $L = c$) are defined as strongly localised states (no overlap between states of different sites). This (very good) approximation leaves them orthogonal

$$\langle \varphi_{\vec{R}' + \vec{s}', c'} | \varphi_{\vec{R} + \vec{s}, c} \rangle = \delta_{c', c} \delta_{\vec{R}' + \vec{s}', \vec{R} + \vec{s}}.$$

The valence orbitals (denoted by $L = v$) are non-orthogonal and overlap with valence and also with core orbitals from neighbouring sites. All valence orbitals are compressed by a confining potential $v^{\text{conf}} = (r/r_0)^4$, where r_0 is given by the nearest neighbour distance r_{NN} and a parameter¹⁰ x_0 with $r_0 = (x_0 r_{NN}/2)^{3/2}$. These compressed valence orbitals have higher energy levels and are more suitable for the construction of extended wave functions compared to their uncompressed counterparts.

Due to the separation of core and valence states, the overlap matrix in the secular equation (2.7) contains four blocks (core-core, 2×core-valence and valence-valence). The core-core block is already diagonal due to the orthogonality of the core states. The remaining blocks can be rewritten, yielding a reduced problem, which only contains the eigenvalue problem of the valence states. This saves calculational effort, since the diagonalization of a matrix scales with the cube of its size N^3 . For more details see Section 2 A in Ref. [2].

Electron density and potential

The total electron density is obtained by summing over all occupied (*occ*) states

$$\begin{aligned} n(\vec{r}) &= \sum_{\vec{k},n}^{\text{occ}} \psi_{\vec{k},n}(\vec{r}) \psi_{\vec{k},n}^*(\vec{r}) \\ &= \sum_{\vec{k},n}^{\text{occ}} \sum_{\vec{R} + \vec{s}, L} \sum_{\vec{R}' + \vec{s}', L'} c_{\vec{s}L}^{\vec{k},n} c_{\vec{s}'L'}^{*\vec{k},n} \varphi_{\vec{s},L}(\vec{r} - \vec{R} - \vec{s}) \varphi_{\vec{s}',L'}(\vec{r} - \vec{R}' - \vec{s}') e^{i\vec{k}(\vec{R} + \vec{s} - \vec{R}' - \vec{s}')}. \end{aligned} \quad (2.14)$$

This sum can be split into on-site $\vec{R} - \vec{s} = \vec{R}' - \vec{s}'$ and off-site $\vec{R} - \vec{s} \neq \vec{R}' - \vec{s}'$ contributions. For the core-core density, only the on-site (there is no off-site contribution) and for the core-valence and valence-valence density both contributions are calculated separately. Details are given in Section 2 B in Ref. [2].

¹⁰The parameter x_0 is optimised with respect to the total energy in each iteration step, *i.e.*, FPLO version 5 is not a fixed basis scheme.

In the end, for each lattice site \vec{s} the radial component of the density $n_{\vec{s},L}$ is given in spherical representation

$$n(\vec{r}) = \sum_{\vec{R}+\vec{s},L} n_{\vec{s},L}(|\vec{r} - \vec{R} - \vec{s}|) Y_L(\vec{r} - \vec{R} - \vec{s}). \quad (2.15)$$

The potential¹¹ is also expanded in spherical harmonics

$$v(\vec{r}) = \sum_{\vec{R}+\vec{s},L} v_{\vec{s},L}(|\vec{r} - \vec{R} - \vec{s}|) Y_L(\vec{r} - \vec{R} - \vec{s}). \quad (2.16)$$

The radial component of the potential Eq. (2.16) is calculated from the radial solution of the Poisson equation $\Delta v(\vec{r}) = -4\pi n(\vec{r})$ ¹²

$$v_{\vec{s},L}(r) = \frac{4\pi}{2l+1} \left[\frac{1}{r^{l+1}} \int_0^r dx x^{l+2} n_{\vec{s},L}(x) + r^l \int_r^\infty dx x^{-l+1} n_{\vec{s},L}(x) \right]. \quad (2.17)$$

Here, the radial component of the density Eq. (2.15) is inserted. The angular momentum components of the local charge density give rise to multipole moments, which determine the Coulomb potential for large distances

$$v_{\vec{s},L}(r) = \frac{4\pi}{2l+1} \frac{Q_{\vec{s},L}}{r^{l+1}} \quad \text{with} \quad Q_{\vec{s},L} = \int_0^\infty dx x^{l+2} n_{\vec{s},L}(x).$$

Taking into account the nuclear (point) charge (which will partially compensate the $l=0$ part), the excess multipole moments at each lattice site are given by

$$A_{\vec{s},L} = Q_{\vec{s},L} - \frac{Z}{\sqrt{4\pi}} \delta_{L,0}.$$

In order to handle the long-range tails of the Coulomb potential, FPLO uses the so-called Ewald method: Gaussians are chosen to screen the excess moments

$$g_l = N_l r^l e^{-r^2 p^2}, \quad \text{with} \quad \int_0^\infty r^{2+l} g_l(r) dr \equiv 1.$$

Inserting a modified density¹³ $\tilde{n}_{\vec{s},L}(r)$

$$\tilde{n}_{\vec{s},L}(r) = n_{\vec{s},L}(r) - n_{\vec{s},L}^{Ew}(r), \quad \text{with} \quad n_{\vec{s},L}^{Ew}(r) = A_{\vec{s},L} g_l, \quad (2.18)$$

in Eq. (2.17) results in the local Hartree potential, where the asymptotic behaviour is $v_{\vec{s},L}^H(r) = +\sqrt{4\pi} Z \delta_{L,0} / r$. This is exactly cancelled by the nuclear potential. Thus, in the Coulomb potential (which adds the nuclear potential to the Hartree potential) the long-range tails are well compensated.

In order to obtain the correct potential, the Ewald potential ($n_{\vec{s},L}^{Ew}(r)$ in Eq. (2.17)) has to be added to the Coulomb potential. Since this contribution contains the troublesome long-range tails, this is done in Fourier space. The Fourier transformation of the Ewald density yields (see Ref. [30] for a detailed derivation)

$$n_{\vec{G}}^{Ew} = \frac{(4\pi)^{\frac{3}{2}}}{V_{uc}} \sum_{\vec{s},L} A_{\vec{s},L} (-i)^l e^{-i\vec{G}\vec{s}} Y_{lm}(\vec{G}) \frac{N_l G^l}{(2p)^3 (2p^2)^l} e^{-\frac{G^2}{4p^2}}. \quad (2.19)$$

¹¹The potential will be important in Section 4.1 and is therefore discussed more in detail.

¹²In SI units, the Poisson equation is $\Delta v(\vec{r}) = -n(\vec{r})/\epsilon = -n(\vec{r})4\pi a_0 \text{Ha}/e^2$. In order to be consistent with Refs. [2, 30], we will use the definition as given above.

¹³The definitions deviate in prefactors and signs between Refs. [2] and [30], however, the results are of course identical. In this thesis (this chapter and Section 4.1) the definitions of Ref. [30] are used.

The Ewald potential is obtained by applying the Poisson equation to a Fourier sum

$$\Delta \sum_{\vec{G}} e^{i\vec{G}\vec{r}} v_{\vec{G}} = - \sum_{\vec{G}} G^2 e^{i\vec{G}\vec{r}} v_{\vec{G}} = -4\pi \sum_{\vec{G}} e^{i\vec{G}\vec{r}} n_{\vec{G}}^{Ew} \Rightarrow v_{\vec{G}} = \frac{4\pi}{G^2} n_{\vec{G}}^{Ew}. \quad (2.20)$$

The correct potential is obtained, when the Ewald potential

$$v^{Ew}(\vec{r}) = \sum_{\vec{G}} e^{i\vec{G}\vec{r}} v_{\vec{G}} \quad (2.21)$$

(with Eq. (2.19) and Eq. (2.20)) is added to the local Coulomb potential, given above.

The exchange and correlation potential depends in a non-linear way on the density and hence requires a special treatment. To achieve local decomposition, the shape function technique is applied. The shape function [30] is defined as

$$\sum_{\vec{R}+\vec{s}} f_{\vec{s}}(\vec{r} - \vec{R} - \vec{s}) \equiv 1.$$

This provides a locally finite lattice sum. The same method (also known as “partitioning of unity”) is applied for the Ewald potential. See Section 2 D in Ref. [2] for more details.

Super cells, VCA and CPA

There are four different possibilities to describe disorder (vacancies, interstitial atoms, substitution) within the FPLO code. The easiest way to simulate disorder is the rigid-band approximation. Here, the Fermi level in the DOS and band structure is shifted according to the number of electrons added to or taken out of the system. This approximation is of course very crude, since neither the Hamiltonian, nor the wave function is modified. It was used about 40 years ago, when less computational power was available. Today, the rigid-band approximation is mainly used to simplify discussions.

An improvement to the rigid-band approximation is to describe disorder with the virtual crystal approximation (VCA). In this approximation, the atom under consideration is replaced by a “virtual” atom, where the number of valence electrons is adjusted to the average number of valence electrons of that site, which is in general a non-integer number. The nuclear charge is modified by the same amount of protons to guarantee neutrality.

The coherent potential approximation (CPA) is a more accurate approximation to describe disorder, but it is more expensive. It needs more calculational effort and is not available in the newer FPLO versions (6-8). In CPA, the structure is described by an ensemble of configurations of atoms. But instead of introducing an ensemble of effective single-particle Hamiltonians, corresponding to these configurations, and summing over the squares of the Kohn-Sham orbitals, single-particle Green’s functions are used. Then the one-electron Green’s functions are expanded in the basis of modified atomic orbitals, yielding the spectral function $A(k, \omega)$ for the energy ω .

Another possibility to describe vacancies or substitution is to construct super cells. In this method, no approximation is made in calculating the properties and a perfectly ordered superstructure is obtained. Further advantages are that often different patterns can be compared and local distortion can be observed. However, the approximation here is the large (and often infinite) number of possible configurations is presented by a finite (and often very small) number of configurations. Another disadvantage is that super cells are demanding in computational time. The smaller the impurity concentration, the larger the super cells have to be. For instance, for AlB_2 , where the Al site is not fully occupied, a 4-fold super cell is needed to describe a vacancy concentration of 25 %, an 8-fold super cell is needed for vacancy concentration of 12.5 % and so on.

A promising approach to obtain all relevant information about a disordered compound is a combination of CPA and super cells. Since CPA includes the scattering of the impurity (potential), which is not the case for super cells and super cells describe local distortion, which is not the case for CPA, all aspects (random and local) are accounted for.

Except for CPA, the other three methods are also available in the WIEN2k code.

An example where all four methods are applied and their dis- and advantages can be seen is given in Section 5.2 for $\text{Al}_{1-x}\text{B}_2$.

Differences in the FPLO versions

The main difference between version 5 and version 6 is the construction of the basis. First of all, in version 6 the basis is not optimised in each iteration step anymore but fixed. The second difference is that the basis set can not be changed by the user (unless (s)he modifies the code). This is not necessary, because the basis is per default completed by polarisation states and a second/third set of valence orbitals. Containing 4(3) radial functions per nl shell this basis is larger and more complete than the default basis in FPLO 5 [31]. The same accuracy in FPLO 5 can be obtained by including polarisation states, which is especially important for the EFG calculation, see Section 4.2. The next difference is the construction of the potential. In version 5, the potential is stored site-centred. This makes CPA possible, because the total potential for each site must be known. In version 6, only the Hartree potential is stored site-centred. The Ewald and exchange-correlation potential is calculated on a fixed real space grid. Therefore, the total potential is stored point-wise on a partitioned 3D grid (Becke) [31]. This is beneficial for calculating open structures, but impedes the implementation of CPA. The main advantage of version 6 is that calculations are more accurate and much faster.

From version 6 to version 8, there were no changes in the conceptional method and the FPLO code was improved by implementing features like for instance a GGA functional, Wannier functions, VCA and a finite nucleus, which is very important for the correction to the quadrupole interaction, see Section 6.3. Furthermore, a molecule module has been implemented.

3 The electric field gradient: EFG

In this chapter, the electric field gradient (EFG) is introduced. In combination with spectroscopic methods, like for example nuclear magnetic resonance (NMR), the EFG is a valuable tool for extracting structural information (for instance about disorder) or for probing (indirectly) the chemical bond.

Here, we will present the definition and the properties of the EFG tensor and explain how it can be determined experimentally and theoretically.

3.1 Why is it interesting to study the EFG?

The chemical bonding in intermetallic compounds is far from being fully understood and presently under intense investigation. For a better understanding of the chemical bonding, a precise knowledge of the electron density is a precondition. A direct reconstruction of the electron density from X-ray data is limited in resolution up to now. Spectroscopic methods, like NMR measurements of the EFG, allow a much higher resolution, but provide only indirect information about the electron density. Electronic structure calculations can provide a straightforward relation between spectroscopic data and the electron density.

A concrete aspect is the fact, that many phases have a non-stoichiometric composition which has a significant impact on the properties in the solid state. This was investigated for CuAl_2 by the combined application of NMR spectroscopy and super cell calculations for various models describing the structural realisation of the deviation from the stoichiometric composition (*e.g.*, substitutions at the atoms or vacancies) and provided more insight in the local ordering of the atoms [32].

Other motives to study the EFG are for example impurities in semiconductors [33] or on surfaces [34]. This is possible due to the high sensitivity of the EFG to the local structure: each defect modifies the the local electrostatic potential at the position of the probe atom and creates its own characteristic EFG.

Furthermore, one can study the valency in *e.g.*, rare earth (*RE*) structures: REX_3 , where *X* is an element from group IIIa or IVa. The EFG is different for trivalent RE^{3+} and for divalent RE^{2+} [35]. In a simple picture this can be explained by the fact that a different valency results in a different distribution of the valence electrons, and hence a different degree of (an)isotropy of the electron charge density. As a consequence, the EFG will be larger or smaller.

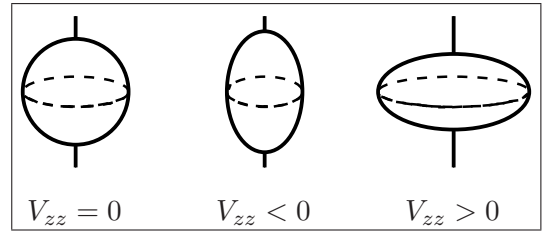
3.2 What is the EFG?

First of all, the EFG reflects the local structural symmetry of the crystalline solid. The EFG is nonzero if the charge density surrounding the nucleus violates cubic symmetry and therefore generates an inhomogeneous electric field at the nucleus.

The EFG is a traceless symmetric tensor of rank 2, defined as the second partial derivative (with respect to the spatial coordinates) of the electrostatic potential $v(\vec{r})$ evaluated at the position of the nucleus ($\vec{r} = 0$) [36]

$$V_{ij} = \left(\frac{\partial^2 v(\vec{r})}{\partial i \partial j} - \frac{1}{3} \delta_{ij} \Delta v(\vec{r}) \right) \Bigg|_{\vec{r}=0} \quad i, j = \{x, y, z\}. \quad (3.1)$$

Figure 3.1: Schematic picture of different electron charge distributions causing different EFGs: **left:** cubic electron charge density $\Rightarrow V_{zz} = 0$, **centre:** prolate electron charge density $\Rightarrow V_{zz} < 0$ and **right:** oblate electron charge density $\Rightarrow V_{zz} > 0$.



Only five independent quantities have to be provided in order to determine the tensor unambiguously: due to the commutation of partial derivatives, the tensor is symmetric and by definition, the tensor is traceless¹. Hence, it is possible to transform the EFG tensor in its principal axis system (PAS) with only three non-vanishing diagonal components, which are defined as $|V_{zz}| \geq |V_{yy}| \geq |V_{xx}|$.

It is a convention, to characterise the EFG tensor by its main component V_{zz} (often referred to as EFG) and the anisotropy parameter η defined as $\eta = (V_{xx} - V_{yy})/V_{zz}$ with $0 \leq \eta \leq 1$ ². The three remaining degrees of freedom are the three Euler angles from the transformation to the PAS of the EFG tensor. Depending on the symmetry of the crystal, the EFG tensor may already be diagonal and the PAS of the EFG tensor coincides with the coordinate system of the crystal structure. This is the case, for instance, for tetragonal symmetry, where V_{zz} points along the c axis and $V_{xx} = V_{yy}$ point along the a and b axis of the crystal structure. In general, these two coordinate systems can be different and V_{zz} must not be parallel to any of the axes of the crystal structure.

In the physical interpretation, the main component V_{zz} is a measure for the amount of deviation from cubic symmetry of the electron charge density in the proximity of the nucleus³. The sign of the EFG reveals additional information about the charge distribution, see Figure 3.1. If the electronic charge density is elongated along the z direction and assumes the shape of a cigar (so-called prolate distribution), V_{zz} is negative. If the electronic charge density is compressed along the z direction and takes the form of a pancake (so-called oblate distribution), V_{zz} is positive. The anisotropy parameter η contains information about the symmetry: η is zero if the site under consideration has a (at least) three-fold rotation axis.

Since the EFG tensor is traceless, $\sum_i V_{ii} = 0$, the EFG is zero for a charge density of cubic symmetry, where all three components are identical $V_{xx} = V_{yy} = V_{zz}$. In a crystal, such symmetry conditions appear if the point group of the site under consideration has cubic symmetry. For crystals, there are five such point groups: three tetrahedral ones (23 , $\bar{4}3m$ and $m\bar{3}$) and two octahedral ones (432 and $m\bar{3}m$). Or in Schönflies notation: T , T_d , T_h , O and O_h [41].

The EFG can be expressed in spherical notation as well, which will be particularly useful for the implementation of the EFG in band structure codes. Therefore, it is necessary to transform the Cartesian expression Eq. (3.1) into a spherical expression, which yields a symmetric and traceless

¹The trace of the first term in Eq. (3.1) is $\sum_i v_{ii} = \Delta v(0) \propto n(0)$. The electronic density at the nucleus $n(0)$ is nonzero, since s electrons and in relativistic treatment also $p_{\frac{1}{2}}$ electrons have a nonzero radial part at $r = 0$. Therefore, the trace has to be subtracted to guarantee five degrees of freedom. This condition appears naturally in the transformation from the Cartesian to the spherical notation, see Eq. (B.7) in Appendix B.

²This definition of η and $|V_{zz}| \geq |V_{yy}| \geq |V_{xx}|$ is most commonly used in the literature, *e.g.*, in Refs. [37, 38]. In the chemical community, also the convention $|V_{zz}| \geq |V_{xx}| \geq |V_{yy}|$ with $\eta = (V_{yy} - V_{xx})/V_{zz}$ (which also yields $0 \leq \eta \leq 1$) is used [39].

³That the EFG depends predominantly on the electronic density only and not on the nuclear charge contribution has been shown in by previous investigations, *e.g.*, Ref. [40] and in our work, see Chapter 5. It will be explained in more detail in Section 4.1.2.

3×3 -matrix with five independent angular momentum components v_{lm} ($l = 2, m = 0, \pm 1, \pm 2$) (see Appendix B):

$$V_{ij} = \sqrt{\frac{15}{4\pi}} \lim_{r \rightarrow 0} \frac{1}{r^2} \cdot \begin{pmatrix} v_{22}(r) - \frac{1}{\sqrt{3}}v_{20}(r) & v_{2,-2}(r) & v_{21}(r) \\ v_{2,-2}(r) & -v_{22}(r) - \frac{1}{\sqrt{3}}v_{20}(r) & v_{2,-1}(r) \\ v_{21}(r) & v_{2,-1}(r) & \frac{2}{\sqrt{3}}v_{20}(r) \end{pmatrix}. \quad (3.2)$$

3.3 Where does the EFG play a role in physics?

The EFG is the electronic part of the quadrupole interaction (QI), which in the classical picture is defined as

$$E_Q = \frac{1}{6} \sum_{i,j} V_{ij} Q_{ij}. \quad (3.3)$$

Here, V_{ij} is the symmetric and traceless EFG tensor as defined in Eq. (3.1). The nuclear part of the QI is the symmetric and traceless electric quadrupole moment tensor, which is defined as $Q_{ij} = \int (3x_i x_j - \delta_{ij} r^2) \rho(\vec{r}) d\vec{r}$, with ρ being the nuclear charge density, see Appendix A. Like the EFG tensor, which is represented by its main component V_{zz} , also the nuclear quadrupole moment tensor is represented by its zz component, the electric quadrupole moment $Q \equiv Q_{zz}$. Values for Q can be found in the literature, *e.g.*, in Refs. [42, 43].

In the quantum mechanical picture, the QI is described by the quadrupole Hamiltonian (see Appendix C)

$$\hat{H}_Q = \frac{eQV_{zz}}{4(2I-1)I\hbar^2} \left[(3\hat{I}_z^2 - \hat{I}^2) + \eta (\hat{I}_x^2 - \hat{I}_y^2) \right]. \quad (3.4)$$

Here, \hat{I} is the nuclear spin operator, with $\hat{I}^2 |I, m_I\rangle = \hbar^2 I(I+1) |I, m_I\rangle$. From its components $\hat{I} = (\hat{I}_x, \hat{I}_y, \hat{I}_z)$, an eigenvalue equation is given only for the z component $\hat{I}_z |I, m_I\rangle = \hbar m_I |I, m_I\rangle$. The QI is nonzero if two conditions are fulfilled: (*i*) non-cubic (electronic) charge density (hence nonzero EFG) and (*ii*) a non-cubic nuclear charge distribution, which causes a nonzero nuclear quadrupole moment Q . The latter condition is fulfilled for nuclei with nuclear spin $I \geq 1$. Nuclei with $I \leq \frac{1}{2}$ do not fulfil the condition $2I \geq L$ for multipole moments (2^L pole).

The quadrupole interaction is the dominating part in the second order contribution of the interaction energy of a nuclear charge density ρ in the electrostatic potential $v(\vec{r})$. This is explicitly shown in Chapter 6.

3.4 How can the EFG be measured?

The quadrupole interaction energy of a given nuclear state $|I, m_I\rangle$ is the expectation value of the quadrupole Hamiltonian Eq. (3.4) in that state. For illustration, we will consider an axially symmetric case ($\eta = 0$), where the energy eigenvalues are

$$\begin{aligned} E_Q &= \frac{eQV_{zz}}{4(2I-1)I\hbar^2} \langle I, m_I | (3\hat{I}_z^2 - \hat{I}^2) | I, m_I \rangle \\ &= \frac{eQV_{zz}}{4(2I-1)I} (3m_I^2 - I(I+1)) \\ \Rightarrow \Delta E_{m_I, m'_I} &= \frac{eQV_{zz}}{4I(2I-1)} 3|m_I^2 - m_I'^2|. \end{aligned} \quad (3.5)$$

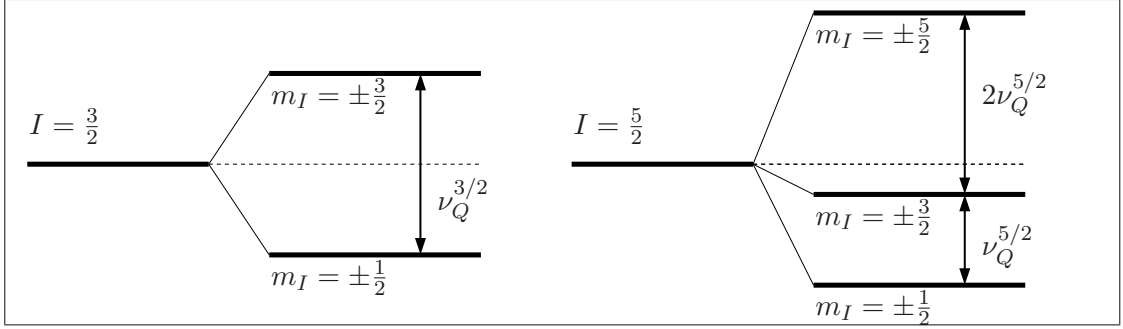


Figure 3.2: Nuclear energy levels due to the quadrupole interaction for a nuclear spin of $I = 3/2$ (left) and $I = 5/2$ (right). The frequencies $\nu_Q^{3/2}$ and $\nu_Q^{5/2}$, respectively, can be measured with nuclear quadrupole resonance (NQR).

If the two conditions for the QI are fulfilled, the m_I degeneracy from the monopole interaction is partially lifted. Since m_I enters Eq. (3.5) quadratically, the sign of m_I is still degenerate. For nuclei with spins $I = 3/2$ or $I = 5/2$, the energy level will split like shown in Figure 3.2. The definition of the quadrupole frequency⁴ [37]

$$\nu_Q = \frac{3eQV_{zz}}{2I(2I-1)\hbar} \quad (3.6)$$

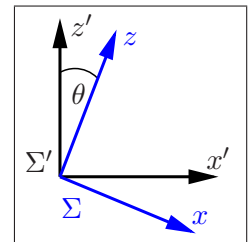
yields therefore

$$I = \frac{3}{2} : \quad \nu_Q^{3/2} = \frac{1}{2} \frac{eQV_{zz}}{\hbar} \quad \text{and} \quad I = \frac{5}{2} : \quad \nu_Q^{5/2} = \frac{3}{20} \frac{eQV_{zz}}{\hbar}.$$

The quadrupole frequency ν_Q Eq. (3.6) can directly be obtained from nuclear quadrupole resonance (NQR).

Another frequent method to measure ν_Q is nuclear magnetic resonance (NMR), where the sample is exposed to a magnetic field. The external magnetic field complicates the situation, because now we do not only have to consider the PAS of the EFG tensor (Σ), but also the the quantisation axis system (Σ') of the static magnetic field \vec{B}_0 , parallel to the z' axis, see Figure 3.3. We choose without loss of generality the y' axis to be parallel to y (rotation symmetry around a magnetic field) and obtain an angle θ between z' and z . If the quadrupole coupling is weak compared to the magnetic interaction⁵, the nuclear spin I will be quantised along the z' axis and the energy

Figure 3.3: The two coordinate systems Σ and Σ' needed to understand nuclear magnetic resonance: Σ describes the principal axis system of the EFG tensor and Σ' the quantisation axis system of the external magnetic field, parallel to the z' axis. The angle θ is needed for evaluating the spectrum, see also Eq. (3.7).



⁴Note, that there is also a definition without I , the nuclear quadrupole coupling constant (NQCC) is defined as $C_Q = eQV_{zz}/\hbar$.

⁵This is the case, if the energy E_{Zee} from the Zeeman effect due to the magnetic interaction is at least one order of magnitude larger than the energy E_Q due to the quadrupole interaction [44].

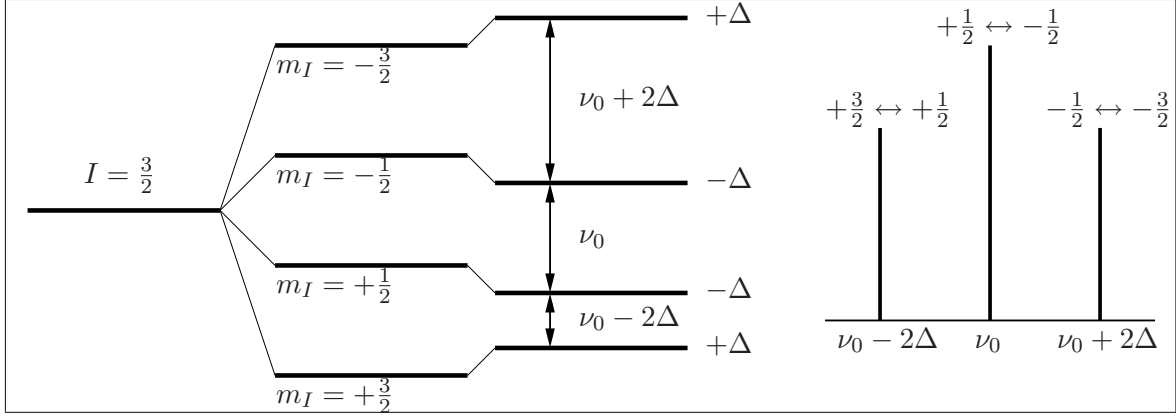


Figure 3.4: Nuclear energy levels due to the Zeeman effect (equidistant energy levels) and the quadrupole interaction (shifts in the energy levels) for a nucleus with $I = 3/2$ for fixed θ and $\eta = 0$. The three frequencies ν_0 , $\nu_0 + 2\Delta$ and $\nu_0 - 2\Delta$ can be measured with nuclear magnetic resonance (NMR).

eigenvalues become angular dependent (see Ref. [38]) (still for the case $\eta = 0$)

$$E_Q = \frac{eQV_{zz}}{4(2I-1)I} \frac{3\cos^2\theta - 1}{2} (3m_I^2 - I(I+1)). \quad (3.7)$$

Furthermore, the Zeeman effect has to be taken into account and perturbation theory has to be applied: the QI is treated as a perturbation to the Zeeman effect. If the quadrupole interaction is at least two orders of magnitude smaller than the magnetic Zeeman interaction, *i.e.*, $E_Q \ll E_{Zee}$, it is sufficient to consider only the first order in perturbation theory. For a nuclear spin of $I = 3/2$ the energy levels split and shift like shown in Figure 3.4.

The energy level is split by the Zeeman effect into four equidistant energy levels (m_I degeneracy lifted) with only one transition frequency ν_0 . The QI splits this single Zeeman transition frequency ν_0 into three frequencies by shifting the energy levels with same $|m_I|$ by the same amount. Therefore, three spectral lines will be obtained: a main transition ν_0 and two satellite transitions $\nu_0 \pm 2\Delta$. The transition rule $\Delta m_I = \pm 1$ applies here.

If the quadrupole interaction is only one order of magnitude smaller than the magnetic Zeeman interaction, *i.e.*, $E_Q < E_{Zee}$, also the second order perturbation theory must be taken into account [44]. This modifies the central transition, as it can be seen clearly in the NMR spectrum in Figure 3.5: the central transition for the nucleus corresponding to the red line (marked by a red circle) has a complex line shape instead of a sharp peak, as it is the case for the nucleus corresponding to the blue line.

The quadrupole frequency can be determined from the distance of the satellites $\nu_Q = 4\Delta$ with $\Delta = [eQV_{zz}/(8h)](3\cos^2\theta - 1)$ or from the central transition. If $\eta \neq 0$, both methods are possible [44]. Often, the NMR experiment is carried out on a powder sample - and not on a single crystal - smearing the sharp peaks into broader signals. The peaks for the satellite shoulders (highest intensity) are obtained for $\theta = 90^\circ$.

In the left panel of Figure 3.5, an example of an NQR spectrum for the two isotopes ^{63}Cu and ^{65}Cu in $\text{Cu}_2(\text{PO}_3)_2\text{CH}_2$, see Section 5.4, is shown. There is one spectral line for the ^{63}Cu and one for the ^{65}Cu isotope. Different isotopes have different quadrupole frequencies since they have different quadrupole moments Q , compare Eq. (3.6). The quadrupole frequency can directly be read off from the spectrum. The right panel shows an example of an NMR spectrum for ^{71}Ga in SrGa_4 , see Section 5.1. In this spectrum, only one isotope is shown. But SrGa_4 contains two

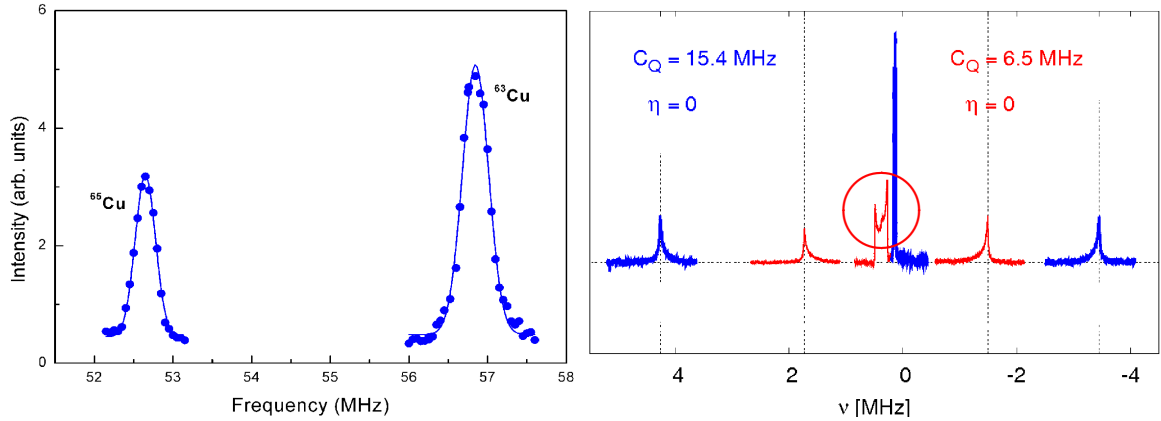


Figure 3.5: **Left:** NQR spectrum (taken from Ref. [108]) for ^{63}Cu and ^{65}Cu in $\text{Cu}_2(\text{PO}_3)_2\text{CH}_2$. Two frequencies due to two different isotopes. **Right:** NMR spectrum for ^{71}Ga in SrGa_4 . Two sets of frequencies (main and satellite transitions) due to two crystallographic non-equivalent Ga atoms. The red circle marks the second order perturbation to the central transition, see text.

crystallographic (and therefore chemical) non-equivalent Ga atoms, located at different Wyckoff positions, see Figure 5.2. Crystallographic non-equivalent atoms have different EFGs due to different local environments and hence different quadrupole frequencies. Therefore, there are three spectral lines for ^{71}Ga at the Wyckoff positions ($4d$) and three for ^{71}Ga at ($4e$). Here, the quadrupole frequency is obtained from the distance of the satellites⁶.

In general one can write the electric hyperfine splitting as

$$\Delta E_Q = C(I)eQV_{zz}.$$

With $C(I)$ (constant for a given nuclear spin), the electronic charge e and the quadrupole moment Q known, it is possible from such experiments to obtain a value for V_{zz} . Be aware that from NMR and NQR experiments, only the absolute value of V_{zz} can be determined and its sign can not be provided. This can be understood from the spectra shown above, since only differences in the frequency are obtained. Perturbed angular correlation (PAC) and Mössbauer spectroscopy, which use radioactive isotopes, are other methods to measure the quadrupole interaction. While NMR and NQR require only weak conditions for the ground state of the isotope ($I \geq 1$, Q sufficiently large), these “radioactive” methods work only when the excited nuclear states, as well as transitions between them, fulfil several conditions. This severely limits the number of isotopes for which these methods can be applied. The main advantage of the “radioactive” methods is their higher sensitivity: because the probe isotopes emit radiation themselves, much fewer of them are needed compared to NMR/NQR: $\mathcal{O}(10^{11})$ vs. $\mathcal{O}(10^{17})$. Another advantage of the latter methods is that the sign of the quadrupole frequency can be obtained.

3.5 How can the EFG be calculated?

In former times, only the point charge model (PCM) was available to calculate a value for V_{zz} . The PCM is an attempt to describe the EFG in solids in the language of classical electrostatics.

⁶Here, the NQCC $C_Q = eV_{zz}Q/h = \nu_Q/2$ (for $I = 3/2$) is used

It has a long tradition in the analysis of EFG experiments.

$$V_{zz} = (1 - \gamma_{\infty})V_{zz}^{ext} + (1 - R)V_{zz}^{loc}. \quad (3.8)$$

The first term in Eq. (3.8) describes the contribution to the EFG by point charges, which represent the ions surrounding the nucleus of interest. The factor γ_{∞} is the so-called Sternheimer anti-shielding factor, which represents the deformation from spherical symmetry of the local electron distribution, a deformation induced by an aspherical arrangement of the surrounding ionic point charges. This leads usually to an amplification of the EFG ($\gamma_{\infty} \gg 1$), hence the name ‘anti-shielding factor’. The second term in Eq. (3.8) describes the part of the EFG that is intrinsic to the local electron distribution, *i.e.*, it is not induced by an external cause. A partially filled $4f$ shell is an example of this.

Since 1985 it is also possible to calculate EFGs more accurately from first principle DFT codes. The full-potential linearised-augmented-plane-wave code WIEN [1] was the first DFT code in which the formalism to calculate the EFG was implemented [4]. There have been many good agreements between WIEN EFG calculations and ν_Q measurements since then, as can be found in, *e.g.*, Refs. [4, 33, 34, 35, 40, 45, 46].

As already said in the introduction, one task of this PhD work was to implement an EFG module in the full-potential local-orbital code FPLO [2]. This was done successfully in 2007. The implementation is explained in Section 4.1 and results are shown in Section 4.2 and Chapter 5.

4 Implementation of the EFG

After having explained the basics of the band structure code FPLO (Section 2.3.2) and after having introduced the electric field gradient (EFG) (Chapter 3), we will now discuss the implementation of the EFG in FPLO. Furthermore, expressions for the orbital contributions to the EFG are shown, for the FPLO and WIEN2k (Section 2.3.1) band structure code. Finally, results of the newly implemented EFG module are presented: EFGs obtained with FPLO will be compared with EFGs obtained from experiments and from other band structure codes.

4.1 Implementation in FPLO

We start with restating the connection between the Cartesian and spherical notation of the EFG tensor. With the definition

$$V_{2m} \equiv \sqrt{\frac{15}{4\pi}} \lim_{r \rightarrow 0} \frac{1}{r^2} v_{2m}(r), \quad (4.1)$$

the Cartesian EFG tensor can be expressed in (real) spherical components ($l = 2, m = \pm 2, \pm 1, 0$) (compare Eq. (3.2))

$$V_{ij} = \begin{pmatrix} V_{22} - \frac{1}{\sqrt{3}}V_{20} & V_{2,-2} & V_{21} \\ V_{2,-2} & -V_{22} - \frac{1}{\sqrt{3}}V_{20} & V_{2,-1} \\ V_{21} & V_{2,-1} & \frac{2}{\sqrt{3}}V_{20} \end{pmatrix}. \quad (4.2)$$

This connection between V_{ij} and V_{2m} will be important later. We start with the Cartesian notation. In FPLO, the EFG on a nucleus at a given lattice site \vec{s}_0 may be represented as the sum of two contributions, an on-site EFG due to v^{on} and an off-site EFG due to v^{off}

$$V_{ij} \equiv \left(\frac{\partial^2}{\partial_i \partial_j} - \frac{1}{3} \delta_{ij} \Delta \right) [v^{on}(\vec{r}) + v^{off}(\vec{r})] \quad (4.3)$$

$$v^{on}(\vec{r}) = \sum_L \int d^3\vec{r}' \frac{n_{\vec{s}_0,L}(|\vec{r}'|) Y_L(\vec{r}')}{|\vec{r} - \vec{s}_0 - \vec{r}'|}, \quad (4.4)$$

$$v^{off}(\vec{r}) = \sum_{\vec{R} + \vec{s} \neq \vec{s}_0, L} \int d^3\vec{r}' \frac{n_{\vec{s},L}(|\vec{r}'|) Y_L(\vec{r}')}{|\vec{r} - \vec{R} - \vec{s} - \vec{r}'|} - \sum_{\vec{R} + \vec{s} \neq \vec{s}_0} \frac{Z_{\vec{s}}}{|\vec{r} - \vec{R} - \vec{s}|}, \quad (4.5)$$

where Y_L are the (real) spherical harmonics, \vec{R} is a lattice vector, and \vec{s} is an atom position in the unit cell. In case of the density n , the index $L = lm$ also absorbs the spin and the principal quantum number. The first term in Eq. (4.3), the on-site contribution v^{on} , comes from the contribution of the electron density of the site \vec{s}_0 , and the second term, the off-site contribution v^{off} , comes from the potential due to all other atoms.

Since the angular momentum components of the local charge density give rise to multipole moments, which determine the Coulomb potential for large distances, FPLO uses the Ewald method to handle the long-range behaviour (see Section 2.3.2, page 10). The density is modified with a Gaussian auxiliary density $\tilde{n}_l(r) = n_l(r) - n_l^{Ew}(r)$. Inserting this modified density in the potentials Eq. (4.4) and Eq. (4.5) yields

$$v(\vec{r}) = \tilde{v}^{on}(\vec{r}) + v^{Ew,on}(\vec{r}) + \tilde{v}^{off}(\vec{r}) + v^{Ew,off}(\vec{r}) = \tilde{v}^{on}(\vec{r}) + \tilde{v}^{off}(\vec{r}) + v^{Ew}(\vec{r}). \quad (4.6)$$

The EFG is obtained by calculating the radial $2m$ components (according to Eq. (4.1) and Eq. (4.2)) of these three contributions.

We start with calculating the radial $2m$ component of the first contribution in Eq. (4.6): $\tilde{v}^{on}(\vec{r})$. This is obtained by inserting the modified density $\tilde{n}_{\vec{s}_0,L}(r)$ in Eq. (4.4) and then applying the Poisson equation. This yields (compare Eq. (2.17), with R_{max} being the last point on the radial mesh)

$$\tilde{v}_{\vec{s}_0,L}(r) = \frac{4\pi}{2l+1} \left[\frac{1}{r^{l+1}} \int_0^r dx x^{l+2} \tilde{n}_{\vec{s}_0,L}(x) + r^l \int_r^{R_{max}} dx x^{-l+1} \tilde{n}_{\vec{s}_0,L}(x) \right].$$

Taking the limit $r \rightarrow 0$ and using l'Hôpital's rule, we obtain for the $2m$ component divided by r^2

$$\lim_{r \rightarrow 0} \frac{\tilde{v}_{\vec{s}_0,2m}(r)}{r^2} = \frac{4\pi}{5} \left[\frac{n_{\vec{s}_0,2m}(0)}{5} + \int_0^{R_{max}} dx x^{-1} \tilde{n}_{\vec{s}_0,2m}(x) \right]. \quad (4.7)$$

The first term in Eq. (4.8) is the $2m$ component of the electronic density at the nucleus $n_{\vec{s}_0,2m}(0) \equiv \tilde{n}_{\vec{s}_0,2m}(0)$. The n_{2m} component of a spherical harmonic expansion of an analytic function around a given point behaves as $n_{2m} = \mathcal{O}(r^2)$. The only non-analyticities of the electron density are caused by the singularities of the spherical nuclear potential. Therefore, $n_{2m}(0) = 0$. This can be shown explicitly both in a non-relativistic and full relativistic theory [47]. Therefore, we obtain for the \tilde{V}_{2m}^{on} component (from which \tilde{V}_{ij}^{on} is obtained via Eq. (4.2))

$$\tilde{V}_{2m}^{on} = 2\sqrt{\frac{3\pi}{5}} \int_0^{R_{max}} dx x^{-1} \tilde{n}_{\vec{s}_0,2m}(x). \quad (4.8)$$

Now, we focus on the radial $2m$ component of the second contribution in Eq. (4.6): $\tilde{v}^{off}(\vec{r})$. This potential is given by inserting the modified density $\tilde{n}_{\vec{s},L}(r')$ in Eq. (4.5). Since the density $\tilde{n}_{\vec{s},2m}$ is not given at the site \vec{s}_0 , where the atom under consideration is sitting, this equation has to be expanded around \vec{s}_0 . This expansion and the resulting (lengthy) expression for \tilde{V}_{2m}^{off} (from which \tilde{V}_{ij}^{off} is obtained via Eq. (4.2)) is explicitly presented in Appendix F.

The third and last contribution we have to calculate is $v^{Ew}(\vec{r})$ in Eq. (4.6). Here, no $2m$ component has to be calculated since V_{ij}^{Ew} can be obtained directly. This is due to the Fourier expansion of the Ewald potential Eq. (2.21). V_{ij}^{Ew} is obtained by differentiating $v^{Ew}(\vec{r}) = \sum_{\vec{G}} e^{i\vec{G}\vec{r}} v_{\vec{G}}^{Ew}$:

$$V_{ij}^{Ew} = - \sum_{\vec{G}} \left(G_i G_j - \frac{1}{3} \vec{G}^2 \delta_{ij} \right) \Re(e^{i\vec{G}\vec{s}} v_{\vec{G}}^{Ew}). \quad (4.9)$$

The total EFG tensor V_{ij} is given by the sum of these three contributions

$$V_{ij} = \tilde{V}_{ij}^{on} + \tilde{V}_{ij}^{off} + V_{ij}^{Ew}. \quad (4.10)$$

In order to analyse the on-site and off-site contributions, we define the on-site EFG as being the first term in Eq. (4.3), but calculated from the unmodified density, which is Eq. (4.8) without the tilde

$$V_{2m}^{on} = 2\sqrt{\frac{3\pi}{5}} \int_0^{R_{max}} dx x^{-1} n_{\vec{s}_0,2m}(x). \quad (4.11)$$

The off-site EFG is then given by

$$V_{2m}^{off} = V_{2m} - V_{2m}^{on}. \quad (4.12)$$

4.1.1 Orbital contributions to the EFG

In FPLO, the electron density is separated into a net density and an overlap density (see Eq. (2.14) in Section 2.3.2). The dominating net density is calculated from two orbitals at the same site $\vec{R} + \vec{s} = \vec{R}' + \vec{s}' \equiv \vec{s}_0$

$$n_{\vec{s}_0}^{net}(\vec{r}) = \sum_{\vec{k}, n, L_1, L_2}^{occ} c_{\vec{s}_0 L_1}^{\vec{k}, n} \varphi_{\vec{s}_0, L_1}(\vec{r} - \vec{s}_0) \cdot c_{\vec{s}_0 L_2}^{\star \vec{k}, n} \varphi_{\vec{s}_0, L_2}(\vec{r} - \vec{s}_0), \quad (4.13)$$

where the basis functions $\varphi_{\vec{s}_0, L}$ are localised on the atomic site \vec{s}_0 , cf. Eq. (2.13)

$$\varphi_{\vec{s}_0, L}(\vec{r} - \vec{s}_0) \equiv \phi_{\vec{s}_0}^L(|\vec{r} - \vec{s}_0|) Y_L(\vec{r} - \vec{s}_0).$$

The $2m$ component of the radial net density, which is needed for the net EFG¹, can be decomposed into a sum of a product of radial wave functions (inserting Eq. (4.13) in the definition of the $2m$ component)

$$\begin{aligned} n_{\vec{s}_0, 2m}^{net}(r) &= \int n_{\vec{s}_0}^{net}(\vec{r}) Y_{2m}(\vec{r} - \vec{s}_0) d\Omega \\ &= \sum_{L_1, L_2} c_{L_1 L_2} \phi_{\vec{s}_0}^{l_1}(|\vec{r} - \vec{s}_0|) \phi_{\vec{s}_0}^{l_2}(|\vec{r} - \vec{s}_0|) G_{l_1, l_2, 2}^{m_1, m_2, m}, \end{aligned} \quad (4.14)$$

where $G_{l_1, l_2, 2}^{m_1, m_2, m}$ are the (real) Gaunt coefficients and $c_{L_1 L_2} = \sum_{\vec{k}, n}^{occ} c_{\vec{s}_0 L_1}^{\vec{k}, n} c_{\vec{s}_0 L_2}^{\star \vec{k}, n}$. Due to the properties of the Gaunt coefficients², $n_{\vec{s}_0, 2m}^{net}$ can consist only of pp , dd , and sd (and if present pf and ff) contributions. These contributions to the on-site net EFG, $V_{zz}^{on, net}$, are obtained by inserting Eq. (4.14) into Eq. (4.11). For instance, the pp contribution $V_{2m, pp}^{on, net}$ is calculated from

$$\begin{aligned} V_{2m, pp}^{on, net} &= 2\sqrt{\frac{3\pi}{5}} \int_0^{R_{max}} dx x^{-1} n_{\vec{s}_0, 2m}^{net, pp}(x) \\ \text{with } n_{\vec{s}_0, 2m}^{net, pp}(x) &= [\phi_{\vec{s}_0}^1(x)]^2 \sum_{m_1, m_2} c_{1,1}^{m_1, m_2} G_{1,1,2}^{m_1, m_2, m}. \end{aligned} \quad (4.15)$$

The main component $V_{zz, pp}^{on, net} = \frac{2}{\sqrt{3}} V_{20, pp}^{on, net}$ is calculated from

$$n_{\vec{s}_0, 20}^{net, pp}(x) = \sqrt{\frac{1}{5\pi}} [\phi_{\vec{s}_0}^1(x)]^2 \sum_{\vec{k}, n}^{occ} \left(c_{\vec{s}_0, 1, 0}^{\vec{k}, n} c_{\vec{s}_0, 1, 0}^{\star \vec{k}, n} - \frac{1}{2} \left(c_{\vec{s}_0, 1, -1}^{\vec{k}, n} c_{\vec{s}_0, 1, -1}^{\star \vec{k}, n} + c_{\vec{s}_0, 1, 1}^{\vec{k}, n} c_{\vec{s}_0, 1, 1}^{\star \vec{k}, n} \right) \right). \quad (4.16)$$

We see that this density is proportional to the difference of occupation in p_z ($m = 0$) and $p_{x,y}$ ($m = \pm 1$) states. If the contribution of the overlap density and the contribution of the off-site atoms to the EFG are small ($V_{zz, pp} \approx V_{zz, pp}^{on, net}$) and if the pp contribution dominates ($V_{zz} \approx V_{zz, pp}$), we can relate V_{zz} to the anisotropy function Δp

$$\Delta p = \frac{1}{2}(n_x + n_y) - n_z, \quad (4.17)$$

where n_i , with $i = \{x, y, z\}$, is the number of electrons occupying the orbital p_i . This value can be obtained by integrating the orbital resolved partial DOS up to the Fermi energy.

¹The total EFG is calculated from the total density, which consists of the net and the overlap density. Hence, the net EFG is calculated from the (dominating) net density only.

² $l_1 + l_2 + l_3 = 2n$ with $n \in \mathbb{N}$, $|l_1 - l_2| \leq l_3 \leq |l_1 + l_2|$ and $m_1 + m_2 + m_3 = 0$.

For $l_3 = 2 \Rightarrow 1.$) $l_1 = l_2 \geq 1$ (pp , dd , and ff) and 2.) $|l_1 - l_2| = 2$ (sd and pf).

Note, that the orbital contributions to the EFG are calculated only for the on-site net EFG, *i.e.*, without the off-site contribution of the EFG and overlap contributions of the density. In order to have a descriptive picture, this can (in a first approximation) be compared to calculating the EFG only inside an atomic sphere, as used in the WIEN2k code, where the contributions of the other atoms are neglected³. In many cases, the off-site contribution to the EFG can be neglected, and in most cases, the overlap density contributes well below 10 % to the total EFG. Therefore, this approximation is valid for many compounds. However, it should always be checked carefully before drawing too hasty conclusions, see *e.g.*, Section 5.3, where in the perovskites SrTiO₃ and BaTiO₃ the off-site EFG is unusually large.

In WIEN2k, the EFG consists of two contributions, the so-called “valence” EFG, which is the EFG inside the atomic sphere only, and the “lattice” EFG, which is due to the interstitial region and all other atoms, that do not reach inside the atomic sphere under consideration. The latter is calculated from the difference of the total and the valence EFG. In WIEN2k, the orbital contributions to the EFG are calculated for the valence EFG, *i.e.*, inside the atomic sphere of the atom under consideration. This means, a similar approximation for the orbital contributions is made like in FPLO. Inside the sphere, the electronic charge density $n(\vec{r})$ is expressed as a spherical expansion [41]

$$n_{LM}(r) = \sum_{E < E_F} \sum_{l_1 m_1} \sum_{l_2 m_2} R_{l_1 m_1}(r) R_{l_2 m_2}(r) G_{L l_1 l_2}^{M m_1 m_2}. \quad (4.18)$$

The R_{lm} are radial functions with angular momentum l_1 or l_2 , and the $G_{L l_1 l_2}^{M m_1 m_2}$ are the Gaunt coefficients. For $L = 2$ we obtain the same conclusions as before. Hence, the EFG consists of pp , dd , sd , pf and ff contributions. If the lattice EFG is negligible, the total EFG may be expressed by the valence EFG, $V_{zz} \approx V_{zz}^{val}$. In many cases, the pp and dd contribution dominate, hence, $V_{zz} \approx V_{zz}^{pp} + V_{zz}^{dd}$.

Finally, we want to make a remark about the sign of the EFG. In the early days of the WIEN code (1985), the naive definition for the EFG was used, *e.g.*, in Ref. [4]. In this definition the sign is given as presented in this chapter. Shortly afterwards, the “experimental” convention was chosen [48], where the EFG has per definition the opposite sign⁴. The same convention (with the minus sign) is used in FPLO. This sign convention is the reason for the different signs in Eq. (4.16) and Eq. (4.17).

4.1.2 Remark about the potential

In the older literature from 10 to 20 years ago, the EFG is correctly defined as the second derivative of the total electrostatic potential, which is determined from the Poisson equation of the total (the nuclear and electronic) charge density, *e.g.*, in Refs. [36, 40, 49]. To be more precise: the total density is the density of all electrons and all nuclei, except for the nucleus under consideration, located at $r = 0$. Because the classical electrostatic interaction energy describes the interaction of that nucleus in the potential caused by the other nuclei and the electrons and the EFG is the second derivative of that potential.

In the newer literature, however, the EFG is sometimes introduced as the second derivative of the electronic potential only, *e.g.*, in Ref. [35, 45].

As we have seen in this chapter, the on-site EFG (or valence EFG), is indeed calculated from the electronic charge density only. Since it is calculated from an integral over the n_{2m} charge

³In the WIEN2k code, the contributions of the other atoms to that atomic sphere are of course not neglected: density from the neighbouring atoms that reaches into the present muffin tin sphere, is re-expanded in s, p, d, f, \dots contributions inside that sphere. Neglecting these contributions of the neighbouring atoms is comparable with neglecting the overlap density in FPLO.

⁴In the WIEN code, an “artificial” minus sign is introduced in the module lapw0.F of the WIEN2k source code: `efgb(jatom)%V20 = -V(nuc,LM1,jatom)`.

Table 4.1: V_{zz} in $10^{21}\text{V}/\text{m}^2$ for the hcp metals obtained by different band structure codes. The first column contains V_{zz} calculated 20 years ago with the WIEN code [40]. The values in the second column are obtained 20 years later with the same (but over the years modified) code⁶. The third column shows the EFG obtained with the Korringa-Kohn-Rostoker (KKR) method from 2005 [50]. The fourth column contains the EFG obtained from the FPLO code (version 5.00-19)⁵. The last column gives the experimental values, which were obtained in the 1980s, as given in [50]. Only for six elements the sign has been determined and is explicitly mentioned (no sign means undetermined).

Element	WIEN ^[40]	WIEN2k ⁶	KKR ^[50]	FPLO 5 ⁵	Exp. ^[50]
Be	−0.04	−0.06	−0.05	−0.05	0.04
Mg	+0.05	+0.04	+0.03	+0.05	0.05
Sc	+0.96	+0.96	+1.14	+0.86	0.38
Ti	+2.07	+1.75	+2.05	+1.68	1.61
Co	−0.19	−0.29	−0.14	−0.36	−2.90
Zn	+3.75	+4.29	+3.90	+4.13	+3.48
Zr	+4.29	+4.14	+4.15	+3.86	4.40
Tc	−1.47	−1.74	−1.53	−2.07	1.83
Ru	−1.23	−1.62	−1.37	−2.00	0.97
Cd	+7.62	+8.13	+8.53	+8.40	+6.50
La	−	+0.91	+1.28	+1.12	1.62
Hf	−	+8.12	+9.11	+7.42	+7.33
Re	−	−6.49	−3.37	−7.15	−5.12
Os	−	−7.02	−4.84	−7.42	−4.16

density inside the atomic sphere, in which only the nucleus at $r = 0$ is located. The potential caused by the other nuclei comes into play, however, when the off-site EFG (or lattice EFG) is calculated. In both WIEN2k and FPLO, this is done as a multipole summation in Fourier space see *e.g.*, Ref. [40] and Eq. (2.19), respectively. The Fourier sum is also the reason why no orbital contribution for the lattice (or off-site) EFG can be calculated.

As it was shown in previous investigations and will be shown in Chapter 5, the off-site contribution is negligible in many cases. Therefore, the EFG is a measure for the amount of deviation from cubic symmetry of the electron charge density in the proximity of the nucleus – as it was introduced in Section 3.2.

4.2 Implementation tests

In order to check the correctness of the EFG module, we calculated⁵ the EFGs for the hcp metals and compared them with experimental EFGs and EFGs obtained from other band structure codes⁶, see Table 4.1.

⁵FPLO 5: The calculations (using LDA) were performed in space group 194 (P63/MMC), with the atom at the Wyckoff position $2d$ (1/3,2/3,3/4). To ensure a converged k mesh, 819 k points were used in the irreducible part of the Brillouin zone. The experimental lattice parameters a and c as given in [50] were employed. Since the scalar relativistic treatment yields slightly too large EFGs for heavy elements (see also second remark at the end of this section), the full relativistic treatment was applied for the elements Tc to Os.

⁶WIEN2k: Same parameters as for the FPLO calculation with default values for all WIEN-specific parameters.

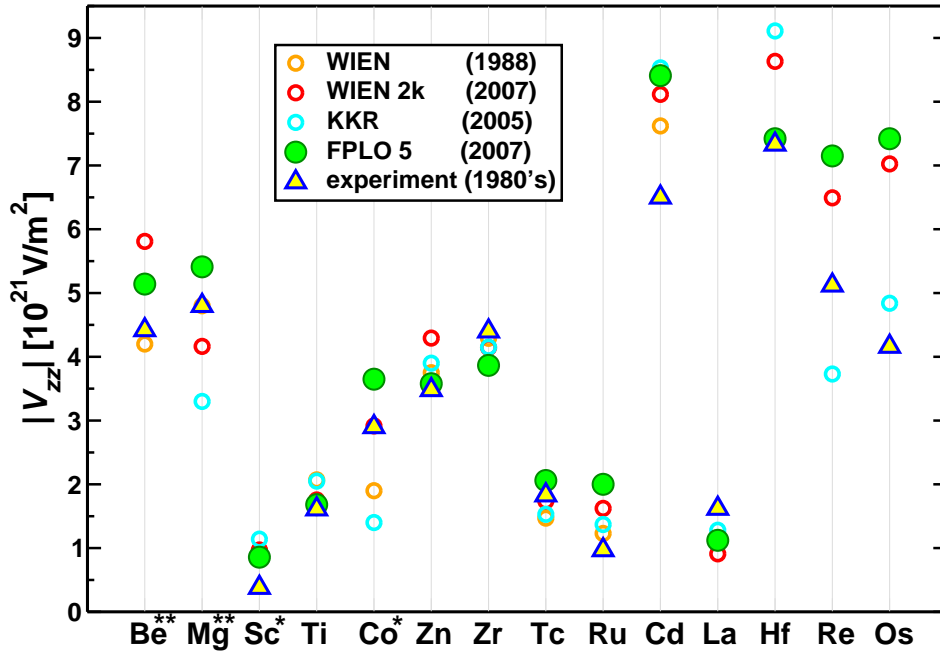


Figure 4.1: V_{zz} for the hcp metals obtained by different methods, WIEN [40], WIEN2k⁶, KKR [50], FPLO 5⁵ and experiment [50], *cf.* Table 4.1. For better visual comparison, all values are potted in 10^{21} V/m². A star * at the element symbol means this EFG value has to be divided by 10 (* by 100), see text.

The results of Table 4.1 are plotted in Figure 4.1. For better visual comparison, all values are potted with the first pre-decimal position in the unit 10^{21} V/m². The hcp metals with smaller EFGs are marked by stars *, which means this EFG value has to be divided by 10(*) or 100(**). In Table 4.1, we see that all codes agree in the sign of the EFG for any hcp element. Besides, also the absolute values of the EFGs obtained with the different band structure codes agree quite well. There are elements where the quantitative agreement is better (*e.g.*, Ti, Zn, Zr and Tc) and others, where the deviation is larger (*e.g.*, Re and Os). Focusing on FPLO and WIEN2k, also for the heavy elements Re and Os a good agreement is obtained.

FPLO gives also good results compared to the experimental values. We obtain the same sign (if determined) and in most cases also good agreement with the absolute value. Since such a comparison relies on the accuracies of the quadrupole moment Q , this could be one reason for the deviation for the heavy elements Re and Os, where FPLO and WIEN2k agree well.

In Chapter 5, there will be more comparisons of EFGs that have been calculated with FPLO and EFGs from WIEN2k and experiments. Since also there, good agreement is obtained, we conclude that the implementation of the EFG module in the FPLO code was successful.

But there are two points to consider. First, the EFG is very dependent on the basis. In FPLO 5, the standard basis is often not good enough and one must therefore carefully improve the basis (by adding polarisation states and checking grouping) to obtain a converged EFG, see Figure 4.2. Although many properties (*e.g.*, the bulk modulus) do not crucially depend on the basis, the same basis set dependence has been observed for the electron localisation function (ELF) [51]. In the new FPLO versions (6 to 8), the basis set has been improved and the default basis is sufficient.

The second point to consider is the scalar relativistic treatment, which also works quite well for most purposes. But as it will be explained in more detail in Section 6.3.2, there is an inherent

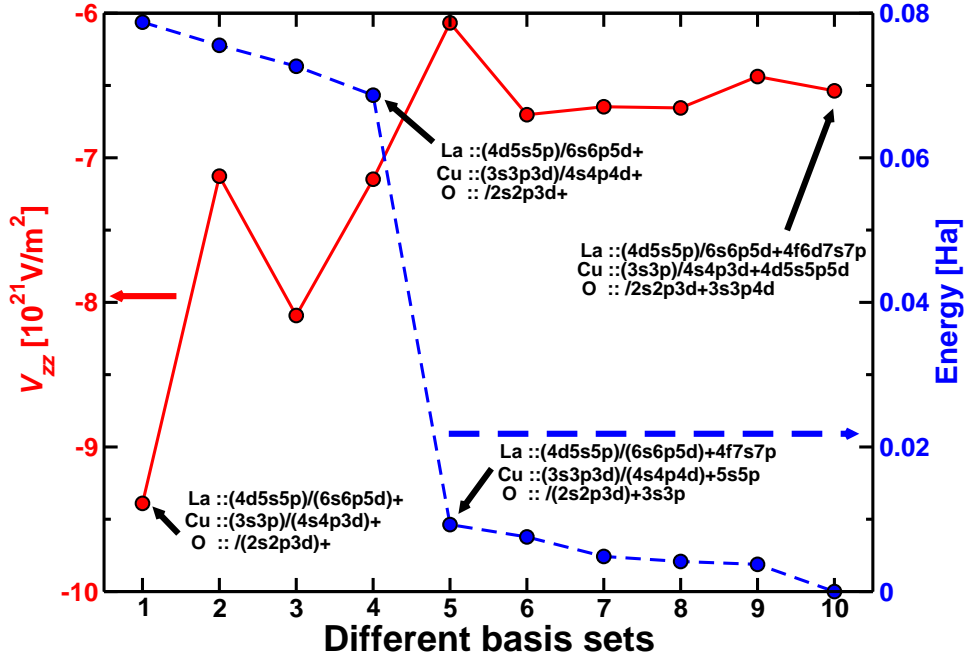


Figure 4.2: Basis dependence of the EFG (red, full line) and the energy (blue, dashed line) in FPLO 5 for the compound La_2CuO_4 as an example. For four examples the basis sets are given explicitly: modifications are done in the semicore/valence+polarisation states and in the grouping indicated by brackets () (*i.e.*, all states within the brackets have the same x_0 value, *cf.* page 10).

problem with any formulation of the scalar relativistic approximation for the $l = 2, m$ density, which is used to calculate the EFG. Two divergent $p_{1/2}$ functions cause to some extent wrong nonzero $n_{2m}(r)$ density components for $r \rightarrow 0$, which cause too large EFGs. This is less crucial in FPLO 5 and more crucial in FPLO 6 to FPLO 8. To avoid this problem for heavy elements, the full relativistic treatment should be and was chosen.

5 Application of the EFG: studied compounds

5.1 The di- and tetragallides MGa_2 and MGa_4

5.1.1 Introduction

Contrary to the ionic and covalent bond, which are rather well understood in their idealised form, the interplay of different bonding types is often complex. This is in particular the case for many intermetallic compounds. Since these often have a non-stoichiometric composition, a local probe method will be a valuable tool to examine the local geometry of the atoms. Nuclear magnetic resonance spectroscopy (NMR) is an example of such a method. In order to interpret the experimental data correctly, the observable quantity that is used to probe the local geometry needs to be well understood. In our case, we use the electric field gradient (EFG) as observable quantity. The EFG can be measured through the quadrupole interaction. This interaction between a non-cubic charge distribution and non-spherical nuclear charge distribution, can be measured by, *e.g.*, NMR, yielding the quadrupole coupling constant. The EFG can also be obtained from density functional theory (DFT) band structure calculations, which provides a straightforward relation between the spectroscopic data and the electron density. Hence, the evaluation of the EFG provides us with (indirect) information about the chemical bond. To investigate the reliability of EFG calculations for intermetallic compounds, two series of intermetallic compounds were chosen as model compounds: the digallides MGa_2 with $M = Ca, Sr$ and Ba and the tetragallides MGa_4 with $M = Na, Ca, Sr$ and Ba . These compounds fulfil the structural requirement of the Zintl concept, as the Ga atoms form poly-anionic components and the M atoms are isolated cations, but they do not fulfil the “8 – N counting rule”, except for the digallides in a first approximation [52].

Ga shows a high flexibility with respect to the chemical bonding: the hexagonal MGa_2 with $M = Sr, Ba$ crystallises in the AlB_2 -type structure (space group $P6/mmm$) [53], whereas $CaGa_2$ crystallises in the $CaIn_2$ -type structure (space group $P6_3/mmc$) [54], see Figure 5.1. MGa_2 with $M = Sr, Ba$ consists of a planar network of 3-bonded Ga atoms. In $CaGa_2$, the Ga layer is puckered and from the inter-atomic distances it can be concluded that the Ga atoms are 3+1-bonded, rendering a transition from a 2D net to a 3D framework [52, 54].

The tetragonal MGa_4 with $M = Na, Sr$ and Ba crystallises in the $BaAl_4$ -type structure (space group $I4/mmm$) [52, 55], see left panel of Figure 5.2. $CaGa_4$ crystallises in its own structure

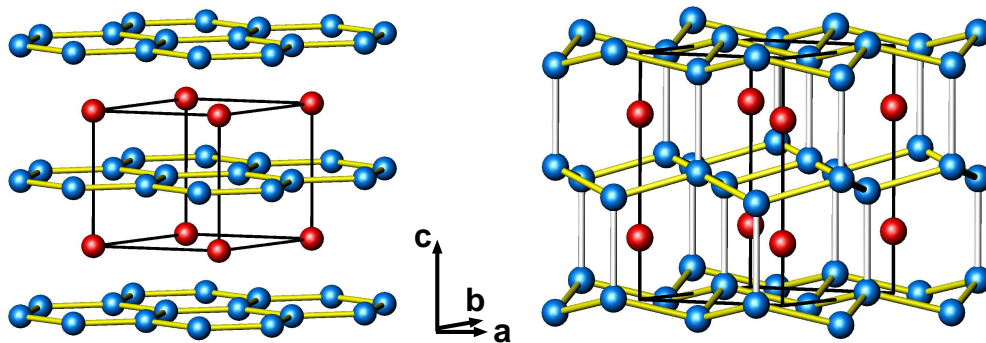


Figure 5.1: Crystal structure of MGa_2 ($M = Sr, Ba$) (left) and $CaGa_2$ (right), M is represented by the red and Ga by the blue spheres. The unit cells are shown by the black lines.

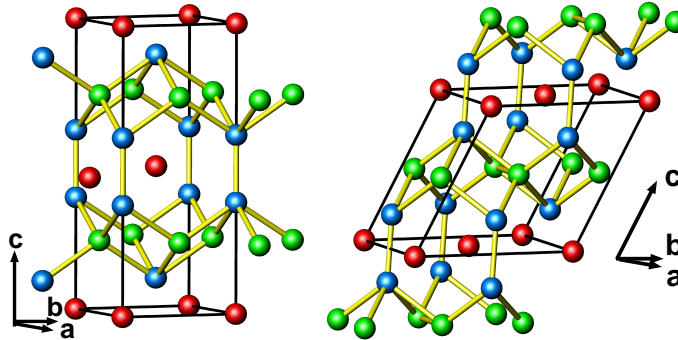


Figure 5.2: Crystal structure of MGa_4 ($M = Na, Sr, Ba$) (left) and $CaGa_4$ (right). M is represented by the red, the 4-bonded Ga(4b) by the green and the 5-bonded Ga(5b) by the blue sphere. The unit cell is shown by the black lines.

type, which is a monoclinic distorted version of the $BaAl_4$ -type (space group $C2/m$) [54], see right panel of Figure 5.2. In all four compounds, the Ga atoms form a 3D framework by four- and five-bonded Ga atoms, abbreviated with Ga(4b) and Ga(5b), respectively. In case of MGa_4 , Ga(4b) is located at the Wyckoff position $4d$ and Ga(5b) at $4e$ while in case of $CaGa_4$, Ga(4b) is located at the Wyckoff position $4h$ and Ga(5b) at $4i$.

We present a study of the electric field gradient for the different Ga environments in these compounds. For the di- and tetragallides, the quadrupole coupling constants were measured by NMR, and the EFG was calculated using two DFT band structure codes: FPLO and WIEN2k.

Furthermore, these compounds were used to test the newly implemented EFG module in the FPLO code by comparing the results to EFGs calculated with the well-established WIEN2k code, see Section 3.5.

5.1.2 Methods

As already mentioned in the introduction, the band structure codes FPLO and WIEN2k were used to calculate the EFG. The structural parameters were optimised with the FPLO code (version 5.00-19) [2], within the local density approximation. In the scalar relativistic calculations, the exchange and correlation functional of Perdew and Wang [15] was employed. As basis sets Ga(3s3p/4s4p3d+5s5p), Na(2s2p/3s3p3d+4s4p), Ca(3s3p/4s4p3d+5s5p), Sr(3p3d4s4p/5s5p4d+6s6p) and Ba(4s4p4d5s5p/6s6p5d+7s7p) were chosen for semicore/valence + polarisation states. The polarisation states were only applied in the EFG calculation. The lower lying states were treated fully relativistic as core states. 504, 432 and 455 k points were used in the irreducible part of the Brillouin zone (IBZ) for MGa_2 with $M = Ba, Sr$ and Ca , respectively. 349, 476, 405 and 405 k points were used in the IBZ for MGa_4 with $M = Na, Ca, Sr$ and Ba , respectively. The EFG and the Fermi surfaces were calculated with FPLO using the optimised structural parameters.

The EFG and the density of states (DOS) were also calculated with the full-potential augmented plane wave plus local orbitals (APW+lo) code WIEN2k [1], using the optimised structural parameters. To be consistent, the exchange and correlation potential of Perdew and Wang and the same number of irreducible k points as for the optimisation of the lattice parameters were used. The chosen atomic sphere radii (R_{MT}) are $R_{MT} = 2.5$ a.u. for M , and for Ga in the digallides: $R_{MT} = 2.46$ a.u. in $CaGa_2$, $R_{MT} = 2.33$ a.u. in $SrGa_2$ and $R_{MT} = 2.38$ a.u. in $BaGa_2$ and for Ga in the tetragallides: $R_{MT} = 2.29$ a.u. in $NaGa_2$, $R_{MT} = 2.27$ a.u. in $CaGa_2$, $R_{MT} = 2.31$ a.u. in $SrGa_2$ and $R_{MT} = 2.39$ a.u. in $BaGa_2$. In all compounds, the number of basis functions was determined by a value of $R_{MT}K_{max}$ of 8.5. The separation energy was set to -6.0 Ry, treating

Table 5.1: Experimental [52] and optimised (with the FPLO code [2]) lattice parameters for the $M\text{Ga}_2$ structures.

Compound	$a(\text{exp})$ [Å]	$a(\text{opt})$ [Å]	Dev. [%]	$c(\text{exp})$ [Å]	$c(\text{opt})$ [Å]	Dev. [%]
CaGa_2	4.4731(1)	4.3982	-1.7	7.3838(5)	7.1206	-3.6
SrGa_2	4.3484(2)	4.2911	-1.3	4.7360(5)	4.5470	-4.0
BaGa_2	4.4322(1)	4.3933	-0.9	5.0824(6)	4.8972	-3.6

Ga(3d4s4p), Na(2s2p3s), Ca(3s3p4s), Sr(4s4p5s) and Ba(5s5p6s) as semicore and valence states. The maximum l value for partial waves inside the atomic spheres was set to 10.

5.1.3 Results

We start with focusing on the digallides. The obtained optimised lattice parameters for the digallides are given in Table 5.1. The deviation between the optimised and experimental lattice parameters [52] are well within the typical range of the LDA over-binding problem, predicting too small lattice parameters. The Ga z coordinate in CaGa_2 was relaxed from the experimentally observed $z_{\text{exp}} = 0.0421(2)$ [56] to $z_{\text{opt}} = 0.0447$.

The total density of states (DOS) for these three compounds is shown in the left panel of Figure 5.3. While the total DOS is quite similar on the whole, it differs somewhat when looking at the details – especially at the Fermi energy. Whereas for CaGa_2 , the Fermi level is located in a pseudo gap, this is different for the compounds with AlB_2 -type structure: for SrGa_2 , the Fermi level is on the high energy shoulder and for BaGa_2 on top of a flat maximum of the DOS. This challenges the structural stability. We will come back to this point later. In the right panel of Figure 5.3, the partial (m resolved) DOS of the Ga 4p states is shown. We observe the same behaviour at the Fermi level. Furthermore, for all three compounds, the Ga p_x states, which are due to the hexagonal symmetry identical to the p_y states, are more occupied than the p_z states: $n_x = n_y > n_z$. This corresponds to an oblate electron density at the Ga atoms: since

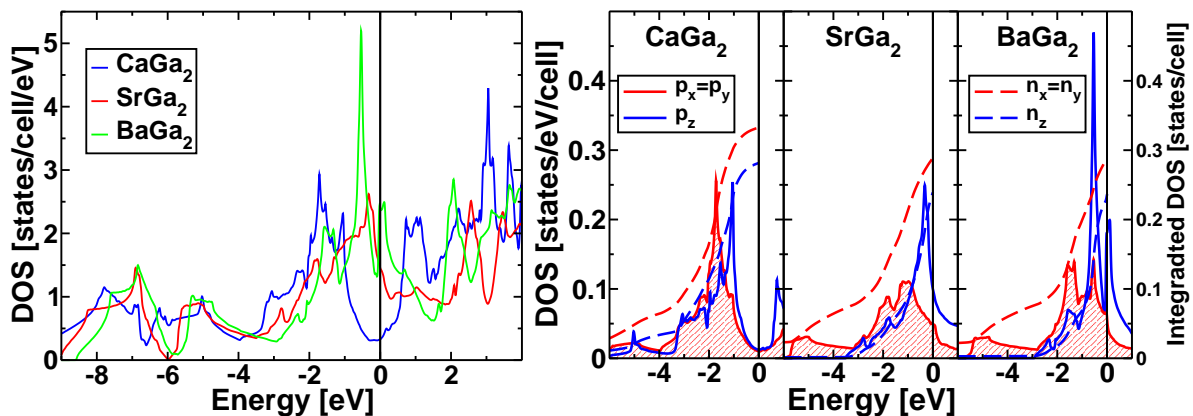


Figure 5.3: **Left:** total electronic density of states (DOS) for $M\text{Ga}_2$, with $M = \text{Ca}$ (blue), Sr (red) and Ba (green). **Right:** partial (m resolved) DOS for Ga in the three compounds, $p_x = p_y$ and p_z (full red and blue line, respectively) and the integrated partial DOS, $n_x = n_y$ and n_z (dashed red and blue line, respectively).

EFG	CaGa ₂	SrGa ₂	BaGa ₂
V_{zz}^{exp}	4.44(8)	5.22(9)	4.48(8)
V_{zz}^F	3.74	4.31	4.41
V_{zz}^W	3.77	4.13	4.38
V_{zz}^{lat}	-0.10	-0.14	-0.10
V_{zz}^{val}	3.87	4.27	4.48
V_{zz}^{pp}	4.29	4.48	4.51
V_{zz}^{sd}	0.02	0.02	0.02
V_{zz}^{dd}	-0.47	-0.29	-0.09

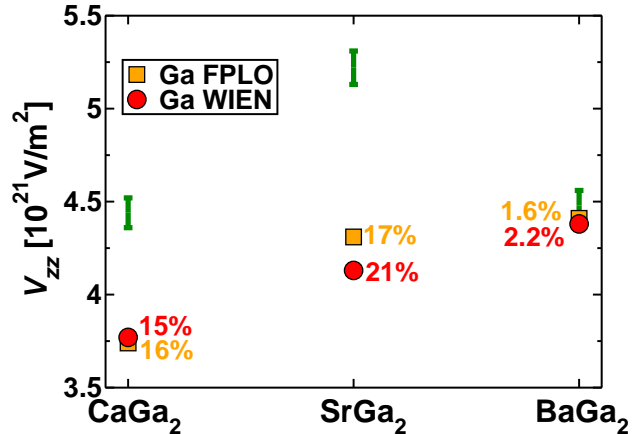


Figure 5.4: **Left:** experimental [52] and calculated EFGs for Ga using FPLO (indicated by F) and WIEN2k (indicated by W) in 10^{21} V/m². For V_{zz}^W also the different contributions, according to Section 4.1.1, are given. **Right:** V_{zz} obtained from the experiment (V_{zz}^{exp} , green bar), from FPLO (V_{zz}^F , orange square) and from WIEN2k, (V_{zz}^W , red circle). Deviations of V_{zz}^F and V_{zz}^W from the experimental EFGs are given in percent.

the orbitals of the core states are fully and the orbitals of the semicore states¹ are almost fully occupied, only the valence states can cause a significant deviation from spherical symmetry. Since s orbitals are spherical, the $4p$ states are the only relevant valence states for the EFG. That the valence electrons are responsible for the EFG can also be checked with the EFG module within the WIEN2k code: the EFG can be calculated for different energy intervals. The upper energy limit is the Fermi energy, since there are no occupied states at higher energies. If one calculates the EFG by decreasing the lower energy limit from the Fermi energy to lower energies, the EFG increases from zero until it saturates at roughly 9 eV below the Fermi energy – the edge of the valence states, see Figure 5.3. Taking into account even deeper lying states changes the EFG only insignificantly, *i.e.*, the polarisation from core and semicore states is small. Hence, the EFG is sensitive to the electrons responsible for the chemical bonding.

Next, we compare the EFG for Ga measured with NMR [52] and calculated with WIEN2k and FPLO, using the optimised structural parameters. The results are shown in Figure 5.4. The obtained values for FPLO and WIEN2k agree well with each other. For BaGa₂, the calculated and measured EFGs are in perfect agreement. For CaGa₂, the calculated EFGs are on the edge of the usually considered range of deviation from the experiment, which is ± 15 %². For SrGa₂, the deviation is even larger.

Before discussing this deviation, we will first analyse the EFG, according to the definitions given in Section 4.1.1 on page 24. As it can be seen from the table in Figure 5.4, the lattice contribution V_{zz}^{lat} to the EFG is negligible for all three compounds. The total EFG is almost identical to the valence EFG V_{zz}^{val} , which can be decomposed into further contributions. For all three compounds, the pp contribution dominates clearly - the EFG of Ga is mainly caused by anisotropic $4p$ electrons. The same results are also obtained for FPLO: the off-site EFG is negligible and the pp contribution to the on-site EFG is predominant. The positive sign of the EFG is in line with the obtained oblate $4p$ electron density, see above.

¹This includes the Ga $3d$ states, their anisotropy is negligible compared to the anisotropy of the $4p$ states.

²Although there are no error bars given for the calculated EFGs in table in Figure 5.4, be aware that also for these EFGs a “numerical” error bar exists: the k mesh, the basis set, the (accuracy of the) convergence criteria and the exchange functional influences the EFG to a greater or lesser extent. Furthermore, the calculated EFG is very sensitive to structural parameters.

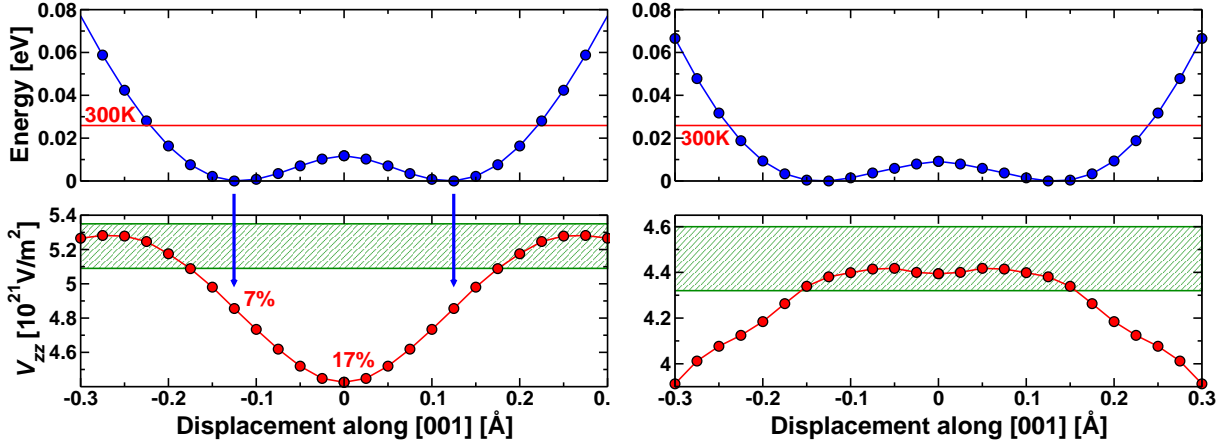


Figure 5.5: Energy per Ga atom (top) and V_{zz} (bottom) for SrGa_2 (left) and BaGa_2 (right) in dependence of the displacement of Ga along [001] in the CaIn_2 -type structure. The thermal energy at ambient temperature is marked by a red line (top) and the experimental EFG by a green error bar (bottom).

The unusual large deviation between the measured and calculated EFG of Ga in SrGa_2 (Figure 5.4) is resolved in the following. Single-crystal X-ray diffraction experiments at ambient temperature showed a strong anisotropic displacement of the Ga atoms in SrGa_2 [52]. However, using the CaIn_2 - ($P6_3/mmc$), the EuGe_2 -type structure ($P\bar{3}m1$) or the space group $P3m1$ in the refinement of the crystallographic X-ray data, an ordered deviation of the Ga atoms from the position in the AlB_2 -type structure was excluded. Yet, a split-site model for the Ga position within the AlB_2 -type structure with a displacement of $\pm 0.086 \text{ \AA}$ does not only model the statistic puckering of the Ga layers but results also in a similar quality in the structure refinement [52].

In order to approximate this split-site model theoretically, we calculated SrGa_2 in the CaIn_2 -type structure. In the according space group ($P6_3/mmc$), the position of the Ga atom can be relaxed with respect to the total energy along [001]. For the calculation we used the corresponding optimised lattice parameters from SrGa_2 in the AlB_2 -type structure (Table 5.1). Total energy calculations for different z positions yield a minimum in energy for a displacement of $\pm 0.125 \text{ \AA}$, see top graph in the left panel of Figure 5.5. We cross-checked this calculation in the CaIn_2 -type model also for the experimental lattice parameters (Table 5.1) and using the GGA PBE xc-functional [16] – neither the position of the energy minimum, nor the energy difference changed significantly. The energy gain for the Ga atom being at the minimum position with $d = \pm 0.125 \text{ \AA}$ is about 0.01 eV. This is well below the thermal energy at ambient temperature ($300 \text{ K} \cong 0.026 \text{ eV}$), see top graph in the left panel of Figure 5.5. At ambient temperature, dynamical disorder of the Ga atoms is expected for such a flat potential curve and therefore no ordering of the Ga atoms is expected which is in line with the experimental observation. In order to determine whether the anisotropic displacement parameters are due to a thermal motion or a static statistic displacement of the Ga atoms, temperature dependent experiments have to be performed, for instance, single-crystal X-ray diffraction. If the thermal motion is the cause of the anisotropic displacement parameters, they should go to zero for $T \rightarrow 0$ measurements. Another possibility to distinguish experimentally between static and thermal displacement is to measure the quadrupole coupling as a function of temperature on the cation, *i.e.*, on Ba^3 . The thermal movement of the Ga atoms should result

³This NMR experiment should be done on Ba and not Sr for two reasons: (i) whereas ^{135}Ba and ^{137}Ba have a nuclear spin of $I = 3/2$, ^{87}Sr has $I = 9/2$ and hence more complicated spectra, and (ii) the absolute value of the EFG (and therefore the quadrupole frequency) is larger for Ba, $V_{zz} = -4.01 \cdot 10^{21} \text{ V/m}^2$, than for Sr,

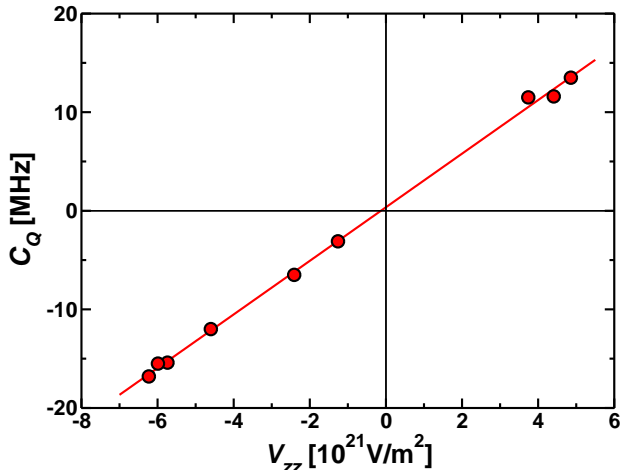


Figure 5.6: The quadrupole frequency $C_Q = eQV_{zz}/h$ [52, 57] in dependence of the electric field gradient V_{zz} for ^{71}Ga in $M\text{Ga}_2$ ($M = \text{Ca}, \text{Sr}, \text{Ba}$) and $M\text{Ga}_4$ ($M = \text{Na}, \text{Sr}, \text{Ba}$). V_{zz} was calculated with FPLO, Figure 5.4 (except for SrGa_2 : $V_{zz} = 4.86 \cdot 10^{21} \text{ V/m}^2$, see text) and Table 5.4. The slope of the fit results in the quadrupole moment $Q = 112 \text{ mb}$ for ^{71}Ga .

in a reduced quadrupole frequency at the cation. At temperatures below the thermally activated process, the quadrupole coupling parameter should increase [44].

This displacement of the Ga atoms along [001] determined from the analysis of the total energy, is not only in line with single-crystal X-ray diffraction experiments (split-site model), but also with the agreement of the EFG of the NMR experiment. In the bottom graph in the left panel of Figure 5.5, we see that V_{zz} increases with increasing Ga displacement. For the displacement of $\pm 0.125 \text{ \AA}$, the calculated EFG agrees with 7 % deviation well with the experimental EFG. Comparing the calculated EFGs for all di- and tetragallides with the experimental ones (see Figures 5.4 and 5.10), we observe a systematic deviation in direction of smaller values for the calculated EFGs. This indicates a slightly too small quadrupole moment, as Q enters the equation to convert the quadrupole frequency to the EFG: $C_Q = eQV_{zz}/h$. Indeed, if we plot the measured quadrupole coupling frequencies for ^{71}Ga [52, 57] as a function of the EFGs calculated by FPLO (Figure 5.6), we obtain a quadrupole moment of $Q = 112 \text{ mb}$, which is slightly larger than the one reported in literature of $Q = 107 \text{ mb}$ [58] for ^{71}Ga .

We also performed calculations in the EuGe_2 -type structure. The main difference between these two structure types is the stacking of the Ga layers. In the EuGe_2 -type model, the Ga atoms are displaced in the same direction and every layer is the same. In the CaIn_2 -type structure, the Ga atoms are displaced towards each other and every other layer is the same. Relaxing the position of the Ga atoms along [001] in the EuGe_2 type structure yields the same trend for the total energy and the EFG in SrGa_2 . However, compared to the relaxation in the CaIn_2 -type structure, the energy gain in the EuGe_2 -type structure is roughly 0.01 eV smaller. Furthermore, the discrepancy in the measured and calculated EFG for Ga in SrGa_2 still remains as the EFG increases less drastically. Therefore, an atomic model, where the Ga atoms are displaced in the same direction as it is modelled with the EuGe_2 -type structure can be excluded.

Applying the CaIn_2 -type structure to BaGa_2 results in a very similar behaviour for the total energy. Also here, a minimum in energy is obtained for a displacement of Ga along [001] by $\pm 0.125 \text{ \AA}$, see top graph in the right panel of Figure 5.5. This is in line with the displacement of the Ga atoms obtained from X-ray diffraction of $\pm 0.071 \text{ \AA}$ [52].

Since the EFG does not change significantly for a displacement of $-0.125 \text{ \AA} < d < 0.125 \text{ \AA}$, see bottom graph in the right panel of Figure 5.5, no deviation between the experimentally and theoretically obtained EFG was observed for the calculation using the AlB_2 -type structure. Although the dependence of the total energy on the Ga z position is very similar for SrGa_2 and BaGa_2 , the

$V_{zz} = 0.62 \cdot 10^{21} \text{ V/m}^2$, in $M\text{Ga}_2$ (FPLO calculation).

Table 5.2: Plasma frequencies obtained from the Fermi velocity tensor in-plane ($\omega_P^x = \omega_P^y = \omega_P^\parallel$) and out-of-plane $\omega_P^z = \omega_P^\perp$ for the relaxed digallides, all in the CaIn_2 -type structure, cf. Figure 5.5.

Compound	ω_P^\parallel [eV]	ω_P^\perp [eV]	$\omega_P^\parallel/\omega_P^\perp$
CaGa_2	2.48	1.53	1.62
SrGa_2	3.51	2.22	1.58
BaGa_2	3.04	1.55	1.96

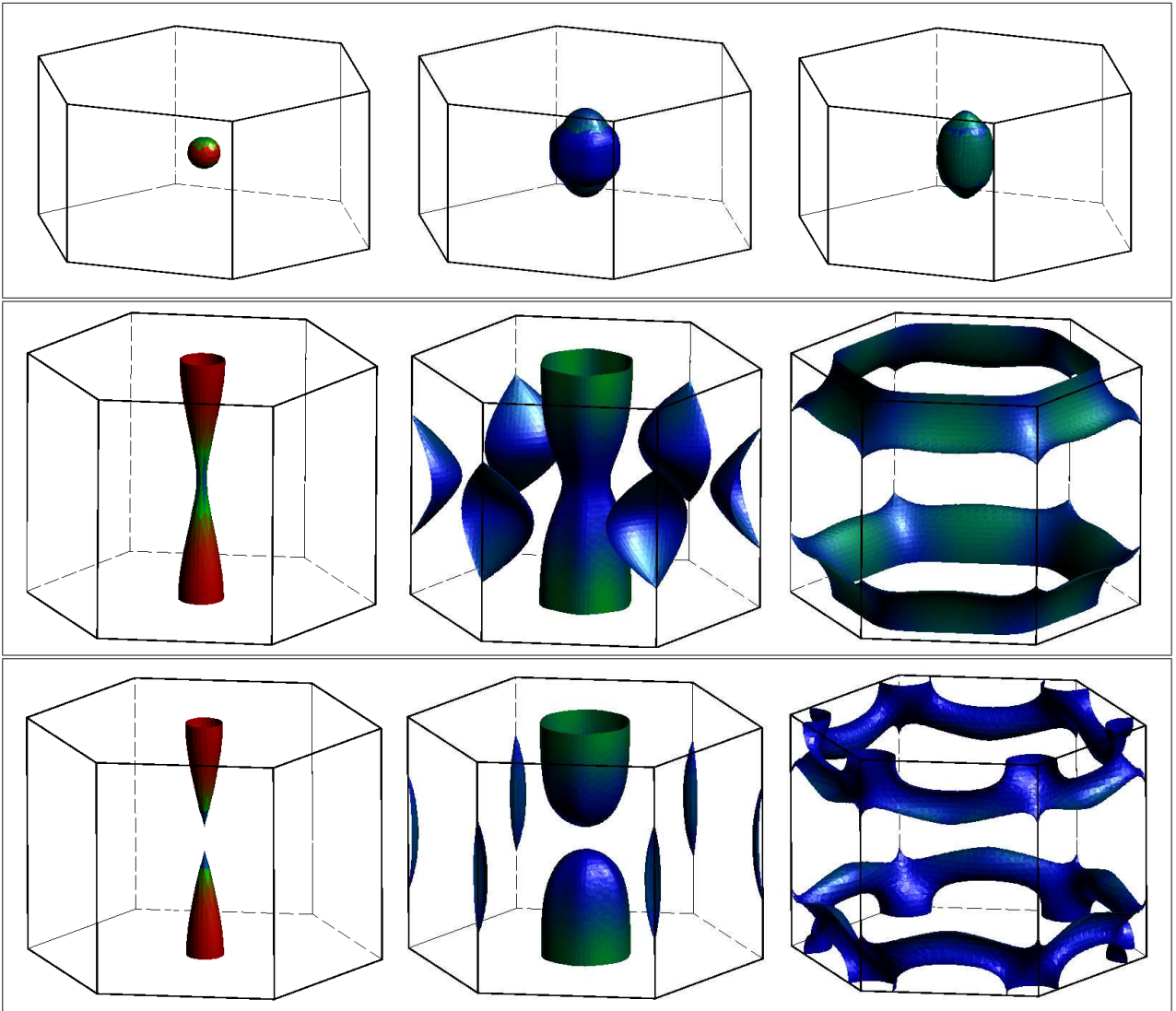


Figure 5.7: Fermi surfaces for different bands for CaGa_2 (CaIn_2 -type structure, top row), SrGa_2 (AlB_2 -type structure, middle row) and BaGa_2 (AlB_2 -type structure, bottom row). The Fermi velocity is indicated by the colouring, from high (red) to low (blue) velocity.

dependence of V_{zz} on the Ga z position shows a very different behaviour. This demonstrates again the complexity of the electric field gradient and is not yet fully understood. The difference in the absolute value of the EFGs on Ga in the isotypic structures $SrGa_2$ and $BaGa_2$, and $SrGa_4$ and (an artificial tetragonal) $CaGa_4$ may result from different Ga-Ga and cation-Ga distances or alkaline earth metal-Ga interactions. These questions are currently investigated in the collaboration of Frank Haarmann and Peter Jeglič.

Furthermore, an analysis of the DOS for $BaGa_2$ in the $CaIn_2$ -type structure with Ga at the energetically optimised z position shows that the maximum at the Fermi level, *cf.* Figure 5.3, is shifted to lower energies. Thus, the distortion is driven by the large DOS at the Fermi energy.

Finally, we analyse the Fermi surfaces and velocities and the plasma frequencies obtained from the Fermi velocity tensor for these three compounds, see Figure 5.7 and Table 5.2. For the Ca digallide, the Fermi surfaces are different compared to the other two digallides. The unit cell in the $CaIn_2$ -type structure contains two formula units and compared to the unit cell in the AlB_2 -type structure it is twice as large along $[001]$ in real space. Therefore, the Fermi surfaces are compressed along $[001]^*$ for $CaGa_2$. The Fermi surfaces for $SrGa_2$ and $BaGa_2$ are shown for the AlB_2 -type structure. Taking into account the distortion (*cf.* Figure 5.5), *i.e.*, calculating the Fermi surfaces in the $CaIn_2$ -type structure, yields five instead of three Fermi surfaces: the three Fermi surfaces shown in Figure 5.7 remain basically the same and two additional cylinder shaped Fermi surfaces appear. The underlying physics, however, remains the same. Therefore, we will show and discuss the fewer Fermi surfaces from the AlB_2 -type structure. The Fermi velocity is perpendicular to the Fermi surface. On the average, the Fermi velocity is largest in the (001) plane, which is the same in k space and in real space due to the hexagonal space group. The same conclusion is obtained from the plasma frequencies ω_P , see Table 5.2, where the distortion for $SrGa_2$ and $BaGa_2$ is taken into account (ω_P is calculated in the $CaIn_2$ -type structure for all three digallides). The plasma frequency ω_P^{\parallel} in the (001) plane is almost twice as large as ω_P^{\perp} perpendicular to that plane. Hence, the Lorentz force $\vec{F} = q(\vec{v} \times \vec{B})$, which occurs if the sample is put into a magnetic field \vec{B} , is minimal if \vec{v} is parallel to \vec{B} . This is what is observed in the NMR experiment: the (001) planes of the crystallites are oriented parallel the magnetic field \vec{B} , which is parallel to $[001]$. Analysing the orbital characters of the bands, we conclude that the high Fermi velocities in the (001) plane are due to the p_x and p_y electrons, which hybridise with each other and the s states. Therefore, the electron transport in MGa_2 , with $M = Ca, Sr$ and Ba is predominantly conducted via the p_x - and p_y -like electrons, taking place parallel to the honeycomb-like Ga layers, which are formed by strong Ga bonds.

Now, we turn to the tetragallides. The obtained optimised lattice parameters are given in Table 5.3. The deviations between the optimised and experimental lattice parameters [57] are well within the typical range of the LDA over-binding problem, similar to the digallides. Furthermore, for MGa_4 with $M = Na, Sr$ and Ba , the optimised z coordinates of Ga(5b) at the Wyckoff position 4e and for $CaGa_4$, the optimised x and z coordinates of Ga(5b) at the Wyckoff position 4i, and the optimised y coordinate of Ga(4b) at the Wyckoff position 4h are given.

The total density of states for the four tetragallides is shown in the left panel of Figure 5.8. We observe that the total DOS is quite similar for these four compounds. The DOS of the tetragallides containing the lighter cations, $NaGa_4$ and $CaGa_4$, and the DOS containing the heavier cations, $SrGa_4$ and $BaGa_4$ share even more similarities: the DOS has almost the same shape, but the peaks are shifted with respect to each other. Contrary to the undistorted digallides, the Fermi level is located in a pseudo gap for all four tetragallides. This is in line with the obtained good agreements for the EFG, see below.

In the right panel of Figure 5.8, the partial (m resolved) DOS for the $4p$ states of Ga(5b) and Ga(4b) for $SrGa_4$ are shown. Also here, we checked with the WIEN code that the valence electrons

Table 5.3: Experimental [57] and optimised (with the FPLO code [2]) lattice parameters for MGa_4 , with $M = Na, Ca, Sr$ and Ba . The monoclinic angle in $CaGa_4$ was determined by X-ray powder diffraction to be $\beta = 118.922^\circ$ [44], in perfect agreement with $\beta = 118.94(2)^\circ$ from Ref. [55]. The experimental [59, 55, 60, 61] and optimised z coordinates of Ga(5b) are given for $M = Ba, Ca, Na$ and Sr , respectively. For $M = Ca$, also the internal x and y coordinates were relaxed from $x(\text{exp})=0.4050(3)$ [55] to $x(\text{opt})=0.4042$ for Ga(5b) and $y(\text{exp})=0.2328(3)$ [55] to $y(\text{opt})=0.2345$ for Ga(4b).

		NaGa ₄	CaGa ₄	SrGa ₄	BaGa ₄
$a(\text{exp})$	[Å]	4.2257(8) [57]	6.1823(1) [57]	4.4466(2) [57]	4.5660(1) [57]
$a(\text{opt})$	[Å]	4.1654	6.0393	4.3597	4.4838
Dev.	[%]	-1.4	-2.3	-2.0	-1.8
$b(\text{exp})$	[Å]		6.1350(3) [57]		
$b(\text{opt})$	[Å]		6.0140		
Dev.	[%]		-2.0		
$c(\text{exp})$	[Å]	11.197(2) [57]	6.1190(2) [57]	10.7451(7) [57]	10.7753(5) [57]
$c(\text{opt})$	[Å]	11.0722	6.0282	10.6063	10.7012
Dev.	[%]	-1.1	-1.5	-1.3	-0.7
$z(\text{exp})$	Ga(5b)	0.3888(6) [60]	0.7692(3) [55]	0.38299(9) [61]	0.3799(1) [59]
$z(\text{opt})$	Ga(5b)	0.3898	0.7713	0.3840	0.3810

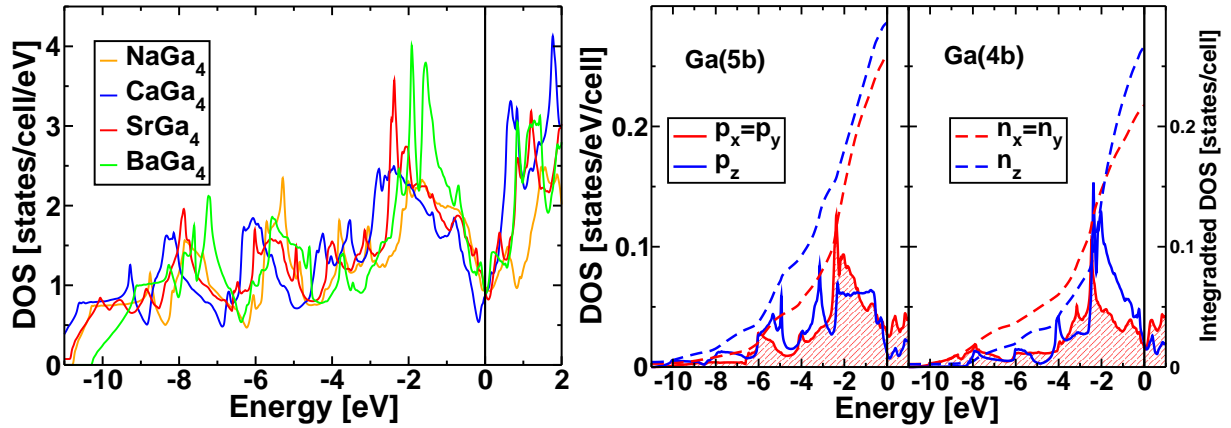


Figure 5.8: **Left:** total density of states (DOS) for MGa_4 , with $M = Na$ (orange), Ca (blue), Sr (red) and Ba (green). **Right:** m resolved partial DOS for the 5-bonded Ga(5b) (left) and the 4-bonded Ga(4b) (right) in $SrGa_4$, *cf.* Figure 5.2, $p_x = p_y$ and p_z (full red and blue line, respectively) and the integrated partial DOS, $n_x = n_y$ and n_z (dashed red and blue line, respectively).

Table 5.4: V_{zz} in 10^{21} V/m² for Ga obtained from the experiment [57] and band structure codes FPLO (indicated by ^F) and WIEN2k (indicated by ^W). For V_{zz}^W , also the different contributions, according to Section 4.1.1, are given. For MGa_4 , with $M = Na, Sr$ and Ba , η is zero, for $CaGa_4$, $\eta^{exp}=0.28(10)$ for Ga(5b) and $\eta^{exp}=0.34(10)$ for Ga(4b). The calculated η is identical for FPLO and WIEN2k: $\eta^{F/W}=0.23$ for Ga(5b) and $\eta^{F/W}=0.26$ for Ga(4b).

Compound	Atom	$ V_{zz}^{exp} $	V_{zz}^F	V_{zz}^W	V_{zz}^{lat}	V_{zz}^{val}	$V_{zz}^{val}(pp)$	$V_{zz}^{val}(dd)$
NaGa ₄	Ga(5b)	6.49(10)	-6.23	-6.18	0.12	-6.30	-6.54	0.29
NaGa ₄	Ga(4b)	4.64(8)	-4.60	-4.44	-0.03	-4.41	-4.59	0.17
CaGa ₄	Ga(5b)	2.89(10)	-2.94	-2.80	0.10	-2.90	-3.18	0.33
CaGa ₄	Ga(4b)	4.87(16)	-4.90	-4.73	-0.03	-4.70	-4.86	0.16
SrGa ₄	Ga(5b)	2.51(6)	-2.41	-2.24	0.08	-2.32	-2.56	0.28
SrGa ₄	Ga(4b)	5.95(9)	-5.74	-5.64	-0.03	-5.61	-5.80	0.18
BaGa ₄	Ga(5b)	1.20(3)	-1.26	-1.01	0.06	-1.07	-1.22	0.18
BaGa ₄	Ga(4b)	5.99(9)	-5.99	-5.96	-0.03	-5.94	-6.12	0.17

are responsible for the EFG: applying the same procedure as for the digallides, the EFG saturates at roughly 10 eV below the Fermi energy, the edge of the valence states (Figure 5.8), *i.e.*, the polarisation from core and semicore states is small. For both, Ga(5b) and Ga(4b), the p_x states, which are due to the tetragonal symmetry identical to the p_y states, are less occupied than the p_z states: $n_x = n_y < n_z$. This corresponds to a prolate electron density at both Ga atoms. The situation is very similar for the other three tetragallides – note that $CaGa_4$ has no tetragonal symmetry and hence $n_x \neq n_y$. Nevertheless, the anisotropy function $\Delta p = \frac{1}{2}(n_x + n_y) - n_z$ (*cf.* Eq. (4.17)) is negative for all four tetragallides (prolate electron density), contrary to the digallides, where the electronic density at the Ga atom was compressed along z (oblate).

Next, we compare the EFGs for Ga(5b) and Ga(4b) measured with NMR [57] and calculated with WIEN2k and FPLO. The results are shown in Table 5.4 and in the left graph in Figure 5.10. The values obtained by FPLO and WIEN2k agree well with each other. Compared to the experimentally obtained EFGs, we obtain good agreement for both codes. In many cases, the calculated EFGs are even within the experimental error bars, see Figure 5.10. Also for the asymmetry parameter η , which is nonzero for $CaGa_4$, a good agreement between the calculations and the experiment is obtained.

Analysis of the EFG shows that also in the tetragallides, the lattice contribution V_{zz}^{lat} to the EFG is negligible for all four compounds, see Table 5.4. Decomposing the valence EFG into further contributions yields that the pp contribution dominates clearly for all four compounds – the EFG of Ga(5b) and Ga(4b) is mainly caused by anisotropic $4p$ electrons. The same results are also obtained from FPLO: the off-site EFG is negligible and the pp contribution to the on-site EFG is predominant. The negative sign of the EFG is in line with the obtained prolate $4p$ electron density, see above.

Here, we note that in the experiment the (001) planes of the crystallites of the tetragallides with $M = Sr$ and Ba are oriented parallel the magnetic field \vec{B}_z – as it was also observed for the digallides. In $NaGa_4$, however, the situation is different. Here, the [001] axis of the crystallites is oriented parallel to the magnetic field along the z -direction [44]. Qualitatively, the Fermi surfaces are different for the three tetragonal tetragallides: whereas the Fermi surfaces for $SrGa_4$ and

Table 5.5: Plasma frequencies obtained from the Fermi velocity tensor in-plane ($\omega_P^x = \omega_P^y = \omega_P^{\parallel}$) and out-of-plane $\omega_P^z = \omega_P^{\perp}$ for the tetragonal tetragallides.

Compound	ω_P^{\parallel} [eV]	ω_P^{\perp} [eV]	$\omega_P^{\parallel}/\omega_P^{\perp}$
NaGa ₄	6.00	2.86	2.10
SrGa ₄	4.20	2.67	1.57
BaGa ₄	3.88	2.57	1.51

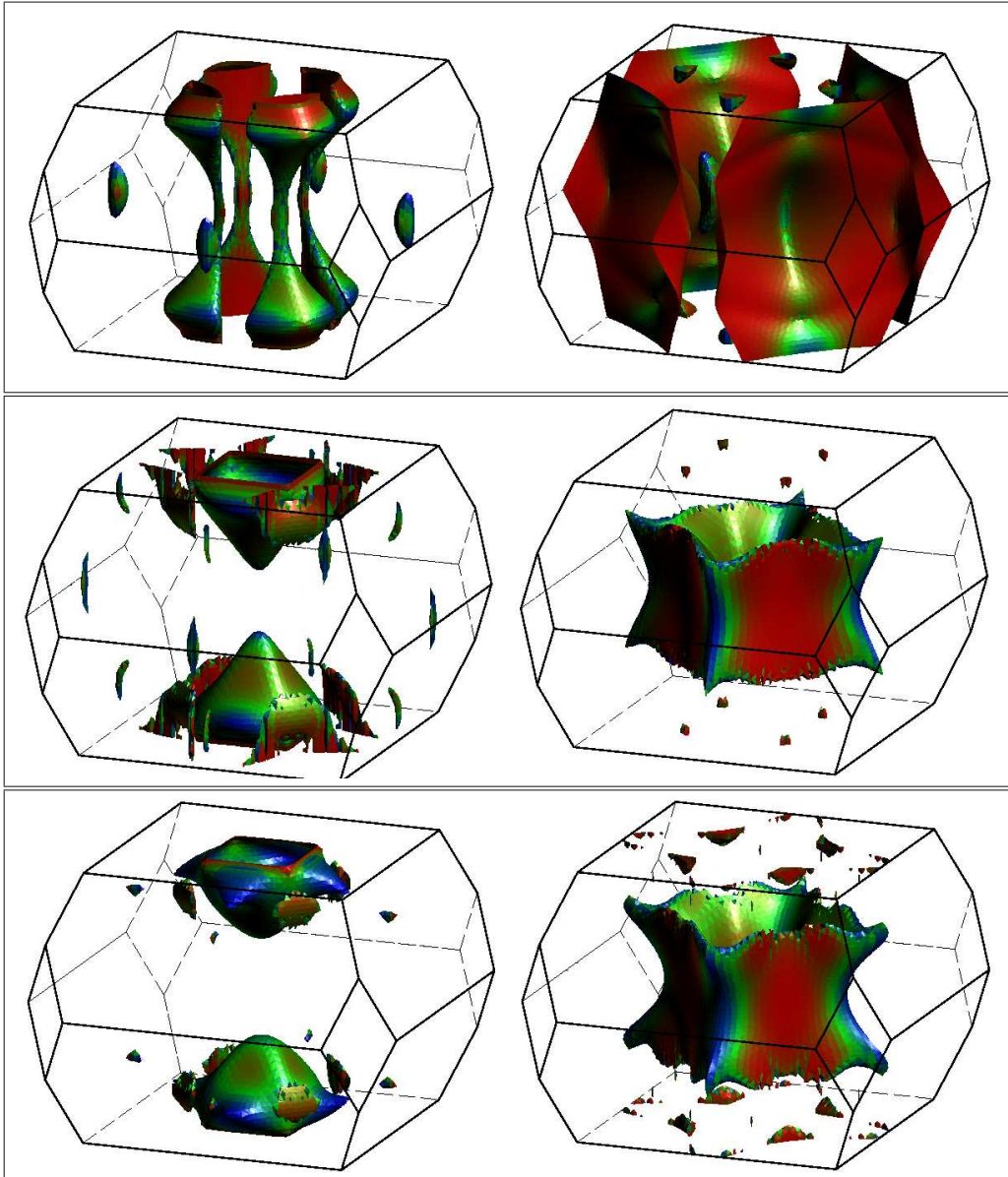


Figure 5.9: Fermi surfaces for different bands for NaGa₄ (top row) SrGa₄ (middle row) and BaGa₄ (bottom row). The Fermi velocity is indicated by the colouring, from high (red) to low (blue) velocity.

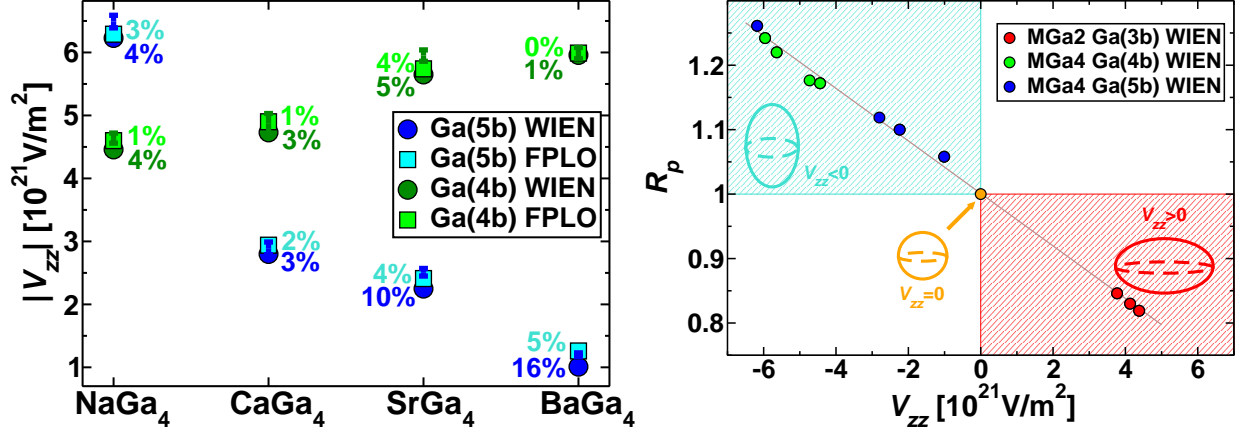


Figure 5.10: **Left:** V_{zz} calculated with WIEN2k (circle) and FPLO (square) for Ga(5b) (green) and Ga(4b) (blue). Deviations to the experimental EFGs (green error bar) are given in percent. **Right:** the ratio R_p Eq. (5.1) of the occupation of p_z and p_x and p_y states as a function of V_{zz} for all di- and tetragallides, calculated with WIEN2k.

$BaGa_4$, and especially the red shaded areas (which represent the fast electrons) are very similar, the Fermi surfaces (and the red shaded areas) for $NaGa_4$ are very different, see Figure 5.9. Contrary to the digallides, analysing the Fermi surfaces for the tetragallides is more complex. Yet, a quantitative analysis can be obtained from the plasma frequencies, see Table 5.5. Also for these compounds, the plasma frequency is largest in the (001) plane with the same ratio of in- and out-of-plane frequencies of roughly two. Hence, the experimental observation can not be understood from the Fermi velocities, $NaGa_4$ is not different from the other di- and tetragallides. Further investigations are necessary to find the underlying reason for this.

Finally, we will give an analysis of the axes of the EFG tensor. For the tetragonal MGa_4 , with $M = Na, Sr$ and Ba , V_{zz} is parallel to $[001]$ and the asymmetry parameter η is zero due to symmetry. In $CaGa_4$, the situation is different due to the monoclinic symmetry. In the monoclinic crystal axis system (CAS), the angle⁴ between the a and c axis is $\beta = 118.922^\circ$ (Table 5.3). The orientation of the principal axis system (PAS) of the EFG tensor with respect to the CAS is given by the eigen vectors of the EFG tensor. According to the site symmetry of both Ga positions, one principal axis of the PAS has to be parallel to the $[010]$. This is V_{xx} for both Ga(4b) and Ga(5b). V_{yy} and V_{zz} are therefore in the (010) plane of the unit cell. The angles of V_{zz} with respect to $[001]$ are 21.2° for Ga(4b) and 19.9° for Ga(5b)⁵. This corresponds to a tilt of V_{zz} by about 8° with respect to the pseudo tetragonal c axis. The orientation of V_{zz} and the nonzero asymmetry parameter η reflect the influence of the monoclinic distortion on the charge distribution in the vicinity of the Ga atom. Since the quadrupole frequency was determined using a powder sample, NMR on a single-crystal should be done to verify this prediction on the orientation of the EFG tensor.

The ratio of the occupation of the p_x and p_z states for all investigated gallides, the anisotropy ratio

$$R_p \equiv \frac{n_z}{\frac{1}{2}(n_x + n_y)}, \quad (5.1)$$

⁴FPLO and WIEN2k use different conventions for the unit cell: in FPLO $\beta \neq 90^\circ$, in WIEN2k $\gamma \neq 90^\circ$. The text describes the results of the FPLO calculation.

⁵In WIEN2k, the obtained angles are 20.6° and 20.4° , respectively

does not weight the absolute occupation numbers like the anisotropy function $\Delta p = (n_x + n_y)/2 - n_z$ does and is better suited to compare the anisotropy of one element in different compounds, as it is needed for our purpose. This ratio as a function of V_{zz} for all di- and tetragallides is shown in the right graph in Figure 5.10. The obtained values can be fitted very nicely with a linear fit, which goes through zero: $V_{zz} = 0$ at a ratio of $R_p = 1$. This is expected, since a spherical p electron density, which has cubic symmetry and hence no EFG corresponds to $R_p = 1$. Therefore, this fit confirms again that the EFG is predominately due to the anisotropic p electron density. Repeating this procedure for the corresponding values obtained with the FPLO code, we also obtain a linear fit. However, the slope is slightly different and the values scatter more from the obtained fit. This is due to the m resolved DOS, from which the ratio R_p is obtained. Partial properties can be different in different band structure codes due to different implementations of *e.g.*, the basis. Only total quantities, like the EFG, can be compared and as we have seen, this quantity agrees very well between these two codes.

As already said in the introduction, Ga shows a high flexibility with respect to the chemical bonding. In these intermetallic compounds, there are three-, three+one-, four- and five-bonded Ga atoms. The combined analysis of the integrated m resolved DOS and the electric field gradients (Figure 5.10) clearly shows the ability of Ga to be incorporated into compounds with significantly varying charge distributions. This leads to the suggestion that the p valence electrons are the key for the flexibility of the Ga atoms with respect to the chemical bonding.

5.1.4 Summary and conclusion

The here developed and implemented EFG module in FPLO gives results comparable with WIEN2k.

The combination of NMR spectroscopy with DFT based EFG calculations provides new insight in the chemical bonding and structural information in intermetallic compounds.

The hexagonal digallides SrGa_2 and BaGa_2 were believed to crystallise in the AlB_2 -type structure. However, a large discrepancy between the measured and calculated EFG of Ga in SrGa_2 revealed a deviation from this structure motif. Total energy calculations show that puckered Ga layers (like in CaGa_2) are energetically more favourable for SrGa_2 and BaGa_2 . This result is in agreement with the crystallographic data obtained from single-crystal X-ray diffraction measurements, which showed a strong anisotropic displacement of the Ga atoms in SrGa_2 and BaGa_2 [52]. The experimental diffraction data could be described by a split-site model for the Ga position. Additional support is obtained from NMR experiments: the agreement between the calculated and the measured EFG for Ga is improved when the CaIn_2 -type structure model is used in the calculation. Furthermore, for BaGa_2 , the structural distortion is attended by a reduction of the DOS at the Fermi level, which is in line with the expectation of a stable structure.

For the digallides $M\text{Ga}_2$ with $M = \text{Ca}, \text{Sr}$ and Ba , the Fermi velocities are largest in the hexagonal plane, thus resulting in an anisotropic electronic transport, which occurs predominantly parallel to the honeycomb-like Ga planes. This is confirmed experimentally by an orientation of the hexagonal axis of the powder particles parallel to the magnetic field used in the NMR experiment.

For the tetragallides $M\text{Ga}_4$ with $M = \text{Na}, \text{Ca}, \text{Sr}$ and Ba , no peculiarities are observed. The Fermi level is situated in a pseudo gap for all four compounds and the EFGs at the Ga atoms calculated with the band structure codes WIEN2k and FPLO agree well with each other and the EFGs obtained experimentally.

For all investigated di- and tetragallides, the lattice (or off-site) contribution to the EFG of Ga is negligible and the valence (or on-site) EFG is mainly due to an anisotropic charge distribution caused by the Ga $4p$ electrons. The sign of the EFG for Ga is in line with the anisotropic

charge distribution of the Ga $4p$ electrons, which is oblate (compressed along $[001]$) for the digallides and prolate (elongated along $[001]$) for the tetragallides. The linear dependence of the EFG on the anisotropy ratio, *i.e.*, the ratio of occupied in- and out-of-plane Ga $4p$ states, also demonstrates the predominance of the Ga $4p$ electrons contributing to the EFG. This strongly varying charge distribution of the Ga $4p$ electrons in similar intermetallic compounds leads to the conclusion that the Ga $4p$ electrons are the key for the flexibility of the Ga atoms with respect to the chemical bonding. In order to support this surmise, subsequent investigations on other intermetallic compounds should be carried out, *e.g.*, a widespread study on aluminides of different alkaline earth metals.

5.2 Aluminium diboride $\text{Al}_{1-x}\text{B}_2$

5.2.1 Introduction

The AlB_2 structure type is the prototype structure (aristotype) not only for diborides but also for many other compounds. It consists of graphite-like nets of boron atoms separated by aluminium in hexagonal prismatic voids, see Figure 5.11. Important representatives of this structure type are transition metal diborides due to their particular hardness and refractory properties. The most famous representative, however, is magnesium diboride, where superconductivity with a transition temperature T_c of 39 K was discovered only a few years ago [62].

Lattice vacancies are one of the most common point defects in crystals. Non-stoichiometry of metal diborides is a quite new field of research [63], since the progress in studies of metal diborides increased rapidly only after the discovery of superconductivity in MgB_2 .

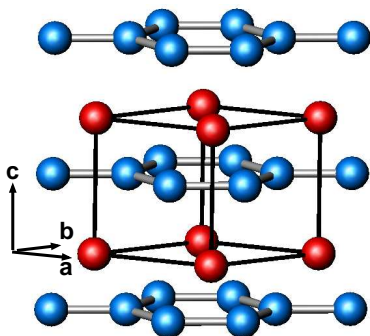


Figure 5.11: The hexagonal structure of AlB_2 with Al (red) and B (blue).

Aluminium diboride has been known for a long time. In the early twentieth century, it was believed to be stoichiometric [64]. Several years later, density measurements indicated defects in the structure [65, 66]. Motivated by the varying data in the literature and the only scarcely described chemical analysis which yielded $\text{Al}_{1.0}\text{B}_2$ [64] and $\text{Al}_{0.9}\text{B}_2$ [66], aluminium diboride was re-examined and further characterised. In 2002, Loa *et al.* determined a composition of $\text{Al}_{0.89}\text{B}_2$ from a high pressure synchrotron X-ray powder diffraction study [67]. The same year, Nakamura *et al.* reported a composition of $\text{Al}_{0.93}\text{B}_2$, determined from X-ray emission and absorption spectroscopy data [68]. One of the main questions that arose was: are the vacancies intrinsic or due to the processing? Therefore, two years later, Burkhardt *et al.* processed aluminium diboride with Al excess and showed that the

synthesis of stoichiometric $\text{Al}_{1.0}\text{B}_2$ is not possible since under normal conditions single-crystals of aluminium diboride with defects on the Al-site grow in an aluminium flux [69]. From mass density measurements, the composition $\text{Al}_{0.85}\text{B}_2$ and from single-crystal X-ray structure refinement the composition of $\text{Al}_{0.9}\text{B}_2$ was found. In order to understand the experimental findings, we investigate the vacancies in the Al sublattice in a first-principles study.

The calculation of phase diagrams was initiated by Van Laar a century ago [70, 71], but until the last decade of the twentieth century, these calculated phase diagrams were determined by thorough and costly experimentation (since experimental data was used in the calculations). The tremendous progress in computer power and methodical development in the last two decades made the first-principles calculation of phase diagrams come within reach [72]. However, there are only a few codes capable of calculating first-principles phase diagrams. The CPA module makes the FPLO code one of them. Nevertheless, complicated structures with many atoms require large computational effort, which makes the hexagonal system $\text{Al}_{1-x}\text{B}_2$ the perfect candidate for a first-principles study.

5.2.2 Methods

The band structure calculations were performed using the full-potential local-orbital minimum basis code FPLO (version 5.00-19) [2] within the local density approximation (LDA). For the calculation of the electric field gradient (EFG), also version 8.00-31 was used, because this version has an improved basis, which is very important for the EFG calculation, see Section 4.2. In the scalar relativistic calculations the exchange and correlation functional of Perdew and Wang [15] was employed. In order to check the dependence of the results on the exchange functional, also

Table 5.6: Structural data (including Wyckoff positions (WP)) for the calculation of the 4- and 8-fold super cells for $Al_{0.75}B_2$ and $Al_{0.875}B_2$, respectively. E stands for empty site. The lattice parameters a_0 and c_0 are given in Table 5.7.

	4-fold super cell	8-fold super cell
composition	$Al_{0.75}B_2$	$Al_{0.875}B_2$
space group	$Pmmm$	$Pmmm$
(a, b, c)	$(2a_0, 2 \cos(30)a_0, c_0)$	$(2a_0, 2 \cos(30)a_0, 2c_0)$
WP for Al1	$2i (x=1/4)$	$2j (x=1/4)$
WP for Al2	$1e$	$1g$
WP for Al3	-	$2i (x=1/4)$
WP for Al4	-	$1e$
WP for Al5	-	$1f$
WP for E	$1f$	$1h$
WP for B1	$2p (y=1/6)$	$4v (y=1/6, z=1/4)$
WP for B2	$4z (x=1/4, y=1/3)$	$8\alpha (x=1/4, y=1/3, z=1/4)$
WP for B3	$2n (y=1/6)$	$4u (y=1/6)$

GGA [16] (PBE) was applied. As basis set Al (2s2p/3s3p3d) B (/2s2p3d) E (/1s2p) were chosen for semicore/valence states. The lower lying states were treated fully relativistically as core states. The symbol E stands for empty site and was only used in the CPA calculations. A well converged k mesh of at least 484 k points was used in the irreducible part of the Brillouin zone. In order to investigate the influence of the vacancies, CPA [73] and VCA were applied, see page 12. Since LDA can not directly be compared with CPA (due to the different numerical methods there are differences in the energy), the unsubstituted structures (AlB_2 and Al) were calculated (and optimised) with the Blackman-Esterling-Berk (BEB) module [74]. The BEB method extends the use of CPA to random off-diagonal matrix elements of the Hamiltonian (off-diagonal disorder) [74] and results in a difference in energy of roughly 20 meV for AlB_2 compared to LDA. The BEB calculation serves also for adjusting the DOS and band structure relevant parameters in the CPA

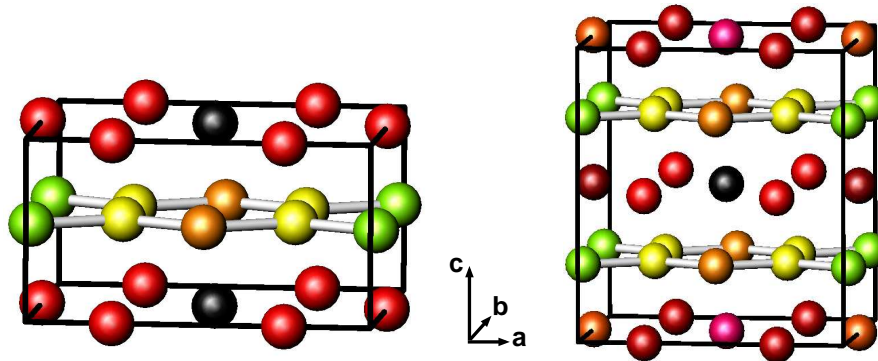


Figure 5.12: The super cells for $Al_{0.75}B_2$ (left) and $Al_{0.875}B_2$ (right). The different Wyckoff positions for B are shown by different colours (B1 orange, B2 yellow, B3 green, cf. Table 5.6). Al is red for all Wyckoff positions and the empty site is black.

Table 5.7: Experimental and optimised lattice parameters for aluminium diboride and aluminium.

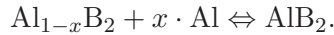
AlB ₂	a_0 [Å]	c_0 [Å]	Al	a [Å]
exp [75]	3.009(1)	3.262(1)	exp [76]	4.1161(8)
opt	3.000	3.231	opt	4.009

menu: $\text{imag}(e)=5 \cdot 10^{-3}$ and $\text{epoints}=5000$ for the DOS and $\text{imag}(e)=10^{-4}$ and $\text{epoints}=1000$ for the band structure. For the scf (self-consistent field) calculation with CPA, the default parameters were used, except for the confining potential exponent n , which was set to 5.

Furthermore a 4-fold and 8-fold super cell were calculated. In both super cells one Al is replaced by a vacancy, see Figure 5.12. This corresponds to a composition of $\text{Al}_{0.75}\text{B}_2$ and $\text{Al}_{0.875}\text{B}_2$, respectively. The structural data for the super cells is given in Table 5.6.

5.2.3 Results

First, we investigate in the equilibrium



Therefore, we calculate the energy for $\text{Al}_{1-x}\text{B}_2$ for different values of x with CPA and the energy of AlB_2 and Al with BEB, see methods. The energy

$$E = E(\text{Al}_{1-x}\text{B}_2 + x \cdot \text{Al}) - E(\text{AlB}_2)$$

is plotted in Figure 5.13. The first approximation is to calculate $\text{Al}_{1-x}\text{B}_2$ for a constant volume for all values of x , *i.e.*, no structural relaxation is taken into account. For Al the optimised lattice parameter, shown in Table 5.7, is used. For this approximation an aluminium concentration of 88 % ($x = 0.12$) is energetically most favourable (green circles in Figure 5.13). To improve the calculation of the phase diagram, we will take lattice relaxation taken into account. *I.e.*, for each value of x , the volume and the c/a ratio is optimised with respect to the total energy of $\text{Al}_{1-x}\text{B}_2$ (orange squares in Figure 5.13). We see, that the lattice relaxation has an impact on energy, the obtained curve is much lower in energy than the previous one and an aluminium concentration of 85 % ($x = 0.15$) is energetically most favourable. Another improvement is to use the experimental lattice parameter at the melting point at 933 K for Al (Table 5.7) since in the experiment of Burkhardt *et al.* [69], aluminium diboride grows in an Al flux. This results in a curve (blue diamonds in Figure 5.13) that is slightly shifted in direction of higher energy compared to the previous one. As a last improvement, we add the heat of fusion energy, $\Delta Q = 10.79$ kJ/mol [77]⁶, to model liquid Al (Al flux in the experiment). This curve (red triangles in Figure 5.13) lies between the others and an aluminium concentration of 87 % ($x = 0.13$) is energetically most favourable. These results of $x \in [0.12, 0.15]$ agree well with the experimental results of Burkhardt *et al.* with $x = 0.10$ and $x = 0.15$ [69] and Loa *et al.* with $x = 0.11$ [67] but less good with $x = 0.07$ [68] obtained from Nakamura *et al.*, see introduction.

We checked the first approximation (no structural relaxation and optimised Al lattice parameter) also for GGA to make sure that the exchange-correlation functional will not influence the result. In the inset of Figure 5.13 we see that it does not matter, if LDA or GGA is applied as exchange-correlation functional, since both curves are almost identical up to the minimum in

⁶This can be converted in $\Delta Q = 112$ meV per atom via the Avogadro constant $N_A = 6.022 \cdot 10^{23}$ mol⁻¹.

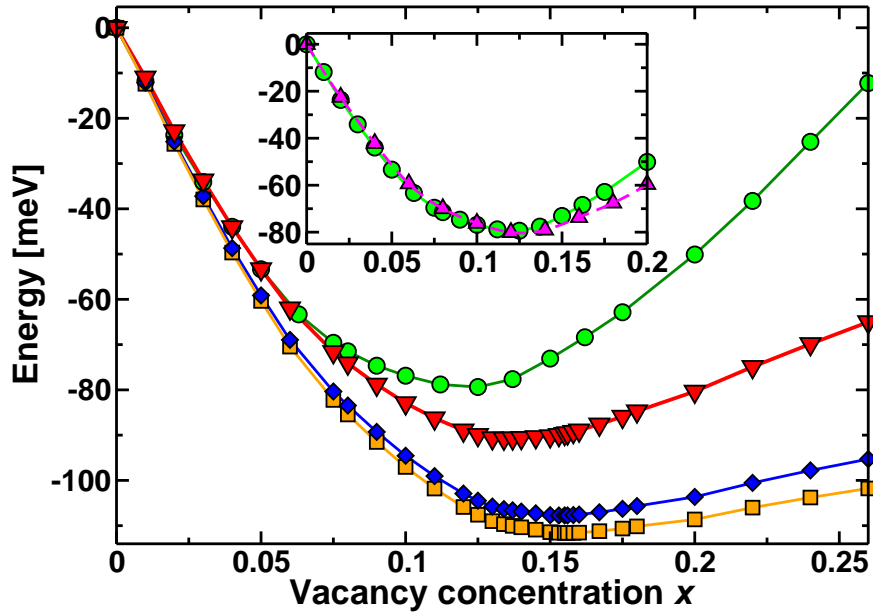


Figure 5.13: The equilibrium $Al_{1-x}B_2 + x \cdot Al \Leftrightarrow AlB_2$. No structural relaxation for $Al_{1-x}B_2$ and optimised Al lattice parameter (green circles), structural relaxation and optimised Al lattice parameter (orange squares), structural relaxation and experimental Al lattice parameter (blue diamonds) and structural relaxation, experimental Al lattice parameter and added heat of fusion (red triangles). **Inset:** comparison of LDA (green circles) and GGA (magenta triangles) for optimised Al lattice parameter without structural relaxation.

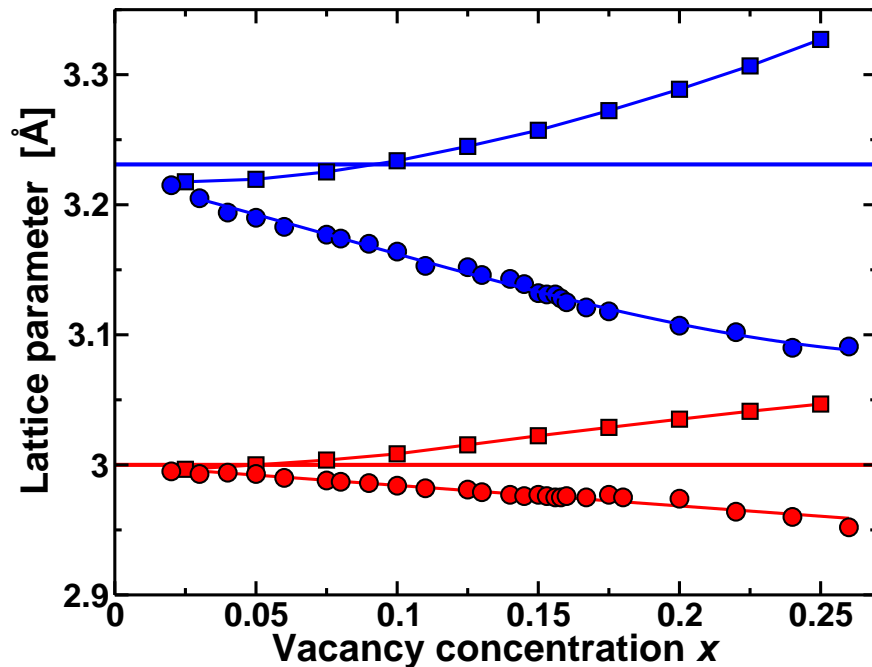


Figure 5.14: Optimised lattice parameters a (red) and c (blue) for $Al_{1-x}B_2$ for different levels of doping calculated with CPA (circle) and VCA (square). The straight lines show the experimental lattice parameters [75].

energy. Differences for the concentration x at the minimum in energy are obtained only in the third decimal: fits for the calculated data points yield for the minimum $x = 0.116$ for LDA and $x = 0.123$ for GGA. Regarding the approximations that were made (*e.g.*, no dynamics), these results are essentially identical. Hence, no “physical” difference is caused by using GGA instead of LDA.

Next, we compare the lattice parameters a and c optimised with CPA and VCA [78] for different levels of doping. The results are shown in Figure 5.14. Since a depends mainly on the σ bonds of the boron atoms it should not change much. Indeed, the CPA results agree with the expected behaviour, a is almost constant and decreases only very little with increasing vacancy concentration. The lattice parameter c , on the other hand, depends on the metallic bonding between the Al and the B atoms. This can be approximated as a free electron gas, where the volume should shrink if electrons are taken out. Indeed, c decreases quite strongly with increasing vacancy concentration. For VCA we observe the opposite trend, both lattice parameters increase with increasing vacancy concentration. This is no surprise, because VCA modifies only the valence electrons. The core is still there. If electrons are taken away, the bonding states are depleted. Therefore the lattice parameters should increase, as it can be seen in Figure 5.14. If we compare the lattice parameters optimised with VCA with the experimental ones for the vacancy concentration of $x = 0.15$, we see that c is as large and a even larger than the experimental counterpart. This is in contradiction to the well-known over-binding problem of LDA: lattice parameters optimised with LDA are always shorter than experimental lattice parameters. This is clearly observed for the CPA optimised lattice parameters. Here, for $x = 0.15$ a is roughly 1 % and c roughly 3 % smaller than the experimental correspondent. Hence, we see that VCA, which is good to describe doping of elements next to each other in the periodic table (*e.g.*, K doped with Ca), is not suitable to obtain the observed behaviour for vacancy disorder. CPA can handle this kind of disorder much better. However, the combination of CPA and VCA yields information about the influence of the valence electrons (*i.e.*, bonding) via VCA and the core electrons on the structure (*i.e.*, volume) via CPA, as it was discussed in this paragraph.

Since CPA describes the defect structure in a good approximation, we take a look at the density of states (DOS). In Figure 5.15, the DOS of the fully occupied ($x = 0$, blue) and the defect ($x = 0.15$, red) structure are shown. If we take into account that there are electrons missing in the latter structure, we can plot the two curves on top of each other, with a shifted Fermi level, as indicated by the red line in Figure 5.15. This way, we observe that the DOS has the same shape in both cases. Hence, the disordered structure can be described in reasonable approximation by the rigid-band approximation. Moreover, the Fermi level is at the minimum in both cases, which is consistent with the Al vacancies. The different smoothness of the curves is partially due to different numerical methods used in CPA and LDA.

To get more information about the difference between the full occupied and the defect structure, we analyse the band structure for the above vacancy concentrations of $x = 0$ (blue) and $x = 0.15$ (red), see Figure 5.16. Due to different numerical methods, the energy bands have different properties. LDA diagonalises a matrix in order to get the eigenvalues and therefore yields sharp energy bands. CPA uses the method of Green functions and yields a spectral function $A(k, \omega)$ (see Section 2.3.2) which in general is not a Dirac δ -distribution. Plotting the maximum of the spectral function yields something that can be compared to smeared energy bands. Like the DOS, the band structure can be described in reasonable approximation with the rigid-band approximation: the curves have the same structure and are shifted with respect to each other due to the different number of electrons in the full- and non-stoichiometric compound. However, contrary to the DOS, which is obtained by an integration over the whole k space, the band structure displays the effect of the vacancy on individual bands. Figure 5.16 clearly shows that different bands are shifted and broadened differently. To understand that, we analyse the characters of the bands,

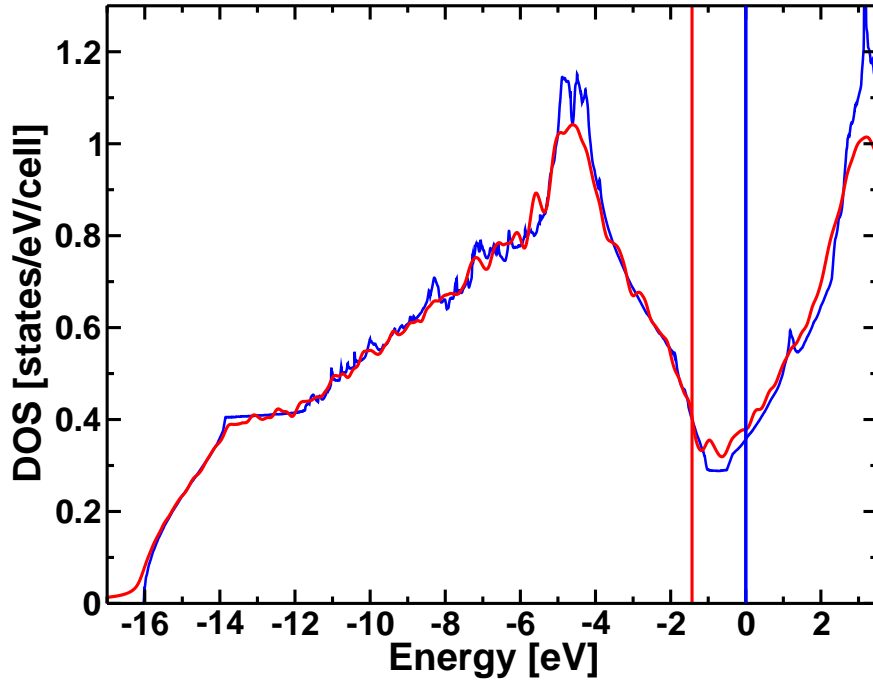


Figure 5.15: Density of states for $Al_{1-x}B_2$ for LDA with $x = 0$ (blue) and CPA with $x = 0.15$ (red). The CPA curve is shifted due to fewer electrons, as indicated by the red Fermi energy E_F , which is lower in energy compared to E_F of the LDA curve.

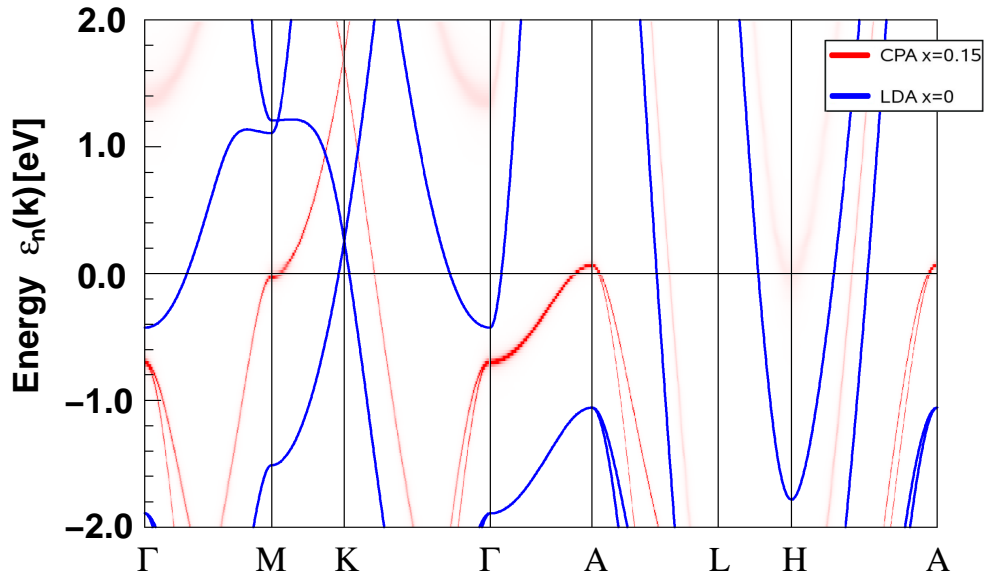


Figure 5.16: Band structure for $Al_{1-x}B_2$ for LDA with $x = 0$ (blue) and CPA with $x = 0.15$ (red). Contrary to the plot of the density of states, Figure 5.15, here the Fermi energy is set to zero for both cases ($x = 0$ and $x = 0.15$).

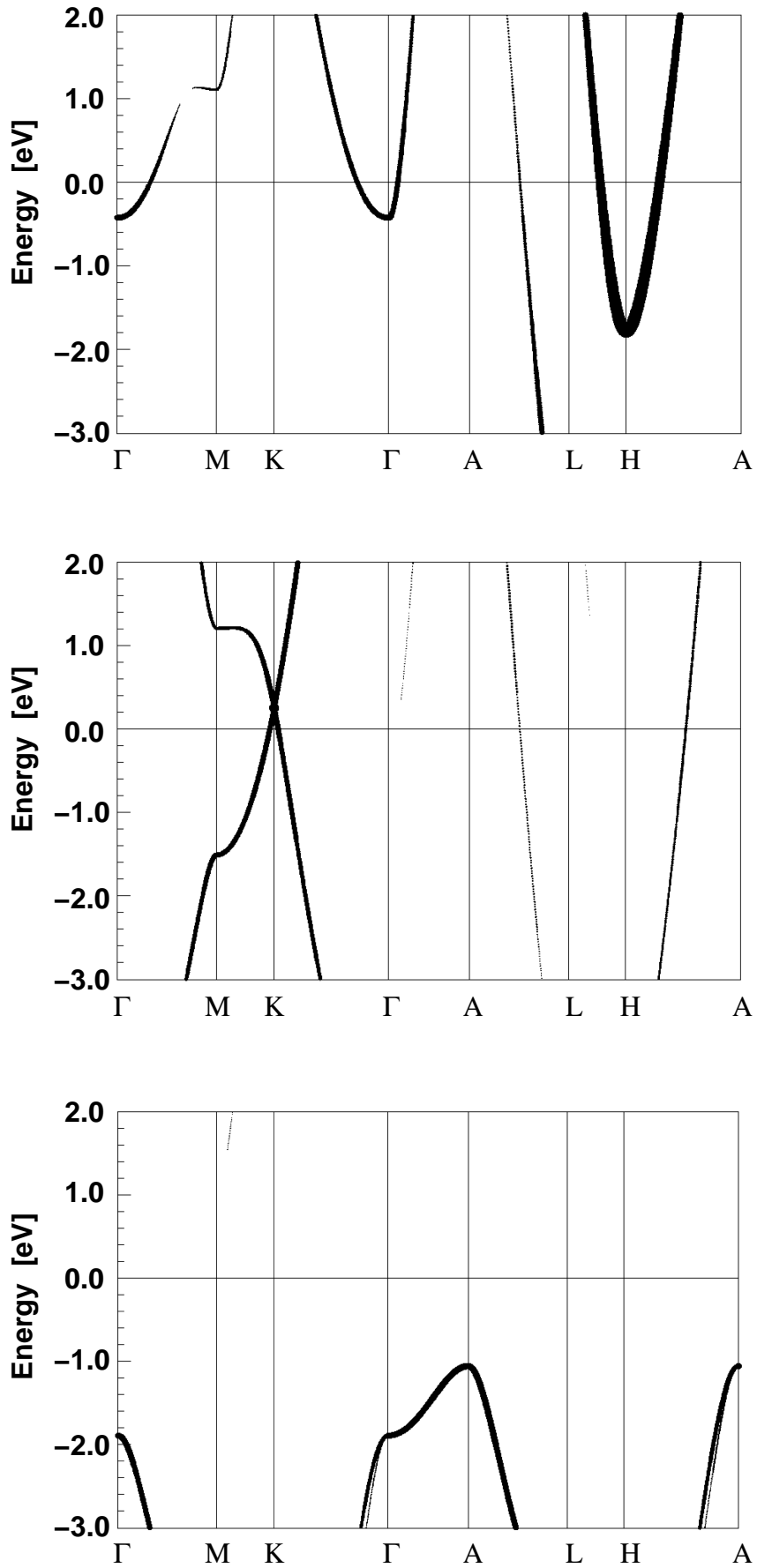


Figure 5.17: Band characters for $\text{Al}_{1-x}\text{B}_2$ for LDA with $x = 0$ (blue band structure in Figure 5.16): Al s states (top), B π states (middle) and B σ states (bottom).

see Figure 5.17. The CPA bands of the boron $p_x = p_y$ states, called σ states, see bottom panel in Figure 5.17, are the least shifted and quite sharp. This can be seen best in the band between Γ and A in the region from -2 to -1 eV for LDA (blue) and in the region from -2 to 0 eV for CPA (red). This is in agreement with the expectations: an Al vacancy will not have a large effect on this band, since it is due to electrons forming a σ bond between the boron atoms in the boron plane. This is different for the CPA bands for the Al s states, see top panel in Figure 5.17. These bands have a small admixture from boron p_z states, called π states, see middle panel in Figure 5.17. Here, the shift of the corresponding bands of the non-stoichiometric structure is larger and the bands are much more broadened (which is why they are hard to see). This is best seen in the band around the Γ point in the region from -0.5 to 2 eV for LDA (blue) and 1.5 to 2 eV for CPA (red). Also this is in agreement with the expectations: these electrons are more strongly exposed to the aluminium vacancy, which is located between the boron layers. Hence, for these bands the spectral function yields larger shifts and more broadened bands.

In order to capture local (distortion) effects, which is not possible with CPA, we will investigate the influence of the vacancies on the boron atoms using super cells, where one Al is replaced by a vacancy. In case of the 4-fold super cell, which yields a composition of $Al_{0.75}B_2$, there are vacancies above and below each boron layer. Due to this symmetry, the boron atoms surrounding this vacancy (yellow and orange spheres in Figure 5.12) will only relax within the (002) plane. Since the green B atoms are not directly exposed to the vacancy and they can be fixed in space in good approximation. Calculating the energy for different positions along the straight line between the yellow B atoms and the centre of the hexagonal boron net (and for the orange B atom, respectively) yields the red curve in Figure 5.18. The energy is lower (by 3.3 meV) if the yellow and orange B atoms are relaxed by 0.005 \AA towards the centre of the boron hexagon. In case of the 8-fold super cell, which yields a composition of $Al_{0.875}B_2$ – which is very close to the experimental composition – there is a vacancy only above every second boron layer, *i.e.*, the symmetry in z direction is lifted. We will therefore relax the yellow B atom along the straight line between this B atoms and the vacancy. The orange B atom is relaxed in the same manner and the green B atoms are still fixed in good approximation. Here, the displacement gives also an energetically lower state, if the (yellow and orange) B atoms are relaxed towards the vacancy. But here the energy gain is almost one order of magnitude smaller compared to the 4-fold super cell: a displacement of 0.004 \AA is 0.7 meV lower in energy compared to the original positions, see blue curve in Figure 5.18. There are two reasons, why this displacement has not been observed experimentally. First, this displacement of 0.004 \AA changes the atomic coordinates of the (yellow and orange) boron atoms only in the fourth digit, which is on the verge of the experimental accuracy [79] and can therefore not easily be observed. Secondly, the isotropic displacement due to thermal vibrations of the B atoms is 0.06 \AA [69]. This is one order of magnitude larger, than the calculated displacement of 0.004 \AA . Hence, low temperature measurements would be desirable. However, one should keep in mind that the results obtained from the 8-fold super cell corresponds to an ordered super structure. Thus, the displacement of 0.004 \AA should be considered as indicative only.

From this investigation we see that the influence of the vacancy on the boron network is quite small. The smaller the vacancy concentration (the larger the super cell), the smaller the influence gets. This is in agreement with our previous results: replacing Al by vacancies has a mostly local effect on the boron network. This can also be seen in pictures of the charge density, Figure 5.19. The boron layer is unchanged for both the 4-fold and 8-fold super cell.

An experiment, that is sensitive to local details in the structure is NMR. Therefore, we calculate the EFG for the B atom and compare it with the experimental result for ^{11}B of $V_{zz}^{exp} = (1.10 \pm 0.04) 10^{21} \text{ V/m}^2$ [69]. Here, the measured frequency of $\nu_Q = (540 \pm 20) \text{ kHz}$, reported for $x = 0.10$, and the quadrupole moment $Q = (40.59 \pm 0.10) \text{ mb}$ [58] were inserted in $\nu_Q = eQV_{zz}/(2h)$, since

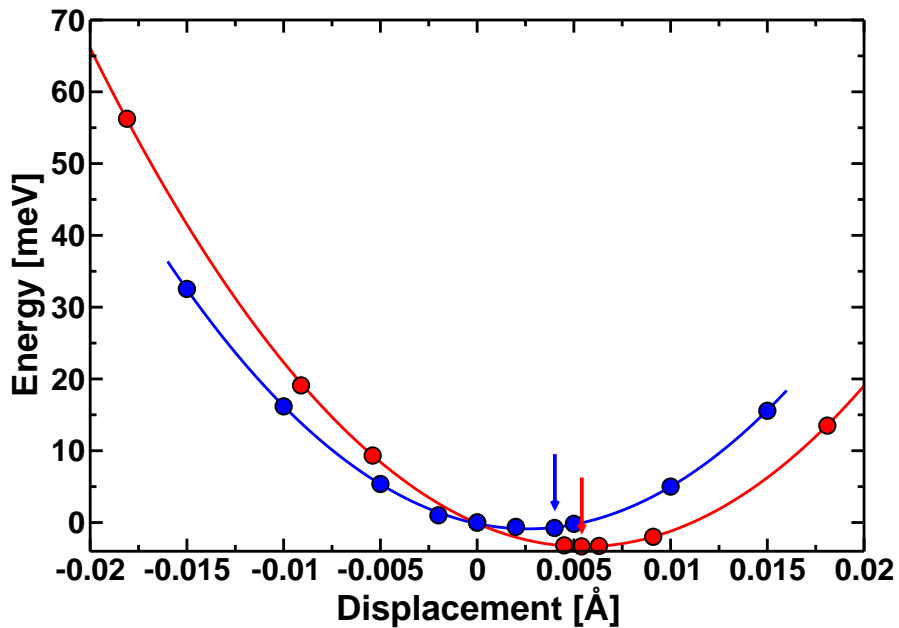


Figure 5.18: Displacement of B towards the vacancy in the 4-fold (red) and 8-fold (blue) super cell, see text. The energy scale is chosen in a manner, that both curves cross at zero displacement. The minimum in energy is marked by an arrow (red for the 4-fold and blue for the 8-fold super cell).

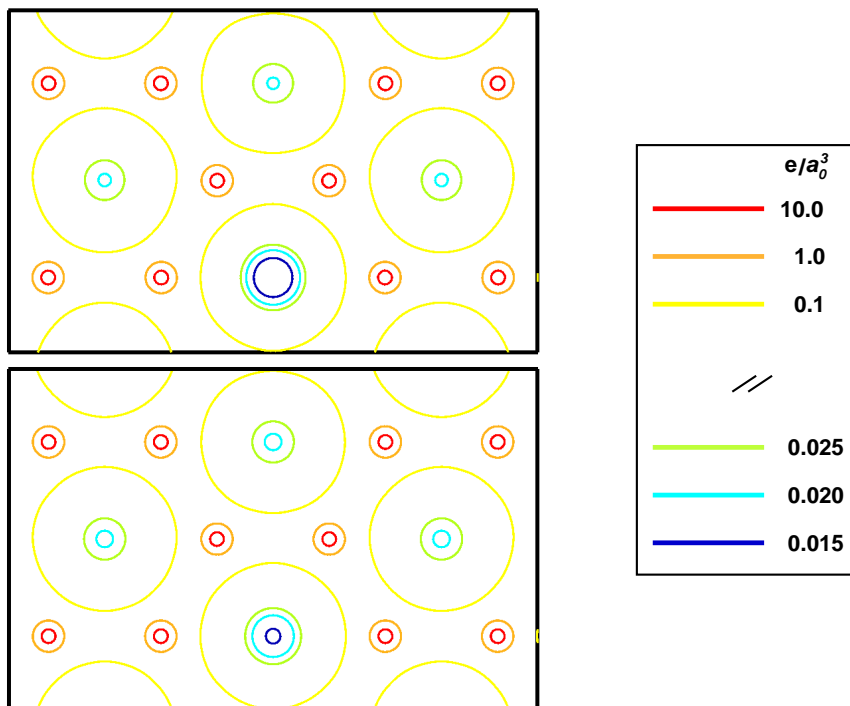


Figure 5.19: Charge density at the boron layer: $z = 0.5$ for the 4-fold super cell (top) and $z = 0.25$ (identical to $z = 0.75$) for the 8-fold super cell (bottom). The legend (right) shows the number of electrons in Bohr radii cubed. The legend shows two different scales so that the hexagonal boron layer (red and orange circles) and the effect of the Al vacancies (blue circles) from the layer above/below can be seen.

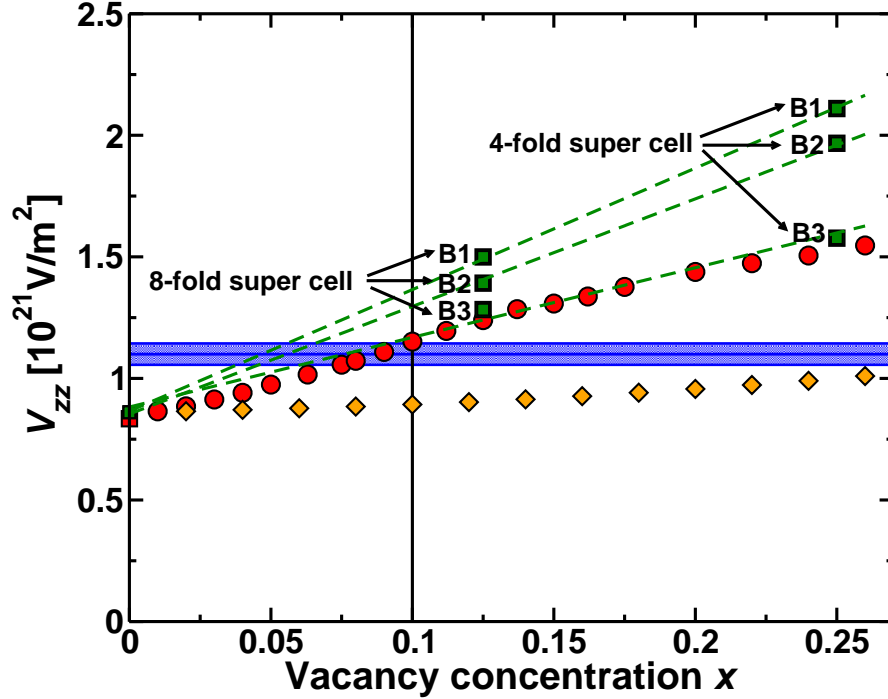


Figure 5.20: V_{zz} for B in $Al_{1-x}B_2$ in dependence of the vacancy concentration x , calculated with CPA (red circles), VCA (orange diamonds) and super cells (green squares). V_{zz} obtained from NMR is shown by the blue error bar.

B has a nuclear spin of $I = 3/2$ and the asymmetry parameter η is zero. Since the EFG is very sensitive to the structural parameters, the correctly established lattice parameters, reported for $Al_{0.9}B_2$ [69], were used for these calculations. First, we calculate the EFG using CPA, which is only available in FPLO 5, see Section 2.3.2. Therefore, we have to ensure first that the basis (as given on page 42, *i.e.*, without polarisation states) is sufficient (*cf.* Section 4.2). Comparison with FPLO 8, which yields $V_{zz} = 0.86 \cdot 10^{21} \text{ V/m}^2$, shows that FPLO 5 results in an only slightly smaller EFG: $V_{zz} = 0.83 \cdot 10^{21} \text{ V/m}^2$. Hence, the CPA module can also be used to calculate the EFG in dependence of the vacancy concentration. In Figure 5.20 we see that V_{zz} increases from $0.83 \cdot 10^{21} \text{ V/m}^2$ for the stoichiometric composition to $1.55 \cdot 10^{21} \text{ V/m}^2$ for a vacancy concentration of 26 %. For a vacancy concentration of 10 %, as reported in Ref. [69], the EFG calculated with CPA, $V_{zz}^{CPA} = 1.15 \cdot 10^{21} \text{ V/m}^2$, agrees with the experimental one.

On the other hand, if the EFG is calculated with VCA, we obtain less good agreement with the experiment. Although the EFG increases with increasing vacancy concentration its slope is too small. Even for a vacancy concentration of 26 % the experimental EFG is not reached yet. The reason, why also here CPA is a better method than VCA might be explained by the same fact as before: taking away only valence electrons, but not the whole core, as CPA does, leaves the structure more isotropic and hence a smaller EFG is obtained compared to CPA.

The opposite behaviour is obtained when the disordered compound is calculated with super cells: as VCA underestimates the anisotropy, super cells overestimate the anisotropy. Due to the three different Wyckoff positions for the B atoms, see Table 5.6, there are now three different EFGs, labelled B1, B2 and B3 in Figure 5.20. The EFG increases linearly with increasing vacancy concentration: for the 4-fold super cell, the vacancy concentration is higher ($x = 0.25$) and the EFGs are larger, then for the 8-fold super cell ($x = 0.125$). This is in agreement with the VCA and CPA result and the expectation: in the 4-fold super cell, there are vacancies in each Al layer,

whereas in the 8-fold super cell, the vacancies are only in every second Al layer. Therefore, the electronic density of the B atoms are less distorted, resulting in a smaller EFG in the 8-fold super cell. The boron atoms, that have the largest distance to the vacancy, B3, the green spheres in Figure 5.12, have the smallest EFGs, they lie very close to the CPA curve. The boron atoms B1 and B2 have the same distance to the vacancy, but B2 (yellow spheres), have a larger distance to the vacancies from the neighbouring cells and have therefore smaller EFGs than the boron atoms labelled B1 (orange spheres).

5.2.4 Summary and conclusion

AlB_2 is one of the basic structural archetypes of intermetallic compounds. Only in the last decade, numerous experiments revealed a non-stoichiometric composition of aluminium diboride with vacancies on the Al site.

In order to investigate if the origin of the vacancies is intrinsic or due to the processing, we performed CPA calculations and obtained excellent accordance with the experimental results. The calculated equilibrium yields a composition of $\text{Al}_{0.87}\text{B}_2$ which is in perfect agreement with the experimental findings (composition of about $\text{Al}_{0.9}\text{B}_2$ [67, 69]).

Comparing the electronic density of states of the fully occupied and the defect structure shows no new features: the DOS of the defect structure is primarily shifted and can be described with the rigid-band approximation. The same is observed in the band structure. Due to the Al vacancies, the bands of the defect structure are primarily shifted. However, the band structure displays the effect of the vacancies on the individual bands. We observe that the in- and out-of-plane bands are shifted differently.

Since CPA does not describe local distortion, we performed super cell calculations for an 8-fold super cell, which is in the range of the experimentally reported compositions, to investigate if local distortion effects are relevant. Total energy calculations for this super cell show only a negligible deformation of the boron network due to the Al vacancies. Hence, local distortion effects can be excluded.

The EFG calculated with CPA for a vacancy concentration of 10 %, $V_{zz} = 1.15 \cdot 10^{21} \text{ V/m}^2$, is on the verge of the error bar of the experimental EFG, $V_{zz}^{exp} = (1.10 \pm 0.04)10^{21} \text{ V/m}^2$, reported for $\text{Al}_{0.9}\text{B}_2$ [69]. This agreement is an additional argument in favour of the presence of Al vacancies.

Band structure calculations show that the defects in the Al sublattice in $\text{Al}_{0.9}\text{B}_2$ in equilibrium conditions are intrinsic and can be understood from the interplay of the occupation of the bonding boron σ states and the Al states.

5.3 The perovskites SrTiO₃ and BaTiO₃

5.3.1 Introduction

Perovskites are described as ionic⁷ crystals with cubic symmetry (space group $Pm\bar{3}m$). They named after the mineral CaTiO₃. The general formula for perovskites containing oxygen is ABO_3 . The A ions are arranged at the corners of the cube, the B ion is at the centre of the cube and the O^{2-} ions are at the centres of the cube faces, see Figure 5.21. Hence, the B ion is 6-fold coordinated and located in the centre of an octahedral void of oxygen ions. In order to form a perovskites, there is not only a condition on the charge of the cations (their sum must compensate the negative charge of the oxygen) but also on their radii (empirical rule): $R_A + R_O = \sqrt{2}(R_B + R_O)$. However, the latter requirement is not very strict, both the A and B ion may vary slightly in their size resulting in a tolerance factor on the right hand side of the equation [82]. Therefore, many compounds crystallise in the ABO_3 structure type. There are also many perovskites, ABX_3 , where oxygen is replaced by another anion X , which may also be a complex ion [82].

The perovskite-like compounds ABO_3 attract much attention because of their importance for both fundamental science and technological applications [83]. Although the high-temperature cubic phase has a very simple crystal structure, this does not prevent these compounds from exhibiting a large variety of physical properties rendering the perovskites to model compounds for studies of a large variety of different physical phenomena. Within the perovskite family, we find superconductivity, *e.g.*, in $K_xBa_{1-x}BiO_3$ [84], giant magnetoresistance, *e.g.*, in $LaMnO_3$ [85], orbital ordering, *e.g.*, in $YTiO_3$ [86] and ferroelectricity, *e.g.*, in $BaTiO_3$ [83, 87]. The latter phenomenon is of large interest because of technological applications.

In this section, we will focus on the compounds $SrTiO_3$ and $BaTiO_3$, which are usually believed to be isovalent. The valence and conduction bands of the two perovskites are formed by oxygen p states and titanium d states. In the high-temperature cubic phase (space group $Pm\bar{3}m$), the Ti and O sub-lattices have identical geometry for $SrTiO_3$ and $BaTiO_3$, the lattice parameters are $a=3.900 \text{ \AA}$ [88] and $a=4.009 \text{ \AA}$ [83], respectively. As the temperature lowers, $BaTiO_3$ exhibits a succession of phase transitions, from the high-temperature cubic phase to ferroelectric structures with tetragonal, orthorhombic and rhombohedral symmetry [83]. $SrTiO_3$ remains paraelectric down to the lowest temperatures. It undergoes a phase transition at 105 K to a tetragonal phase, but this transition has little influence on the dielectric properties [89].

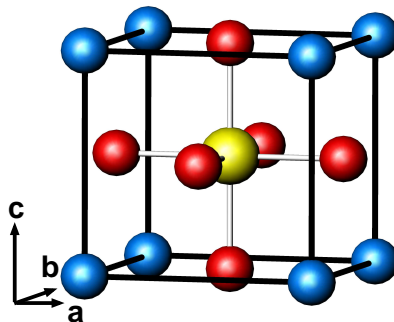


Figure 5.21: The perovskite structure of $SrTiO_3$ ($BaTiO_3$). The Sr^{2+} (Ba^{2+}) ions (blue) are at the cube corners, the O^{2-} ions (red) are at the centres of the cube faces and the Ti^{4+} ion (yellow) is at the centre of the cube.

⁷We will show in this section that the ionic description, as is it used in standard solid state physics textbooks, *e.g.*, Refs. [80, 81], is not ideal. But for now (and also in Figure 5.21) we keep the ionic terminology.

Table 5.8: Experimental and calculated values of the EFG (in 10^{21} V/m²) on the oxygen site in the cubic phase of the two perovskites. The last 4 rows are calculated with FPLO, the definitions for the different EFGs are given in the last column (referring to the equations as given in Section 4.1.1).

EFG	SrTiO ₃	BaTiO ₃	Reference
$ V_{zz}^{exp} $	1.62	2.46	Ref. [90]
V_{zz}^{cal}	-1.00	-2.35	Ref. [90]
V_{zz}^{cal}	+1.00	+2.44	Eq. (4.10)
V_{zz}^{on}	-0.21	+1.39	Eq. (4.11)
V_{zz}^{off}	+1.21	+1.05	Eq. (4.12)
$V_{zz,pp}^{on,net}$	96%	107%	Eq. (4.16)

5.3.2 Motivation

Though, the perovskite structure ABO_3 is cubic, there can be an electric field gradient (EFG) at the oxygen site due to its tetragonal site symmetry. The first determination of the oxygen EFG in SrTiO₃ and BaTiO₃ was reported recently together with first-principles calculations (where a linearised augmented plane wave (LAPW) method was used) [90]. The most striking feature is the large difference of the EFGs between the two compounds, obtained from both the experimental and theoretical data. From their calculational investigation, Blinc *et al.* conclude that the magnitude of the EFG of oxygen in BaTiO₃ is larger than in SrTiO₃ due to two effects: (i) larger lattice parameters in BaTiO₃ compared to SrTiO₃ and (ii) a larger ionic radius of Ba compared to Sr. While the experimental determination (they used nuclear magnetic resonance (NMR)) can not provide the sign of the EFG, the LAPW calculation yields a negative sign for the EFG. A negative EFG corresponds to a prolate electron density, which implies the importance of covalence effects. In order to elucidate the origin of the sign of and the different contributions to the EFG, we have performed first-principle calculations using the on density functional theory (DFT) based code FPLO. Since the representation of the potential and the density in FPLO allows easy decomposition, FPLO is especially suited to address these questions.

5.3.3 Methods

The electronic band structure calculations were performed with the full-potential local-orbital minimum-basis code FPLO (version 5.00-19) [2] within the local density approximation. In the scalar relativistic calculations the exchange and correlation functional of Perdew and Wang [15] was employed. As basis sets Ba (4d5s5p/6s6p5d+4f7s7p), Sr (4s4p/5s5p4d+6s6p), Ti (3s3p3d/4s4p4d+5s5p) and O (2s2p3d+3s3p) were chosen for semicore/valence+polarisation states. The high lying states improve the basis which is especially important for the EFG calculation. The lower lying states were treated fully relativistically and as core states. A well-converged k mesh of 455 k points was used in the irreducible part of the Brillouin zone.

5.3.4 Results

In FPLO, the EFG at a given lattice site may be represented as the sum of two contributions: the on-site contribution V_{zz}^{on} Eq. (4.11), which comes from the on-site contribution of the electron

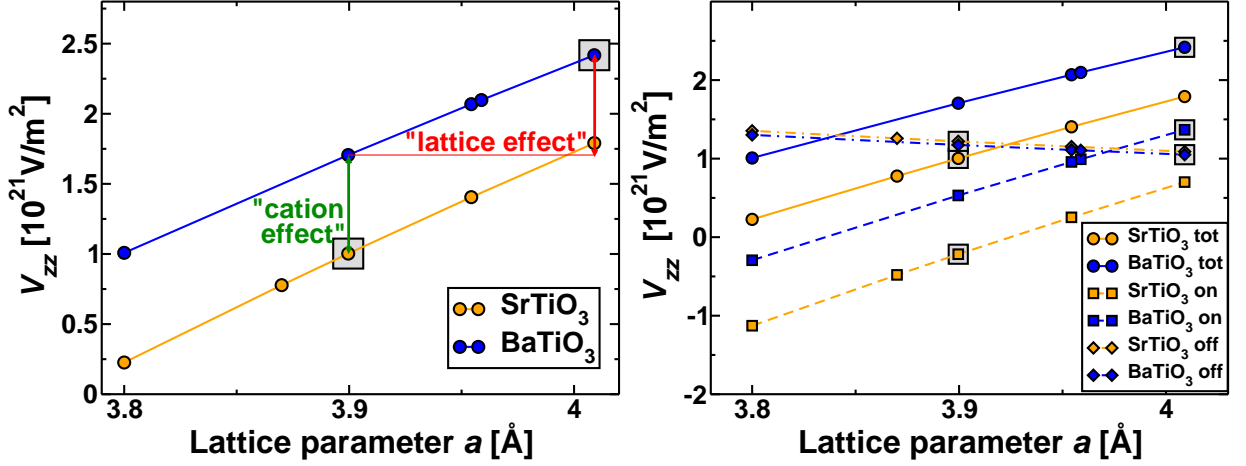


Figure 5.22: **Left:** calculated V_{zz} in dependence of the lattice parameter a . V_{zz} for the experimental lattice parameter is marked by shaded squares. The “cation” and “lattice effect”, which are responsible for the difference in V_{zz} for these two compounds are indicated by the green and red arrow, respectively. **Right:** the on-site V_{zz}^{on} , off-site V_{zz}^{off} and total EFG as a function of the lattice parameter a . The grey shaded squares mark the experimental lattice parameter for V_{zz} .

density of the given lattice site and the off-site contribution V_{zz}^{off} Eq. (4.12), which results from the potential of all other atoms (see Section 4.1). The on-site contribution can be analysed further, it can be split up in pp , sd and dd contributions (see Section 4.1.1).

The on- and off-site contributions, as well as their sum and the dominating pp contribution (see Eq. (4.16)) are shown in Table 5.8. Whereas the total EFG for oxygen in BaTiO₃ agrees well with the experiment (1 % deviation), the total EFG for oxygen in SrTiO₃ is in discrepancy⁸ with the experiment (38 % deviation), see Table 5.8. Compared to the EFGs calculated with the LAPW code in Ref. [90], we obtain almost the same absolute value for V_{zz} but the opposite sign, see Table 5.8. Our calculated EFGs as a function of the lattice parameter a for both compounds reveal the same tendency as observed in Ref. [90]: the absolute value of the EFG increases under the lattice expansion (see left graph in Figure 5.22). From that graph, we also conclude that the EFG of BaTiO₃ is not only larger than the EFG of SrTiO₃ due to larger lattice parameters (“lattice effect”), but also due to an “cation effect”, which is the shift between the two EFG curves in the left graph in Figure 5.22 marked by the green arrow. The lattice effect is demonstrated by the red arrow between the two EFG curves.

The increase of the (absolute value of) the EFG upon lattice expansion is rather counter-intuitive. In the traditional approach, where the perovskite is described by an ionic crystal, the spherically symmetric electronic shell of an ion is perturbed by the potential of the other external (point) charges of the solid. This external potential causes the total EFG at the nucleus of that ion. It is clear that this approach predicts the opposite tendency: the strength of the external potential is inversely proportional to the lattice parameters and thus the (absolute value of the) EFG should diminish under the lattice expansion. The failure of this approach to describe the observed behaviour of the EFG indicates that a fully ionic description of the perovskites is inappropriate. In an alternative approach, the electronic shell of an atom is disturbed by the hybridisation of its wave functions with the states of the neighbouring atoms. The hybridisation results in the

⁸We also calculated the EFG for the low symmetry phases of BaTiO₃ and SrTiO₃. Whereas the calculational results for BaTiO₃ agree well with the experiment, the discrepancy for SrTiO₃ remains unchanged and of unclear reason.

asymmetry of the electronic cloud of the atom and the EFG on its nucleus. Apparently, this second approach predicts the same tendency as the first one: as a rule of thumb, hybridisation diminishes with the increase of the bond length.

Therefore, in both approaches we may say: when expanding the lattice, we diminish its influence on the atom and the electronic shell should become closer to that of a free atom. Hence, we come to the conclusion: the (absolute value of the) EFG should diminish under the lattice expansion, which is opposite to the experimental observation and the results of both first-principles calculations. We will tackle this problem in Section 5.3.5.

First, we will resolve the problem of the different sign of the EFGs obtained from the two different band structure codes, *cf.* Table 5.8. If the sign of the EFG is taken into account, the slope in our graph (left graph in Figure 5.22) is opposite to the slope in the graph obtained with the LAPW code (Figure 5 in Ref. [90]). Since the NMR experiment is not sensitive to the sign of the EFG, we will investigate the influence of the lattice expansion on the different contributions to the EFG to get more insight in this issue.

Our calculations show that both the on-site and the off-site contribution to the EFG have comparable values for the perovskite lattice, see Table 5.8 and the right graph in Figure 5.22. The unusual large off-site EFG is due to the ionic character of the perovskites. This is different in metals, where due to screening, the off-site contribution to the EFG is usually very small, *cf.* Section 5.1. In that graph, the two contributions V_{zz}^{on} (dashed line) and V_{zz}^{off} (dash point line) and the total EFG (full line) are shown. Whereas the off-site EFG decreases only slightly upon lattice expansion, the on-site EFG increases strongly with increasing lattice parameters, resulting in the significant increase of the total EFG. We also observe that the off-site EFG is almost identical for these two structures, which is in line with the observed very weak dependence of V_{zz}^{off} on the lattice parameters. The on-site EFG is mainly caused by electrons with p character, see Table 5.8. Therefore, we will investigate the anisotropy function $\Delta p = (n_x + n_y)/2 - n_z$ (*cf.* Eq. (4.17) in Section 4.1.1). In the perovskite structure ABO_3 , the oxygen site has axial symmetry. The z axis is directed along the B-O bond, see Figure 5.21. Thus, the anisotropy function is the difference between the populations of the oxygen $2p$ σ (corresponding to p_z) and π (corresponding to $p_{x,y}$) orbitals: $\Delta p = n_x - n_y$ ($n_x = n_y$ due to the axial symmetry). In the left graph in Figure 5.23, we see that the anisotropy function Δp increases with the lattice expansion. This is in agreement with the increasing on-site EFG. If we focus on $BaTiO_3$, where the experimental and calculated (for the experimental lattice parameter $a = 4.009 \text{ \AA}$) values for the EFG agree very well, we see that this positive V_{zz} corresponds to a positive Δp . That means the p electron density (responsible for the EFG) has an oblate shape, since more electrons are occupying the $p_{x,y}$ orbitals than the p_z orbital, which is in agreement with the positive sign of the EFG. In addition, cross-checking the oxygen EFG for $BaTiO_3$ with the LAPW code WIEN2k (using the same parameters as in FPLO), yields a positive sign for V_{zz} as well. The sign in the other LAPW code might be opposite due to a different definition of V_{zz} , *cf.* page 24.

After concluding that the sign of V_{zz} for O for both $SrTiO_3$ and $BaTiO_3$ should be positive, we come back to the counter intuitive behaviour of the increasing EFG upon lattice expansion. As stated before, the increase of the total EFG upon lattice expansion is due to the on-site EFG, as the off-site EFG decreases upon lattice expansion, as predicted by the intuitive approaches. The left graph in Figure 5.23 shows that the increase of the on-site EFG under lattice expansion is due to the increase of the anisotropy function Δp . The right graph in Figure 5.23 reveals that the increase of Δp under lattice expansion is due to an increasing occupation of π (corresponds to $p_{x,y}$) and an decreasing population of σ (corresponds to p_z) orbitals. Analysis of the occupation of the oxygen orbitals under the lattice expansion shows an electron transfer from the p_σ to the s orbitals. Since the latter is spherically symmetric it gives no contribution to the EFG.

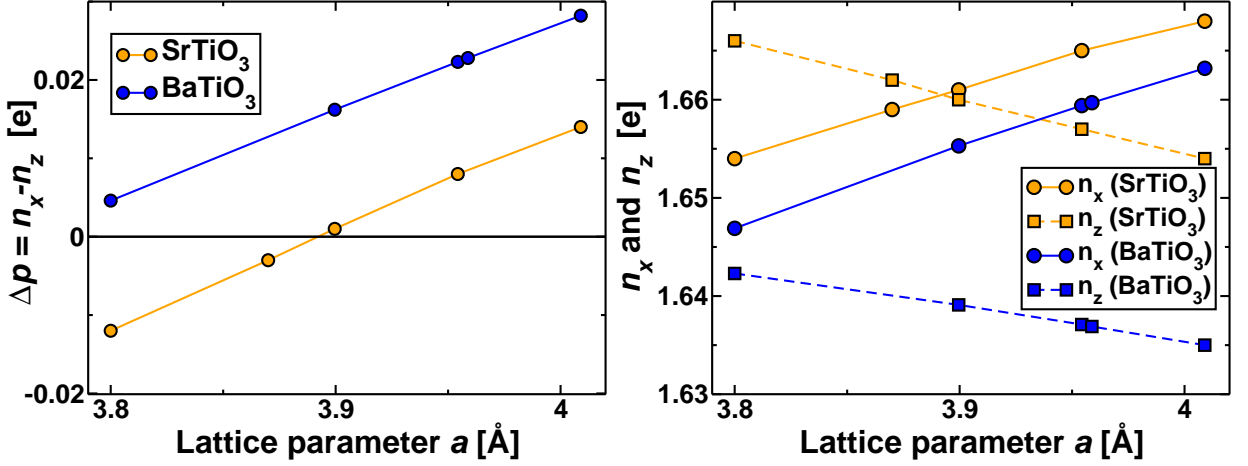


Figure 5.23: **Left:** the anisotropy function Δp in dependence of the lattice parameter a . **Right:** the occupation of p_x and p_z states ($=n_x$ and n_z , respectively) in dependence of the lattice parameter a .

5.3.5 Discussion

In order to understand this anomalous behaviour of the σ orbital, we will analyse the main features of the electronic structure of perovskites. Detailed band structure studies of perovskite compounds were performed by Mattheiss [91, 92, 93], who also proposed a first tight-binding fit for the band dispersions. Wolfram *et al.* [94, 95, 96] (*cf.* also Ref. [97]) developed a very simple model (Wolfram and Ellialtioglu, WE) for the valence and conduction bands, which reflects their basic properties. The WE model includes the d orbitals of the B ion and the p orbitals of the oxygen. Wolfram *et al.* pointed out a quasi-two-dimensional character of the bands, which is due to the symmetry of the orbitals. If one retains only nearest neighbour hoppings, the total 14×14 Hamiltonian matrix (5 d orbitals and 9 p orbitals) acquires block-diagonal form at each value of \vec{k} . The three 3×3 matrices describe the π_{ij} bands ($ij = xy, yz, xz$). Every d_{ij} orbital of the t_{2g} symmetry couples with its own combination of oxygen $2p$ π orbitals, which lie in the same plane perpendicular to the bond direction. They form a pair of bonding and anti-bonding states. The remaining combination of the $2p$ π orbitals in the same plane form the non-bonding bands. Wolfram *et al.* call this group of bands π bands. The states described by the 5×5 block matrix are called σ bands, since they are formed by oxygen $2p$ σ orbitals, which are coupled with the e_g ($d_{x^2-y^2}$ and d_{z^2}) orbitals of the B ion. This matrix decouples into one non-bonding band and two pairs of bonding and anti-bonding bands.

Figure 5.24 shows the calculated band structure for SrTiO₃ for two different lattice parameters a . The features mentioned above are clearly seen (*cf.* Figure 2 of Ref. [95]). The anti-bonding π_{ij} bands (red coloured) are situated between 2 and 4 eV, where the π_{yz} band is almost dispersionless in the direction $\Gamma \rightarrow X$. This manifests the quasi-two-dimensional character of the bands. The bands originating from the d_{eg} orbitals (green coloured) are in the range from 4 to 8 eV, where the band expressing d_{z^2} character is dispersionless along the $\Gamma \rightarrow X$ direction. The valence band has a more complex character due to additional mixing from the direct p - p hopping. This is neglected in the simple version of the WE model. Nevertheless, we see that the non-bonding bands (orange coloured) lie on top of the valence band and have a much smaller dispersion than the bonding bands, which lie below -1 eV (π_{ij} , cyan coloured) and below -3 eV (σ bands, blue coloured). The latter have a larger dispersion due to much larger d - p hoppings.

Although the Kohn-Sham theory is not good for excitation spectra, or obtaining the correct energy

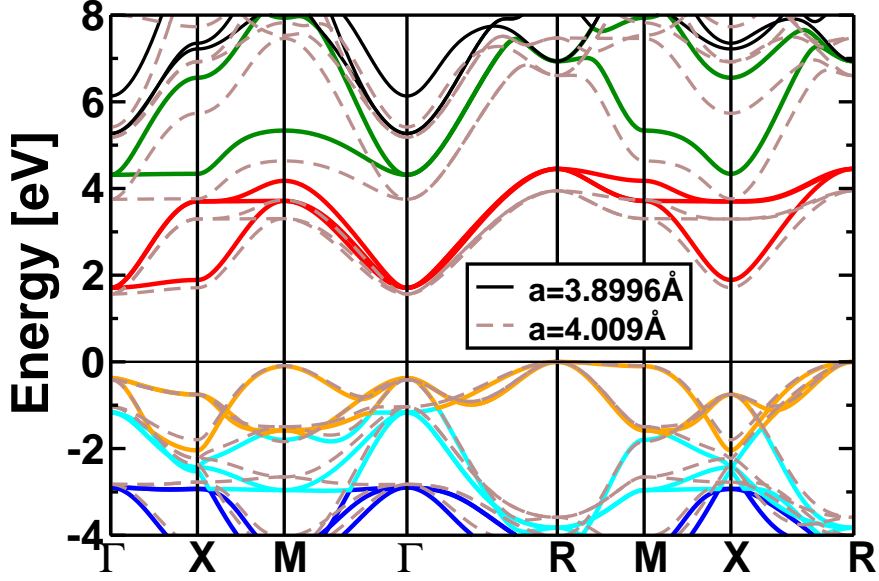


Figure 5.24: SrTiO₃: band structure for two different lattice parameters $a = 3.8996 \text{ \AA}$ (full lines) and $a = 4.009 \text{ \AA}$ (dashed lines). The different band characters are given by different colours: blue (bonding, σ), cyan (bonding, π), orange (non-bonding), red (anti-bonding, π_{ij}) and green (anti-bonding, d_{eg}), see text. Since it is not easy to interpret the valence band, the colours in the valence band are only approximate.

gap, it yields reliable occupation numbers, on-site energies and transfer integrals, especially in the absence of strong correlations. Therefore, we can use our LDA band structure to obtain reliable parameters as input for further treatment using model Hamiltonians.

In the following, we explore within the WE model how the occupation numbers and the resulting anisotropy count for the p orbitals depend on the lattice parameters. In dielectric compounds like SrTiO₃ and BaTiO₃, the bonding and non-bonding states are fully occupied. Contrary to the non-bonding bands, which have almost pure p character, the bonding and anti-bonding bands are mixed p - d bands. The population of the p orbitals is given by the sum of the occupation numbers of the non-bonding and the bonding bands, whereof the latter are lattice parameter dependent. Every pair of bonding and anti-bonding states is described by an effective two-level model [96]

$$\hat{H}_m = \Delta_m \left(|d, \vec{k}\rangle \langle d, \vec{k}| - |p, \vec{k}\rangle \langle p, \vec{k}| \right) + V_m f_{m\vec{k}} \left(|d, \vec{k}\rangle \langle p, \vec{k}| + |p, \vec{k}\rangle \langle d, \vec{k}| \right). \quad (5.2)$$

Here, m describes the character of the band $m = \pi, \sigma$ and $f_{m\vec{k}}$ is a dimensionless function, which depends on the dimensionless variable $\vec{k}a$ (note that \vec{k} is measured in units of π/a , so neither $\vec{k}a$ nor $f_{m\vec{k}}$ depends on a). The state mixing is defined by the interplay of the on-site energy difference Δ_m and the transfer integral V_m , which determines the bandwidth of the corresponding band. The eigenstates of the Hamiltonian Eq. (5.2) have the form

$$|\vec{k}, \nu\rangle = c_{d\vec{k}\nu} |d, \vec{k}\rangle + c_{p\vec{k}\nu} |p, \vec{k}\rangle, \quad (5.3)$$

and the following energies and occupation numbers are obtained

$$E_{\vec{k}m\nu} = \nu \sqrt{\Delta_m^2 + V_m^2 (f_{m\vec{k}})^2}, \quad \nu = \pm 1 \quad (5.4)$$

$$n_{p\vec{k}m\nu} \equiv 2 |c_{p\vec{k}\nu}|^2 = 1 - \frac{\Delta_m}{E_{\vec{k}\nu}}. \quad (5.5)$$

$$n_{d\vec{k}m\nu} \equiv 2 \left| c_{d\vec{k}\nu} \right|^2 = 2 \left(1 - \left| c_{p\vec{k}\nu} \right|^2 \right) = 1 + \frac{\Delta_m}{E_{\vec{k}\nu}}. \quad (5.6)$$

Here, $\nu = +1$ describes the anti-bonding and $\nu = -1$ describes the bonding band. In this two-level system, two asymptotic behaviours are possible. First, $\Delta_m/V_m \rightarrow \infty$, which yields for the occupation numbers of the bonding bands $n_{p\vec{k}m,-1} \rightarrow 2$ and $n_{d\vec{k}m,-1} \rightarrow 0$. In this case, both electrons are in the p state of the ligand ion and the d states are empty, called ionic limit. Second, $\Delta_m/V_m \rightarrow 0$, which yields for the occupation numbers $n_{p\vec{k}m,-1} \rightarrow 1$ and $n_{d\vec{k}m,-1} \rightarrow 1$. In this case, the electrons are equally shared by the p and d states, called covalent limit. From the trends in Figure 5.23, we observe that while the population of the p_π orbitals increases, the population of the p_σ orbitals decreases. This means the Ti-O π bond gets more ionic under lattice expansion (as expected) whereas the Ti-O σ bond gets more covalent, which we will try to explain with this model.

The parameters of this model may be extracted from the band energies at symmetry points of the Brillouin zone in Figure 5.24 (see the Appendix G for more details).

For example, the on-site energies Δ_m can be obtained from the Γ point, since due to symmetry, the d - p mixing vanishes at this point and the band states acquire a pure d or p character. For $a = 3.8896 \text{ \AA}$ we have for SrTiO₃ $E_{d_{t2g}} \approx 1.7 \text{ eV}$, $E_{d_{eg}} \approx 4.3 \text{ eV}$ and $E_p \approx -1.2 \text{ eV}$. This yields (using Eq. (G.11) and Eq. (G.10)) $2\Delta_\pi = E_{d_{t2g}} - E_p \approx 2.9 \text{ eV}$ and $2\Delta_\sigma = E_{d_{eg}} - E_p \approx 5.5 \text{ eV}$. From these values and the $f_{m\vec{k}}$ as given in Refs. [95, 96], we obtain the Slater-Koster hopping parameters $V_\sigma \approx 2.1 \text{ eV}$ (Eq. (G.13)), $V_\pi = V_{pd\pi} \approx 1.6 \text{ eV}$ (Eq. (G.12)) and $V_{pd\sigma} \approx 2.7 \text{ eV}$ (Eq. (G.15))⁹.

As already said, we are interested in the occupation numbers. Since the occupation numbers of the non-bonding bands do not depend on the lattice parameter and the anti-bonding bands ($\nu = +1$) are not occupied, we consider the bonding bands ($\nu = -1$) only. The contributions from the bonding bands to the population of the p_m orbitals are obtained by summing up $n_{p\vec{k}m,-1}$ over the whole Brillouin zone,

$$n_{p_m} = N^{-1} \sum_{\vec{k}} n_{p\vec{k}m,-1} + \text{const.}, \quad (5.7)$$

where N is the number of sites in the crystal. In order to analyse the occupation in dependence of the lattice expansion, we need the derivative of the occupation number with respect to the lattice parameter a . From Eq. (5.5) we obtain for the derivative (denoted by \prime)

$$n'_{p\vec{k}m,-1} = \frac{V_m^2 (f_{m\vec{k}})^2 \Delta_m}{\left(\sqrt{\Delta_m^2 + V_m^2 (f_{m\vec{k}})^2} \right)^3} \left(\frac{\Delta'_m}{\Delta_m} - \frac{V'_m}{V_m} \right). \quad (5.8)$$

The derivative of n_{p_m} is proportional to

$$n'_{p_m} \propto \left(\frac{\Delta'_m}{\Delta_m} - \frac{V'_m}{V_m} \right). \quad (5.9)$$

The left graph of Figure 5.23 shows that n'_{p_m} has a different behaviour for $m = \sigma$ (n'_{p_σ} is negative) and $m = \pi$ (n'_{p_π} is positive). Thus, within the WE model, the observed increase of the EFG, which is due to the decreasing occupation of the p_σ orbitals would yield

$$-\frac{V'_\sigma}{V_\sigma} < -\frac{\Delta'_\sigma}{\Delta_\sigma}. \quad (5.10)$$

⁹The parameters V_π and V_σ are from the WE (p - d) model and $V_{pd\pi} = V_\pi$ and $V_{pd\sigma}$ are from the Harrison (s - p - d) model, see Appendix G.

Both Δ_σ and V_σ decrease with the lattice expansion: Figure 5.24 shows that the energies at the Γ point $E_{d_{eg}}$ and $E_{d_{t2g}}$ and the bandwidths are smaller for the larger lattice parameter $a = 4.009 \text{ \AA}$, than for the smaller lattice parameter $a = 3.8996 \text{ \AA}$. Now, we will estimate an approximation for both side of the inequality Eq. (5.10). We start with the left hand side. A commonly accepted estimate [98] for the dependence of hopping integrals on a is $V_\sigma \propto a^{-\alpha}$ with $\alpha \in [3.5, 4]$ (from the LDA band structure, we obtain $\alpha = 3.5 \pm 0.5$). This gives

$$-a \frac{V'_\sigma}{V_\sigma} = \alpha \geq 3. \quad (5.11)$$

On the right hand side, we have Δ_σ , which is the difference in energy of the atomic levels corrected by the crystal field (CF)¹⁰ $\Delta_\sigma = \varepsilon_d - \varepsilon_p + \delta_{CF,\sigma}$.

The crystal field consists of two contributions [99]: a (dominating) electrostatic contribution, which is the difference of the Madelung potentials of Ti and O, hence $\delta_{CF,el} \propto a^{-1}$, and a hybridisation contribution, which, in our case (octahedral coordination), contains a large and strongly a -dependent contribution for $m = \sigma$ from the semi-core s states of the ligand. Indeed, the change due to the increasing lattice parameter a is much larger for Δ_σ than for Δ_π , cf. Figure 5.24. The main electrostatic contribution, which implies $\delta_{CF,el} \propto a^{-1}$, leads to

$$-a \frac{\Delta'_\sigma}{\Delta_\sigma} = \frac{\delta_{CF,el}}{\Delta_\sigma}.$$

Since $\varepsilon_d - \varepsilon_p + \delta_{CF,el} > \delta_{CF,el}$, is $\delta_{CF,el}/\Delta_\sigma < 1$ and therefore

$$-a \frac{\Delta'_\sigma}{\Delta_\sigma} < 1. \quad (5.12)$$

Combining these estimations, Eq. (5.11) and Eq. (5.12), we get

$$-a \frac{\Delta'_\sigma}{\Delta_\sigma} < 1 < 3 \leq -a \frac{V'_\sigma}{V_\sigma}. \quad (5.13)$$

This is in contradiction to the inequality (5.10), leading to the conclusion that the WE model, though consistent with the intuitive expectations is unable to predict the observed behaviour of the σ orbital occupation in Figure 5.23.

A possible reason for the failure of the WE model is that according to Ref. [92], a large contribution to the CF comes from the oxygen $2s$ orbitals, which lie almost 18 eV below the Ti $3d$ level, $\Delta_{sd} = 17.9 \text{ eV}$, but have a large matrix element $V_{sd\sigma} = 3.0 \text{ eV}$ with the e_g orbitals. This suggests to extend the WE model by taking into account the oxygen $2s$ states in order to explain the increasing EFG upon lattice expansion. This is Harrison's model, where $V_{sd\sigma}$ is obtained from Eq. (G.14)

$$\Gamma_{12} = \frac{\varepsilon_s + \varepsilon_d}{2} \pm \sqrt{\left(\frac{\varepsilon_s - \varepsilon_d}{2}\right)^2 + 6V_{sd\sigma}^2},$$

with $\varepsilon_s = -16.2 \text{ eV}$, $\varepsilon_d = 1.7 \text{ eV}$ and $\Gamma_{12} = 4.3$ taken from the band structure.

Taking the s orbitals into account, we have on the left hand side of the inequality Eq. (5.10) $V_{sd\sigma}$. Harrison [98] argues that the a dependence of $V_{sd\sigma}$ is similar to the one of $V_{pd\sigma}$. This suggestion is confirmed by our LDA calculations. Thus, we obtain

$$\frac{V'_{sd\sigma}}{V_{sd\sigma}} = -\frac{\alpha}{a}. \quad (5.14)$$

¹⁰ ε denotes the energy of the atomic level and E , as used before, denotes the energy level corrected by the crystal field: $\Delta_\sigma = E_d - E_p = \varepsilon_d - \varepsilon_p + \delta_{CF,\sigma}$, cf. Eq. (G.11). Note that $\delta_{CF,m}$ is different for $m = \pi$ and $m = \sigma$, since ε_d is the atomic energy level, and thus does not depend on m . This is the main reason that $\delta_{CF,\sigma} > \delta_{CF,\pi}$. Furthermore, $\delta_{CF,\sigma}$ depends strongly on a .

On the right hand site, we have the on-site energy difference, which is given by $\Delta_\sigma \approx \Delta_\pi + 3V_{sd\sigma}^2/\Delta_{sd}$, *cf.* Eq. (G.18). The derivative of this expression is

$$\Delta'_\sigma \approx \frac{6}{\Delta_{sd}} V_{sd\sigma} V'_{sd\sigma}. \quad (5.15)$$

Note that here we assumed $\Delta'_\pi = \Delta'_{sd} = 0$, which is only an assumption, *cf.* Figure G.1 in Appendix G.

Dividing Eq. (5.15) by Δ_σ and inserting $V'_{sd\sigma}$ from Eq. (5.14) gives

$$-\frac{\Delta'_\sigma}{\Delta_\sigma} = \frac{\alpha}{a} \frac{6V_{sd\sigma}^2}{\Delta_{sd}\Delta_\pi + 3V_{sd\sigma}^2}. \quad (5.16)$$

Inserting Eq. (5.14) and Eq. (5.16) in the inequality Eq. (5.10), we obtain within the Harrison model the observed increase of the EFG, due to the decreasing occupation of the p_σ orbitals, if the following inequality is fulfilled:

$$\begin{aligned} \frac{\alpha}{a} = -\frac{V'_\sigma}{V_\sigma} &< \quad \frac{\Delta'_\sigma}{\Delta_\sigma} = \frac{\alpha}{a} \frac{6V_{sd\sigma}^2}{\Delta_{sd}\Delta_\pi + 3V_{sd\sigma}^2} \\ \frac{1}{3}\Delta_{sd}\Delta_\pi &< \quad \Leftrightarrow \quad V_{sd\sigma}^2. \end{aligned} \quad (5.17)$$

Using the values obtained from the LDA band structure ($V_{sd\sigma} = 3.0$ eV, $\Delta_{sd} = 17.9$ eV and $\Delta_\pi = 1.4$), we see that Eq. (5.17) is fulfilled.

The considered systems, SrTiO₃ and BaTiO₃, are not strongly correlated, since the Ti $3d$ shell is formally empty¹¹. For magnetic ions with partially filled d shells, the influence of the O $2s$ orbitals will be diminished because the charge transfer energy Δ_{sd} will include the on-site Coulomb repulsion within the d shell.

After revealing the origin of the counter-intuitive behaviour of the on-site EFG, we will discuss the unusually large value of the off-site EFG of the considered compounds. The dependence of this contribution with respect to the lattice parameter can be estimated in the following way: from the multipole expansion of a potential of a given ion, the sum of the monopole contributions to $v^{off}(\vec{r})$ Eq. (4.5) has the slowest convergence. This contribution may be calculated within a point charge model (PCM). Therefore, we note that the value of V_{zz} created at the origin by an unit charge situated at the point \vec{R} equals the value of the z component of the electric field E_z , created at the origin by the unit dipole directed along z axis and situated at the same point \vec{R} : $V_{zz} = (3Z^2 - R^2)/R^5$. That means, for the calculation of the EFG within the PCM, we need the electric field $S(\vec{r})$ of dipoles located at the sites \vec{R} , which are polarised along the z direction and whose polarisation is unity, at various points \vec{r} through the cubic lattice: $S(\vec{r}) = \sum_{\vec{R}} E_z(\vec{R} - \vec{r})$. Here, $\vec{r} = a(x, y, z)$ and $\vec{R} = a(l, m, n)$ with a being the lattice parameter and $l, m, n = 0, \pm 1, \pm 2$. Using Eq. (16) of Ref. [100], we obtain for the EFG in the PCM at the oxygen site

$$\begin{aligned} V_{zz}^{PCM} &= -\frac{e}{a^3} \left[n_{Ti} S\left(0, 0, \frac{1}{2}\right) + n_A S\left(\frac{1}{2}, \frac{1}{2}, 0\right) \right. \\ &\quad \left. + 2n_O S\left(0, \frac{1}{2}, \frac{1}{2}\right) \right] \\ &= -\frac{e}{a^3} [30.080n_{Ti} - 8.668(n_A - n_O)]. \end{aligned} \quad (5.18)$$

Here, n_{Ti} is the monopole moment of the ionicity of Ti. If we insert the charges of the Ti ion n_{Ti} , the O ion n_O , and the A ion $n_A = -(n_{Ti} + 3n_O)$ (with $A = \text{Sr, Ba}$) obtained from the FPLO

¹¹The Ti d shell is occupied by roughly 1 electron. Analysis of the m resolved density shows that each Ti d orbital is occupied by less than one electron per orbital and therefore yields an uncorrelated system.

calculations, we obtain *e.g.*, for SrTiO₃ $V_{zz}^{PCM} = 1.30 \cdot 10^{21}$ V/m². This value is very close to $V_{zz}^{off} = 1.19 \cdot 10^{21}$ V/m², see Table 5.8. So, we obtain a good agreement for the EFGs obtained from the simple PCM model and the more complex calculation. This means, the FPLO code yields realistic relations of the charge distributions.

The prefactor e/a^3 in Eq. (5.18) is responsible for the observed decrease of the off-site contribution in case of lattice expansion, see right graph in Figure 5.22. Also the charge redistribution may change the value of V_{zz}^{off} , but as we see in the right graph in Figure 5.22, it has a minor effect: the off-site EFG for BaTiO₃ is smaller than for SrTiO₃, but the distance between the two curves is smaller than the lattice parameter dependence of the two curves.

5.3.6 Summary and Conclusion

First-principles calculations of the electric field gradient on the oxygen site for the cubic SrTiO₃ and BaTiO₃ for different lattice parameters a were performed. For the experimental lattice parameters, the absolute values of the calculated EFGs agree fairly with the measured ones [90]. Apart from the sign, which is likely due to a different definition of the EFG, there is also good agreement with the calculated (LAPW) EFGs from Ref. [90].

For both compounds, a counter-intuitive dependence of the EFG on the lattice parameter a is obtained: the EFG increases upon lattice expansion. An analysis of the EFG shows that this behaviour is due to the on-site EFG. The off-site EFG, which is unusually large due to the ionic character of the perovskites, remains basically constant. The on-site EFG, which originates from the oxygen $2p$ shell, increases under lattice expansion due a decreasing occupation of the p_σ orbital. Simple ionic and covalent approaches, as well as the effective two-level Hamiltonian proposed by Wolfram and Ellialtioglu, which describes the relevant states of the valence region (oxygen p and titanium d states) fail to describe the observed behaviour. Extending this standard p - d model Hamiltonian for perovskites by additionally taking into account the relevant oxygen $2s$ states finally results in a consistent picture: lattice expansion causes a charge transfer from the p_σ to the s orbital of oxygen, whereas the population of the oxygen π orbital increases with a . This charge redistribution leads to the increase of the EFG, which is the main reason for the surprisingly large difference of the EFGs between BaTiO₃ and SrTiO₃.

This leads to the conclusion that the ionic description, as is it used in standard solid state physics textbooks *e.g.*, in Refs. [80, 81], is not ideal.

The observed feature, the increase of the anisotropy of the p shell with the bond length, is expected to be common to all d metal-oxygen bonds and should be taken into account accordingly in the interpretation of the relevant experiments.

As a side effect, this investigation sounds a note of caution: when performing a mapping of a complex DFT band structure calculation onto a microscopically based minimal model in order to gain deeper physical understanding, care has to be taken that all relevant interactions are included.

5.4 Strongly correlated low-dimensional cuprates

5.4.1 Introduction

The discovery of high-temperature superconductivity (HTSC) in cuprates 20 years ago [101] highly stimulated the development of better methods to describe the strongly correlated undoped parents of these systems. One of these methods is the LSDA+ U approach, where the strong Coulomb repulsion U is treated in a mean field-like approximation. A considerable improvement in the realistic description of the electron density for transition metal oxides, like the cuprates, is achieved. Unfortunately, the parameter U is not known and needs to be evaluated, *i.e.*, in comparison of calculated properties and experimental measurements.

Here, we present calculations for the electric field gradient V_{zz} on the Cu^{2+} sites in strongly correlated low dimensional cuprates. Since V_{zz} calculated with LDA is far too small, LDA+ U has to be applied to take into account the orbital polarisation caused by the correlations. By comparing the calculated $V_{zz}(U)$ with the V_{zz} from NMR experiments for these compounds, we can evaluate $U_{V_{zz}}$. To avoid numerical ambiguity, we used two different full-potential DFT band structure schemes: FPLO and WIEN2k. The results are consistent with respect to each other. However, the resulting values of $U_{V_{zz}}$ compared to U_J , which are obtained from the (nearest neighbour) exchange integral J , show a considerable deviation in direction of smaller U values. A possible cause for this deviation will be discussed.

5.4.2 The relation of J and U

It is well-known that L(S)DA fails in describing strong electron correlations. An effective and popular way to improve L(S)DA is the LSDA+ U method, see Section 2.2.2.

The Coulomb energy U is an additional parameter, which is not known per se and needs to be evaluated. This can be done by comparing calculated properties with experimental results. One popular property for this comparison are the exchange integrals J_{ij} . The parameters J_{ij} describe the nearest (next nearest, next next nearest and so on) neighbour exchange in the Heisenberg model

$$H = \sum_{\langle i,j \rangle} J_{ij} \vec{S}_i \vec{S}_j$$

(if only spin degrees of freedom are considered). Here, \vec{S}_i and \vec{S}_j are the spin operators of the CuO_4 units at site i and j . Negative J_{ij} favour electrons with parallel spins (FM exchange) and positive J_{ij} electrons with anti-parallel spins (AFM exchange). For cuprates with corner-shared geometry, it is often sufficient to take into account the nearest neighbour exchange only $J_{ij} \rightarrow J$. The exchange integral J can be obtained by calculating ferro- and antiferromagnetic super cells for different values of U . Since the obtained energies can be mapped onto the Heisenberg model, it is possible to determine J in dependence of U by solving a system of linear equations [102]. Comparing these curves with measured values for J yields finally a value for U . Experimentally, J can be obtained for example from susceptibility, specific heat, neutron scattering, Raman or saturation field measurements. However, whatever method is chosen, J can not be measured directly – the experimental data has to be fitted with a model. Since different methods measure different physical properties, the obtained J can vary significantly, see below. Furthermore, in the case of susceptibility measurements different models (*i.e.*, different combinations of two or more J_{ij} parameters) can yield very similar susceptibilities, that can not be distinguished within the error bar. Results of such comparisons are shown in Figure 5.25 (taken from Ref. [103]). In this graph, some of the experimentally best investigated cuprates are shown. For these we observe a trend: corner-shared systems with 180° degree Cu-O-Cu bond (red curves) have larger J 's and smaller U 's, than two dimensional cuprates (black curves), which have smaller J 's, which corresponds to larger U 's.

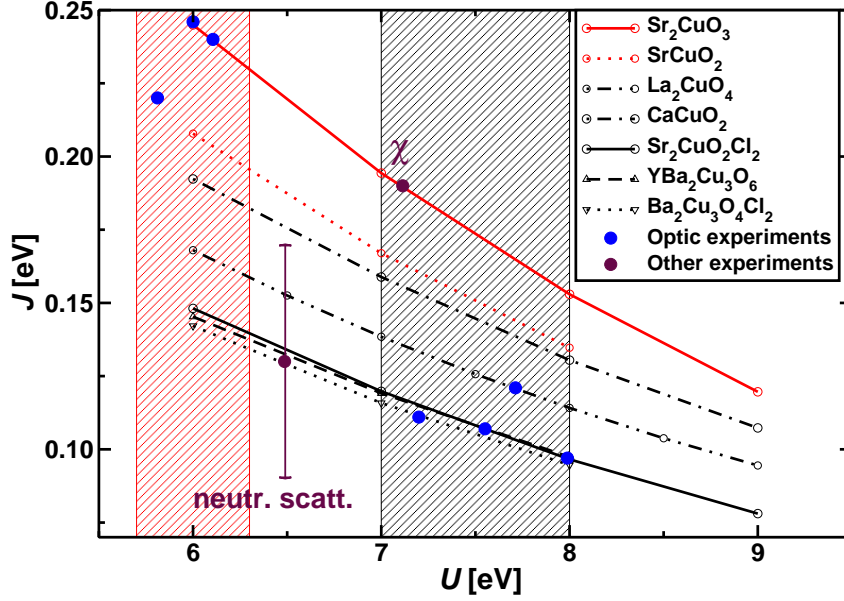


Figure 5.25: (Figure taken from Ref. [103].) Calculated nearest neighbour curves exchange integrals $J(U)$ (FPLO code, version 5) compared with experimental determined exchange integrals J 's (blue and black circles). Obtained values for the parameter U are in the red shaded area for quasi 1D cuprates (red curves) and in the black shaded area for 2D cuprates (black curves).

However, in Figure 5.25 we see that different experimental methods yield quite different results. Therefore, it would be nice to have an additional property, where the experiments are more precise and the underlying theory is better understood. This is the case for NMR (NQR) experiments and the quadrupole interaction. This method yields the EFG as property to compare theory with experiment. No model has to be applied to evaluate the EFG from the experiment, like it is the case for J . The question of this section is: will U obtained from $V_{zz}(U)$ show the same trend for one and two dimensional cuprates as U obtained from $J(U)$? From now on we will use the definitions $U_{V_{zz}}$, when U is obtained from the former, and U_J , when U is obtained from the latter method. We will study the following compounds: La_2CuO_4 , CuGeO_3 , Sr_2CuO_3 , SrCuO_2 and $\text{Cu}_2(\text{PO}_3)_2\text{CH}_2$.

5.4.3 Methods

The electronic band structure calculations were performed with the full-potential local-orbital minimum-basis code FPLO (version 7) [2] within the local density approximation. In the scalar relativistic calculations the exchange and correlation functional of Perdew and Wang [15] was employed. To treat the Cu $3d$ state adequately, LDA+ U around mean field was deployed with various values of U (between 2 and 9 eV). For the Slater integrals, $F_2=8.6$ eV and $F_4=5.4$ eV have been chosen, yielding $J_t = 1$ eV, see Section 2.2.2.

In order to obtain FM and AFM ordered Cu spins (except for $\text{Cu}_2(\text{PO}_3)_2\text{CH}_2$), super cells (or a lowered symmetry by using a lower space group) were applied, see Table 5.9. In this table, also the number of k points in the irreducible part of the Brillouin zone (IBZ) and the references for the lattice parameters are given.

For comparison, La_2CuO_4 was also calculated with the augmented plane wave plus local orbitals (APW+lo) code WIEN2k, with an alternative full-potential scheme [1]¹².

¹² $R_{MT}(\text{Cu}) = 1.88$ a.u., $R_{MT}(\text{La}) = 2.35$ a.u., $R_{MT}(\text{O}) = 1.67$ a.u., $R_{MT}K_{max} = 7.0$ and separation energy =

Table 5.9: Super cells, space groups, k points in the irreducible part of the Brillouin zone and references for the lattice parameters of the calculated cuprates in this section.

Compound	Super cell	Space group	k points	Reference
La ₂ CuO ₄	$\sqrt{2} \cdot \sqrt{2}(a, b \text{ plane})$	$Cmmm$	301	[104]
CuGeO ₃	double (along b)	$P2/m$	518	[105]
Sr ₂ CuO ₃	double (along b)	$Pmm2$	294	[106]
SrCuO ₂	unit cell	$Amm2$	546	[107]
Cu ₂ (PO ₃) ₂ CH ₂	unit cell	$Pnma$	40	[108]

5.4.4 La₂CuO₄

We start the investigation with the two dimensional [109] La₂CuO₄. This structure consists of corner-shared CuO₄ plaquettes, as it can be seen in the left panel of Figure 5.26. The EFG for Cu obtained from NMR experiments is $|V_{zz}^{\text{exp}}| = (12.0 \pm 0.8) \cdot 10^{21} \text{ V/m}^2$ [110]. Since NMR and NQR experiments can not provide the sign of the EFG, we will consider only the magnitude of the EFG obtained from the calculations. The EFG calculated with LDA is too small: $|V_{zz}^{\text{LDA}}| = 5.7 \cdot 10^{21} \text{ V/m}^2$. This was expected, since LDA underestimates the polarisation of the correlated orbitals. The LDA occupation of the d orbitals is too isotropic and the calculation results in a too small EFG. If U is applied, the polarisation becomes stronger and the EFG increases, as it can be seen in the right panel of Figure 5.26. La₂CuO₄ is an AFM ordered insulator. Nevertheless, we plot the EFG also for the FM ordered state in order to find out, how the different magnetic orders influence the EFG. In Figure 5.26, we see that the EFG curve is similar, *i.e.*, has the same slope, for FM and AFM ordered Cu spins, if U is larger than 5.25 eV. The FM curve changes its slope below that U value, because the system changes from an insulator to a metal. The AFM ordered structure remains insulating for all U values and there is no kink in the EFG curve. Hence, we conclude that for the EFG the description of the correct insulating behaviour is more important than the description of the correct magnetic order. Comparing the experimental EFG with the AFM calculated EFG curve yields $U_{V_{zz}} = (4.4 \pm 0.4) \text{ eV}$. This $U_{V_{zz}}$ is about 2 eV smaller than U_J obtained by comparing the measured and calculated exchange integral J (with $J = 128 \text{ meV}$ [111] and $J = 140 \text{ meV}$ [112]), which yields $U_J = (6.7 \pm 0.2) \text{ eV}$. To rule out that this difference between $U_{V_{zz}}$ and U_J is code dependent, we repeated the calculations with the WIEN2k code. The results are shown in Figure 5.27. For both codes we obtain a difference between $U_{V_{zz}}$ and U_J , depending on if it was obtained from comparing the calculation with the experiment for V_{zz} or for J . For FPLO this difference is $\Delta U = U_J - U_{V_{zz}} = 2.3 \text{ eV}$ and for WIEN2k it is $\Delta U = 2.7 \text{ eV}$. However, the absolute values for the Coulomb repulsion parameter U_J and $U_{V_{zz}}$ differ, since U is basis dependent and different codes will therefore need different values of U to obtain the same result: $U_J = (8.1 \pm 0.2) \text{ eV}$, obtained with the WIEN2k code, is 1.4 eV larger than U_J obtained by the FPLO code. Also the WIEN2k EFG curve $V_{zz}(U)$ is shifted in direction of larger U compared to the FPLO EFG curve. By shifting the WIEN2k EFG curve by 1.4 eV to the left, as shown in the right panel of Figure 5.27, we see that both codes indeed yield the same result: the $V_{zz}(U)$ curves for the AFM order are consistent with respect to the different band structure codes¹³.

–6.0 Ry. Same settings like for FPLO otherwise: LDA xc-functional, 343 k points in the IBZ. LSDA+ U (around mean field) with $J_t = 1 \text{ eV}$ and U between 5 and 10 eV.

¹³La₂CuO₄ has been investigated with WIEN2k before [113]. Blaha *et al.* applied different xc-functionals (LDA and GGA) as well as different LSDA+ U functionals (around mean field (AMF), fully localised limit and a

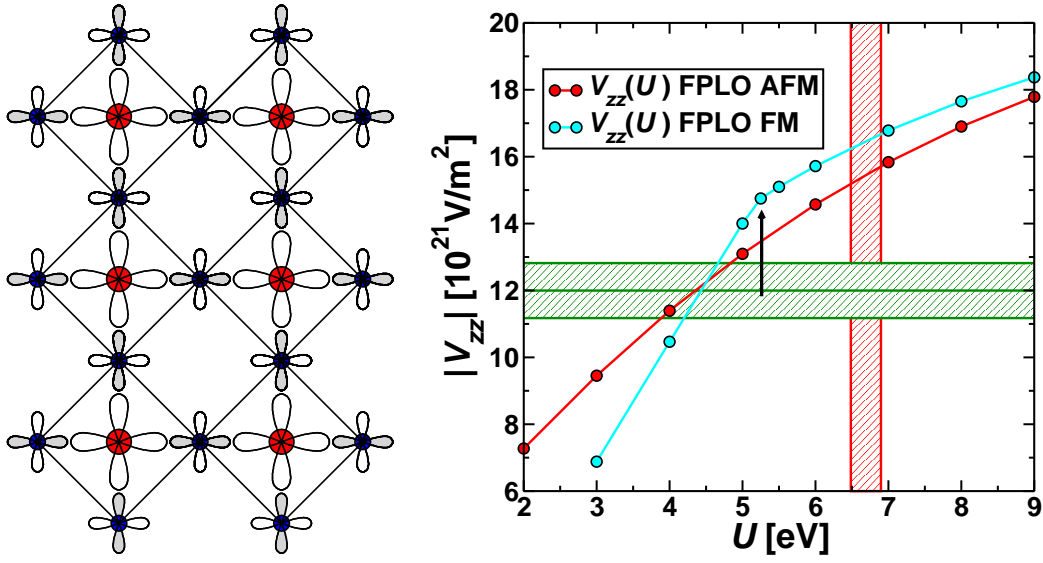


Figure 5.26: **Left:** corner-shared CuO_4 plaquettes in La_2CuO_4 : red=Cu and blue=O. **Right:** V_{zz} in dependence of U for FM (blue) and AFM (red) ordered Cu spins. The experimental V_{zz} [110] for Cu is shown by the green error bar. U_J obtained from the nearest neighbour exchange integral J is shown by the red shaded bar. The black arrow points to a change in the FM curve: the compound is metallic below and insulating above $U = 5.25$ eV.

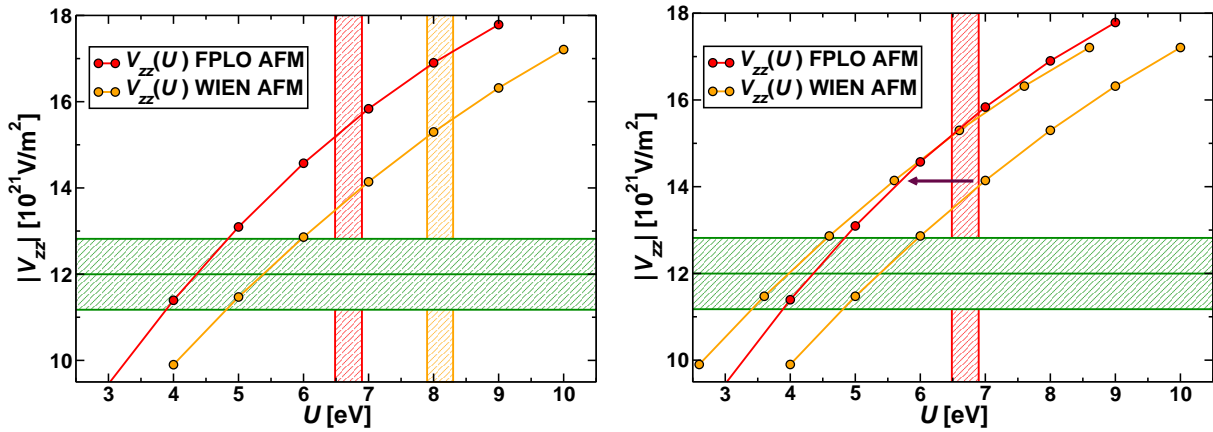


Figure 5.27: **Left:** V_{zz} and U_J for La_2CuO_4 obtained from J for FPLO (red) and WIEN2k (orange). The experimental V_{zz} [110] is shown by the green error bar. **Right:** the WIEN2k V_{zz} curve is shifted by the difference in U_J from the two codes.

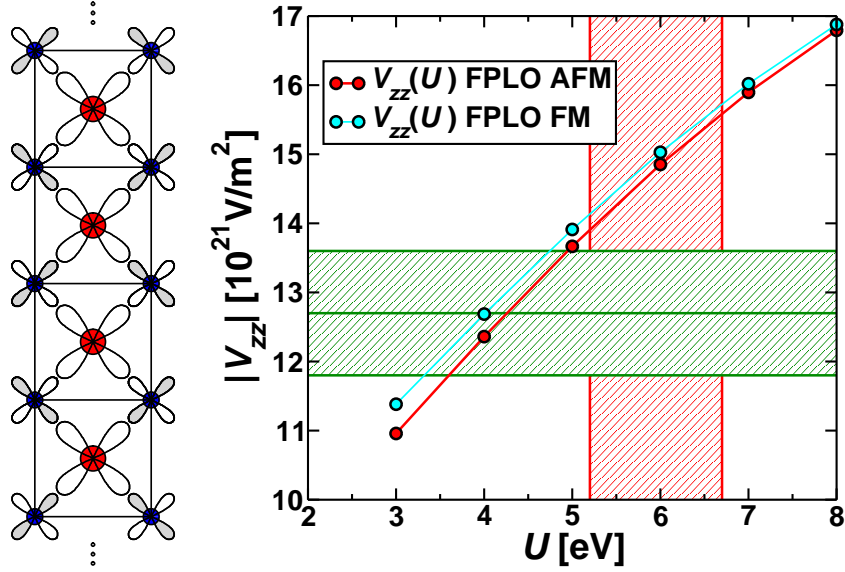


Figure 5.28: **Left:** edge-shared CuO_4 plaquettes in CuGeO_3 : red=Cu and blue=O. **Right:** V_{zz} in dependence of U for FM (blue) and AFM (red) ordered Cu spins. The experimental V_{zz} [115] is shown by the green error bar. U_J obtained from the exchange integral J is shown by the red shaded bar.

5.4.5 CuGeO_3

Now we take a look at the quasi¹⁴-one dimensional [114] CuGeO_3 . This structure consists of edge-shared chains, as shown in the left panel of Figure 5.28. We observe the same as before. LDA gives an EFG, $|V_{zz}^{\text{LDA}}| = 6.8 \cdot 10^{21} \text{ V/m}^2$, that deviates by about 50 % from the experimental EFG, $|V_{zz}^{\text{exp}}| = (12.7 \pm 0.9) \cdot 10^{21} \text{ V/m}^2$ [115]. Applying LSDA+ U increases the EFG with increasing value of U , see right panel of Figure 5.28. We observe again, that the magnetic order (FM or AFM) has only little influence on the EFG: the two different EFG curves have the same slope and are only slightly shifted with respect to each other. There is no kink in neither of the curves since the bandwidth in CuGeO_3 is smaller than in LaCuO_4 [116] and therefore a smaller U is sufficient to obtain an insulating state for CuGeO_3 . For the AFM EFG curve, a similar U as before, $U_{V_{zz}} = (4.3 \pm 0.7) \text{ eV}$, yields an EFG that agrees with the experimental EFG. There are several similarities to La_2CuO_4 . First, the EFG is similar, which is consistent with the planar, and not distorted, CuO_4 plaquettes (contrary to $\text{Cu}_2(\text{PO}_3)_2\text{CH}_2$, see below). Second, there is a difference in the obtained U 's: $U_J = (6.0 \pm 0.8) \text{ eV}$, where $J = 11 \text{ meV}$ [117] and $J = 22 \text{ meV}$ [118] were applied, is also about 2 eV larger than $U_{V_{zz}}$. And third, the spin pattern (*i.e.*, FM or AFM ordered Cu spin) has only a small influence on the V_{zz} curve. Hence, we conclude that U is mostly a local quantity.

5.4.6 Sr_2CuO_3

The one dimensional [120] compound Sr_2CuO_3 consists of single chains of corner-shared CuO_4 plaquettes, as it can be seen in the left panel of Figure 5.29. For this structure, $U_{V_{zz}} = (3.8 \pm 0.1) \text{ eV}$ describes the experimental EFG, $|V_{zz}^{\text{exp}}| = (1.4 \pm 0.1) \cdot 10^{21} \text{ V/m}^2$ [119], correctly. This

mixture of these two). Their results using LDA and AMF agree with the results obtained in this work.

¹⁴Quasi-one dimensional means that there is a nonzero (but small compared to the in-chain) inter-chain coupling. In CuGeO_3 , the inter-chain couplings are stronger than in the other 1D systems presented in this section: Sr_2CuO_3 and SrCuO_2 .

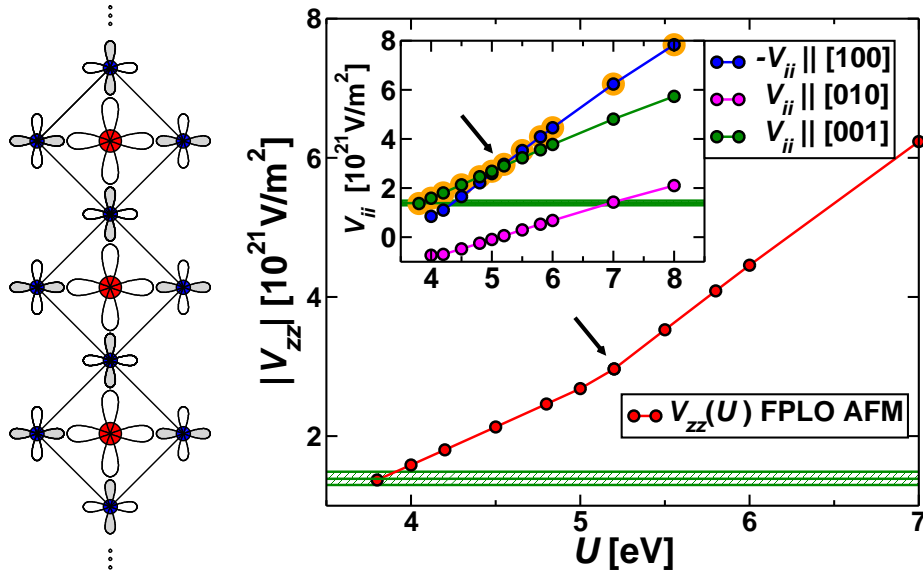


Figure 5.29: **Left:** corner-shared CuO_4 plaquettes in Sr_2CuO_3 : red=Cu and blue=O. **Right:** V_{zz} in dependence of U for AFM ordered Cu spins, the kink is due to a change in V_{zz} , see inset and text. The experimental V_{zz} [119] is shown by the green error bar. **Inset:** the three components of the EFG tensor: the (negative) component parallel to the crystallographic a axis (blue), the (sign changing) component parallel to the b axis (magenta) and the (positive) component parallel to the c axis (green). V_{zz} is indicated by the large orange circle.

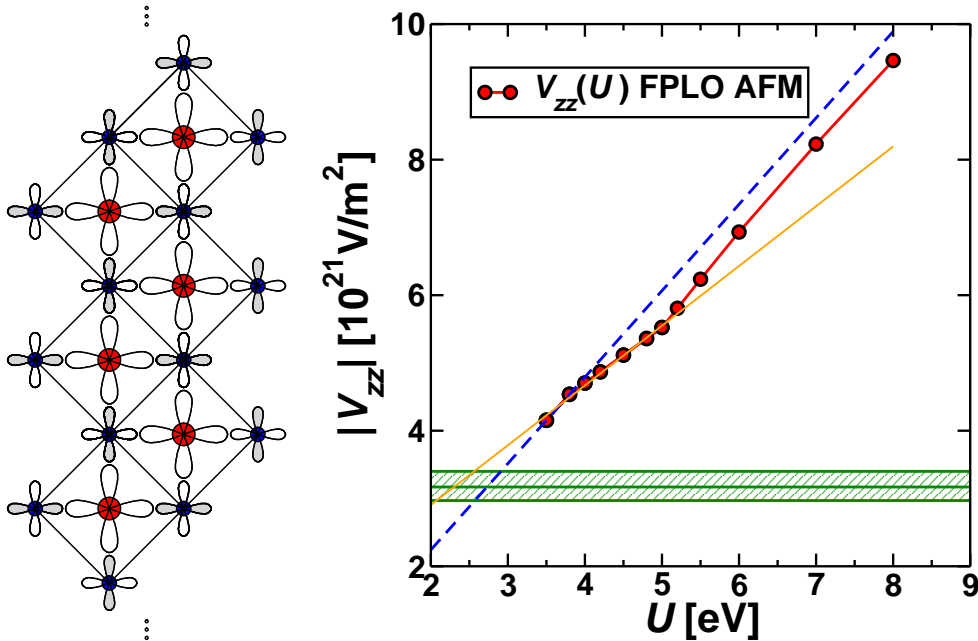


Figure 5.30: **Left:** corner-shared CuO_4 plaquettes in SrCuO_2 : red=Cu and blue=O. **Right:** V_{zz} in dependence of U for AFM ordered Cu spins. The orange line and the blue dashed line are fits from all points for $U < 5$ (orange) and for the last two points (blue), respectively. The experimental V_{zz} [119] is shown by the green error bar.

value of $U_{V_{zz}}$ is slightly smaller than the one for La_2CuO_4 . Increasing U increases the EFG, see right panel of Figure 5.29. For this compound, a kink is obtained at $U = 5$ eV. Here, the kink is not due to a change from metallic to insulating behaviour but due to a change in V_{zz} according to its definition: $|V_{zz}| \geq |V_{yy}| \geq |V_{xx}|$. The directions of these three components depend on the symmetry. For instance, for tetragonal symmetry, V_{zz} is parallel to the crystallographic c axis and $V_{xx} = V_{yy}$ are parallel to the crystallographic a and b axis, respectively. Also in this case, each component is parallel to one crystallographic axis, but in a more complicated way. They all change smoothly with U , as it can be seen in the inset in Figure 5.29. But while the component with the smallest magnitude, V_{xx} , is parallel to the b axis for all U (magenta symbols in Figure 5.29), this is not the case for the other two components. For $U > 5$ eV, the component with the largest magnitude, V_{zz} , is negative and parallel to the crystallographic a axis (blue symbols in Figure 5.29). For $U < 5$ eV, the component with the largest magnitude, V_{zz} , is positive and parallel to the crystallographic c axis (green symbols in Figure 5.29). Since V_{zz} is by definition the component with the largest magnitude it can change its direction by varying a parameter, as it is the case for this compound.

5.4.7 SrCuO_2

The quasi-one dimensional [121] compound SrCuO_2 consists of double chains of corner-shared CuO_4 plaquettes, see left panel of Figure 5.30. As before, the EFG calculated with LDA is too small compared with the experimental EFG: $|V_{zz}^{\text{LDA}}| = 2.3 \cdot 10^{21} \text{ V/m}^2 < |V_{zz}^{\text{exp}}| = (3.2 \pm 0.2) \cdot 10^{21} \text{ V/m}^2$ [119]. Applying LSDA+ U yields a similar EFG curve as for Sr_2CuO_3 . Also here, there is a kink in the EFG curve at $U = 5$ eV, which is due to the same change in the EFG as discussed for Sr_2CuO_3 . Since the calculations for $U < 3.5$ eV did not converge correctly, the EFG curve had to be extrapolated from the empirical experience of the other cuprates. This way we to obtain $U_{V_{zz}} = (2.3 \pm 0.3)$ eV (orange fit from all points for $U < 5$) and $U_{V_{zz}} = (2.7 \pm 0.2)$ eV (blue dashed fit for the last two points). These values are even smaller than the one for Sr_2CuO_3 but more uncertain.

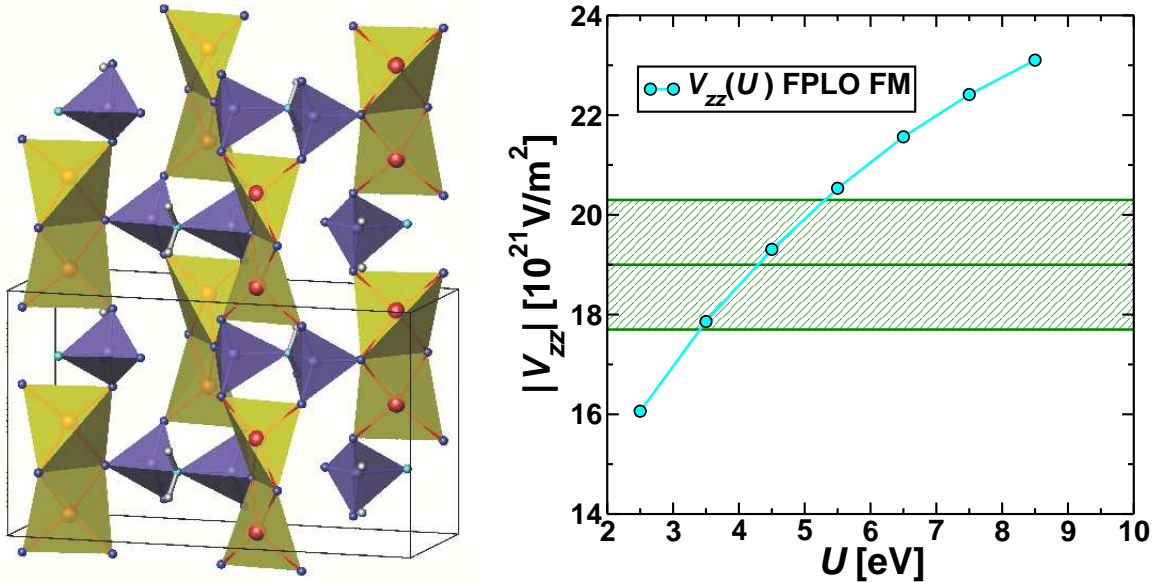


Figure 5.31: **Left:** strongly distorted CuO_4 plaquettes (tetrahedrons) in $\text{Cu}_2(\text{PO}_3)_2\text{CH}_2$: red=Cu and blue=O. **Right:** V_{zz} in dependence of U for FM ordered Cu spins. The experimental V_{zz} [108] is shown by the green error bar.

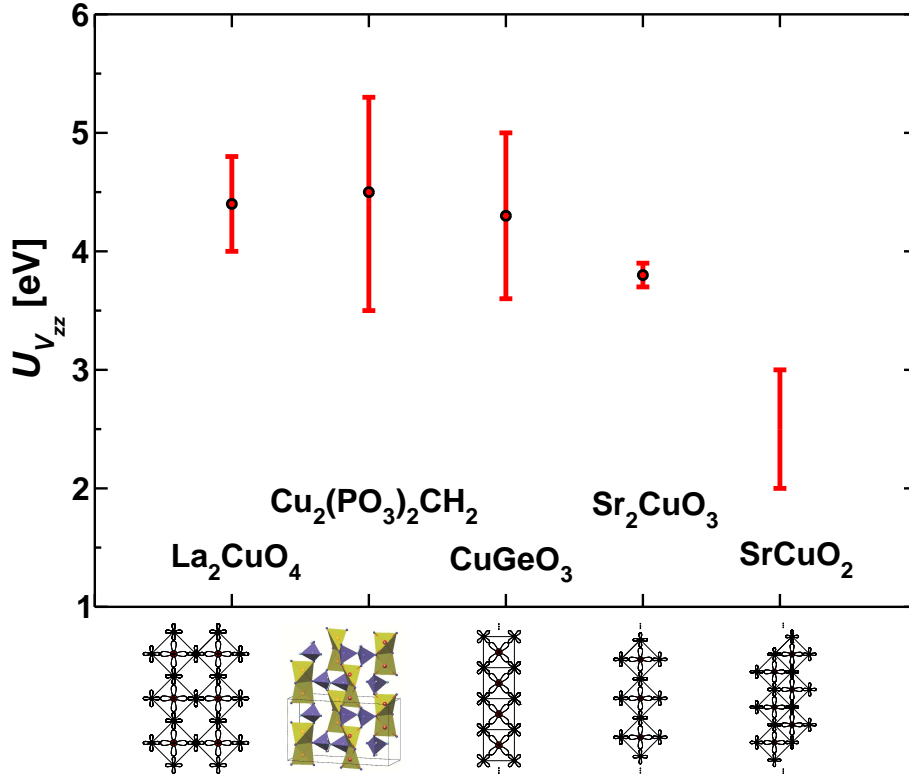


Figure 5.32: $U_{V_{zz}}$ obtained by comparing the calculated $V_{zz}(U)$ (FPLO, version 7) with the experimentally determined V_{zz} [110, 108, 115, 119, 119] for La_2CuO_4 , $\text{Cu}_2(\text{PO}_3)_2\text{CH}_2$, CuGeO_3 , Sr_2CuO_3 , and SrCuO_2 , respectively.

5.4.8 $\text{Cu}_2(\text{PO}_3)_2\text{CH}_2$

As an example for a strongly distorted cuprate, due to strongly twisted CuO_4 plaquettes, we study $\text{Cu}_2(\text{PO}_3)_2\text{CH}_2$ [108]. The structure is shown in the left panel of Figure 5.31. Also here, the EFG calculated with LDA, $|V_{zz}^{\text{LDA}}| = 10.3 \cdot 10^{21} \text{ V/m}^2$, is about 50 % too small compared to the experimental EFG of $|V_{zz}^{\text{exp}}| = (19.0 \pm 1.3) \cdot 10^{21} \text{ V/m}^2$ [108]. Applying LSDA+ U with $U_{V_{zz}} = (4.4 \pm 0.9) \text{ eV}$ yields an EFG, that agrees with the experimental EFG. This $U_{V_{zz}}$ is very similar to the one of La_2CuO_4 , whereas the EFG is almost twice as large as the one of La_2CuO_4 . The large EFG, due to a less isotropic Cu electron density, is consistent with the large distortion of the CuO_4 units.

Figure 5.32 gives an overview of the obtained $U_{V_{zz}}$ for the studied cuprates. From that figure, we conclude that for two dimensional systems, (if we include the quasi 1D CuGeO_3 due to the large inter-chain coupling to the 2D systems) a larger Coulomb parameter $U_{V_{zz}}$ is needed than for the one dimensional systems with corner-shared CuO_4 units and 180° degree Cu-O-Cu bond. As a matter of fact, $U_{V_{zz}}$ is almost identical for three systems LaCuO_4 , $\text{Cu}_2(\text{PO}_3)_2\text{CH}_2$ and CuGeO_3 , except for the different size of the error bars, which is due to the different size of the absolute value of V_{zz} . On the other hand, for the one dimensional corner-shared systems, $U_{V_{zz}}$ decreases quite drastically from the single to the double chained system.

5.4.9 Summary and conclusion

Calculations of the EFG for strongly correlated systems within LDA yields values that are usually too small, as LDA results in a too isotropic orbital occupation due to an underestimation of the

strong Coulomb repulsion. The LSDA+ U approach can improve the description of the correlated orbital. Its occupation becomes more polarised and the value of the EFG increases.

The unknown Coulomb parameter U is usually obtained from comparing physical quantities that are determined experimentally and theoretically. The obtained value for U is not unique but depends on the physical property. To investigate this dependence on different properties, we chose the exchange integral J and the electric field gradient V_{zz} for this comparison for the low dimensional cuprates La_2CuO_4 , CuGeO_3 , Sr_2CuO_3 , SrCuO_2 and $\text{Cu}_2(\text{PO}_3)_2\text{CH}_2$.

As a result, we find a deviation between the Coulomb repulsion U_J , obtained by comparing the $J(U)$ with the experimental J , and $U_{V_{zz}}$, obtained by comparing $V_{zz}(U)$ with the experimental V_{zz} . This basically constant shift of 2 eV is code (*i.e.*, basis set) independent: FPLO and WIEN2k show quite similar behaviour, as it was shown for La_2CuO_4 . One possible explanation for this discrepancy are the different time scales of the underlying mechanism of the two properties: the exchange process is determined by the hopping integral¹⁵, of the order of 10^{-13} s. On the other hand, quadrupole interaction frequencies, measured by NMR or NQR are in the MHz range (10^{-6} s). This means that processes like shielding, which are more efficient on larger time scales, can play a role here.

Focusing on the EFG, we conclude that for two dimensional systems, a larger Coulomb parameter $U_{V_{zz}}$ is needed than for the one dimensional systems. This trend is in agreement with previous evaluations [103]: the larger the anisotropy (dimensionality), the larger the needed Coulomb parameter U . Furthermore, the same trend was obtained from constrained LDA calculations [122]. Since the shift of U obtained from the exchange integral and the EFG, respectively, is constant, the EFG provides an experimentally easy and unambiguously accessible property to obtain values for the Coulomb parameter U that also allows for a reliable calculation of the related exchange J .

In order to get a more complete and reliable picture, this systematic study of comparing measured and calculated properties in dependence of U should be continued.

¹⁵Typical hopping integral energies of 0.05 eV to 0.5 eV correspond to a frequency $\nu = E/h \approx 10^{13}$ Hz to 10^{14} Hz

5.5 The recently emerged high T_c superconductors

5.5.1 Introduction

In February 2008, Kamihara *et al.* published their findings on high-temperature superconductivity (HTSC) for doped LaFeAsO. Doping the oxygen site with fluorine renders LaFeAsO_{0.89}F_{0.11} superconducting with a transition temperature T_c of 26 K [123]. This discovery raised a new ‘gold rush’ in HTSC since until then HTSC was limited to layered copper oxides, where it was discovered in 1986 [101]. Replacing La by rare earth elements with smaller ionic radii, like Ce, Pr, Nd or Sm, expanded this class of iron oxypnictides, $REFeAsO$, to another HTSC family. For these systems, F doping results in even higher transition temperatures of 41 K [124], 52 K [125], 52 K [126], and 55 K [127], respectively. Applying pressure increases the transition temperature of LaFeAsO_{0.89}F_{0.11} to 43 K at 4 GPa [128].

Only a few weeks later, Rotter *et al.* reported HTSC for hole doped BaFe₂As₂: a partial substitution of Ba with K, yielded a T_c of 38 K [129]. Shortly afterwards, many other compounds from this family of iron arsenides, AFe_2As_2 , were reported to become superconducting upon hole doping, *e.g.*, (Sr,K)Fe₂As₂ with $T_c = 37$ K [130], (Eu,K)Fe₂As₂ with $T_c = 32$ K or (Ca,Na)Fe₂As₂ with $T_c = 20$ K [131]. Thus, a new family of Fe-based layered compounds with relative high T_c has been discovered. For some of these compounds, also doping the Fe site with *e.g.*, Ru, Rh, Ir, Ni or Co yields superconductivity, for instance Sr(Fe,Co)₂As₂ with $T_c = 20$ K [132]. Applying pressure increases T_c also for these compounds [133]. For CaFe₂As₂, applying pressure (2.3 kbar) yields a T_c of 12 K even for the undoped compound [134]. However, the absence of superconductivity for CaFe₂As₂ under hydrostatic pressure was reported later [135].

Meanwhile, also other parent compounds were reported, where doping or pressure induces superconductivity, *e.g.*, LiFeAs [136] or FeSe [137]. Since these systems are not subject of this thesis, they will not be discussed further.

The new iron arsenide superconductors, especially the AFe_2As_2 family, have one advantage for application. Compared to the cuprates, the AFe_2As_2 contain no oxygen and can therefore be processed like ductile intermetallic compounds. Also the upper critical field ($B_{c2} > 60T$ [138]) is large enough to make this new class of superconductors attractive for technological utilisation.

5.5.2 Structural similarities of AFe_2As_2 and $REFeAsO$

The $REFeAsO$ compounds crystallise in the ZrCuAsSi-type structure. In a naive approach, the structure can be split in alternating $(Fe_2As_2)^{2-}$ and $(RE_2O_2)^{2+}$ layers. The former layer is build by a square Fe lattice with As in the centre of the squares, but alternately shifted above and below that plane, see left picture in Figure 5.33. If the $(RE_2O_2)^{2+}$ layer is replaced by a layer with single, divalent atoms A , the AFe_2As_2 compounds are obtained, see right picture in Figure 5.33. These compounds crystallise in the ThCr₂Si₂-type structure. However, to describe the iron oxypnictides $REFeAsO$ and iron arsenides AFe_2As_2 as layered systems should be done with care. While for the $REFeAsO$ systems such an approach is alright, the AFe_2As_2 systems are not anisotropic enough for such a description. Amongst others, this can be concluded from the ratio of the in- and out-of-plane plasma frequencies ω_p^a and ω_p^c , respectively [139]: whereas this ratio is rather small in the AFe_2As_2 systems and decreasing from $\omega_p^a/\omega_p^c = 3.3$ to 1.4 with decreasing cation (Ba → Sr → Ca), it is much larger for the $REFeAsO$ systems, *e.g.*, $\omega_p^a/\omega_p^c = 8.9$ in LaFeAsO. Hence, the AFe_2As_2 compounds are more isotropic (more 3D-like) than the $REFeAsO$ compounds, which are more anisotropic (more 2D-like).

That both structures are similar on the large scale, can be seen by comparing the density of states (DOS), see Figure 5.34. Here, LaFeAsO is chosen as representative for the $REFeAsO$ compounds and SrFe₂As₂ as representative for the AFe_2As_2 compounds. The total DOS is very

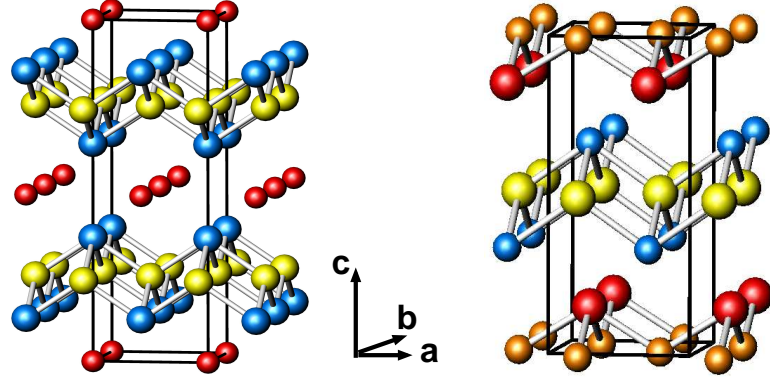


Figure 5.33: Crystal structure of AFe_2As_2 (left) and $REFeAsO$ (right) with A red, RE red, O orange, As blue and Fe yellow.

similar, especially in the relevant low energy region around the Fermi energy, which is dominated by the $Fe\ 3d$ states, as it can be seen from the inset of Figure 5.34. The $As\ 4p$ states are slightly shifted to lower energies for the AFe_2As_2 systems, and the main differences are obtained below $-4\ eV$ and above $2\ eV$, due to the occupied $O\ 2p$ and the unoccupied $La\ 4f$ states, respectively, which are absent in the AFe_2As_2 systems.

5.5.3 The electric field gradient as a tool to study the Fe-As interaction

The Fe-As interaction, determined by the $As\ z$ position, is most likely one of the key features for the understanding of the superconductivity in the iron pnictides. Present day DFT-based calculations using LDA [139, 140], as well as GGA [140, 141] are not able to reproduce all the experimental findings consistently, especially the $As\ z$ position (experimental vs. optimised) influences the theoretical findings drastically. For example, the connection between the SDW magnetic pattern and the orthorhombic distortion is confirmed for the fully optimised (including the $As\ z$ position) AFe_2As_2 compounds, whereas the c/a collapse under pressure in $CaFe_2As_2$ is only obtained for the experimental $As\ z$ position. Also the magnetism shows an unexpected sensitivity to the $As\ z$ position: the magnetic moment of Fe decreases drastically when As is relaxed from the experimental to the optimised z position (see also Figure 5.35). Yet, there is a better agreement between theory and experiment regarding the magnetic moment of Fe in the AFe_2As_2 systems compared to the $REFeAsO$ systems [139]. The deviation is usually explained to be a result of large spin fluctuations [142], which are stronger in lower dimensional systems. This is in line with the observed increasing discrepancy from the AFe_2As_2 systems (3D-like) to the $REFeAsO$ systems (2D-like).

Nuclear magnetic resonance (NMR) and nuclear quadrupole resonance (NQR) are local probe methods that are extremely sensitive to small details of the structure. As the $As\ z$ position is a key determinant of many of the electronic properties of the FeAs systems, the quadrupole frequency ν_Q from NMR or NQR measurements can provide a direct measure to the Fe-As interaction. For nuclei with $I = 3/2$ (e.g., ^{75}As), the connection between the quadrupole frequency ν_Q , the asymmetry parameter $\eta = (V_{xx} - V_{yy})/V_{zz}$ and the electric field gradient (EFG) V_{zz} is given by

$$\nu_Q = \frac{eQV_{zz}}{2h} \sqrt{1 + \frac{\eta^2}{3}} \Leftrightarrow V_{zz} = \frac{2h\nu_Q}{eQ\sqrt{1 + \frac{\eta^2}{3}}}. \quad (5.19)$$

Since ν_Q and η can be obtained from, e.g., NMR experiments, it is possible to determine V_{zz} for As from Eq. (5.19) using the ^{75}As quadrupole moment $Q = (3.14 \pm 0.06)\ b$ [58]. Note, that from

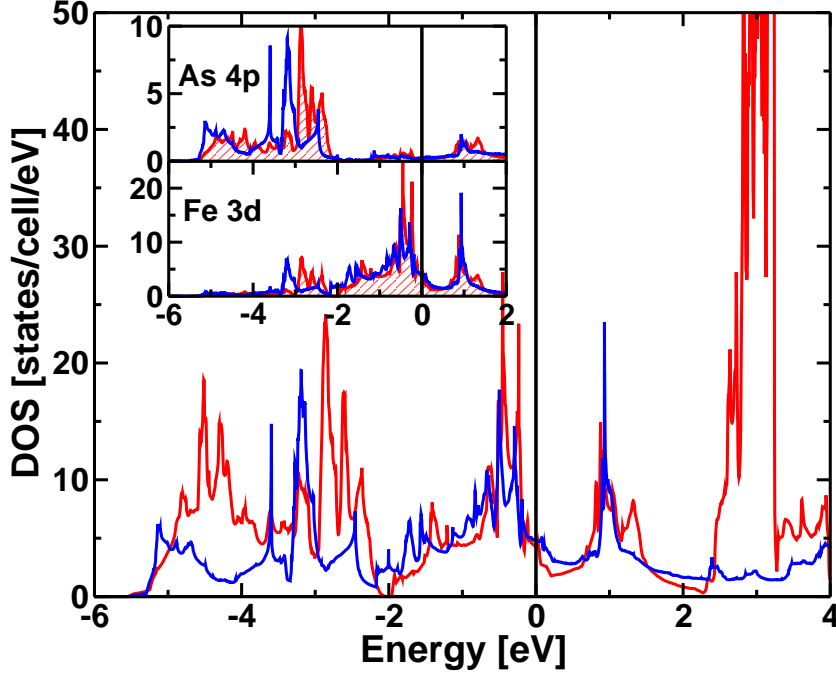


Figure 5.34: Total electronic density of states (DOS) for LaFeAsO (red) and SrFe₂As₂ (blue).
Inset: partial DOS for As 4p and Fe 3d for LaFeAsO (red) and SrFe₂As₂ (blue).

NMR and NQR experiments, only the absolute value of ν_Q (and therefore V_{zz}) can be obtained. Comparing experimentally and theoretically obtained EFGs will provide further insight for these systems. Therefore, we focus on the EFG of As in this section. We will discuss the *R*FeAsO and *A*Fe₂As₂ systems separately, starting with the latter one.

5.5.4 The iron arsenides *A*Fe₂As₂

At ambient temperature, all *A*Fe₂As₂ compounds crystallise in the tetragonal ThCr₂Si₂-type structure. Undoped *A*Fe₂As₂ compounds exhibit a structural transition to an orthorhombic lattice at $T_0 \approx 171$ K for $A = \text{Ca}$ [143], $T_0 \approx 205$ K for $A = \text{Sr}$ [144] and $T_0 \approx 140$ K for $A = \text{Ba}$ [145]. The structural transition is coupled with an antiferromagnetic ordering of the Fe moments. This ordering is described by the wave vector $\vec{Q} = (1, 0, 1)$ and is widely called spin-density-wave pattern (SDW). A certain range of doping on the *A* (or the Fe) site can suppress the magnetic ordering and the compounds become superconducting, *e.g.*, Ca_{0.5}Na_{0.5}Fe₂As₂ with $T_c = 20$ K [131], Sr_{0.5}K_{0.5}Fe₂As₂ with $T_c = 37$ K [130] and Ba_{0.6}K_{0.4}Fe₂As₂ with $T_c = 38$ K [129]. Compared to the *R*FeAsO family, the compounds of this family are easier to handle experimentally: the sample composition, the sample quality and the single-crystal growth are better controllable.

For the parent compounds with $A = (\text{Ca}, \text{Sr}, \text{Ba})$, we investigated the influence of the As z position, the structural phase transition, the magnetism and the pressure on the EFG. We also studied the effects of doping on the EFG.

Methods

We have performed density functional band structure calculations using the full-potential all-electron local-orbital code FPLO [2] (version 5.00-19) within the local density approximation

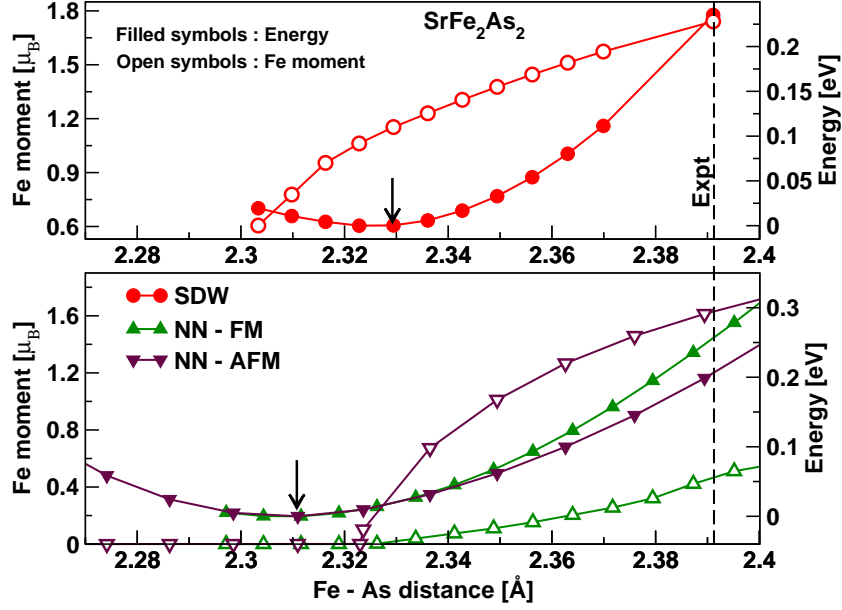


Figure 5.35: (Figure from Ref. [139].) Energy (full symbols) and Fe magnetic moment (empty symbols) as a function of the Fe-As distance using different spin patterns for SrFe₂As₂ at the experimental volume around 90 K [148]. Optimisation using FM and NN-AFM pattern leads to a nonmagnetic solution, while the SDW pattern stabilises with a Fe moment of $1.13 \mu_B$. The energy curves have been shifted by setting the minimum energy value to zero. The dashed vertical line refers to the experimental Fe-As distance obtained from Ref. [148]. The arrows indicate the position of the energy minima.

(LDA). As basis set: Ca ($3s3p/4s4p3d+5s5p$), Sr ($3d4s4p/5s5p4d+6s6p$), Ba ($4d5s5p/6s6p5d+4f7s7p$), Fe ($3s3p/4s4p3d+5s5p$) and As ($3s3p3d/4s4p4d+5s5p$) were chosen for semicore/valence+polarisation states. The high lying states improve the basis which is especially important for the calculation of the EFG. For the exchange-correlation functional the Perdew-Wang [15] parametrisation was employed. A well converged k mesh of 1063 k points in the irreducible part of the Brillouin zone (IBZ) was used in the calculations. In accordance with the widespread agreement that in the new Fe-based superconducting compounds the Fe $3d$ electrons have a rather itinerant character, and thereby are much less correlated in comparison to the Cu $3d$ electrons in the high- T_c cuprates, we did not apply the LSDA+ U approximation to the Fe $3d$ states. Effects of doping on the cation site were studied using the virtual crystal approximation (VCA). The results obtained via VCA were cross-checked using super cells for certain doping concentrations. The experimental lattice parameters (for the tetragonal and orthorhombic symmetry), including the As z position, are taken from Ref. [146] for CaFe₂As₂, Ref. [147] and Ref. [144] for SrFe₂As₂ and Ref. [145] for BaFe₂As₂.

Results

z position of As

First, we focus on the As z dependence. The Fe-As distance, determined by the As z position, has a quite large influence on the magnetic moment of Fe: in Figure 5.35 (taken from Ref. [139]), we see the energy and the magnetic moment of Fe for SrFe₂As₂ for the three, in the literature discussed, possible orders of the Fe spin in dependence of the Fe-As distance. These spin patterns

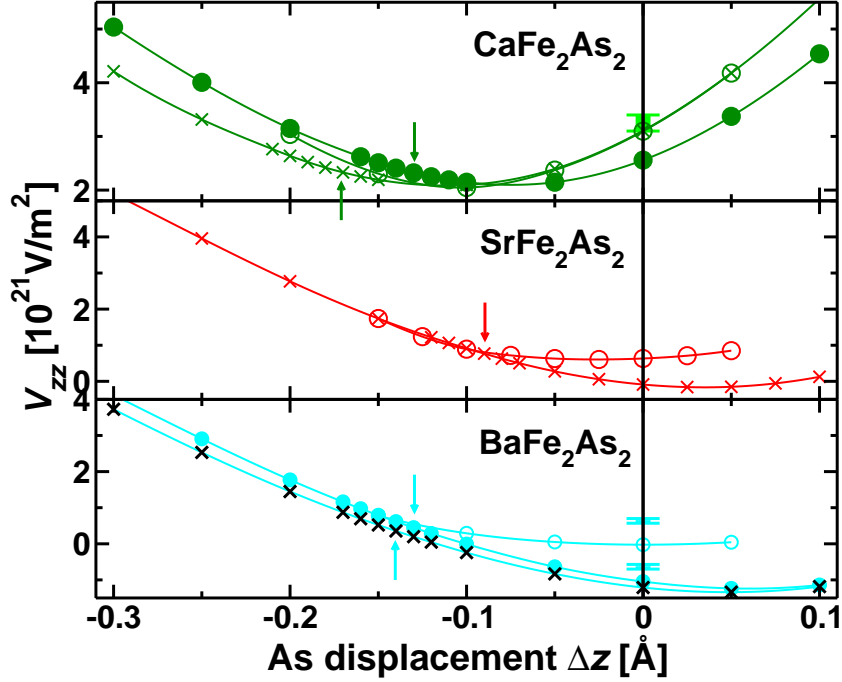


Figure 5.36: Dependence of the EFG of As on the As z position. $\Delta z = z - z_{\text{exp}}$. Different symbols show different calculations: cross = nonmagnetic (NM) with tetragonal symmetry, full circle = NM with orthorhombic symmetry (almost identical to tetragonal symmetry for SrFe_2As_2 and therefore not shown) and empty circle = magnetic (SDW pattern) with orthorhombic symmetry. The total energy minimum is marked by an arrow for each NM curve. The error bars show the experimental results for the tetragonal phase (at 250 K for CaFe_2As_2 and at 200 K for BaFe_2As_2 (the two error bars show both possible signs of the EFG (experimentally unknown))).

are the ferromagnetic (FM), the checkerboard (nearest neighbour) antiferromagnetic (NN-AFM) and the columnar/stripe-type antiferromagnetic order (SDW) of the Fe spin, whereof the SDW pattern is the lowest-total-energy spin pattern. For all three spin patterns, the optimised As z position yields a shorter Fe-As distance than obtained experimentally. For the FM and NN-AFM pattern, the magnetic moment decreases for decreasing Fe-As distance and vanishes before the energetically most favourable distance is reached, see lower panel of Figure 5.35. For the SDW pattern, the magnetic moment of Fe decreases as well, but less strongly and is still $1.13 \mu_B$ at the energetically most favourable distance, see upper panel of Figure 5.35. Similar results are obtained for the other AFe_2As_2 systems [139].

Also the EFG is found to display a strong As z dependence, see Figure 5.36. The As z displacement is described by $\Delta z = z - z_{\text{exp}}$. The Fe-As distance is smaller compared to the experimental one if Δz is negative. The EFG for the nonmagnetic tetragonal phase (crosses in Figure 5.36) increases strongly for all three compounds, as the Fe-As distance decreases, *i.e.* as Δz decreases. In case of CaFe_2As_2 , there is a minimum in the EFG for a displacement of roughly $\Delta z = -0.1 \text{ \AA}$ from the experimental position, while for larger Fe-As distances the EFG increases again. The same trend is observed for the other two compounds, middle and lower panels in Figure 5.36. They exhibit the minimum in the EFG at about $\Delta z = +0.05 \text{ \AA}$. For CaFe_2As_2 we observe a good agreement between the calculated EFG at the experimental As z position (for 250 K) and the measured EFG at 250 K [149] (the light green error bar in the upper panel of Figure 5.36). In a preliminary measurement for SrFe_2As_2 the quadrupole frequency ν_Q was determined to be less

Table 5.10: V_{zz} in 10^{21} V/m² of As for the nonmagnetic (NM) and different magnetic orders, all in orthorhombic phase.

Compound	NM	FM	NN-AFM	SDW
CaFe ₂ As ₂	+2.6	+2.4	+2.7	+3.1
SrFe ₂ As ₂	+0.2	+0.3	+0.2	-1.3
BaFe ₂ As ₂	-1.1	-1.0	-1.3	+1.3

than 2 MHz [151], corresponding to a V_{zz} of less than $0.5 \cdot 10^{21}$ V/m². This is also consistent with the calculated EFG of $0.09 \cdot 10^{21}$ V/m² at the experimental As z position. In case of BaFe₂As₂, the magnitude of the measured EFG at 200 K is roughly $0.7 \cdot 10^{21}$ V/m² [150]. Since the sign cannot be extracted from the NQR measurements, in Figure 5.36 the experimental EFG values with both signs are shown. The calculated V_{zz} for the experimental As z position is -1.1×10^{21} V/m². If the experimental EFG would be negative, reasonable agreement between experiment and calculation is obtained. Our results for three representative members of the AFe₂As₂ family as shown above follow a trend: the calculated EFGs for the NM tetragonal phase agree better with the measured EFG using the experimental As z positions, than using the (energetically) optimised As z positions, which are marked by arrows in Figure 5.36.

Structural phase transition

Although the structural and magnetic phase transitions occur simultaneously, the calculation allows to investigate their influence on the EFG separately. First we study the influence of the orthorhombic distortion. Therefore we perform non-magnetic calculations both in tetragonal and orthorhombic symmetry. We observe, that the orthorhombic splitting of the axes in the (a, b) plane has a rather small influence on the EFG. In case of SrFe₂As₂, the effect of the orthorhombic splitting is so small, that the orthorhombic EFG curve (full circles in Figure 5.36) would overlap with the tetragonal one, and is therefore not shown (see middle panel of Figure 5.36). For CaFe₂As₂ and BaFe₂As₂, we observe a similar behaviour: the EFG is larger for the orthorhombic symmetry for small Fe-As distances, the tetragonal and orthorhombic EFG curves cross close to the EFG minimum and the EFG is larger for the tetragonal symmetry for larger Fe-As distances. For all three compounds, we find that V_{zz} is parallel to the crystallographic c axis for the non-magnetic calculations in both the tetragonal and orthorhombic symmetry.

Magnetism

Investigation of the influence of the magnetism on the EFG in the orthorhombic symmetry shows that neither the FM nor the NN-AFM ordering of the Fe spins changes the EFG much, however, the SDW order has a huge influence on the EFG, *cf.* Table 5.10. For all the three systems, as the Fe-As distance is decreased, the magnetic moment is reduced and finally tends to zero. At this displacement value, the SDW EFG curves (empty circles in Figure 5.36) smoothly join the non-magnetic orthorhombic EFG curves (full circles) as one would expect. In Figure 5.36, the component of the EFG calculated for the SDW, that is parallel to the c axis of the crystal is shown (empty circles). As mentioned before, V_{zz} is found to be parallel to the crystallographic c axis in all non-magnetic calculations. For the magnetic SDW phase, the same behaviour is observed for CaFe₂As₂, but not for SrFe₂As₂ and BaFe₂As₂. For the latter two compounds, V_{zz} changes the axis, *i.e.*, the axis, along which the EFG tensor has the largest component according to the amount (which is the definition of V_{zz}), changes as the Fe-As distance is varied (*cf.* Section 5.4.6). The three diagonal components of the EFG tensor V_{ii} , which are parallel to the a , b and c axis of

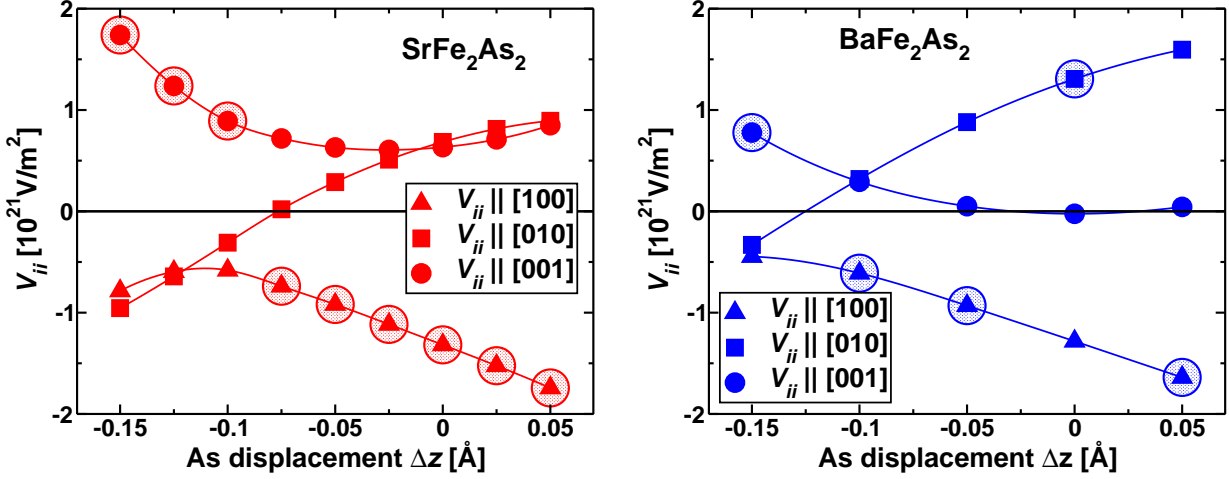


Figure 5.37: **Left:** the three components of the EFG tensor for SrFe_2As_2 in the orthorhombic SDW phase as a function of the As z position, $\Delta z = z - z_{\text{exp}}$. The component of the EFG parallel to $[100]$ is shown by upright triangles, the component parallel to $[010]$ by squares and the one parallel to $[001]$ by solid circles. V_{zz} , the largest one of these three, $|V_{xx}| \leq |V_{yy}| \leq |V_{zz}|$, is marked by a large shaded circle for each As z position. **Right:** the three components of the EFG tensor for BaFe_2As_2 in the orthorhombic SDW phase as a function of the As z position. The rest of the notation is the same as for the left panel.

the crystal, vary continuously as a function of the As z position, as can be seen in Figure 5.37. In case of SrFe_2As_2 , V_{zz} is parallel to the a axis for a displacement of As between $+0.05 \text{ \AA}$ and -0.075 \AA (which includes the experimental As z position) and parallel to the c axis for a displacement between -0.1 \AA and -0.15 \AA . For BaFe_2As_2 , V_{zz} fluctuates between all the three different axes. In particular, V_{zz} is parallel to the b axis at the experimental As z position. We also observe that the component parallel to the a axis is very similar for both the Sr and Ba AFe_2As_2 compounds. The components parallel to the b and c axis show the same variation with the As z position, but the curves for the two compounds are shifted by a small almost constant amount. For BaFe_2As_2 , a change of the direction of V_{zz} , when going from the high-temperature NM tetragonal phase to the low temperature SDW phase, was also observed experimentally [150]. Unfortunately, for CaFe_2As_2 only the quadrupole frequency parallel, and not perpendicular to the crystallographic c axis is provided in Ref. [149]. Hence, no conclusion about a change of the direction of V_{zz} can be drawn.

Figure 3 in Ref. [149] shows the temperature dependence of the quadrupole frequency ν_Q for CaFe_2As_2 , see Figure 5.38: ν_Q increases drastically as the temperature decreases from 300 K to 170 K. At 170 K, there is a large jump in the frequency due to the orthorhombic SDW phase transition. Between 170 K and 20 K, ν_Q is rather constant. The EFGs for the tetragonal NM and orthorhombic SDW phase were calculated using lattice parameters determined at 250 K and 50 K, respectively (marked by red arrows in Figure 5.38). For these two temperatures, the quadrupole frequency (parallel to the crystallographic c axis) is almost identical and roughly $\nu_Q \simeq 12.3 \text{ MHz}$ (marked by red boxes in Figure 5.38), which corresponds to $V_{zz} \simeq 3.2 \cdot 10^{21} \text{ V/m}^2$. This is in agreement with our result for the experimental As z position as seen in the upper panel of Figure 5.36: V_{zz} is $3.1 \cdot 10^{21} \text{ V/m}^2$ for both the tetragonal NM and the orthorhombic SDW phase.

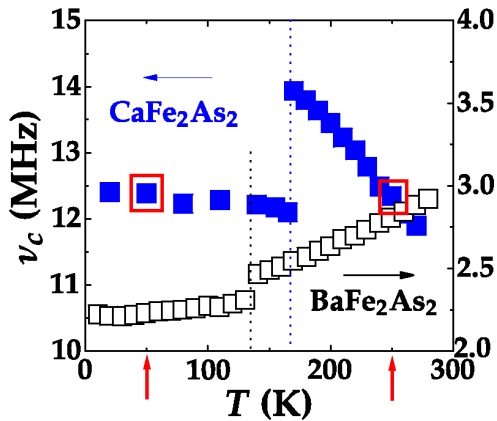


Figure 5.38: (Figure from Ref. [149].) Temperature dependence of the quadrupole frequency ν_Q in MHz for CaFe_2As_2 (full blue squares) and BaFe_2As_2 (empty black squares). The red squares mark ν_Q at the temperature of 50 K and 250 K (red arrows), from which temperatures the lattice parameters for the calculated EFGs for CaFe_2As_2 are taken, see text.

Pressure

We also investigated the influence of pressure on the EFG. V_{zz} was calculated for CaFe_2As_2 and SrFe_2As_2 using the experimental structural parameters as a function of pressure, as reported in Ref. [146] and Ref. [133], respectively. Our result is shown in the inset of Figure 5.39. In case of CaFe_2As_2 , the EFG increases slightly when the applied pressure is increased from 0 GPa to 0.24 GPa. For these pressure points, the structure is in the (orthorhombic) SDW phase. The next experimental pressure point is larger than the critical pressure of 0.3 GPa, where the c/a collapse takes place [146]. The structure changes into the nonmagnetic tetragonal phase and the calculated EFG increases drastically from roughly 3 to $10 \cdot 10^{21}$ V/m². Experimentally, the applied pressure for SrFe_2As_2 was much higher (up to 4 GPa) than for CaFe_2As_2 , but no indications of a collapsed phase was found until now [133]. Contrary to the jump in the calculated EFG at 0.3 GPa for CaFe_2As_2 , the EFG for SrFe_2As_2 increases monotonously without any kinks up to 4 GPa. It is worthwhile to measure the EFG for these systems to get a more clear picture.

Doping

Finally, the EFG for As of the (on the A site) doped compounds was calculated with VCA. The validity of the VCA was checked by super cell calculations for SrFe_2As_2 and BaFe_2As_2 . Due to the super cell construction, there are three different Wyckoff positions for As and hence three different EFGs, which lie reasonably close to the VCA EFG curve. In the VCA calculation, we keep the structural parameters fixed for the different levels of doping. In Figure 5.39, EFGs calculated in this manner are shown for CaFe_2As_2 , SrFe_2As_2 and BaFe_2As_2 . In case of CaFe_2As_2 , the EFG increases when electrons are taken out and decreases when electrons are added to the system. This implies that the As electron density gets more isotropic, when the system is electron doped. For BaFe_2As_2 , the trend is the same as in CaFe_2As_2 whereas for SrFe_2As_2 the situation is slightly different: hole doping does not change the EFG much, while electron doping increases the EFG. Note however, that the calculated EFG for SrFe_2As_2 are quite small.

5.5.5 The iron oxypnictides REFeAsO

At ambient temperature, all REFeAsO compounds crystallise in the tetragonal ZrCuSiAs -type structure. Undoped REFeAsO compounds exhibit a structural transition to an orthorhombic lattice at $T_0 \approx 155$ K for $R = \text{La}$ [152] and at $T_0 \approx 160$ K for $R = \text{Nd}$ [153]. Contrary to AFe_2As_2 , where the structural and magnetic transitions are found to be coupled, the magnetic transition temperature for the REFeAsO systems is about 10 K to 20 K lower than the structural one. For $R = \text{La}$, the antiferromagnetic ordering of the Fe moments, described by the same SDW

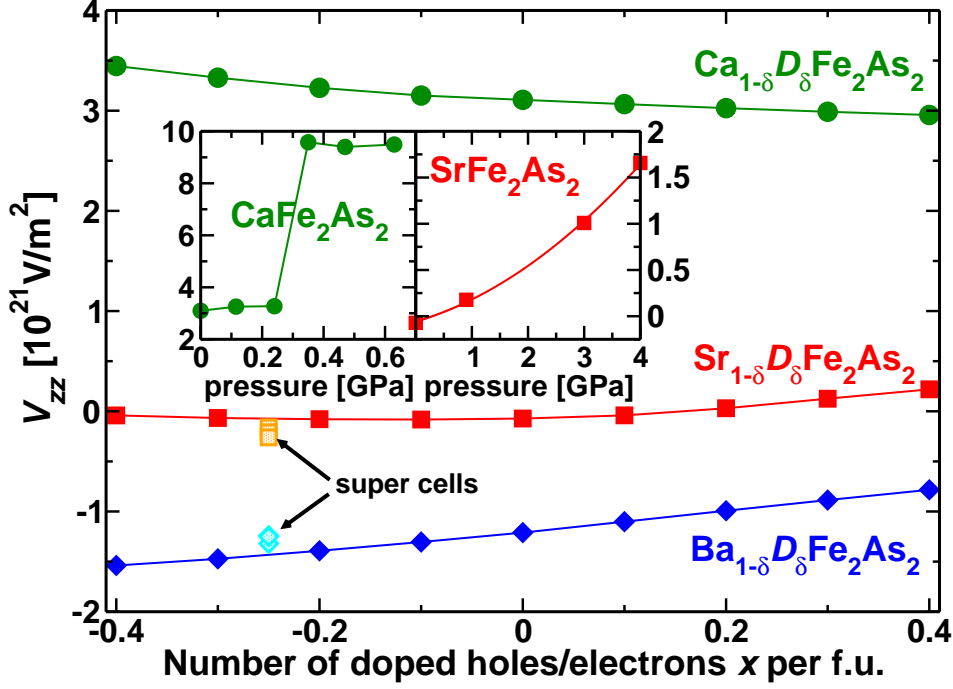


Figure 5.39: EFGs calculated for doped CaFe_2As_2 (green circles), SrFe_2As_2 (red squares) and BaFe_2As_2 (blue diamonds) using VCA. The symbol D represents the dopant. Depending on the element D , both electron doping ($x > 0$) and hole doping ($x < 0$) is possible. Results obtained from a four-fold super cell for $x = -0.25$ for SrFe_2As_2 (shaded orange squares) and BaFe_2As_2 (shaded blue diamonds) in the nonmagnetic tetragonal phase are also shown. **Inset:** dependence of the EFG on pressure for CaFe_2As_2 (left) and SrFe_2As_2 (right). The latter is in the (nonmagnetic) tetragonal phase.

pattern with $\vec{Q} = (1, 0, 1)$, occurs at $T_N \approx 137 \text{ K}$ [152] and for $R = \text{Nd}$, the SDW forms at $T_N \approx 140 \text{ K}$ [153]. A certain range of electron doping on the oxygen site suppresses the magnetic ordering and the compounds become superconducting, *e.g.*, $\text{LaFeAsO}_{0.9}\text{F}_{0.1}$ at $T_c = 26 \text{ K}$ [154] and $\text{NdFeAsO}_{0.85}\text{F}_{0.15}$ at $T_c = 43 \text{ K}$ [153].

For the $R\text{FeAsO}$ compounds, we studied the EFG for LaFeAsO and NdFeAsO . For these compounds, we focused on the nonmagnetic¹⁶ tetragonal phase. We also investigated the influence of doping.

Methods

The band structure calculations were performed using the full-potential local-orbital minimum-basis code FPLO (version 5.00-19) [2] within the local density approximation (LDA). In the scalar relativistic calculations the exchange and correlation functional of Perdew and Wang [15] was employed. As basis set La ($5s5p/6s6p5d+4f7s7p$), Nd ($4p4d4f5s5p/6s6p5d+7s7p$), Fe ($3s3p/4s4p3d+4d5s5p$), As ($4s4p3d+4d5s5p$)¹⁷ and O ($2s2p3d+3s3p$) were chosen for semicore/valence

¹⁶Due to the $4f$ electrons in NdFeAsO , it is not possible to obtain a nonmagnetic solution (for the Nd atoms), since LDA+ U has to be applied, see text below. Our choice of ordering the Nd spins antiferromagnetic renders a zero net moment on the Fe site.

¹⁷For NdFeAsO , $4d$ was not added to the polarisation states for Fe and As, since they changed the EFG only by $0.1 \cdot 10^{21} \text{ V/m}^2$.

+polarisation states. The high lying states improve the basis which is especially important for the calculation of the EFG. The lower lying states were treated fully relativistic as core states. To treat the Nd $4f$ states adequately, LSDA+ U in the atomic limit was employed with $U = [7, 9]$ eV and $J = 0.7$ eV for NdFeAsO. In accordance with the widespread agreement that in the new Fe-based superconducting compounds the Fe $3d$ electrons have a rather itinerant character, and thereby are much less correlated in comparison to the Cu $3d$ electrons in the high- T_c cuprates, we did not apply the LSDA+ U approximation to the Fe $3d$ states. A well converged k mesh of 275 (252) k points was used in the IBZ for LaFeAsO (NdFeAsO). In order to investigate the influence of F substitution on the O site, the virtual crystal approximation (VCA) was applied and cross-checked with the calculation of super cells¹⁸.

Results

z position of As

Also for these compounds, we investigate the EFG dependence on the As z position first. In Section 5.5.4, it was shown that the AFe_2As_2 systems are highly sensitive to the Fe-As distance, which is determined by the As z position. The displacement of As along the z -axis showed a strong impact on the magnetic moment of the Fe and the EFG of As. The same is true for the $REFeAsO$ systems: the Fe-As distance effects the magnetic moment of Fe [140] and from our calculations for LaFeAsO and NdFeAsO, we observe a strong dependence of the EFG on the As z position, see Figure 5.40. The As z displacement is described by $\Delta z = z - z_{\text{exp}}$. The Fe-As distance is smaller compared to the experimental one if Δz is negative. We observe a very similar behaviour for the EFG curve like for the AFe_2As_2 systems: the EFG increases strongly for both compounds, as the Fe-As distance decreases (note the negative sign of the EFG), there is a minimum in the EFG for a displacement of roughly $\Delta z = 0.10$ ($R = \text{La}$) and $\Delta z = 0.15$ ($R = \text{Nd}$), respectively, and for larger Fe-As distances the EFG increases again.

Experiment vs. calculation

Inserting the measured NQR frequency, obtained by Grafe *et al.* [155], (and $\eta = 0$) in Eq. (5.19) yields for the experimental EFG of As in LaFeAsO $|V_{zz}^{\text{exp}}| = (2.50 \pm 0.05) \cdot 10^{21}$ V/m² (red error bar in Figure 5.40). Using the 175 K lattice parameters and atomic positions as given in Ref. [152], we obtain a fair agreement for the calculated EFG¹⁹: $V_{zz}^{\text{calc}} = -3.14 \cdot 10^{21}$ V/m². However, the calculated EFG is much closer to the experimentally obtained one if the Fe-As distance is decreased and As is shifted in negative z -direction to $z = 0.6438$, where the energy has a minimum (in Figure 5.40 marked by an arrow) and the structure has a shorter Fe-As distance of 2.3748 Å. This yields $V_{zz}^{\text{calc,opt}} = -2.67 \cdot 10^{21}$ V/m². Inserting the measured NMR frequency and η , obtained by Jeglič *et al.* [153], in Eq. (5.19) yields for the experimental EFG of As in NdFeAsO $|V_{zz}^{\text{exp}}| = (3.11 \pm 0.09) \cdot 10^{21}$ V/m² (blue error bar in Figure 5.40). Using the experimental structural parameters at ambient temperature and $U = 8$ eV (for the Nd $4f$ states), we obtain a good agreement for the calculated EFG: $V_{zz}^{\text{calc}} = -3.39 \cdot 10^{21}$ V/m². Varying U by ± 1 eV (within the physically reasonable range) changes the EFG only by $\mp 0.01 \cdot 10^{21}$ V/m², which is well below the experimental error bars. Also here, the agreement between the calculated and the experimental EFG is a little bit better for the energetically optimised As z position, $z = 0.6515$, with a shorter Fe-As distance of 2.3729 Å, yielding $V_{zz}^{\text{calc,opt}} = -2.92 \cdot 10^{21}$ V/m².

¹⁸In order to come close to the experimental F concentration of 10 %, a 4-fold super cell (doubled along a and b), with 8 formula units was calculated. Therefore the space group $Pmm2$ was chosen. Replacing one O by F yields a composition of LaFeAsO_{0.875}F_{0.125}.

¹⁹The experimental lattice parameters for La $REFeAsO$ at ambient temperature were published [156] only after our calculations for this compound were performed. Our calculated properties are for the lattice constants at 175 K, but will be compared with experimental properties at ambient temperature. This will partly limit the agreement that can be expected. However, using the structural parameters at ambient temperature changes the EFG in only slightly: $V_{zz}^{\text{calc}} = -3.21 \cdot 10^{21}$ V/m², compare Table 5.11.

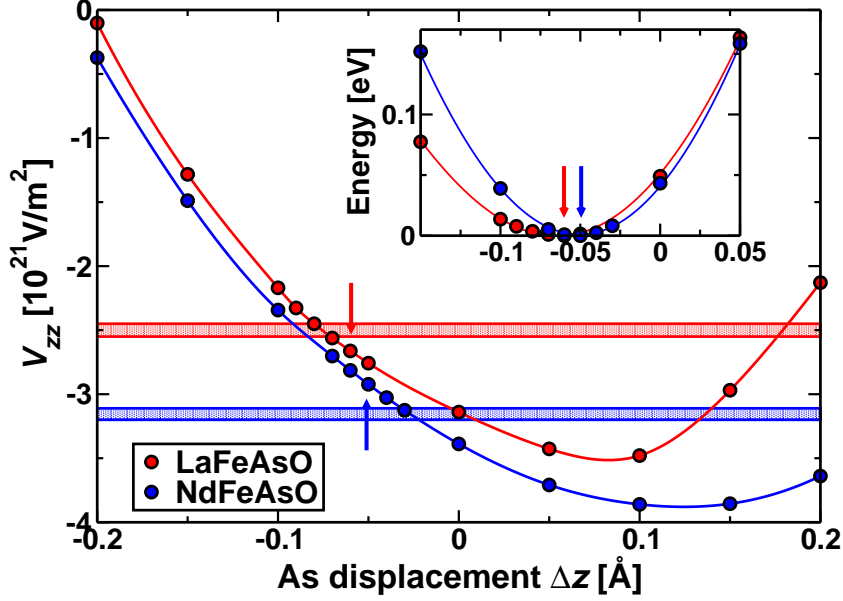


Figure 5.40: Dependence of V_{zz} of As on the As z position, $\Delta z = z - z_{\text{exp}}$, for LaFeAsO (red) and NdFeAsO (blue). The energetically optimised As z positions are marked by arrows. The experimental V_{zz} is represented by the shaded bar. **Inset:** energy in dependence of the As z position for LaFeAsO (red) and NdFeAsO (blue). The minima are marked by arrows.

Our results for two representative members of the $R\text{FeAsO}$ family as shown above follow a different trend than the members of the $A\text{Fe}_2\text{As}_2$ family: the calculated EFGs agree better with the measured EFG values for the (energetically) optimised As z position, than for the experimental As z position.

LaFeAsO vs. NdFeAsO

Analogous to the experiments, where the quadrupole frequency for ^{75}As is larger for the Nd than for the La compound, the magnitude of the calculated EFG is larger for the Nd compound $V_{zz} = -3.39 \cdot 10^{21} \text{ V/m}^2$ than for the La compound $V_{zz} = -3.21 \cdot 10^{21} \text{ V/m}^2$ – but less drastically. In order to understand this difference, we need to understand how the main component V_{zz} is calculated. Since the main component V_{zz} is obtained from the density component n_{20} , which again can be decomposed in radial functions R_l with angular momentum l and a Gaunt coefficient G , it can be shown, that V_{zz} contains only of sd , pp and dd contributions, see Section 4.1.1. For both the La parent and the Nd parent, the pp contribution to the EFG dominates clearly: $V_{zz} \simeq V_{zz}^{pp}$. This contribution to the EFG is proportional to the anisotropy function Δp (see Section 4.1.1)

$$V_{zz}^{pp} \propto \Delta p \quad \text{with} \quad \Delta p = \frac{1}{2}(n_x + n_y) - n_z.$$

The anisotropy function Δp for the As $4p$ electrons is negative for both compounds. This corresponds to a prolate p electron distribution and is in agreement with the negative V_{zz} for both compounds. For the La compound, Δp is less negative than for the Nd compound: $\Delta p^{\text{La}} = -0.018$ and $\Delta p^{\text{Nd}} = -0.062$, respectively. Thus, the $4p$ orbitals are less isotropic for the Nd compound and hence the absolute value of the EFG is enhanced. The observed difference between the La and Nd compounds could arise from either the additional $4f$ electrons due to screening effects or from the smaller lattice parameters in the Nd compound. To separate the influence of the

Table 5.11: Calculated V_{zz} of As for $REFeAsO$ for two sets of lattice parameters: set 1 (LaFeAsO [156]): $a=4.03007(9)$ Å, $c=8.7368(2)$ Å, As: $z = 0.6507(4)$ and La: $z = 0.1418(3)$; set 2 (NdFeAsO [153]): $a = 3.96629(1)$ Å and $c = 8.59886(6)$ Å, As: $z = 0.65735(9)$ and Nd: $z = 0.13887(6)$. LaFeAsO with set 1 and NdFeAsO with set 2 are the experimental data, the other combinations are models.

Compound	V_{zz} for set 1	V_{zz} for set 2
LaFeAsO	$-3.21 \cdot 10^{21}$ V/m ²	$-3.60 \cdot 10^{21}$ V/m ²
NdFeAsO	$-2.92 \cdot 10^{21}$ V/m ²	$-3.39 \cdot 10^{21}$ V/m ²

change in the lattice geometry from the change in the electronic configuration, we compare the real EFGs with fictitious EFGs, which are obtained by exchanging the lattice parameters for both compounds, see Table 5.11.

The absolute value of the EFG, $|V_{zz}|$, increases with lattice compression both for the LaFeAsO and NdFeAsO electronic configurations (Table 5.11 from the left to the right). Next, we checked the role of the RE $4f$ electrons. In this case we find the opposite trend, *i.e.*, for given lattice parameters, $|V_{zz}|$ is smaller for the Nd than for the La compound (Table 5.11 from top to bottom). One can therefore conclude that $|V_{zz}|$ increases with lattice contraction and decreases with increasing number of RE $4f$ electrons. For these two compounds, the influence of the $4f$ electrons is less dominant and therefore NdFeAsO, which has smaller lattice parameters due to the usual lanthanide contraction has a slightly larger EFG than LaFeAsO.

Doping

Now, we discuss the influence of doping on the EFG. We start with LaFeAsO. The EFGs of the doped compounds were calculated with the virtual crystal approximation (VCA). The validity of the VCA was confirmed by super cell calculations.

First, we consider solely the effect of electron doping. Therefore, we keep the structural parameters fixed for different levels of doping. Figure 5.41 shows two such VCA curves. When the experimentally determined As z position is used (empty squares in Figure 5.41), the calculated EFG agrees quite well with the measured EFG value for 10 % doping (red error bar in Figure 5.41). Also Lebègue *et al.* found good agreement for the 10 % doped compound [157] using the WIEN2k code. If the optimised As z position is used, the obtained VCA curve is shifted in the direction of smaller $|V_{zz}|$ (full diamonds in Figure 5.41). This curve was cross-checked with a super cell calculation. Due to the super cell construction, there are two different Wyckoff positions for As and hence two different EFGs, whereof one is lying on top of this VCA curve and the other one very close to it (black triangles in Figure 5.41).

Now, we investigate the structural change on top of the doping by calculating the EFG within VCA for the structural parameters of LaFeAsO_{0.92}F_{0.08}, obtained at 175 K, as given in Ref. [152]. The structural change has only a minor effect on the EFG. The obtained EFG (empty circle in Figure 5.41) lies very close to the VCA curve, which was obtained by using the structural parameters of LaFeAsO at 175 K (empty squares). Our calculations result in a decrease in $|V_{zz}|$ upon electron doping for LaFeAsO_{0.9}F_{0.1}, although in the experiments an increase is observed. This is not pointed out by Lebègue *et al.* [157], although they obtain the same discrepancy for the trend in the V_{zz} calculation.

Next, we repeat the same procedure for the Nd compound. Here, the EFGs of the doped compounds were calculated with the VCA only. Since the EFG is calculated on the As site, whereas the doping takes place on the oxygen site, a very similar behaviour is expected for the Nd com-

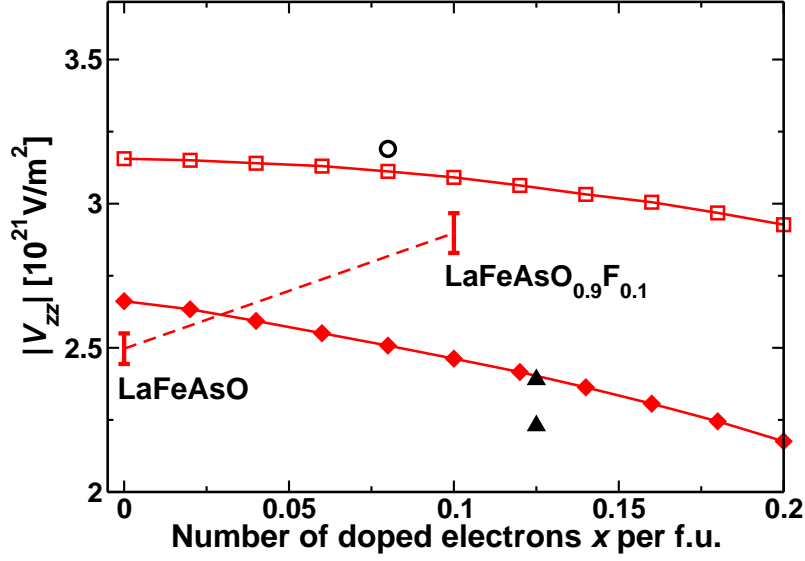


Figure 5.41: LaFeAsO. Calculated V_{zz} of As obtained from the virtual crystal approximation (VCA) using the experimental structural parameters at 175 K for LaFeAsO [152]: empty squares (red) for As at $z_{exp} = 0.6507$ and filled diamonds (red) for As at $z_{opt} = 0.6438$. VCA for structural parameters of LaFeAsO_{0.92}F_{0.08} at 175 K [152]: empty circle (black). The filled triangles (black) show the EFGs from the super cell calculation using the experimental lattice parameters at 175 K for LaFeAsO [152] and the optimised As z position, $z_{opt} = 0.6438$. The measured EFGs for the pure and the 10 % F-doped compound [155] are shown by red error bars.

pound and there is no need for repeating the super cell calculation.

First, we consider solely the effect of electron doping. Therefore, we keep the structural parameters fixed for different levels of doping. In Figure 5.42 two such VCA curves are shown. When the experimentally determined As z position (NdFeAsO at ambient temperature) is used, the calculated EFG (empty squares in Figure 5.42) agrees very well with the measured EFG for 15 % doping (blue error bar in Figure 5.42). This agreement is even better compared to the La compound. The VCA curve with the optimised As z position deviates from the experimental curve as it systematically predicts a smaller $|V_{zz}|$. Also here, a behaviour similar to the La compound is obtained.

Next, we investigate the structural change on top of the doping by calculating the EFG within VCA for the ambient temperature structural parameters of NdFeAsO_{0.85}F_{0.15}. We notice that the use of these parameters slightly reduces $|V_{zz}|$ to $V_{zz} = -3.17 \cdot 10^{21} \text{ V/m}^2$ (black circle in Figure 5.42). Also here, the influence of the structural change on the EFG is quite small, but it changes the EFG in the opposite direction compared to the doped La compound.

Our calculations predict a small decrease in $|V_{zz}|$ upon electron doping for NdFeAsO_{0.85}F_{0.15}, although experimentally a slight increase is observed: as it is the case for the La compound where the difference between the slopes of the calculated and the experimental EFGs upon doping is even more pronounced.

Comparing the VCA curves for the AFe_2As_2 systems and the $REFeAsO$ systems, we observe that the absolute value of the EFG decreases when the system is electron doped for all systems (except for SrFe₂As₂, whose EFG is very small).

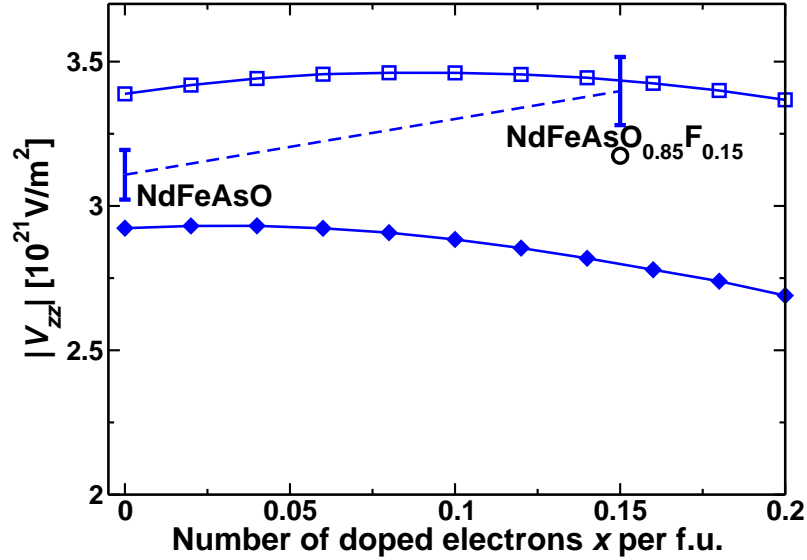


Figure 5.42: NdFeAsO. Calculated V_{zz} of As obtained from the virtual crystal approximation (VCA) using the experimental structural parameters at ambient temperature for NdFeAsO [153]: empty squares (blue) for As at $z_{exp} = 0.6574$ and filled diamonds (blue) for As at $z_{opt} = 0.6515$. VCA for structural parameters of NdFeAsO $_{0.85}$ F $_{0.15}$ at ambient temperature [152]: empty circle (black). The measured EFGs for the pure and the 15 % F-doped compound [153] are shown by error bars.

5.5.6 Summary and conclusion

The mechanism of superconductivity in the recently discovered iron arsenide systems AFe_2As_2 and $REFeAsO$ is still under heavy discussion. A prerequisite for its understanding is the correct description of the underlying electronic structure. However, describing accurately the Fe-As interaction in the context of the present stage of DFT is difficult.

As the Fe-As interaction is reflected by the Fe-As distance and doping leads to the onset of superconductivity in these systems, the EFG and its dependence on doping is an ideal tool to investigate the Fe-As interplay.

There is reasonable agreement between the calculated and the experimentally obtained EFGs for three investigated iron arsenides AFe_2As_2 , with $A = Ca, Sr$ and Ba , for the nonmagnetic tetragonal phase, using the experimental structural parameters. The calculations show that neither the orthorhombic splitting, nor the fictitious FM or NN-AFM ordering of the Fe spins influence the EFG much. Also doping has a quite small effect on the EFG. In contrast, the As z position and pressure have a large influence on the EFG. Also the SDW order changes the calculated EFG noticeable, consistent with the experimental observations for $CaFe_2As_2$ and $BaFe_2As_2$.

Reasonable agreement between the calculated and the experimentally obtained EFGs was obtained for the investigated iron oxypnictides $REFeAsO$, with $RE = La$ and Nd , using the experimental structural parameters. However, the agreement improves, if the optimised As z position is used in the calculation – in contrast to the AFe_2As_2 systems.

The effect of electron doping on the EFG is much smaller than the influence of the As z position. We observe the same behaviour upon electron doping as for the AFe_2As_2 systems: the absolute value of the EFG decreases. Yet, for the $REFeAsO$ systems, the measured quadrupole frequencies show the opposite trend, they increase with electron doping. An experimental check if this

discrepancy also holds for the AFe_2As_2 systems would be desirable.

As demonstrated, similar to the magnetism, also the EFG is highly sensitive to the As z position. But whereas the calculated EFGs for the undoped systems agree with the experimental data, the trends obtained from the calculation for the doped systems is opposite to the the experimental data. These findings emphasise again the crucial importance of a reliable, correct description of the Fe-As interaction as this is connected with the density around As and hence with the As EFG. Further calculational and experimental effort on the “EFG doping” problem may lead to hints why the DFT calculations fail for some physical properties of the iron pnictides.

6 Beyond the EFG: electron penetration in the nucleus – its effect on the quadrupole interaction

A Taylor expansion of the interaction between a nucleus and its surrounding electron distribution provides terms that are well-known in the study of hyperfine interactions: the familiar quadrupole interaction and the less familiar hexadecapole interaction. If the penetration of electrons into the nucleus is taken into account, various corrections to these multipole interactions appear. The best known one is a scalar correction related to the isomer shift, which can be detected by Mössbauer spectroscopy. In this chapter, we will discuss a related tensor correction, which modifies the quadrupole interaction if electrons penetrate the nucleus. This effect has been implemented in the FPLO code.

We discuss how it shows up in experiments, and how it could possibly be exploited to improve the accuracy of experimentally determined quadrupole moments.

6.1 Formalism

6.1.1 Classical interaction energy without charge-charge overlap

The classical electrostatic interaction energy between a positive nuclear charge distribution $\rho(\vec{r})$ and a potential $v(\vec{r})$ due to a surrounding (electron¹) charge distribution $n(\vec{r}')$ is formally given by

$$E = \int \rho(\vec{r})v(\vec{r})d\vec{r} = \frac{1}{4\pi\epsilon_0} \int \int \frac{\rho(\vec{r})n(\vec{r}')}{|\vec{r} - \vec{r}'|} d\vec{r}d\vec{r}', \quad (6.1)$$

and can be expressed by the standard multipole expansion in spherical harmonics [37]:

$$\frac{1}{|\vec{r} - \vec{r}'|} = \sum_{l,m} \frac{4\pi}{2l+1} \frac{r_{<}^l}{r_{>}^{l+1}} Y_{l,m}^*(\Omega) Y_{l,m}(\Omega'), \quad (6.2)$$

with $r_{<} = \min(r, r')$ and $r_{>} = \max(r, r')$. This leads to an infinite sum of double integrals, each with the dimension of energy:

$$E = \sum_{l=0}^{\infty} E_{2l} = E_0 + E_2 + E_4 + \dots \quad (6.3)$$

Odd terms will vanish in the cases of interest here, see Section 6.1.2. It is the second term E_2 that will be of interest in the present work:

$$E_2 = h\nu_Q = \frac{1}{4\pi\epsilon_0} \frac{4\pi}{5} \sum_{m=-2}^{+2} \int \int \rho(\vec{r})n(\vec{r}') \frac{r_{<}^2}{r_{>}^3} Y_{2,m}^*(\Omega) Y_{2,m}(\Omega') d\vec{r}d\vec{r}'. \quad (6.4)$$

The frequency ν_Q is experimentally accessible, and is called the nuclear quadrupole coupling constant (NQCC). Due to the varying assignment of $r_{<}$ and $r_{>}$ to ‘nuclear’ (r) or ‘electron’ (r') coordinates, quantities as E_2 are an intricate mixture of properties of both charge distributions

¹For free atoms, this surrounding charge distribution consists of electrons only, for molecules and solids, it contains all electrons and all nuclei, except for the nucleus under consideration. As we will see later, it is the charge density of the electrons that gives rise to the corrections.

$\rho(\vec{r})$ and $n(\vec{r}')$. Only in the special case where both charge distributions do not overlap ($r_{<} \equiv r$ and $r_{>} \equiv r'$), Eq. (6.1) can be written in terms of properties that depend entirely on only one of the charge distributions²

$$E = \sum_{l,m} Q_{lm}^* V_{lm} , \quad (6.5)$$

where Q_{lm} and V_{lm} are the components of the nuclear multipole moment and electric multipole field tensors of rank l , respectively:

$$Q_{lm} = \sqrt{\frac{4\pi}{2l+1}} \int r^l \rho(\vec{r}) Y_{lm}(\Omega) d\vec{r} \quad (6.6)$$

$$V_{lm} = \frac{1}{4\pi\epsilon_0} \sqrt{\frac{4\pi}{2l+1}} \int \frac{1}{r'^{l+1}} n(\vec{r}') Y_{lm}(\Omega') d\vec{r}' . \quad (6.7)$$

When this formalism is applied to describe nuclei and electrons, the simplification by Eq. (6.5) can never be made: s electrons and in full relativistic treatment also $p_{\frac{1}{2}}$ electrons have a nonzero probability to appear at $r=0$, and therefore, the nuclear and electron charge distributions always overlap. Nevertheless, motivated by the very small size of the region where this overlap happens compared to the volume of the rest of the atom, one can in a first approximation neglect this concern and apply Eq. (6.5) to atoms, molecules and solids. This is where the concept of an electric field gradient tensor (V_{2m}) originates that interacts with a nuclear quadrupole moment tensor (Q_{2m}) to produce an experimentally observable interaction energy (E_2). Although E_2 itself is a well-defined observable property, its description by a quadrupole interaction energy only

$$E_2 = h\nu_Q \approx h\nu_{QI} = \sum_{m=-2}^{+2} Q_{2m}^* V_{2m} \quad (6.8)$$

rather than by Eq. (6.4) is an approximation.

6.1.2 Overlap corrections

We will now derive explicit expressions for the corrections that need to be added to Eq. (6.8) to obtain Eq. (6.4) (and similarly for other values of l). Rather than using the multipole expansion in spherical harmonics from Eq. (6.2), we start from a Taylor expansion of the electrostatic potential $v(\vec{r}) = 1/(4\pi\epsilon_0) \int n(\vec{r}')/|\vec{r} - \vec{r}'| d\vec{r}'$ in the interaction energy of Eq. (6.1):

$$\begin{aligned} E &= \int \rho(\vec{r}) v(\vec{r}) d\vec{r} = v(0) \int \rho(\vec{r}) d\vec{r} + \sum_i v_i(0) \int x_i \rho(\vec{r}) d\vec{r} \\ &+ \frac{1}{2!} \sum_{i,j} v_{ij}(0) \int x_i x_j \rho(\vec{r}) d\vec{r} + \frac{1}{3!} \sum_{i,j,k} v_{ijk}(0) \int x_i x_j x_k \rho(\vec{r}) d\vec{r} \\ &+ \frac{1}{4!} \sum_{i,j,k,l} v_{ijkl}(0) \int x_i x_j x_k x_l \rho(\vec{r}) d\vec{r} + \mathcal{O}(6). \end{aligned} \quad (6.9)$$

In order to recognise in this expression the multipole moments and multipole fields from Eq. (6.6) and Eq. (6.7), one has to make substitutions like shown in Eq. (6.10) for the quadrupole moment:

$$\int x_i x_j \rho(\vec{r}) d\vec{r} = \underbrace{\frac{1}{3} \int (3x_i x_j - r^2 \delta_{ij}) \rho(\vec{r}) d\vec{r}}_{Q_{ij}} + \frac{1}{3} \int r^2 \rho(\vec{r}) d\vec{r} \delta_{ij} . \quad (6.10)$$

²Note, that contrary to Chapter 3 and 4, here we use due to Eq. (6.2) the complex notation for the multipole moment and field tensors, *i.e.*, complex spherical harmonics. However, the (real) physical quantity E is of course identical for both the real and the complex representation.

Here, Q_{ij} are the components of the quadrupole tensor Q_{2m} (Eq. (6.6)), but now in Cartesian form. These substitutions in Eq. (6.9) yield the nuclear monopole, quadrupole and hexadecapole moments in Cartesian form:

$$M = \int \rho(\vec{r})v(\vec{r})d\vec{r} = eZ \quad (6.11)$$

$$Q_{ij} = \int (3x_i x_j - r^2 \delta_{ij})\rho(\vec{r})d\vec{r} \quad (6.12)$$

$$H_{ijkl} = \int 3 \cdot 5 \left(7x_i x_j x_k x_l - f^H(x_i, x_j, x_k, x_l) \right) \rho(\vec{r})d\vec{r} \quad (6.13)$$

with $f^H(x_i, x_j, x_k, x_l) = r^2 [x_i x_j \delta_{kl} + x_i x_k \delta_{jl} + x_i x_l \delta_{kj} + x_j x_k \delta_{il} + x_j x_l \delta_{ik} + x_k x_l \delta_{ij}] - \frac{r^4}{5} [\delta_{ij} \delta_{kl} + \delta_{ik} \delta_{jl} + \delta_{il} \delta_{jk}]$. The corresponding electric multipole fields in Cartesian form are:

$$V = v(0) \quad (6.14)$$

$$V_{ij} = (\partial_i \partial_j v(0) - \frac{1}{3} \Delta \delta_{ij}) \Delta v(0) \quad (6.15)$$

$$V_{ijkl} = \partial_i \partial_j \partial_k \partial_l v(0) - f_{ijkl}^V \Delta v(0) \quad (6.16)$$

with $f_{ijkl}^V = [\partial_i \partial_j \delta_{kl} + \partial_i \partial_k \delta_{jl} + \partial_i \partial_l \delta_{kj} + \partial_j \partial_k \delta_{il} + \partial_j \partial_l \delta_{ik} + \partial_k \partial_l \delta_{ij}] - \frac{\Delta}{5} [\delta_{ij} \delta_{kl} + \delta_{ik} \delta_{jl} + \delta_{il} \delta_{jk}]$. The expressions in Eqs. (6.11) to (6.13) and Eqs. (6.14) to (6.16) are identical to the ones in Eqs. (6.6) and (6.7), respectively. They have the same number of degrees of freedom: 1, 5 and 9 for the zeroth, second and fourth order moment/field.

After having inserted into Eq. (6.9) all substitutions as in Eq. (6.10), the interaction energy can be written as

$$\begin{aligned} E = & \underbrace{M \cdot V}_{\text{MI}} + \underbrace{\frac{1}{3!} \{r^2\} \Delta v(0)}_{\text{MS}^{(1)}} + \underbrace{\frac{1}{5!} \{r^4\} \Delta^2 v(0)}_{\text{MS}^{(2)}} \\ & + \underbrace{\frac{1}{2!} \frac{1}{3} \sum_{ij} Q_{ij} V_{ij}}_{\text{QI}} + \underbrace{\frac{1}{28} \sum_{ij} \left\{ (x_i x_j - \frac{r^2}{3} \delta_{ij}) r^2 \right\} (\partial_i \partial_j - \frac{\Delta}{3} \delta_{ij}) \Delta v(0)}_{\text{QS}^{(1)}} \\ & + \underbrace{\frac{1}{4!} \frac{1}{105} \sum_{ijkl} H_{ijkl} V_{ijkl}}_{\text{HDI}} + \mathcal{O}(6), \end{aligned} \quad (6.17)$$

where all integrations over the nuclear charge density $\rho(\vec{r})$ are noted in short-hand by {curled brackets}. Eq. (6.17) contains no odd order terms (dipole, octupole, ...), since nuclei have no odd order electric moments due to parity and time reversal symmetry³ [158]. We see that Eq. (6.17) contains dot products⁴ between multipole moments and fields as in Eq. (6.5): the monopole (MI), quadrupole (QI), hexadecapole (HDI), ... interactions. These are the only contributions in the case without charge-charge overlap. Additionally, an infinite set of even order correction terms appears now as well: the first and second order monopole shift (MS) and the first order quadrupole shift (QS). Due to parity, there are no odd order corrections. In Table 6.1, a general naming system and a corresponding set of symbols are presented: the n^{th} order *quasi* multipole *moment* multiplied (dot product) with the n^{th} order *quasi* multipole *field* leads to the n^{th} order

³However the search for violations of these symmetries by looking for these moments goes on.

⁴A dot product of two tensors of rank n is defined as $\sum_{1, \dots, n} A_{1, \dots, n} \cdot B_{1, \dots, n}$, as given in Eq. (6.17). It yields a scalar, not a tensor of rank n .

Table 6.1: Systematic overview of nuclear multipole and quasi multipole moments and electric multipole and quasi multipole fields that appear in the multipole expansion of two interacting (and overlapping) classical charge distributions. The first column gives the regular multipole expansion for point nuclei: the monopole, quadrupole and hexadecapole interactions. The next columns give the quasi multipole moments/fields for every multipole interaction, denoted by a tilde: these are corrections to the multipole interactions due to electron penetration into an extended nucleus. Coloured text is by generalisation only, and is not systematically derived in this work. The objects in each line are spherical tensors of a given rank (rank 0 for line 1, rank 2 for line 2, rank 4 for line 3, ...).

Order	Multipole moment / field	First order quasi moment / quasi field	Second order quasi moment / quasi field	...
$\mathcal{O}(0)$	MI: $M \propto r^0 Y_{00}$ $V \propto v(0)$	MS ⁽¹⁾ : $\tilde{M}^{(1)} \propto \{r^2 Y_{00}\}$ $\tilde{V}^{(1)} \propto \Delta v(0)$	MS ⁽²⁾ : $\tilde{M}^{(2)} \propto \{r^4 Y_{00}\}$ $\tilde{V}^{(2)} \propto \Delta^2 v(0)$...
$\mathcal{O}(2)$	QI: $Q \propto r^2 Y_{20}$ $V_{ij} \propto \partial_{ij} v(0)$	QS ⁽¹⁾ : $\tilde{Q}^{(1)} \propto \{r^4 Y_{20}\}$ $\tilde{V}_{ij}^{(1)} \propto \partial_{ij} \Delta v(0)$	QS ⁽²⁾ : $\tilde{Q}^{(2)} \propto \{r^6 Y_{20}\}$ $\tilde{V}_{ij}^{(2)} \propto \partial_{ij} \Delta^2 v(0)$...
$\mathcal{O}(4)$	HDI: $H \propto r^4 Y_{40}$ $V_{ijkl} \propto \partial_{ijkl} v(0)$	HDS ⁽¹⁾ : $\tilde{H}^{(1)} \propto \{r^6 Y_{40}\}$ $\tilde{V}_{ijkl}^{(1)} \propto \partial_{ijkl} \Delta v(0)$	HDS ⁽²⁾ : $\tilde{H}^{(2)} \propto \{r^8 Y_{40}\}$ $\tilde{V}_{ijkl}^{(2)} \propto \partial_{ijkl} \Delta^2 v(0)$...
...

multipole *shift*. From the general trends in this table, one can infer the structure of the higher order corrections that were not explicitly derived in Eq. (6.17) – they are shown in the table in blue.

There is a qualitative difference between the multipole fields in the first column of Table 6.1 and the quasi multipole fields in all other columns. The multipole fields depend on the potential $v(0)$ at the nucleus, which depends via integration on the charge distribution everywhere else in the system, *cf.* Eq. (2.17). Multipole fields are therefore integrated quantities, determined by the entire density. The quasi multipole fields depend on the Laplacian of the potential at the nucleus $\Delta v(0)$, which is by the Poisson equation ($\Delta v(0) = -n(0)/\epsilon_0$) proportional to the electron charge density at the nucleus $n(0)$. Quasi multipole fields are therefore point quantities, determined by the electron density at a single point only.

The core of the present work deals with the first order quadrupole shift QS⁽¹⁾, which is the first order correction to the quadrupole interaction. In the next section, the results of Eq. (6.17) and Table 6.1 for a system of two classical charge distributions will be translated to a quantum formulation. This will make it applicable to atoms, molecules and solids.

6.1.3 Quantum formulation

In order to translate Eq. (6.17) to quantum mechanics, Hamiltonian operators corresponding to all its terms are required. The structure of Eq. (6.17) suggests a perturbation theory treatment, with the monopole interaction term as the unperturbed Hamiltonian, and the other terms as small perturbations. The monopole term depends via r^0 on the (small) nuclear coordinate ($r \propto 10^{-15}$ m) and via $1/r'$ on the electronic coordinate ($r' \propto 10^{-10}$ m). Among all small corrections in Table 6.1, the two largest ones are the quadrupole interaction QI and the first order monopole shift MS⁽¹⁾ – both have a r^2 in their nuclear parts and a second derivative of the electrostatic potential (leading to $1/r'^3$) in their electronic parts. These two leading corrections will be considered as the small perturbation.

The Hamiltonians that correspond to the entries in Table 6.1 operate on the direct product space of wave functions for the nuclear and the electron subspaces. The ground state of the monopole Hamiltonian is a direct product between the nuclear ground state and the electronic ground state wave function. With $\hat{M} = eZ\hat{\mathbb{1}}$ (Eq. (6.11), $\hat{\mathbb{1}}$ is the identity operator on the nuclear space) and $\hat{V} = \hat{v}(0)$ (Eq. (6.14), $\hat{v}(0)$ is an operator on the electronic space that returns the potential at $\vec{r}=\vec{0}$ due to a given wave function ψ), the unperturbed monopole interaction Hamiltonian is

$$\hat{\mathcal{H}}_{MI} = eZ \hat{\mathbb{1}} \otimes \hat{v}(0). \quad (6.18)$$

Evaluating this for the ground state wave function $|I \otimes \psi_0\rangle$ of the combined nuclear+electronic system ($|I\rangle$ is the ground state of the nucleus, and $|\psi_0\rangle$ the ground state of the electron system with a point nucleus) leads to:

$$\begin{aligned} E_0^{pn} &= \langle \psi_0 \otimes I | \hat{\mathcal{H}}_{MI} | I \otimes \psi_0 \rangle \\ &= \langle I | eZ \hat{\mathbb{1}} | I \rangle \cdot \langle \psi_0 | \hat{v}(0) | \psi_0 \rangle \\ &= eZv(0), \end{aligned} \quad (6.19)$$

which is the leading term in Eqs. (6.5) or (6.17). The label *pn* ('point nucleus') emphasises the difference with E_0 from Eq. (6.3). The quantity $v(0)$ – the electrostatic potential at the nuclear site for a point nucleus – is accessible by first-principles codes.

The perturbation is (see Table 6.1 for the notation):

$$\hat{\mathcal{H}}_P = \hat{\mathcal{H}}_{QI} + \hat{\mathcal{H}}_{MS^{(1)}}. \quad (6.20)$$

In first order perturbation theory, the energy corrections due to this perturbation are found by evaluating the perturbing Hamiltonian in the ground state of the unperturbed Hamiltonian. Assuming a non-degenerate ground state in the electron subspace, it is advantageous to write the Hamiltonians immediately in a more familiar form where the electronic matrix elements are already evaluated and are treated as known (=computable) quantities. After similar algebra as for the monopole Hamiltonian, this leads to this form for the monopole shift Hamiltonian. It contains the mean square radius $\langle r^2 \rangle$ of the nucleus and the electron density $n(0)$ at the position of the nucleus

$$\hat{\mathcal{H}}_{MS^{(1)}} = -\frac{eZ}{6\epsilon_0} n(0) \langle r^2 \rangle \hat{\mathbb{1}}. \quad (6.21)$$

The quadrupole Hamiltonian $\hat{\mathcal{H}}_{QI}$ has already been introduced in Section 3.3 and is explicitly derived in Appendix C. It contains the (spectroscopic) quadrupole moment of the nucleus Q and the quadrupole field of the electrons V_{zz} (principle component of the electric field gradient tensor)

$$\hat{\mathcal{H}}_{QI} = \frac{eQV_{zz}}{4(2I-1)I\hbar^2} \left[(3\hat{I}_z^2 - \hat{I}^2) + \frac{1}{2}\eta (\hat{I}_+^2 + \hat{I}_-^2) \right]. \quad (6.22)$$

Diagonalising these two Hamiltonians in the nuclear states leads to the desired energy corrections in first order perturbation. Formally, this can be written as

$$\begin{aligned}
E^{[1]} &= E_0^{pn} + \langle I | \hat{\mathcal{H}}_{MS^{(1)}} + \hat{\mathcal{H}}_{QI} | I \rangle \\
&= E_0^{pn} + \langle I | \hat{\mathcal{H}}_{MS^{(1)}} | I \rangle + \langle I | \hat{\mathcal{H}}_{QI} | I \rangle \\
&= E_0^{pn} + E_{MS^{(1)}}^{[1]} + E_{QI}^{[1]}.
\end{aligned} \tag{6.23}$$

Here, $E_{MS^{(1)}}^{[1]}$ is a correction to the monopole energy E_0^{pn} for a point nucleus due to (s or $p_{\frac{1}{2}}$) electron penetration into the volume of a spherical nucleus. The quadrupole interaction energy $E_{QI}^{[1]}$ is a correction due to the deviation from spherical symmetry of this nucleus. It is this term, which played an important role in Sections 3.3 and 3.4.

There is a second group of entries with even much smaller corrections in Table 6.1: the HDI, $QS^{(1)}$ and $MS^{(2)}$ terms all have r^4 in their nuclear parts and 4 derivatives of the electrostatic potential ($\rightarrow 1/r^{15}$ in their electronic parts). The corresponding Hamiltonians are:

$$\begin{aligned}
\hat{\mathcal{H}}_{HDI} &= \frac{eHV_{zzzz}}{128I(I-1)(2I-1)(2I-3)\hbar^4} \\
&\cdot \left[35\hat{I}_z^4 - 30\hat{I}_z^2\hat{I}^2 + 3\hat{I}^4 + 25\hbar^2\hat{I}_z^2 - 6\hbar^2\hat{I}^2 \right]
\end{aligned} \tag{6.24}$$

$$\hat{\mathcal{H}}_{QS^{(1)}} = -\frac{1}{14\epsilon_0} \frac{e\tilde{Q}n_{zz}}{4(2I-1)I\hbar^2} \left[(3\hat{I}_z^2 - \hat{I}^2) + \frac{1}{2}\eta_{QS} (\hat{I}_+^2 + \hat{I}_-^2) \right] \tag{6.25}$$

$$\hat{\mathcal{H}}_{MS^{(2)}} = -\frac{eZ}{5!\epsilon_0} \Delta n(0) \langle r^4 \rangle \hat{\mathbb{1}}. \tag{6.26}$$

The (diagonal part of the) hexadecapole Hamiltonian, Eq. (6.24), is taken from the literature [159], the quadrupole shift Hamiltonian, Eq. (6.25), is derived explicitly in Appendix E and similar algebra as for the first order monopole shift Hamiltonian leads to the second order monopole shift Hamiltonian, Eq. (6.26). As they are much smaller than the QI and $MS^{(1)}$ terms, it makes little sense to add these corrections to the Hamiltonian of Eq. (6.20) right away. Rather one should consider a first order perturbation to the Hamiltonian of Eq. (6.20), which itself was already a perturbation to the monopole Hamiltonian of Eq. (6.18). This means: find the perturbed eigenstates of Eq. (6.20) in first order, and evaluate the new perturbations as given by the Hamiltonians in Eqs. (6.24)–(6.26) in these eigenstates. In the present work, we are interested in first place in $\hat{\mathcal{H}}_{QS^{(1)}}$, as it has the symmetry of a quadrupole interaction: this Hamiltonian, evaluated in the (approximate) eigenstates for a system with a finite and quadrupolarly deformed nucleus, gives an additional contribution to the regular quadrupole interaction. It can be interpreted as the influence of electron penetration into the nuclear volume on the quadrupole interaction.

There is an alternative way to express this same effect: consider the Hamiltonian of Eq. (6.20) up to second order perturbation. Among others, the second order energy expression will contain a cross term between QI and $MS^{(1)}$, which has the same symmetry as the quadrupole interaction (this can easily be seen because the monopole shift is a scalar quantity that does not change the symmetry). Compared to the previous strategy this method has the advantage that the same Hamiltonian is kept, but the disadvantage that second order matrix elements in excited states have to be evaluated. It is technically easier to evaluate a new perturbation in the ground state of the previous perturbation. The underlying physics, however, is the same.

The second order perturbation description has been applied in 1970 by Pyykkö for approximate and non-relativistic calculations in a few test molecules (see also Figure 6.3) [160]. The first order + first order perturbation description has been used in 2003 by Thyssen *et al.* [161] for the case of LiI, albeit in an implicit way that did not clearly showed the twofold application of first order perturbation theory. It will be the method used in the present work as well, not at least

because it leads to a concise analytical formula (Eq. (6.33)). Our derivation was made completely independent from the one by Thyssen, and the observation that both final expressions agree is a strong test of mutual correctness.

6.1.4 Zooming in on E_2

The regular quadrupole interaction and first order quadrupole shift together provide our approximation to E_2 :

$$E_2 = h\nu_Q \approx E_{QI} + E_{QS^{(1)}} = h\nu_{QI} + h\nu_{QS^{(1)}}. \quad (6.27)$$

Both terms consist of a product between a nuclear quantity and an electron quantity. Since this shows to which nuclear and/or electronic properties one gets access by measuring E_2 , we discuss them now. The two relevant nuclear quantities are (see Eqs. (6.22) and (6.25)):

$$\hat{\mathcal{H}}_{QI} \rightarrow eQ = \int \rho(\vec{r})(3z^2 - r^2)d\vec{r} \propto \langle r^2 Y_{20} \rangle \quad (6.28)$$

$$\hat{\mathcal{H}}_{QS^{(1)}} \rightarrow e\tilde{Q} = \int \rho(\vec{r})(3z^2 - r^2)r^2 d\vec{r} \propto \langle r^4 Y_{20} \rangle. \quad (6.29)$$

The quasi quadrupole moment \tilde{Q} has an additional r^2 in the integral compared to the quadrupole moment Q . It is therefore a quantity that bears similarity with the quadrupole moment $\langle r^2 Y_{20} \rangle$ (through the Y_{20} -dependence) as well as with the hexadecapole moment $\langle r^4 Y_{40} \rangle$ (through the r^4 -dependence).

The corresponding electronic quantities are:

$$\hat{\mathcal{H}}_{QI} \rightarrow V_{zz} = \left(\partial_{zz} - \frac{\Delta}{3} \right) v(0) \quad (6.30)$$

$$\hat{\mathcal{H}}_{QS^{(1)}} \rightarrow n_{zz} = -\frac{1}{\epsilon_0} \left(\partial_{zz} - \frac{\Delta}{3} \right) \Delta v(0). \quad (6.31)$$

The integrated quantity (*cf.* Section 6.1.2) V_{zz} is the principal component of the electric field gradient tensor. The point quantity n_{zz} is the main component of the tensor $n_{ij} = (\partial_i \partial_j - \frac{\Delta}{3} \delta_{ij})n(0)$, which has via the Laplacian two derivatives more than the main component of the EFG tensor. It can be shown that n_{zz} is proportional to $\langle Y_{2m}/r^5 \rangle$ and therefore bears similarities with the electric quadrupole field $\langle Y_{2m}/r^3 \rangle$ as well as with the electric hexadecapole field $\langle Y_{4m}/r^5 \rangle$, *cf.* Eq. (6.7).

6.2 Observable consequences

All entries in the (classical) Table 6.1 correspond to an experimentally observable correction to the total energy. The first row lists energy corrections which are a (dot) product of scalar quantities. The leading term after the monopole contribution MI (or E_0^{pn}) is the first order monopole shift $MS^{(1)}$, which experimentally manifests its presence in the well-known isomer and isotope shifts and is known since 1960 [5]. The second order monopole shift $MS^{(2)}$ is only very rarely taken into account. One example where it matters is the case of muonic atoms [162, 163] (atoms where a muon rather than an electron orbits the nucleus). Because a muon is much heavier than an electron, its orbit is much smaller and the overlap with the nuclear charge distribution becomes much larger. This makes the second order monopole shift for muons much larger than it is for electrons⁵.

⁵To exploit the quadrupole shift (see Section 6.6) for muonic atoms, however, is not possible since no such experiments have been published for a couple of decades and the apparatus has been demounted [43].

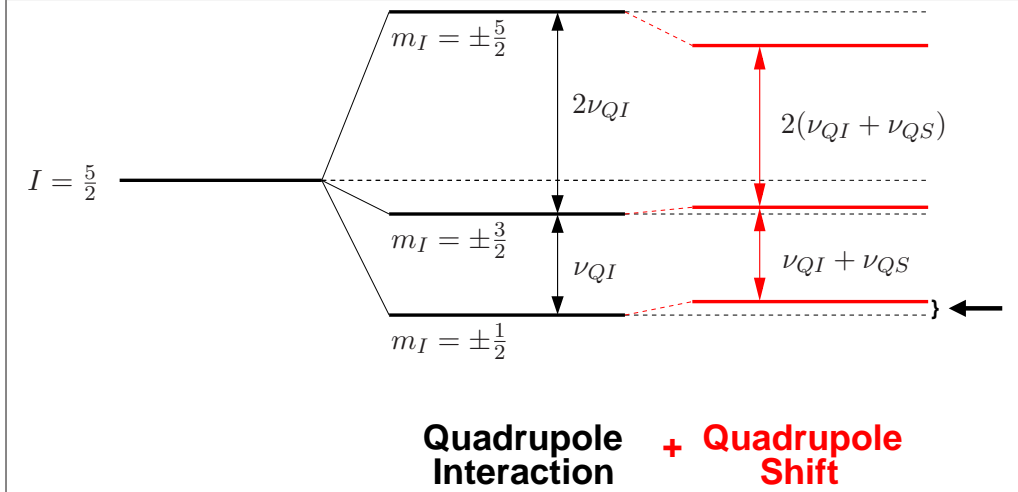


Figure 6.1: Energy levels for a nuclear spin of $I = 5/2$. This picture is not on scale: the shift of the levels as indicated by the arrow is in the most favourable cases (=heavy nuclei) only 0.1 % of ν_{QI} . Note that ν_{QS} has a negative sign, Eq. (6.33).

All entries in the second row of Table 6.1 are dot products between spherical tensors of rank 2. The first one is the quadrupole interaction term QI, which splits according to Eq. (6.22) energy levels that were degenerate under the monopole term. An example for the axially symmetric case ($\eta = 0$) and nuclear spin $I = 5/2$ is given in Figure 6.1. The second term in the second row is the first order quadrupole shift $QS^{(1)}$, which shifts the energy levels that were split by the quadrupole Hamiltonian, but preserves its overall symmetry (Figure 6.1, example for $\eta = \eta_{QS} = 0$ ⁶). The frequencies that set the scale for the quadrupole and quadrupole shift splitting are (still considering $\eta = \eta_{QS} = 0$):

$$\nu_{QI} = \frac{eQV_{zz}}{h} \quad (6.32)$$

$$\nu_{QS} = -\frac{e\tilde{Q}n_{zz}}{14\epsilon_0h}. \quad (6.33)$$

For the sake of shorter notation, we will use from here on ν_{QS} rather than $\nu_{QS^{(1)}}$: we will not consider second order quadrupole shifts and therefore no confusion will be possible. The quadrupole shift does not change the overall symmetry, which in the example of Figure 6.1 means that the 1:2 ratio between the two energy differences is preserved. An experiment that measures such energy differences is not able to distinguish between the contribution by ν_{QI} and the one by ν_{QS} : it measures their sum only. A discussion of the trends in the order of magnitude of the quadrupole shift will be given in Section 6.4.3, and several experimental and computational strategies to exploit the quadrupole shift will be suggested in Sections 6.5 and 6.6.

Finally, the third row in Table 6.1 lists dot products between tensors of rank 4. The leading term here is the hexadecapole interaction for point nuclei. This term can in principle be distinguished experimentally from a quadrupole interaction because its symmetry is different (for instance, in Figure 6.1 the 1:2 ratio would be slightly violated). The HDI appears only for nuclei with $l \geq 2$, since only they have hexadecapole moments ($2I \geq l$ rule for 2^l multipole moments). Whereas the QI is well-known and experimentally accessible since 1939 [3], *e.g.*, by NMR or Molecular Beam

⁶For all spherical tensors of rank two with a three, four or six fold rotation axis it can be shown, that only the $m = 0$ component is nonzero (which is equivalent to $\eta = 0$) [164]. This means, if $\eta = 0$ then also $\eta_{QS} = 0$ and vice versa.

Spectroscopy (see Section 6.5.1), the situation for the HDI is different. Since it was reported for the first time in 1955 [165], it has gone through cycles of confirmatory measurements and refutations. An overview is given in Ref. [161].

6.3 Computational aspects

6.3.1 Formulation in spherical notation

The electronic part n_{zz} of the quadrupole shift will be calculated with a first-principles code and must therefore be translated in spherical form as is common in such codes:

$$n_{zz} = \frac{2}{\sqrt{3}} \sqrt{\frac{15}{4\pi}} \lim_{r \rightarrow 0} \frac{1}{r^2} n_{20}(r). \quad (6.34)$$

The spherical component of the density, $n_{20}(r)$, which enters this expression, is the radial part of the ($l=2, m=0$) component of expansion of the density $n(\vec{r})$ in spherical harmonics:

$$n(\vec{r}) = \sum_{lm} n_{lm}(r) Y_{lm}(\Omega). \quad (6.35)$$

The $l=2$ components are closely related to Cartesian second derivatives, *cf.* Appendix B, which is the reason why they appear in the electric field gradient and related quantities.

6.3.2 Relativity and the role of a finite nucleus

In order to obtain n_{zz} , the limit of $n_{20}(r)/r^2$ for $r \rightarrow 0$ must be calculated, *cf.* Eq. (6.34). It matters whether this is done within a non-relativistic (NREL), a scalar-relativistic (SREL) or a fully relativistic (FREL) framework. In the NREL or FREL formulations (no matter if a point or a finite nucleus is used in the calculation), $n_{2m}(0)$ is exactly zero as it should be due to angular selection rules (see left graph in Figure 6.2). In the SREL approximation, the ($l=2, m$) density, created from two divergent $p_{1/2}$ functions, is to some extent wrongly nonzero at $r=0$. This makes SREL-based methods (with or without a point nucleus) essentially useless for calculating properties that depend on $n_{20}(r \rightarrow 0)$, and we will therefore not consider SREL any further.

For a point nucleus, the ratio of $n_{20}(r)$ and r^2 converges for the limit $r \rightarrow 0$ in a NREL formulation, but not in a FREL formulation (see right graph in Figure 6.2). Since this ratio at $r=0$ is an observable quantity (see Eqs. (6.34) and (6.33)), the divergence for the better method (FREL vs. NREL) cannot be physical. And indeed, the divergence disappears if the approximation of a point nucleus is dropped and a finite nucleus is used in the calculation (right graph in Figure 6.2). Numerical values for this ratio turn out to be much larger for FREL compared to NREL, especially for heavy elements. A finite nucleus was recently implemented in FPLO [2] (version 8.00-31), by which Figure 6.2 was obtained.

The divergence of n_{zz} in a fully relativistic point nucleus calculation might appear to be worrying at first sight. Would that not mean that the quadrupole shift in Eq. (6.33) is infinite? The answer is: no, because the operator corresponding to n_{zz} (Eq. (6.31)) does not have to be evaluated in the ground state for the point nucleus (which is the case that diverges at $r=0$), but in the ground state after having added the two perturbations of Eq. (6.20) that describe the effect of a quadrupolarly deformed finite nucleus (where the divergence is absent). The latter ground state can be constructed from the ground and excited states of the point nucleus case, applying the common expression for the eigenfunctions in first order perturbation. This would, however, lead to rather lengthy expressions and to the inconvenience of having to use excited states. A pragmatic workaround is to use instead the ground state as calculated in a first-principles code that takes a finite nucleus into account. This is hardly an approximation, as it was exactly the purpose of the

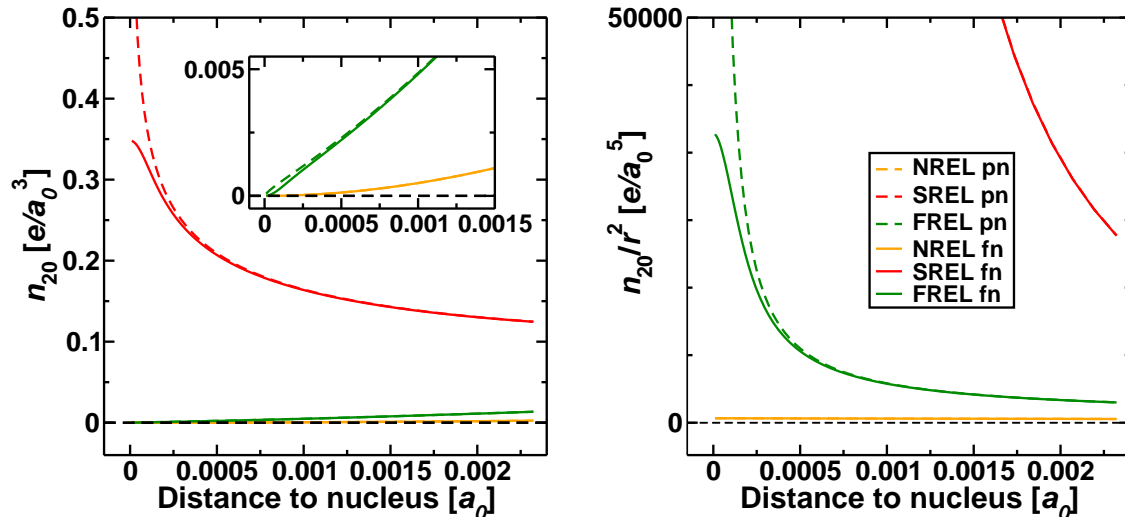


Figure 6.2: The density component $n_{2m}(r)$ (left graph, including inset, which zooms in the region around $r = 0$) and $n_{2m}(r)/r^2$ (right graph) for a point nucleus (pn, dashed lines) and a finite nucleus (fn, full lines) plotted in dependence of r . The different methods are indicated by different colours: non-relativistic (NREL, yellow), scalar relativistic (SREL, red) and full relativistic (FREL, green). This calculation for the hcp metal Re was done by FPLO [2], version 8. All quantities are given in atomic units.

perturbations in Eq. (6.20): to express the presence of a finite nucleus. Therefore, we conclude that the quadrupole shift can be obtained by evaluating the operator for n_{zz} in Eq. (6.31) for the ground state of the atom, molecule or solid calculated fully relativistically and with a finite nucleus taken into account. This quadrupole shift has to be added to the contribution obtained by evaluating the operator for V_{zz} in Eq. (6.30) in the ground state of the point nucleus case (and not in the ground state of the finite nucleus case, as the regular QI is really a perturbation to the point nucleus).

6.3.3 Comparison with the PCNQM method

In the previous sections, we have described a procedure to obtain the influence of electron penetration in a finite nucleus on the quadrupole interaction by two subsequent applications of first order perturbation theory combined with finite nucleus calculations (Eq. (6.33) and Figure 6.2). An alternative to this procedure is the point charge nuclear quadrupole moment method (PCNQM) [166, 167, 168], where the electric field gradient is not obtained as the expectation value of an operator, but is determined from the way how the total energy of the system changes upon inserting an artificial array of point charges around the nucleus. In this method, only total energies are required to obtain the electric field gradient, which makes it particularly useful when the proper operator for the EFG is not explicitly known. The latter is for instance the case as soon as a finite nucleus is used (Eq. (6.22) is valid for a point nucleus only), or for fully relativistic calculations at the 2-component level (a complicated and not yet performed ‘picture change’ transformation would be needed to find the 2-component version of the EFG operator [168].) The difference in EFGs between a ‘finite nucleus + PCNQM’ calculation and a point nucleus calculation (either with the regular EFG operator or with PCNQM) gives the effect of electron penetration in the nucleus. One case where this difference is explicitly calculated is for ^{127}I in LiI (Ref. ([169]) and Figure 6.3). However, with the PCNQM method the quadrupole shift can be obtained only numerically: there is no analytical expression as Eq. (6.33).

Table 6.2: The nuclear radius a , quadrupole moment Q , deformation parameter β_2 and quasi quadrupole moment \tilde{Q} of a few isotopes.

Isotope	a [fm]	Q [fm ²]	β_2	\tilde{Q} [fm ⁴]
⁹ Be	2.84	5.3	0.22	43
⁴⁷ Ti	4.61	30.2	0.09	644
¹¹¹ Cd	5.95	83.0	0.07	2934
¹³⁸ La	6.34	45.0	0.03	1808
¹⁷⁹ Hf	6.84	379.3	0.15	17760
¹⁸⁷ Re	6.93	207.0	0.07	9945
¹⁸⁹ Os	6.95	85.6	0.03	4138

6.4 Numbers and trends

In the present section, we will perform actual calculations with the formalism described in Sections 6.1 and 6.3, and examine trends in the relevant quantities: the nuclear quasi quadrupole moment \tilde{Q} , the electronic point property n_{zz} , and their product: the quadrupole shift ν_{QS} .

6.4.1 Trends in \tilde{Q}

In order to gain more insight in \tilde{Q} , we will consider a phenomenological model⁷ for a nucleus: a deformed sphere, with a radius $R(\theta)$ given by [170]:

$$R(\theta) = a (1 + \beta_2 Y_{20}(\theta) + \beta_4 Y_{40}(\theta) + \dots), \quad (6.36)$$

where a is called the monopole radius and the β_i are deformation parameters. The monopole radius depends in the first place on the atomic mass number A of the nucleus, and the main trend through a lot of experimental values can be summarised by [171]⁸

$$a(A) = 1.489 A^{0.294} \text{ fm}. \quad (6.37)$$

Values for β_2 fall rarely outside the range $[-0.3, +0.3]$ (Ref. [172] in combination with Eq. (6.38)). As β_4 is even smaller and enters only quadratically in the expressions we will need (*cf.* Appendix H.2.2), it can be neglected for our purposes. Keeping only the contributions linear in β_2 , we can now express the quadrupole moment and the quasi quadrupole moment in terms of a and β_2 :

$$eQ \simeq 3\sqrt{\frac{4\pi}{5}} \frac{eZ}{2\pi} \beta_2 a^2 \quad (6.38)$$

$$e\tilde{Q} \simeq a^2 \cdot eQ. \quad (6.39)$$

The term quadratic in β_2 as well as the quadratic β_4 term give corrections to Eqs. (6.38) and (6.39) at the level of a few percent only, while they make the expressions considerably more involved – see Eqs. (H.14) and (H.15) in Appendix H.2.2.

⁷In Appendix H.2.1 a special case of this model is also investigated: an axially symmetric ellipsoid. This simple model gives the same trends as the more realistic nuclear model presented here.

⁸Note, that in Ref. [171], the root-mean-square (RMS) of the nuclear radius is given, while here we use the monopole radius. See Eq. (H.20) in Appendix H.2.3 for details.

Table 6.3: For a few atoms/nuclei that experimentally condense in the hcp crystal structure (except for Pa, bct), this table lists the nuclear properties Q and \tilde{Q} (determined as in Table 6.2), the electronic properties V_{zz} and n_{zz}/ϵ_0 (calculated by FPLO, see text), the quadrupole ν_{QI} and quadrupole shift ν_{QS} frequencies they give rise to (Eqs. (6.32) and (6.33)) (mind the different MHz and kHz units), and the ratio of the latter.

Isotope	I	Q [fm ²]	\tilde{Q} [fm ⁴]	V_{zz} [10 ²¹ V/m ²]	n_{zz}/ϵ_0 [10 ⁴² V/m ⁴]	ν_{QI} [MHz]	ν_{QS} [kHz]	$ \nu_{QS}/\nu_{QI} $
⁹ Be	3/2	5	42	-0.08	-6.07·10 ⁻²	-0.1	10 ⁻⁸	5·10 ⁻⁹
⁴⁷ Ti	5/2	30	644	1.61	3.27·10 ⁺³	11.8	-0.04	3·10 ⁻⁶
⁴⁹ Ti	5/2	25	539	1.61	3.27·10 ⁺³	9.6	-0.04	3·10 ⁻⁶
¹¹¹ Cd	5/2	83	2934	7.48	2.94·10 ⁺⁵	150.0	-14.9	1·10 ⁻⁴
¹⁷⁷ Hf	7/2	337	15652	7.89	1.26·10 ⁺⁶	642.3	-341.4	5·10 ⁻⁴
¹⁷⁹ Hf	9/2	379	17760	7.89	1.26·10 ⁺⁶	723.9	-387.4	5·10 ⁻⁴
¹⁸⁵ Re	5/2	218	10386	-5.51	-1.81·10 ⁺⁶	-290.3	324.9	1·10 ⁻³
¹⁸⁷ Re	5/2	207	9945	-5.51	-1.81·10 ⁺⁶	-275.6	311.1	1·10 ⁻³
¹⁸⁹ Os	3/2	86	4138	-6.65	-2.91·10 ⁺⁶	-137.6	208.1	2·10 ⁻³
²³¹ Pa	3/2	-172	-9357	15.14	8.11·10 ⁺⁶	-629.8	1309.7	2·10 ⁻³

By Eqs. (6.38)-(6.39), one can get a reasonable estimate for \tilde{Q} by inserting the monopole radius from Eq. (6.37) and the experimental quadrupole moment Q (*e.g.*, from Refs. [58, 172, 173]). This way, we obtain values for \tilde{Q} in the order of $10^4 - 10^5$ fm⁴ for heavy elements (Table 6.2). The Eqs. (6.38)-(6.39) show that in order to get a large quasi quadrupole moment \tilde{Q} , the nucleus should be large (a is large) and strongly deformed (Q or β_2 are large). The former implies heavy elements, while the latter is most easily fulfilled for heavy elements as well, see also Appendix H.2.3.

6.4.2 Trends in n_{zz}

In order to get a feeling for the order of the magnitude of the electronic parts of the $\mathcal{O}(2)$ interactions in Table 6.1, we have calculated both V_{zz} (the electronic part of the QI) and n_{zz} (the electronic part of the first order QS) for some hexagonal close-packed (hcp) metals throughout the periodic table. The results are shown in Table 6.3. Both quantities increase with the mass of the element. Compared to V_{zz} , which increases over two orders of magnitude, n_{zz} is much more sensitive to the mass of the element and increases over eight orders of magnitude.

In order to verify to which extent this conclusion obtained from Table 6.3 is valid for other crystal structures than hcp, we investigated two series of purpose-built body-centred tetragonal (bct) crystals with different c/a ratios (0.8 and 1.2), and this for several elements throughout the periodic table. The results are reported in Appendix H.1 and show the same trend as Table 6.3. We conclude that the mass of the element has a larger influence on the magnitude of n_{zz} than the lattice parameters or the crystal structure.

6.4.3 Trends in the quadrupole shift

The frequencies ν_{QI} (for the QI – Eq. (6.32)) and ν_{QS} (for the QS – Eq. (6.33)) for a set of hcp and bct metals are reported in Table 6.3, together with their ratio $|\nu_{QS}/\nu_{QI}|$. For the

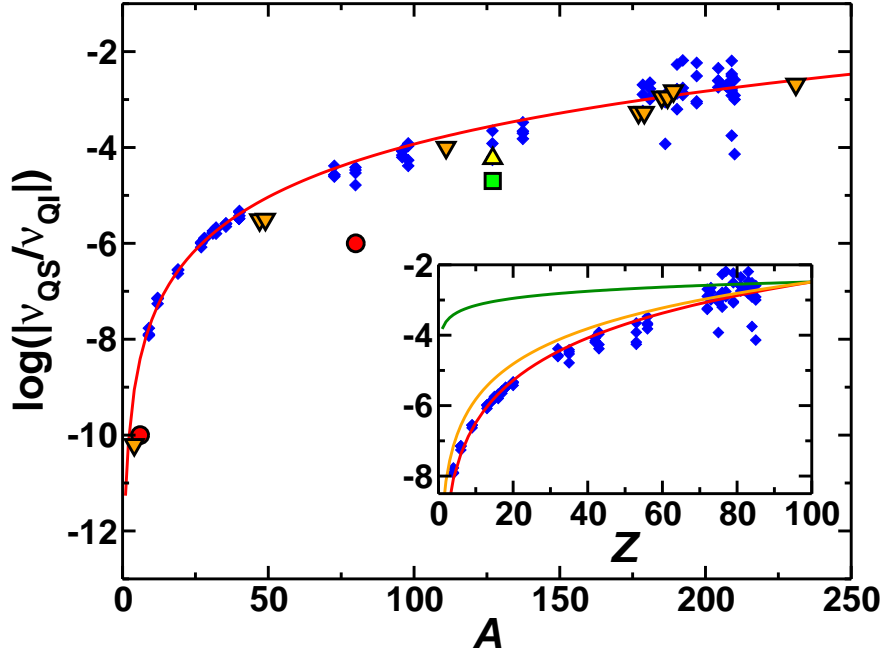


Figure 6.3: The logarithm of the ratio of ν_{QS} and ν_{QI} as a function of the mass number A . Blue diamonds: artificial crystal structures (see text and Appendix H.1), fitted by the red line (Eq. (6.40)). Orange triangles (down): experimental crystal structures (see Table 6.3). The yellow triangle (up) [161], green square [169] and red circles [160] are values from the literature, see text. **Inset:** the same data but now as a function of Z , fit by Eq. (6.41). The nuclear (green) and electronic (orange) contributions of Eq. (6.42) are shown as well, shifted to match in the endpoint.

calculation, experimental lattice parameters were used [50, 174], and n_{zz} and V_{zz} were determined fully relativistically with a finite nucleus for n_{zz} and a point nucleus for V_{zz} (FPLO [2] code, version 8.00-31 using LDA as xc-functional). Q was taken from the literature [58] and \tilde{Q} was determined as explained in Section 6.4.1. The trends of n_{zz} and \tilde{Q} to be larger for heavy elements, cooperate to produce a ν_{QS} of which the relative importance with respect to ν_{QI} is rather smoothly increasing with the atomic number A .

This can be seen more clearly in Figure 6.3, which summarises results for a larger set of 28 elements in different crystal structures (blue diamonds): hcp with $c/a=1.633$ and 0.8 and bct with $c/a=1.2$ and 0.8, always with the experimental volume per atom, *cf.* Appendix H.1. These data can be fit with the simple functions

$$|\nu_{QS}| = 5.46 \cdot 10^{-12} A^{\frac{11}{3}} |\nu_{QI}|, \quad (6.40)$$

$$|\nu_{QS}| = 3.26 \cdot 10^{-11} Z^4 |\nu_{QI}|, \quad (6.41)$$

which are shown in Figure 6.3 (red lines). The orange triangles (down) in Figure 6.3 correspond to the experimental crystal structures from Table 6.3 – they accurately follow the same trend. By taking the ratio of Eqs. (6.33) and (6.32) and by filling out the lowest order expressions for Q and \tilde{Q} (Eq. (6.38)), the following simple analytic analogue for Eqs. (6.40) or (6.41) is obtained:

$$\nu_{QS} = \left(-\frac{1}{14} a^2 \frac{n_{zz}}{\epsilon_0} \frac{1}{V_{zz}} \right) \nu_{QI}. \quad (6.42)$$

Since $a = 1.26 Z^{1/3}$ fm (obtained from the data of Ref. [171] plotted as a function of Z), the nuclear part a^2 scales with $Z^{2/3}$. In order to fulfil the observed Z^4 dependence in Eq. (6.41), the electronic

part should scale with $Z^{10/3}$: $n_{zz}/(\epsilon_0 V_{zz}) = 2.87 \cdot 10^{-10} Z^{10/3} \text{ fm}^{-2}$. These two contributions are shown as the green (nuclear) and orange (electronic) lines in the inset of Figure 6.3. From this picture, it is clear that the electronic term contributes most to the increase of the quadrupole shift with A or Z . From Table 6.3, we see that this is due to the strong increase of n_{zz} .

Eq. (6.41) provides a quick way to estimate the order of magnitude of the quadrupole shift, for any element in any crystal structure, and without the need for a finite nucleus calculation. The only quantity that is required is ν_{QI} , which can be provided by several first-principles codes. As the scatter of the data points for heavier elements shows, such an estimate can be one order of magnitude above or below the actual value. For isotopes with $A > 175$ (*i.e.*, $Z > 60$), the quadrupole shift can reach 0.1-1.0% of the regular quadrupole interaction.

There are a few cases reported in the literature from which QS information can be deduced. These are shown in Figure 6.3 as well. The yellow triangle (up) was calculated by J. Thyssen *et al.* with a method very similar to ours for the single case of the LiI molecule. They found the ratio $|\nu_{QS}/\nu_{QI}|$ for ^{127}I to be $5 \cdot 10^{-5}$. The green square corresponds to ^{127}I in the same LiI molecule, obtained by the PCNQM method by Van Stralen and Visscher [169]. A few estimates for the quadrupole shift obtained by second order perturbation theory were published in 1970 by Pyykkö [160]. Those estimates were given relative to a pseudo quadrupole interaction only (Refs. [175, 176]). After converting these numbers, it turns out that for the LiBr molecule the ratio of ν_{QS} and ν_{QI} is about 10^{-10} for ^6Li and 10^{-6} for ^{81}Br (red circles in Figure 6.3). These numbers follow the same trend as the quadrupole shift in first order perturbation, but are 1-2 orders of magnitude smaller – this might be due to the fact that these were non-relativistic calculations.

6.5 Experimental and computational accuracies

In the previous sections, we have discussed how electron penetration into the nucleus is responsible for an extra contribution to the quadrupole interaction – the quadrupole shift. As shown in Table 6.3 and Figure 6.3, the order of magnitude of the quadrupole shift can reach 0.1 % (and maybe more) of the regular quadrupole interaction. In this section, we will discuss the level of accuracy achievable in condensed matter and molecular quadrupole interaction experiments and calculations and whether this accuracy will be sufficient to be sensitive to the quadrupole shift. This information will be used in Section 6.6 to examine whether it is feasible to use the quadrupole shift to extract additional information from an experimental quadrupole interaction frequency.

6.5.1 Accuracy of quadrupole interaction experiments

Condensed matter experiments

The most common (non-radioactive) methods to determine quadrupole interactions in condensed matter are nuclear quadrupole resonance (NQR) and nuclear magnetic resonance (NMR) spectroscopy, see also Section 3.4. The accuracies of NMR and NQR are comparable: the lowest achievable experimental error bars on ν_Q are about 5 kHz for single-crystals with an axially symmetric EFG ($\eta = 0$) and about 100 kHz for powder samples with a non-axially symmetric EFG ($\eta \neq 0$) [177]. The accuracy is mainly limited by the magnetic dipole-dipole interaction between the nuclei, which broadens the spectrum [44].

There is also a whole family of radioactive methods which can perform the same task. Mössbauer spectroscopy and to a lesser extent perturbed angular correlation (PAC) spectroscopy are the most wide-spread methods of these. In order to get a feeling for the typical accuracy that can be achieved with radioactive methods, we look at the quadrupole interaction at a Cd-site in hcp-Cd. The $I = 5/2$ level in ^{111}Cd is very suitable for PAC spectroscopy, which explains why the

quadrupole interaction for Cd in hcp-Cd has been measured many times [178, 179], often with high statistics and down to very low temperatures [180, 181, 182]. The best available low-temperature value for the quadrupole interaction is 136.0(4) MHz. The 400 kHz error bar on this quantity is considerably larger than the best available NMR/NQR error bars. This is because radioactive methods suffer not only from the same limitations as NMR/NQR, but on top of that have an extra intrinsic inaccuracy due to the line width of the excited nuclear level that is involved.

Molecular experiments

Much better experimental accuracies for quadrupole interactions can be achieved by molecular spectroscopies as molecular beam spectroscopy (MBS) [183, 184, 185, 186]. In molecular spectroscopy, a sparse molecular beam with a known energy distribution is exposed to a known amount of energy at a given frequency, produced for instance by a radio frequency (rf)-field. If the frequency matches with a hyperfine transition in the molecule, the beam absorbs energy. The amount of energy that is present in the beam after passing through the rf-field is recorded. By varying the frequency of the rf-field, a list with all frequencies at which transitions appear is obtained. These can be fit to an appropriate Hamiltonian to determine *e.g.*, the effective nuclear quadrupole coupling constant (NQCC).

As an illustration for the accuracy that can be achieved in this way, we refer to ν_Q of ^{85}Rb in the diatomic molecule RbF, which was determined as -70.7391849(37) MHz [187]: an experimental error bar of 4 Hz on a quantity of 70 MHz, *i.e.*, a relative accuracy of $5 \cdot 10^{-8}$. Further examples of similarly accurate measurements of nuclear quadrupole coupling constants can be found *e.g.*, in the works by Cederberg *et al.* [158, 183, 188, 189, 190].

Sensitivity to the quadrupole shift

In Table 6.3, we see that for heavy nuclei the quadrupole shift contributes typically 0.3 MHz to the total (experimentally accessible) quadrupole interaction, whereof the pure QI is typically 400 MHz. From that table and Figure 6.3 we concluded that due to the Z^4 dependence, the heavier the isotope, the more important the quadrupole shift becomes.

Commonly used NMR/NQR isotopes are *e.g.*, $^{63,65}\text{Cu}$ or ^{75}As due to the high interest in superconductivity, *cf.* Sections 5.4 and 5.5. Also the other elements investigated in Chapter 5: ^{11}B , ^{17}O and $^{69,71}\text{Ga}$ are rather light, and from Figure 6.3 one expects a quadrupole shift of about 10^{-5} to 10^{-4} for the heavier of them. This is outside the best achievable experimental error bars. As the error bars for radioactive methods are larger, the quadrupole shift in those cases will usually drown inside the experimental error bars.

The situation is much better in molecular spectroscopy. As an example, we discuss the results of experimental and theoretical investigations of ^{127}I in the LiI molecule. The total quadrupole frequency (including the QS) was determined by Cederberg *et al.* [158] to be

$$\nu_Q^{exp} = -194.351212(17) \text{ MHz.}$$

As discussed earlier, Thyssen *et al.* [161] calculated the quadrupole shift for the single case of the LiI molecule. For I they obtained

$$\nu_{QI}^{cal} = -169 \text{ MHz} \quad \nu_{QS}^{cal} = 10.0 \text{ kHz.} \quad (6.43)$$

Using the FPLO code with the molecule option, we obtain for I (also using the experimental bond length of 2.391924 Å [191] but contrary to Thyssen *et al.* a full relativistic version in the calculation)

$$\nu_{QI}^{cal} = -166 \text{ MHz} \quad \nu_{QS}^{cal} = 24.9 \text{ kHz.} \quad (6.44)$$

In both cases, V_{zz} was transformed to ν_{QI} using $Q = -0.69$ b [192] and ν_{QS}^{cal} was calculated with $\tilde{Q} = a^2 Q$ using $a = 5$ fm to be consistent with Thyssen [161]. Indeed, we obtain good agreement between the calculated results. For this molecule, the quadrupole shift in the range of 10 kHz is 100 times larger than the experimental error bar in the range of 10 Hz. However, this does not mean that the quadrupole shift itself can be measured in such an experiment: the existence of the quadrupole shift affects the value of the measured quadrupole interaction, but as one cannot ‘switch off’ the quadrupole shift, there is no straightforward way to determine experimentally how much of the total interaction frequency is due to the regular quadrupole interaction and how much due to the quadrupole shift, see also Eq. (6.27).

In Section 6.6, we will ponder on the perspectives for making use of the quadrupole shift to extract more information from a quadrupole interaction experiment. This will crucially depend on the absolute accuracy of first-principles calculations for electric field gradients. Therefore, we will examine first what is the best accuracy which can currently be achieved in EFG calculations.

6.5.2 Accuracy of EFG calculations

Condensed matter calculations

First-principles calculations in solids are commonly done at the level of density functional theory (DFT), or with DFT as a starting point. The level of agreement between a DFT prediction and an experiment depends on the approximation made for the exchange-correlation functional, *cf.* Section 2.2.1. Common exchange-correlation functionals in solid state physics are the local density approximation (LDA) and generalised gradient approximations (GGA’s, in particular the PBE formulation [16]). Strongly correlated systems are adequately treated by LDA+ U functionals, *cf.* Section 2.2.2 and more recently also hybrid functionals [16, 193, 194, 195, 196, 197]. DFT has been used with considerable success to calculate electric field gradients in solids, see for instance, Section 3.5, Chapter 5, and *e.g.*, Refs. [4, 33, 34, 35, 40, 45, 46, 50, 52, 139, 153, 198, 199]. As a rule of thumb, the DFT prediction is within 10% of the experimental value – insofar reliable experimental values for both the quadrupole frequency and the quadrupole moment are known, see Eq. (6.32).

However, even for the same xc-functional and the same numerical and structural input data, the agreement between EFGs obtained from different band structure codes is nowhere near enough to extract useful information for the determination of the quadrupole shift, see for instance, Figure 4.1 in Section 4.2 and Figures 5.4 and 5.10 in Section 5.1.

Furthermore, the entire discussion so far implicitly assumed static molecules or crystals at 0 K without zero-point vibrations. At nonzero temperatures, vibrational states will be populated, and in molecules rotational states as well. These will influence the electric field gradient and therefore the quadrupole interaction. A WIEN2k study of zero-point vibrations for the EFG in hcp-Cd revealed a contribution of 1.6% to the EFG due these vibrations [200].

Molecular calculations

For first-principles calculations on molecules, the choice of available methods is broader. For large molecules, DFT is still the only option, but for sufficiently small molecules much more accurate quantum chemical methods can be afforded. A prominent example is coupled cluster (CC) theory, which is a post-Hartree-Fock method that allows to treat electron correlation. In contrast to DFT, the accuracy of a CC calculation can be systematically improved, as long as computer time allows it. If only ‘single excitations’ are taken into account, one speaks about CCSD. Including also ‘double excitations’ leads to the much more accurate and much more expensive CCSD(T). Adding ‘triple excitations’ in a perturbative way yields the highly accurate CCSD(T)

method, which is presently considered to be the most accurate routinely applicable quantum chemistry method for small to medium sized molecules, see also Ref. [201].

The recent literature [202, 203, 204, 205, 206, 207] shows that CCSD(T) with sufficiently large basis sets and – where needed – with a (semi-)relativistic Hamiltonian, provides highly accurate EFGs for small molecules. It has been claimed [208] that in this way an absolute accuracy with four significant digits can be reached. This is considerably better than the accuracy which DFT can provide for the EFG in solids.

The EFG in small molecules as predicted by DFT using common exchange-correlation functionals has been shown to be rather unreliable [209]. However, a hybrid exchange-correlation functional has been recently proposed – CAMB3LYP – which provides superior consistency for a set of 18 test molecules [209]. This method can be an alternative for molecules containing heavy elements, where fully relativistic CCSD(T) calculations can not yet be performed with full precision.

In molecules, the effect of vibrational and rotational states due to nonzero temperature, can be described with high accuracy using a Dunham treatment [189, 210, 211], and experiments are routinely analysed according to this formalism.

6.5.3 Other small perturbations to the quadrupole interaction

When dealing with a quadrupole-like interaction that is as small as the quadrupole shift, it becomes relevant to take into account similarly small quadrupole-like interactions and perturbations of the quadrupole interaction that have a different origin.

These are the *pseudo quadrupole interaction* and the *isotopologue anomaly*. The former one was discussed by Van Vleck, Rabi, Foley and Ramsey [212, 213, 214] half a century ago and has a magnetic origin. Like the QS, also this interaction consists of a dot product between a nuclear spherical tensor of rank 2 and an electronic spherical tensor of rank 2. The latter one was found by high-precision molecular beam experiments by Cederberg *et al.* and its origin is not yet understood [189, 183].

Given the enormous advances in the possibilities of first-principles calculations since that time, it is worthwhile to discuss these effects shortly, to put them into a general picture and to refer to the original literature. This is done in the appendix of Ref. [175].

6.6 Experimental implications of the quadrupole shift

6.6.1 Determination of Q and \tilde{Q}

The main purpose of measuring quadrupole interactions, is that they serve as a fingerprint for molecules and (defects in) solids. One step further is to use the quadrupole interaction frequency to get access to one of the two objects that determine it: the electric field gradient if the nuclear quadrupole moment is known independently or the nuclear quadrupole moment Q if the electric field gradient is known independently. This has become the preferred procedure to determine nuclear quadrupole moments: a set of measured quadrupole interaction frequencies is plot against a set of calculated electric field gradients. According to

$$\nu_{QI} = Q \frac{eV_{zz}}{h}, \quad (6.45)$$

such a plot should show a linear correlation, provided the errors in experiment as well as in the calculations are sufficiently small. The nuclear quadrupole moment can be obtained from the slope of this linear correlation. Several nuclear quadrupole moments have been determined this way, using solid state as well as molecular experiments and calculations, *e.g.*, [43, 58, 199, 209, 215, 216, 217, 218]. See also Figure 5.6 in Section 5.1. It has been emphasised recently by Thierfelder *et al.* [209] that apart from the correlation coefficient of the linear fit also the fitted

intercept is a strong quality indicator: if it is not really close to zero – which rather often happens to be the case – this indicates a systematic error in the first-principles calculations.

However, the linear fit as described by Eq. (6.45) neglects the contribution by the quadrupole shift. As it was shown in Section 6.1.4, Eq. (6.27), a more accurate⁹ description is given by

$$\nu_Q = \nu_{QI} + \nu_{QS} = Q \frac{eV_{zz}}{h} - \tilde{Q} \frac{en_{zz}}{14\epsilon_0 h}. \quad (6.46)$$

With the experimental accuracies listed in the previous section, it is clear that experimental nuclear quadrupole coupling constants ν_Q for NMR on single-crystals and for MBS on molecules are affected by the quadrupole shift. This means that the experimentally determined value for ν_Q would have a different value (outside the error bar) if the quadrupole shift could be “switched off”. It does not mean, however, that by such an experiment the quadrupole shift itself can be determined: the QS manifests itself as an addition to the regular quadrupole interaction, and is indistinguishable from it. If V_{zz} could be calculated with an arbitrary high precision, the precision of the resulting Q is limited by neglecting ν_{QS} . One could choose not to neglect ν_{QS} , and apply Eq. (6.46) to at least two ν_Q measurements in order to determine simultaneously a more precise value of Q and \tilde{Q} (or Q and a^2). This would be meaningful only in cases where the absolute deviations on the computed V_{zz} and n_{zz} values are small enough to make the uncertainty in ν_{QI} smaller than the value of ν_{QS} . The only hope to realise this is in the case of sufficiently heavy elements, for which, however, it might not yet be feasible to achieve the requested computational accuracy.

6.6.2 Quadrupole moment ratios: the quadrupole anomaly

When it is not possible to know experimentally the value of a quadrupole moment with sufficient accuracy, the next best thing to know are ratios of quadrupole moments for two different isotopes, or for two different isomeric states of the same isotope. As soon as a later experiment succeeds to determine one of the quadrupole moments in the ratio, the other one is known as well.

The ratio Q_1/Q_2 of two quadrupole moments is commonly measured as the ratio $\nu_{Q,1}/\nu_{Q,2}$ of two nuclear quadrupole coupling constants. Indeed, in the absence of a quadrupole shift, both ratios are identical if the two isotopes or isomers are in the same environment and therefore experience the same V_{zz} (Eq. (6.46)). The presence of the quadrupole shift, however, spoils the equality of both ratios. It is straightforward to show that the ratio of quadrupole coupling constants is equal to

$$\frac{\nu_{Q,1}}{\nu_{Q,2}} = \frac{Q_1}{Q_2} (1 + \delta) \quad \text{with} \quad \delta = \frac{n_{zz}}{14\epsilon_0 V_{zz}} (a_2^2 - a_1^2) + O(a_i^4). \quad (6.47)$$

This formulation is strongly reminiscent to the Bohr-Weisskopf effect [219] for magnetic hyperfine interactions, where the ratio between two magnetic hyperfine interaction frequencies for two isotopes/isomers at identical sites is given by

$$\frac{\nu_1}{\nu_2} = \frac{\mu_1}{\mu_2} (1 + \Delta). \quad (6.48)$$

Here μ_1 and μ_2 are the nuclear magnetic moments of the two isotopes/isomers, and Δ is the hyperfine anomaly. The ratio μ_1/μ_2 can be determined from hyperfine experiments on the two free isotopes/isomers in a known externally applied magnetic field. Comparison with the ratio as determined from experiments with the isotopes/isomers incorporated in solids or molecules provides the value for Δ , which can be as large as 2 % for heavy elements like ^{185,187}Re [220].

⁹Note that in contrast to Eq. (6.27), we neglect (even smaller) contribution from higher order here.

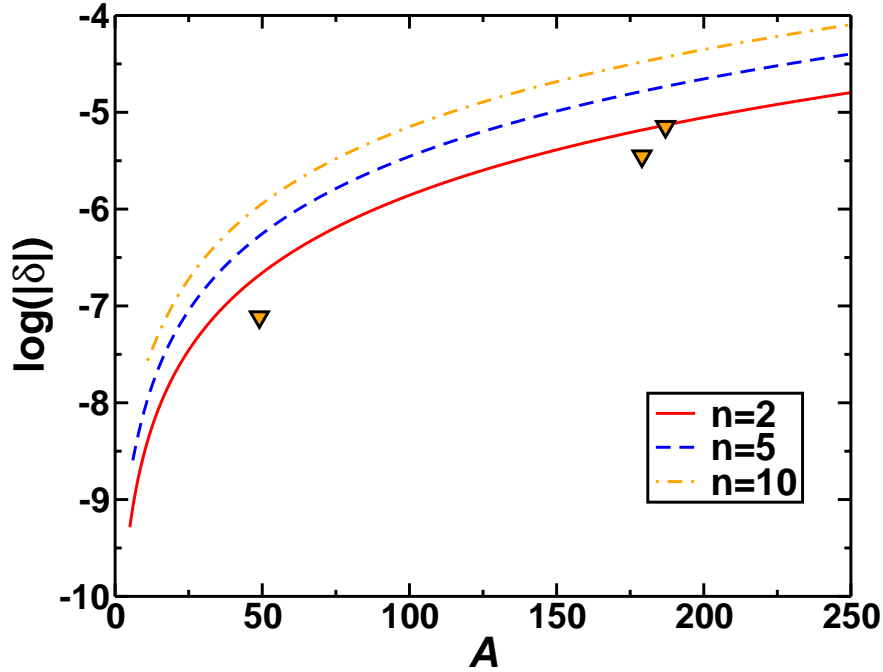


Figure 6.4: The logarithm of the quadrupole anomaly δ as a function of the mass number A , as given by Eq. (6.49). The value of n indicates the mass number difference between the heaviest (A) and lightest ($A - n$) isotope. The curves for $n = 2$ (full red line), $n = 5$ (blue dashed line) and $n = 10$ (yellow dot-dashed line) are shown. For ^{47}Ti , ^{179}Hf and ^{187}Re (all $n = 2$) $\log |\delta|$ can be calculated explicitly from Table 6.3 (orange triangles).

Δ is nonzero because electrons that penetrate the nucleus do not interact with a point nucleus magnetic moment but with the spatial distribution of the magnetic moment over the nuclear volume. This slightly affects the effective hyperfine field. Therefore, the hyperfine anomaly is sensitive to the details of nuclear structure, and can be used to test theoretical nuclear models. In the same way the δ from Eq. (6.47) – which can be called in analogy the quadrupole anomaly – probes details of the nuclear charge distribution by electrons that penetrate into the nuclear volume. From Eq. (6.47), it can be seen that δ is sensitive to the electronic quantities, n_{zz} and V_{zz} , and the difference between the squared monopole radii of the two isotopes/isomers that are involved.

In order to find a general trend and order of magnitude estimate for δ , we combine the analytical function of Eq. (6.42) with the fitted function of Eq. (6.40) and the square of Eq. (6.37) to obtain a numerical approximation for the electronic part $n_{zz}/(14\epsilon_0 V_{zz})$ in Eq. (6.47). By inserting this and the square of Eq. (6.37) for two different isotopes in the definition of δ , the following dependence of $|\delta|$ on the isotope mass number emerges:

$$|\delta(A)| = 5.46 \cdot 10^{-12} A^{3.079} (A^{0.588} - (A - n)^{0.588}). \quad (6.49)$$

This expression estimates the order of magnitude of δ for two isotopes with mass numbers A and $A - n$. Curves for $\log |\delta(A)|$ for $n = 2, 5$ and 10 are shown in Figure 6.4. We observe that the quadrupole anomaly strongly increases with A (or A), due to the increase of n_{zz} . Mass number differences of 10 yield a value for δ that is an order of magnitude larger than mass number differences of 2. For the 3 elements in Table 6.3 for which information for 2 isotopes is provided, Eq. (6.49) can be compared by values obtained by filling out the quantities of Table 6.3 directly into Eq. (6.47). The values are shown by the orange triangles in Figure 6.4 and correspond to the

red fit ($n = 2$). This comparison shows that Eq. (6.49) is within one order of magnitude indeed a good estimate for δ . The experimentally achievable accuracy of quadrupole moment ratios is of the order of 10^{-6} (see Table 6.4). This means that for many isotopes the presence of δ affects the experimental values.

Unfortunately, whereas in Bohr-Weisskopf experiments the unperturbed ratio μ_1/μ_2 can be determined from experiments on free nuclei in an externally applied magnetic field, this is not possible for quadrupole interaction measurements: electric field gradients that can be generated by man-made devices are too small to allow meaningful quadrupole interaction measurements [221]. Therefore, a slightly different method has to be used. One could perform 4 quadrupole interaction experiments on two isotopes (' m ' and ' n ') of the same element, each of them being part of two different molecules (' a ' and ' b '). For instance, mX in mXA and mXB molecules, and nX in nXA and nXB molecules. This yields four experimental frequencies ν_{ma} , ν_{na} , ν_{mb} and ν_{nb} . By applying Eq. (6.47) twice, it can be seen that the NQCC ratios are not necessarily identical to each other for the two different molecules, with the difference being determined by n_{zz}/V_{zz} :

$$\frac{\nu_{ma}}{\nu_{na}} = \frac{Q_m}{Q_n} \left(1 + \frac{n_{zz}^a}{14\epsilon_0 V_{zz}^a} (a_n^2 - a_m^2) \right) \quad (6.50)$$

$$\frac{\nu_{mb}}{\nu_{nb}} = \frac{Q_m}{Q_n} \left(1 + \frac{n_{zz}^b}{14\epsilon_0 V_{zz}^b} (a_n^2 - a_m^2) \right). \quad (6.51)$$

As long as the quadrupole shift ($\propto n_{zz}$) does not play a significant role, the two experimental frequency ratios at the left-hand side are within their error bars identical to each other. If, however, the quadrupole shift would be large enough, these two experimental frequency ratios would differ from each other. This is a completely experimental procedure to detect the presence of the quadrupole shift effect. Table 6.4 lists a collection of experimental NQCC-ratios in diatomic molecules determined for three such sets of 4 experiments, which gives an impression of the experimental accuracy that can be achieved. The estimated order of magnitude for $|\delta|$ (Eq. (6.49)) is given too. For none of these cases, δ is expected to be large enough to affect the experimental ratios. Table 6.4 combined with Figure 6.4 suggests that if the best experimental accuracies of 10^{-6} can be achieved for isotopes with $A \geq 150$, then the influence of δ could be observed. The heavier the element and the larger the size-differences between the two isotopes, the more likely large δ -values are. Interestingly enough, the quadrupole coupling constant ratios for the two K isotopes in the KF and KI molecules differ from each other in the 4th digit, and this difference is an order of magnitude larger than the experimental error bars. Given the estimate for δ , the quadrupole shift is expected to give an effect in the 7th digit at best. It is therefore unlikely that this set of K-experiments represents an experimental observation of the quadrupole shift (it could be due to one of the other effects discussed in the appendix of Ref. [175], or due to an experimental problem). Nevertheless, it would be interesting to perform similar experiments with the same accuracy for heavier elements, where δ is expected to be larger.

One step further is to solve the system of the two equations (6.50) and (6.51) for the unknown quantities Q_m/Q_n and $(a_n^2 - a_m^2)$:

$$\frac{Q_m}{Q_n} = \frac{\frac{\nu_{mb}}{\nu_{nb}} \frac{n_{zz}^a}{14\epsilon_0 V_{zz}^a} - \frac{\nu_{ma}}{\nu_{na}} \frac{n_{zz}^b}{14\epsilon_0 V_{zz}^b}}{\frac{n_{zz}^a}{14\epsilon_0 V_{zz}^a} - \frac{n_{zz}^b}{14\epsilon_0 V_{zz}^b}} \quad (6.52)$$

$$a_n^2 - a_m^2 = \frac{\frac{\nu_{ma}}{\nu_{na}} - \frac{\nu_{mb}}{\nu_{nb}}}{\frac{\nu_{mb}}{\nu_{nb}} \frac{n_{zz}^a}{14\epsilon_0 V_{zz}^a} - \frac{\nu_{ma}}{\nu_{na}} \frac{n_{zz}^b}{14\epsilon_0 V_{zz}^b}}. \quad (6.53)$$

All quantities at the right-hand side of these equations can either be measured or calculated, such that the quantities at the left-hand side are effectively determined by a combination of experiment

Table 6.4: Ratios of experimental quadrupole coupling constants for two different isotopes in two different diatomic molecules, collected from the literature. Only cases where the error bar on this ratio has been determined directly from the fit to the experimental data are reported (this error bar can be slightly different from what one would obtain using the error bars on the individual frequencies, see the discussion in Ref. [187]). The experimental value of the EFG (in $10^{21}\text{V}/\text{m}^2$) and the estimated value of δ (Eq. (6.49)) are given as well.

Molecules	Isotopes	ν_{na}/ν_{ma}	V_{zz}^{exp}	$ \delta $	Ref.
${}^6\text{Li}^{19}\text{F}$, ${}^7\text{Li}^{19}\text{F}$	${}^6\text{Li}/{}^7\text{Li}$	0.020161 ± 0.000013	-0.44	$5.9 \cdot 10^{-10}$	[190]
${}^6\text{Li}^{127}\text{I}$, ${}^7\text{Li}^{127}\text{I}$	${}^6\text{Li}/{}^7\text{Li}$	0.02028 ± 0.00014	-0.18		[189]
${}^{41}\text{K}^{19}\text{F}$, ${}^{39}\text{K}^{19}\text{F}$	${}^{41}\text{K}/{}^{39}\text{K}$	1.217699 ± 0.000055	-5.6	$1.3 \cdot 10^{-7}$	[222]
${}^{41}\text{K}^{127}\text{I}$, ${}^{39}\text{K}^{127}\text{I}$	${}^{41}\text{K}/{}^{39}\text{K}$	1.2174935 ± 0.0000099	-3.0		[183]
${}^{87}\text{Rb}^{19}\text{F}$, ${}^{85}\text{Rb}^{19}\text{F}$	${}^{87}\text{Rb}/{}^{85}\text{Rb}$	0.4838301 ± 0.0000018	-10.7	$9.6 \cdot 10^{-7}$	[187]
${}^{87}\text{Rb}^{35}\text{Cl}$, ${}^{85}\text{Rb}^{35}\text{Cl}$	${}^{87}\text{Rb}/{}^{85}\text{Rb}$	0.483837 ± 0.000022	-8.2		[188]

and theory. Clearly, this is a game with very small numbers. The difference between the two frequency ratios in the numerator of Eq. (6.53) is of the same order of magnitude as the δ in Eq. (6.47): 10^{-5} for heavy elements. The same considerations as in Section 6.6.1 apply here: an extreme accuracy in experiments as well as in calculations is needed in order to get to a reliable conclusion. Furthermore, the procedure as described here can be disturbed by the presence of a few other small quadrupole-like effects that are discussed in Section 6.5.3 and Ref. [175].

6.7 Summary and conclusions

In this chapter, we described how electron penetration in the nuclear volume leads to the quadrupole shift: a small perturbation of the regular quadrupole interaction. The quadrupole shift is described by the quadrupole shift Hamiltonian, which has the same symmetry as the regular quadrupole Hamiltonian. It contains likewise a nuclear and an electronic quantity, denoted by the quasi quadrupole moment \tilde{Q} and the quasi quadrupole field n_{zz} , respectively. These two quantities have the same symmetry as the nuclear quadrupole moment Q and the electric field gradient (quadrupole field) V_{zz} from the quadrupole interaction but the same dimension as the nuclear hexadecapole moment H and the electric hexadecapole field V_{zzzz} from the hexadecapole interaction. Hence, the quadrupole shift contains information on other aspects of the nuclear shape than given by the nuclear quadrupole moment or the hexadecapole moment.

An explicit expression for the quadrupole shift that can be implemented in a band structure code was derived, and DFT calculations were performed for a set of crystalline materials. It was shown that meaningful numerical values for the quadrupole shift can be obtained only for fully relativistic calculations that take a finite nucleus into account. Therefore, the quadrupole shift is one of the few cases where the commonly used scalar-relativistic approximation is definitely insufficient.

The quadrupole shift is a small effect. However, its relevance increases with increasing mass of the element under consideration. Its order of magnitude appears to be related in the first place to the atomic number Z of the element under consideration, and to a lesser extent to the crystal structure. This is predominantly due to the way how n_{zz} depends on Z . The quadrupole shift

is orders of magnitude smaller than the regular quadrupole interaction for most elements. For heavy $5d$ transition metals like Re or Os, the quadrupole shift interactions can reach 0.1 % of the quadrupole interaction.

We have pointed out how the quadrupole shift can play a role in a more accurate determination of quadrupole moments and quadrupole moment ratios. The comparison of two accurately measured quadrupole coupling constant ratios provides a purely experimental way to observe the presence of the quadrupole shift. For suitable cases, the required experimental accuracy can be reached by *e.g.*, molecular beam spectroscopy. With further advances in the absolute accuracy of first-principles calculations for n_{zz} and V_{zz} , awareness of the existence of the quadrupole shift will help to extract more precise nuclear information from quadrupole coupling experiments.

Suggestions for further work are at the conceptual, computational as well as on the experimental level. Conceptual: it remains to be understood which features of the electron density are responsible for the observed Z -dependence of n_{zz} and for the dependence of n_{zz} for a given element on the crystal structure. Understanding those mechanisms would help to single out situations where the quadrupole shift is maximised. Computational: in the present work, only DFT calculations for solids were performed, whereas the most accurate experiments are available for molecules. DFT for molecules is not likely to provide very accurate results, but quantum chemical calculations can do much better in this respect. It would be interesting to examine for instance the value of the quadrupole shift for heavy elements in a set of molecules. Experimental: sets of 4 quadrupole coupling experiments as in Table 6.4, done for heavy elements and with high accuracy, provide a way to observe the presence of the quadrupole shift experimentally. It would be most efficient to make a computational study first of those molecules that are experimentally most easily accessible, to identify the ones in which a large quadrupole shift is most likely.

7 Summary and outlook

In this work, we focused on the electric field gradient as a valuable tool for studying current questions in solid state physics and chemistry. The EFG reflects local structural symmetry properties of the charge distribution surrounding a nucleus and is highly sensitive to structural parameters and to disorder. Hence, the evaluation of the EFG can provide valuable insight into chemical bonding and structural details. The EFG can be obtained from experiments via the quadrupole interaction and from first-principles band structure calculations. In order to calculate the corresponding EFG from a measured quadrupole frequency, accurate knowledge of the nuclear quadrupole moment is a prerequisite. Precise values for quadrupole moments are, however, not always known.

One goal of this work was the implementation of an EFG module within the full-potential local-orbital minimum-basis scheme FPLO. The FPLO code is numerically very efficient and its local-orbital scheme allows an easy analysis of the different contributions to the EFG. We showed that EFGs calculated with the newly implemented EFG module are in good agreement not only with EFGs from other band structure codes, but also with EFGs determined experimentally.

The newly implemented EFG module was applied to different classes of compounds in order to exploit and investigate different aspects of the EFG. Simultaneously, the EFGs for several calculated compounds were determined experimentally by NMR spectroscopists. This close collaboration enabled the comparison of the calculated EFGs with the experimental observations, which made it possible to extract more physical and chemical information regarding structural relaxation, distortion, the chemical bond or the relevance of electron correlation.

The first combined study focused on binary gallides. A large discrepancy between the measured and calculated EFG for Ga lead to a reassignment of the crystal structure type for SrGa₂. According to the calculations, puckered instead of planar Ga layers are energetically favourable in agreement with the single-crystal X-ray diffraction data. In order to get insight into the chemical bond, the EFGs of several di- and tetragallides were analysed: the EFG of Ga is mainly due to an anisotropic electron charge distribution caused by the Ga 4*p* electrons, suggesting that these electrons are the key for the flexibility of the Ga atoms with respect to the chemical bonding.

Next, we investigated aluminium diboride, where recent experiments resulted in a non-stoichiometric composition with vacancies on the Al site under ambient conditions. This lead to the question whether the origin of the vacancies is intrinsic or due to sample processing. Our electronic structure calculations yield a composition of about Al_{0.9}B₂, which is in good agreement with the experimental findings. The EFG calculated for the defect structure agrees well with the experimental value and is another evidence for the reliability of the calculations. Our calculations provide strong evidence that the Al defects in Al_{0.9}B₂ are intrinsic and can be understood from the the interplay of the occupation of the bonding boron σ states and the Al states.

Due to screening, the off-site contribution to the EFG is usually very small in metals. In order to study the influence of the off-site EFG, we calculated the EFGs of oxygen in the weakly correlated oxides BaTiO₃ and SrTiO₃, which are often described as ionic perovskites. The calculated large off-site EFG is almost constant under lattice expansion. Surprisingly, the on-site EFG, caused by an anisotropic oxygen *p* density, increases strongly with lattice expansion. This behaviour can not be understood within ionic models but with an extended *p-d* model Hamiltonian. Hence, a pure ionic description for these materials is not sufficient. The increasing anisotropy of the *p* shell is expected to be common to all *d* metal-oxygen bonds and should be taken into account in the interpretation of the relevant experiments.

In order to describe the orbital polarisation for the calculation of the EFG in strongly correlated systems in a reasonable agreement with the experiment, the explicit inclusion of the Coulomb repulsion U beyond the LDA is necessary. The parameter U is not known and usually determined from comparing measured and calculated physical properties. We demonstrated that there is a basically constant shift in the absolute values for U , whether U was determined from the EFG or the exchange integral J . This code independent shift is assigned to the very different time scales of the underlying mechanism of these two properties. Since the shift in U is constant, the EFG provides an experimentally easy and unambiguously accessible property to obtain values for the Coulomb parameter U that also allow for a reliable calculation of the related exchange J .

Finally, we applied our approach to the recently discovered iron arsenide systems $A\text{Fe}_2\text{As}_2$ and $R\text{FeAsO}$, where the mechanism of superconductivity is still under heavy discussion. The description of the Fe-As interaction in the context of the present stage of DFT is difficult. We find that the EFG is highly sensitive to the As z position and pressure, whereas the effect of electron doping is much smaller. While the calculated and measured EFGs of the undoped compounds agree, there is a discrepancy in the trend for the calculated and measured EFGs of the doped systems. Our findings emphasise the crucial importance of a correct description of the Fe-As interaction for the physical properties of the iron pnictides.

In the last part of this work, contributions to the quadrupole interaction that go beyond the EFG were discussed. Such corrections arise for any multipole order of the hyperfine interactions, and are due to electron penetration into the nucleus. The best known of these corrections is the monopole correction which leads to the isomer shift. A similar correction to the quadrupole interaction, coined here the “quadrupole shift” was examined in detail. The quadrupole shift has the same symmetry as the regular quadrupole interaction. A formalism to calculate the quadrupole shift was developed and it was shown that the quadrupole shift is much smaller than the pure quadrupole interaction. Its effect is too small to be observable by the present experimental methods that are used to determine quadrupole interactions in solids. However, its relevance increases with the fourth power of the nuclear charge Z and is within reach in molecular spectroscopy for heavy elements. In combination with the high accuracy that quantum chemical calculations can achieve for quadrupole and quadrupole shift interactions in small molecules, these measurements could lead to more accurate determinations of nuclear quadrupole moments and their ratios.

The chemical shift and the Knight shift are other effects that contain valuable information about certain aspects of the solid. Both shifts arise from a magnetic coupling of the electrons to the nucleus due to a magnetic field. Whereas the implementation of the EFG is well established and available in several full-potential band structure codes, the situation is very different for these two shifts. While the chemical shift can be calculated within the pseudo potential code Castep [223, 224], the implementation of the Knight shift for metallic systems is still in its early stages [225]. Future work should focus on the implementation of these two relevant shifts, since the combination of NMR experiments with quantum mechanical calculations will eventually provide further deep insight into the fundamental properties of solids.

A Nuclear multipole moments

This appendix shows the derivation of the (electric) nuclear multipole moments in Cartesian notation. Furthermore, the definition in spherical notation is presented. The connection between Cartesian and spherical form is given explicitly for the quadrupole moment.

The Cartesian nuclear multipole moments are obtained from the Taylor expansion of

$$\begin{aligned} \frac{1}{|\vec{r} - \vec{r}'|} &= \frac{1}{r} + \sum_{i=1}^3 \frac{x_i x'_i}{r^3} + \frac{1}{2!} \sum_{i,j=1}^3 \frac{x_i x_j \cdot (3x'_i x'_j - r'^2 \delta_{ij})}{r^5} \\ &+ \frac{1}{3!} \sum_{i,j,k=1}^3 \frac{x_i x_j x_k \cdot 3(5x'_i x'_j x'_k - r'^2(x'_i \delta_{jk} + x'_j \delta_{ik} + x'_k \delta_{ij}))}{r^7} \\ &+ \frac{1}{4!} \sum_{i,j,k,l=1}^3 \frac{x_i x_j x_k x_l \cdot 3 \cdot 5(7x'_i x'_j x'_k x'_l - f(x_i, x_j, x_k, x_l))}{r^9} + \mathcal{O}(5) \end{aligned} \quad (\text{A.1})$$

with

$$\begin{aligned} f(x_i, x_j, x_k, x_l) &= r^2 [x_i x_j \delta_{kl} + x_i x_k \delta_{jl} + x_i x_l \delta_{kj} + x_j x_k \delta_{il} + x_j x_l \delta_{ik} + x_k x_l \delta_{ij}] \\ &- \frac{r^4}{5} [\delta_{ij} \delta_{kl} + \delta_{ik} \delta_{jl} + \delta_{il} \delta_{jk}]. \end{aligned} \quad (\text{A.2})$$

Inserting Eq. (A.1) in the potential of the nuclear charge density $\rho(\vec{r})$

$$\phi(\vec{r}) = \int \frac{\rho(\vec{r}')}{|\vec{r} - \vec{r}'|} d^3 r' \quad (\text{A.3})$$

yields the potential as multipole expansion, see *e.g.*, [226] (only up to second order)

$$\begin{aligned} V(\vec{r}) &= \frac{Q}{r} + \sum_{i=1}^3 \frac{x_i Q_i}{r^3} + \frac{1}{2!} \sum_{i,j=1}^3 \frac{x_i x_j Q_{ij}}{r^5} + \frac{1}{3!} \sum_{i,j,k=1}^3 \frac{x_i x_j x_k Q_{ijk}}{r^7} \\ &+ \frac{1}{4!} \sum_{i,j,k,l=1}^3 \frac{x_i x_j x_k x_l Q_{ijkl}}{r^9} + \mathcal{O}(5). \end{aligned} \quad (\text{A.4})$$

The Cartesian multipole moments are

$$\text{monopole :} \quad Q = \int \rho(\vec{r}) d^3 r \quad (\text{A.5})$$

$$\text{dipole :} \quad Q_i = \int x_i \rho(\vec{r}) d^3 r \quad (\text{A.6})$$

$$\text{quadrupole :} \quad Q_{ij} = \int (3x_i x_j - r^2 \delta_{ij}) \rho(\vec{r}) d^3 r \quad (\text{A.7})$$

$$\text{octupole :} \quad Q_{ijk} = \int 3 \left(5x_i x_j x_k - r^2 (x_i \delta_{jk} + x_j \delta_{ik} + x_k \delta_{ij}) \right) \rho(\vec{r}) d^3 r \quad (\text{A.8})$$

$$\text{hexadecapole :} \quad Q_{ijkl} = \int 3 \cdot 5 (7x_i x_j x_k x_l - f(x_i, x_j, x_k, x_l)) \rho(\vec{r}) d^3 r. \quad (\text{A.9})$$

They contain one, three, five, seven and nine degrees of freedom. For instance, the quadrupole moment is reduced from nine to five degrees of freedom due to symmetry $Q_{ij} = Q_{ji}$ and tracelessness $\sum_i Q_{ii} = 0$. Similar conditions are fulfilled for the octupole and hexadecapole moment.

Alternatively, one can also chose the spherical notation for the multipole expansion. The spherical expansion has the advantage that the higher order multipole moments are less unwieldy

$$\text{monopole :} \quad Q_0 = \sqrt{4\pi} \int \rho(\vec{r}) Y_{00} d^3r \quad (\text{A.10})$$

$$\text{dipole :} \quad Q_{1m} = \sqrt{\frac{4\pi}{3}} \int r \rho(\vec{r}) Y_{1m}(\Omega) d^3r \quad (\text{A.11})$$

$$\text{quadrupole :} \quad Q_{2m} = \sqrt{\frac{4\pi}{3 \cdot 5}} \int r^2 \rho(\vec{r}) Y_{2m}(\Omega) d^3r \quad (\text{A.12})$$

$$\text{octupole :} \quad Q_{3m} = \sqrt{\frac{4\pi}{3 \cdot 5 \cdot 7}} \int r^3 \rho(\vec{r}) Y_{3m}(\Omega) d^3r \quad (\text{A.13})$$

$$\text{hexadecapole :} \quad Q_{4m} = \sqrt{\frac{4\pi}{3 \cdot 5 \cdot 7 \cdot 9}} \int r^4 \rho(\vec{r}) Y_{4m}(\Omega) d^3r. \quad (\text{A.14})$$

Or in a general form

$$Q_{lm} = \sqrt{\frac{4\pi}{2l+1}} \int r^l \rho_n(\vec{r}) Y_{lm}(\Omega) d\vec{r}. \quad (\text{A.15})$$

Translating the Cartesian quadrupole moment Eq. (A.7) into spherical notation Eq. (A.12) using real spherical harmonics (see below) gives

$$Q_{ij} = 3 \cdot \begin{pmatrix} Q_{22} - \frac{1}{\sqrt{3}} Q_{20} & Q_{2,-2} & Q_{21} \\ Q_{2,-2} & -Q_{22} - \frac{1}{\sqrt{3}} Q_{20} & Q_{2,-1} \\ Q_{21} & Q_{2,-1} & \frac{2}{\sqrt{3}} Q_{20} \end{pmatrix}. \quad (\text{A.16})$$

Real spherical harmonics for $l = 0, 1$ and 2 :

$$\begin{array}{ll} Y_{00} = \frac{1}{\sqrt{4\pi}}, & Y_{00} = \frac{1}{\sqrt{4\pi}}, \\ Y_{1,-1} = \sqrt{\frac{3}{4\pi}} \sin \theta \sin \varphi, & rY_{1,-1} = \sqrt{\frac{3}{4\pi}} y, \\ Y_{10} = \sqrt{\frac{3}{4\pi}} \cos \theta, & rY_{10} = \sqrt{\frac{3}{4\pi}} z, \\ Y_{11} = \sqrt{\frac{3}{4\pi}} \sin \theta \cos \varphi, & rY_{11} = \sqrt{\frac{3}{4\pi}} x, \\ Y_{2,-2} = \sqrt{\frac{15}{4\pi}} \sin^2 \theta \sin \varphi \cos \varphi, & r^2 Y_{2,-2} = \sqrt{\frac{15}{4\pi}} xy, \\ Y_{2,-1} = \sqrt{\frac{15}{4\pi}} \sin \theta \cos \theta \sin \varphi, & r^2 Y_{2,-1} = \sqrt{\frac{15}{4\pi}} yz, \\ Y_{20} = \sqrt{\frac{5}{4\pi}} \frac{1}{2} (2 \cos^2 \theta - \sin^2 \theta), & r^2 Y_{20} = \sqrt{\frac{5}{4\pi}} \frac{1}{2} (3z^2 - r^2), \\ Y_{21} = \sqrt{\frac{15}{4\pi}} \sin \theta \cos \theta \cos \varphi, & r^2 Y_{21} = \sqrt{\frac{15}{4\pi}} xz, \\ Y_{22} = \sqrt{\frac{15}{4\pi}} \frac{1}{2} \sin^2 \theta (2 \cos^2 \varphi - 1), & r^2 Y_{22} = \sqrt{\frac{15}{4\pi}} \frac{1}{2} (x^2 - y^2). \end{array}$$

B Spherical notation of the EFG tensor

The goal of this appendix is to find the relation between the Cartesian EFG tensor Eq. (3.1) and the spherical EFG tensor, which is already given by Eq. (3.2). Here, we want to show how this equation is obtained, and why the Cartesian EFG tensor is defined with δ functions as shown in the definition Eq. (3.1) and not simply as $V_{ij} = \frac{\partial^2 v(0)}{\partial_i \partial_j}$.

The band structure codes use a spherical notation, where a function, like the electronic potential $v(\vec{r})$, is given by an expansion of radial functions and spherical harmonics (around the origin):

$$v(\vec{r}) = \sum_{lm} v_{lm}(r) Y_{lm}(\hat{r}), \quad \text{with} \quad v_{lm}(r) = \int v(\vec{r}) Y_{lm}(\hat{r}) d\Omega.$$

In order to calculate the Cartesian components V_{ij} of the EFG tensor Eq. (3.1) from the radial function $v_{lm}(r)$, we need to know their connection. Therefore we compare a Taylor expansion and a spherical expansion of a 3D function $f(\vec{r})$ around the origin:

$$f(\vec{r}) = \sum_{j=0}^{\infty} \frac{1}{j!} (\vec{r} \cdot \vec{\nabla}_{\vec{r}'})^j f(\vec{r}') \Big|_{\vec{r}'=0} \quad (\text{B.1})$$

$$f(\vec{r}) = \sum_{lm} f_{lm}(r) Y_{lm}(\hat{r}) = \sum_{lm} \left(a_{lm} + b_{lm} r + \frac{1}{2} c_{lm} r^2 + \mathcal{O}(r^3) \right) Y_{lm}(\hat{r}). \quad (\text{B.2})$$

Now we substitute the Cartesian variables x_i from the Taylor series Eq. (B.1) with real spherical harmonics (see page 112)

$$\begin{aligned} f(\vec{r}) &= f(0) + \sum_{i=1}^3 \frac{\partial f(x_i)}{\partial x_i} \Big|_{x_i=0} \cdot x_i + \frac{1}{2} \sum_{i,j=1}^3 \frac{\partial^2 f(x_i, x_j)}{\partial x_i \partial x_j} \Big|_{x_i=x_j=0} \cdot x_i x_j + \mathcal{O}(r^3) \\ &= \sqrt{4\pi} f Y_{00} + \sqrt{\frac{4\pi}{3}} \left[Y_{11} f_x + Y_{1,-1} f_y + Y_{10} f_z \right] \cdot r + \frac{\sqrt{4\pi}}{2 \cdot 3} Y_{00} \left[f_{xx} + f_{yy} + f_{zz} \right] \cdot r^2 \\ &\quad + \frac{1}{2} \sqrt{\frac{4\pi}{15}} \left[\left(Y_{22} - \frac{1}{\sqrt{3}} Y_{20} \right) f_{xx} - \left(Y_{22} + \frac{1}{\sqrt{3}} Y_{20} \right) f_{yy} + \frac{2}{\sqrt{3}} Y_{20} f_{zz} \right] r^2 \\ &\quad + \frac{1}{2} \sqrt{\frac{4\pi}{15}} \left[2Y_{2,-2} f_{xy} + 2Y_{2,-1} f_{yz} + 2Y_{2,1} f_{zx} \right] r^2 + \mathcal{O}(r^3). \end{aligned} \quad (\text{B.3})$$

In this notation *e.g.*, f_{xy} means that f is derived with respect to x and y (second partial derivatives commute) and then \vec{r} is set to zero. Furthermore, all Y_{lm} depend on \hat{r} , which is omitted in the notation for convenience. By comparing the different orders of r from the spherical expansion Eq. (B.2) and the modified Taylor expansion Eq. (B.3), we obtain the coefficients a_{lm} , b_{lm} and c_{lm} .

Zeroth order:

$$\sum_{lm} a_{lm} Y_{lm} \stackrel{!}{=} \sqrt{4\pi} f Y_{00} \quad \Rightarrow \quad a_{00} = \sqrt{4\pi} f(0).$$

With $f_{00} = a_{00} + r b_{00} + \dots = a_{00}$, the connection between spherical and Cartesian notation is

$$f(0) = \frac{1}{\sqrt{4\pi}} f_{00}(0). \quad (\text{B.4})$$

First order:

$$\sum_{lm} b_{lm} Y_{lm} \stackrel{!}{=} \sqrt{\frac{4\pi}{3}} [Y_{11} f_x + Y_{1,-1} f_y + Y_{10} f_z] \Rightarrow (b_{1,-1}, b_{10}, b_{1,1}) = \sqrt{\frac{4\pi}{3}} (f_y, f_z, f_x).$$

Using $f_{1m} = a_{1m} + r b_{1m}$ we obtain

$$(b_{1,-1}, b_{10}, b_{1,1}) = \frac{1}{r} (f_{1,-1}, f_{10}, f_{1,1}) = \sqrt{\frac{4\pi}{3}} (f_y, f_z, f_x).$$

Here the connection between spherical and Cartesian notation is

$$\begin{pmatrix} f_x(0) \\ f_y(0) \\ f_z(0) \end{pmatrix} = \sqrt{\frac{3}{4\pi}} \lim_{r \rightarrow 0} \frac{1}{r} \begin{pmatrix} f_{11}(r) \\ f_{1,-1}(r) \\ f_{10}(r) \end{pmatrix}. \quad (\text{B.5})$$

Second order:

$$\begin{aligned} \sum_{lm} c_{lm} Y_{lm} &\stackrel{!}{=} \frac{\sqrt{4\pi}}{3} Y_{00} [f_{xx} + f_{yy} + f_{zz}] + \sqrt{\frac{4\pi}{15}} [2Y_{2,-2} f_{xy} + 2Y_{2,-1} f_{yz} + 2Y_{2,1} f_{zx}] \\ &+ \sqrt{\frac{4\pi}{15}} \left[\left(Y_{22} - \frac{1}{\sqrt{3}} Y_{20} \right) f_{xx} - \left(Y_{22} + \frac{1}{\sqrt{3}} Y_{20} \right) f_{yy} + \frac{2}{\sqrt{3}} Y_{20} f_{zz} \right] \end{aligned}$$

$$\begin{aligned} \Rightarrow \quad c_{00} &= \frac{\sqrt{4\pi}}{3} [f_{xx} + f_{yy} + f_{zz}] \\ c_{20} &= \sqrt{\frac{4\pi}{15}} \left[-\frac{1}{\sqrt{3}} f_{xx} - \frac{1}{\sqrt{3}} f_{yy} + \frac{2}{\sqrt{3}} f_{zz} \right] \\ c_{21} &= \sqrt{\frac{16\pi}{15}} f_{zx} & c_{2,-1} &= \sqrt{\frac{16\pi}{15}} f_{yz} \\ c_{22} &= \sqrt{\frac{4\pi}{15}} [f_{xx} - f_{yy}] & c_{2,-2} &= \sqrt{\frac{16\pi}{15}} f_{xy}. \end{aligned}$$

We rearrange these terms, since we are interested in the f_{ij} :

$$\begin{aligned} f_{xx} &= \sqrt{\frac{15}{16\pi}} \left(c_{22} - \frac{1}{\sqrt{3}} c_{20} \right) + \frac{c_{00}}{\sqrt{4\pi}} & f_{xy} &= \sqrt{\frac{15}{16\pi}} c_{2,-2} \\ f_{yy} &= \sqrt{\frac{15}{16\pi}} \left(-c_{22} - \frac{1}{\sqrt{3}} c_{20} \right) + \frac{c_{00}}{\sqrt{4\pi}} & f_{yz} &= \sqrt{\frac{15}{16\pi}} c_{2,-1} \\ f_{zz} &= \sqrt{\frac{15}{16\pi}} \frac{2}{\sqrt{3}} c_{20} + \frac{c_{00}}{\sqrt{4\pi}} & f_{zx} &= \sqrt{\frac{15}{16\pi}} c_{21}. \end{aligned}$$

Now, we use equation Eq. (B.2) to substitute c_{lm} with f_{lm} : $c_{lm} = 2(f_{lm}(r) - a_{lm} - b_{lm}r)/r^2$. It is sufficient to consider only the terms up to second order in r since we are interested in very small r (the EFG is evaluated in the limit $\vec{r} \rightarrow \vec{0}$).

For the 00 component, we obtain $c_{00} = 2(f_{00}(r) - a_{00})/r^2$ since there is no b_{00} in the linear expression. However, we will use the expression $c_{00} = \frac{\sqrt{4\pi}}{3} [f_{xx} + f_{yy} + f_{zz}] = \frac{\sqrt{4\pi}}{3} \Delta f(0)$, because this has later the physical meaning of $\Delta v(0) \propto n(0)$.

For the $2m$ components we get $c_{2m} = 2f_{2m}(r)/r^2$ since neither a_{2m} nor b_{2m} contributes to the zeroth resp. linear order.

Inserting these c_{lm} yields the connection between spherical and Cartesian notation

$$\left. \frac{\partial^2 f(\vec{r})}{\partial x_i \partial x_j} \right|_{\vec{r}=0} = \begin{pmatrix} f_{xx}(0) & f_{xy}(0) & f_{xz}(0) \\ f_{yx}(0) & f_{yy}(0) & f_{yz}(0) \\ f_{zx}(0) & f_{zy}(0) & f_{zz}(0) \end{pmatrix}$$

$$\frac{\partial^2 f(0)}{\partial x_i \partial x_j} = \sqrt{\frac{15}{4\pi}} \lim_{r \rightarrow 0} \frac{1}{r^2} \begin{pmatrix} f_{22}(r) - \frac{1}{\sqrt{3}} f_{20}(r) & f_{2,-2}(r) & f_{21}(r) \\ f_{2,-2}(r) & -f_{22}(r) - \frac{1}{\sqrt{3}} f_{20}(r) & f_{2,-1}(r) \\ f_{21}(r) & f_{2,-1}(r) & \frac{2}{\sqrt{3}} f_{20}(r) \end{pmatrix} + \frac{1}{3} \Delta f(0). \quad (\text{B.6})$$

Now, we see that when translating the Cartesian EFG tensor into the spherical EFG tensor (if the potential v is inserted for the arbitrary function f) there appears one extra scalar term: $\frac{1}{3} \Delta v(0) \propto n(0)$, which is proportional to the electronic charge density at the nucleus.

This scalar term, which is the trace of the Cartesian EFG tensor, would be zero, if the two charge distributions (nucleus and electron cloud) were non-overlapping. However, in non-relativistic treatment there is a non-vanishing probability to find s electrons at the nucleus. In relativistic treatment (needed for heavy atoms) also $p_{\frac{1}{2}}$ electrons have a small but finite probability to be at the nucleus.

However, this scalar term appears artificially in this second order. It gives a correction to the zeroth order of this expansion: it results in the isomer shift which is measurable with Mössbauer spectroscopy. If one uses the spherical notation from the beginning, this term appears in the zeroth order, where it belongs to. A simple spherical derivation for the zeroth order was done by Mössbauer [227].

Using V_{ij} as symbol for the traceless Cartesian EFG tensor (v_{ij} being the second derivative of the potential) one can also look at Eq. (B.6) like this:

$$V_{ij} \equiv v_{ij} - \frac{1}{3} \Delta v \cdot \delta_{ij} = \begin{pmatrix} v_{xx} - \frac{1}{3} \Delta v & v_{xy} & v_{xz} \\ v_{yx} & v_{yy} - \frac{1}{3} \Delta v & v_{yz} \\ v_{zx} & v_{zy} & v_{zz} - \frac{1}{3} \Delta v \end{pmatrix} \quad (\text{B.7})$$

$$= \sqrt{\frac{15}{4\pi}} \lim_{r \rightarrow 0} \frac{1}{r^2} \cdot \begin{pmatrix} v_{22}(r) - \frac{1}{\sqrt{3}} v_{20}(r) & v_{2,-2}(r) & v_{21}(r) \\ v_{2,-2}(r) & -v_{22}(r) - \frac{1}{\sqrt{3}} v_{20}(r) & v_{2,-1}(r) \\ v_{21}(r) & v_{2,-1}(r) & \frac{2}{\sqrt{3}} v_{20}(r) \end{pmatrix}. \quad (\text{B.8})$$

This has the exact same form as the nuclear quadrupole moment tensor Eq. (A.16). Like the quadrupole moment tensor Q_{ij} the EFG tensor V_{ij} is reduced from nine to five degrees of freedom due to symmetry $V_{ij} = V_{ji}$ and traceless-ness $\sum_i V_{ii} = 0$.

C Derivation of the quadrupole Hamiltonian

In this appendix, the derivation of the quadrupole Hamiltonian (based on Ref. [164]) is presented. We start with the classical quadrupole interaction Eq. (3.3)

$$E_Q = \frac{1}{6} \sum_{i,j=1}^3 V_{ij} Q_{ij}.$$

Where the tensors are given by Eq. (B.7) and Eq. (A.7). In spherical notation (no double counting and $Q_{ij} \hat{=} 3Q_{2m}$) this is

$$E_Q = \sum_{m=-2}^2 \sqrt{\frac{15}{4\pi}} \lim_{r \rightarrow 0} \frac{1}{r^2} V_{2m}(r) \cdot Q_{2m}.$$

The quadrupole Hamiltonian is obtained by replacing the classical functions by its quantum mechanical operators:

$$\begin{aligned} \hat{\mathcal{H}}_{2m} &= \sqrt{\frac{15}{4\pi}} \lim_{\hat{r} \rightarrow 0} \frac{1}{\hat{r}^2} \hat{V}_{2m}(\hat{r}) \cdot \hat{Q}_{2m} \\ &= \sqrt{\frac{15}{4\pi}} \lim_{\hat{r} \rightarrow 0} \frac{1}{\hat{r}^2} \hat{V}_{2m}(\hat{r}) \cdot \sqrt{\frac{4\pi}{15}} eZ \hat{r}^2 \hat{Y}_{2m}, \end{aligned} \quad (\text{C.1})$$

with Z being the number of protons in the nucleus. The Taylor expansion guarantees that the second order contribution will be small. Therefore, we can use perturbation theory to evaluate the eigenvalues of Eq. (C.1)

$$E_{2m} = \sqrt{\frac{15}{4\pi}} \lim_{r \rightarrow 0} \langle \psi_e^{(0)} | \frac{1}{\hat{r}^2} \hat{V}_{2m}(\hat{r}) | \psi_e^{(0)} \rangle \cdot eZ \sqrt{\frac{4\pi}{15}} \langle I | \hat{r}^2 \hat{Y}_{2m} | I \rangle. \quad (\text{C.2})$$

The nucleus is described by a many body wave function $|I\rangle$ and the electron cloud is described by a many body wave function $|\psi_e\rangle$. Both being the eigenstates of the unperturbed system. The electronic part of Eq. (C.2) is solved to a good extent from first principals theory - the operator is known and the eigenfunction¹ can be calculated numerically by DFT codes, see Section 2.3. So we will not bother with that term. The remaining task is to transform the nuclear operator in another form, which allows us to find its eigenvalues.

Therefore, we will use the Wigner-Eckart theorem, which states that the matrix elements of all spherical tensors of rank n are proportional:

$$\langle I' m'_I | T_{nm} | I m_I \rangle = (-1)^{I' - m'_I} \begin{pmatrix} I' & n & I \\ -m'_I & m & m_I \end{pmatrix} \langle I' | T_n | I \rangle. \quad (\text{C.3})$$

For another spherical tensor of the same rank A^n the Wigner-Eckart theorem yields

$$\langle I' m'_I | A_{nm} | I m_I \rangle = (-1)^{I' - m'_I} \begin{pmatrix} I' & n & I \\ -m'_I & m & m_I \end{pmatrix} \langle I' | A_n | I \rangle.$$

¹Actually not $|\psi_e\rangle$ itself, but the corresponding charge density - which is all we need.

Dividing these two equations gives a constant $C_{II'n}$, which is independent of m_I, m'_I and m :

$$\frac{\langle I'm'_I|T_{nm}|Im_I\rangle}{\langle I'm'_I|A_{nm}|Im_I\rangle} = \frac{\langle I'|T_n|I\rangle}{\langle I'|A_n|I\rangle} = C_{II'n}.$$

Now, it is possible to connect the spherical operator $\hat{r}^2\hat{Y}_2$ to the spherical operator $\hat{I}^2\hat{Y}_2$

$$\langle I'|\hat{r}^2\hat{Y}_2|I\rangle = C_{II'2}\langle I'|\hat{I}^2\hat{Y}_2|I\rangle. \quad (\text{C.4})$$

The $m = 0$ components are

$$\hat{r}^2\hat{Y}_{20}(\hat{r}) = \frac{1}{2}\sqrt{\frac{5}{4\pi}}(3\hat{z}^2 - \hat{r}^2) \quad \text{and} \quad \hat{I}^2Y_{20}(\hat{I}) = \frac{1}{2}\sqrt{\frac{5}{4\pi}}(3\hat{I}_z^2 - \hat{I}^2). \quad (\text{C.5})$$

We define the observable quadrupole moment Q (which is actually Q_{zz}) according to the definition Eq. (A.7) as

$$Q \equiv Z\langle I, m_I = I|3\hat{z}^2 - \hat{r}^2|I, m_I = I\rangle = 2\sqrt{\frac{4\pi}{5}}Z\langle I, I|\hat{r}^2\hat{Y}_{20}|I, I\rangle. \quad (\text{C.6})$$

Now, it is possible to determine the constant $C_{II'2}$. First, we apply the Wigner-Eckart-theorem on Eq. (C.6)

$$\langle I|\hat{r}^2\hat{Y}_2|I\rangle = \frac{Q}{2\sqrt{\frac{4\pi}{5}}Z\begin{pmatrix} I & 2 & I \\ -I & 0 & I \end{pmatrix}},$$

then we apply the Wigner-Eckart-theorem on

$$\langle I, I|\hat{I}^2\hat{Y}_{20}|I, I\rangle = \begin{pmatrix} I & 2 & I \\ -I & 0 & I \end{pmatrix}\langle I|\hat{I}^2\hat{Y}_2|I\rangle.$$

Now, we evaluate $\langle I, I|\hat{I}^2\hat{Y}_{20}|I, I\rangle$ using the eigenvalues of \hat{I}^2 and \hat{I}_z :

$$\begin{aligned} \langle I, I|\hat{I}^2\hat{Y}_{20}|I, I\rangle &\stackrel{\text{Eq. (C.5)}}{=} \frac{1}{2}\sqrt{\frac{5}{4\pi}}\langle I, I|(3\hat{I}_z^2 - \hat{I}^2)|I, I\rangle \\ &= \frac{1}{2}\sqrt{\frac{5}{4\pi}}\hbar^2(3I^2 - I(I+1)) \\ &= \frac{1}{2}\sqrt{\frac{5}{4\pi}}\hbar^2(2I-1)I \\ \Rightarrow \langle I|\hat{I}^2\hat{Y}_2|I\rangle &= \frac{\frac{1}{2}\sqrt{\frac{5}{4\pi}}\hbar^2(2I-1)I}{\begin{pmatrix} I & 2 & I \\ -I & 0 & I \end{pmatrix}}. \end{aligned}$$

Now, we insert these results in Eq. (C.4) and obtain for $C_{II'2}$

$$C_{II'2} = \frac{\langle I|\hat{r}^2\hat{Y}_2|I\rangle}{\langle I|\hat{I}^2\hat{Y}_2|I\rangle} = \frac{Q}{Z(2I-1)I\hbar^2}.$$

The constant $C_{II'2}$ does not depend on m_I and m'_I . So this is also true for the other four components:

$$\hat{I}^2\hat{Y}_{22} = \frac{1}{2}\sqrt{\frac{15}{4\pi}}(\hat{I}_x^2 - \hat{I}_y^2) \quad (\text{C.7})$$

$$\hat{I}^2 \hat{Y}_{21} = \sqrt{\frac{15}{4\pi}} \hat{I}_x \hat{I}_z \quad (\text{C.8})$$

$$\hat{I}^2 \hat{Y}_{2-1} = \sqrt{\frac{15}{4\pi}} \hat{I}_y \hat{I}_z \quad (\text{C.9})$$

$$\hat{I}^2 \hat{Y}_{2-2} = \sqrt{\frac{15}{4\pi}} \hat{I}_x \hat{I}_y. \quad (\text{C.10})$$

Now, we have the desired connection between $\hat{r}^2 \hat{Y}_{2m}$ and $\hat{I}^2 \hat{Y}_{2m}$, which makes it possible to evaluate the matrix elements of the nuclear part of Eq. (C.2):

$$\hat{r}^2 \hat{Y}_{2m}(\hat{r}) = \frac{Q}{Z(2I-1)I\hbar^2} \hat{I}^2 \hat{Y}_{2m}(\hat{I}), \quad (\text{C.11})$$

where $\hat{I}^2 \hat{Y}_{2m}(\hat{I})$ is given by Eq. (C.5) and Eq. (C.7) to Eq. (C.10).

To obtain the quadrupole Hamiltonian $\hat{\mathcal{H}}_Q$ we need to sum up all m components of $\hat{\mathcal{H}}_{2m}$ Eq. (C.1) with the relation Eq. (C.11). To make life more simple we go in the PAS of the EFG tensor, because then only the $m = 2$ and $m = 0$ components survive

$$\begin{pmatrix} V_{xx} & 0 & 0 \\ 0 & V_{yy} & 0 \\ 0 & 0 & V_{zz} \end{pmatrix} = \sqrt{\frac{15}{4\pi}} \lim_{r \rightarrow 0} \frac{1}{r^2} \cdot \begin{pmatrix} V_{22}(r) - \frac{1}{\sqrt{3}} V_{20}(r) & 0 & 0 \\ 0 & -V_{22}(r) - \frac{1}{\sqrt{3}} V_{20}(r) & 0 \\ 0 & 0 & \frac{2}{\sqrt{3}} V_{20}(r) \end{pmatrix}.$$

The two contributions are

$$\begin{aligned} '20' &= \sqrt{\frac{15}{4\pi}} \lim_{r \rightarrow 0} \frac{1}{r^2} V_{20}(r) = \frac{\sqrt{3}}{2} V_{zz} \\ '22' &= \sqrt{\frac{15}{4\pi}} \lim_{r \rightarrow 0} \frac{1}{r^2} V_{22}(r) = \frac{1}{2} \eta V_{zz}. \end{aligned}$$

In order to get the full Hamiltonian we need to add up the single terms

$$\begin{aligned} \hat{\mathcal{H}}_Q &= \sum_{m=-2}^2 \mathcal{H}_{2m} = \mathcal{H}_{20} + \mathcal{H}_{22} \\ &= \frac{Q}{Z(2I-1)I\hbar^2} \left(\sqrt{\frac{15}{4\pi}} \lim_{r \rightarrow 0} \frac{1}{r^2} V_{20}(r) \cdot \sqrt{\frac{4\pi}{15}} eZ \hat{I}^2 \hat{Y}_{20} + \sqrt{\frac{15}{4\pi}} \lim_{r \rightarrow 0} \frac{1}{r^2} V_{22}(r) \cdot \sqrt{\frac{4\pi}{15}} eZ \hat{I}^2 \hat{Y}_{22} \right) \\ &= \frac{eQ}{(2I-1)I\hbar^2} \left(\frac{\sqrt{3}}{2} V_{zz} \cdot \frac{1}{2\sqrt{3}} (3\hat{I}_z^2 - \hat{I}^2) + \frac{1}{2} \eta V_{zz} \cdot \frac{1}{2} (\hat{I}_x^2 - \hat{I}_y^2) \right). \end{aligned}$$

Finally, we have the quadrupole Hamiltonian:

$$\hat{\mathcal{H}}_Q = \frac{eQV_{zz}}{4(2I-1)I\hbar^2} \left[(3\hat{I}_z^2 - \hat{I}^2) + \eta (\hat{I}_x^2 - \hat{I}_y^2) \right]. \quad (\text{C.12})$$

Alternatively, one can also use the operators $J_{\pm} = J_x \pm iJ_y$, which yields

$$\hat{\mathcal{H}}_Q = \frac{eQV_{zz}}{4(2I-1)I\hbar^2} \left[(3\hat{I}_z^2 - \hat{I}^2) + \frac{1}{2} \eta (\hat{I}_+^2 + \hat{I}_-^2) \right]. \quad (\text{C.13})$$

D Contributions to the interaction energy from the 4th order Taylor expansion

In this appendix, we derive the classical expressions for the contributions from the fourth order of the electrostatic interaction energy, which are due to electron penetration into the nucleus. The arising contributing from the 4th order to the 2nd order will lead to the ‘‘quadrupole shift’’ and is dealt with quantum mechanically in Appendix E.

We start with the Taylor expansion of the classical interaction energy Eq. (6.9). Here we focus on the fourth order of this expansion. Using Eq. (A.9) we force the nuclear hexadecapole moment and electric hexadecapole field tensor to appear

$$\begin{aligned} E^{(4)} &= \frac{1}{4!} \sum_{i,j,k,l=1}^3 \left(\left. \frac{\partial^4 v(\vec{r})}{\partial x_i \partial x_j \partial x_k \partial x_l} \right|_{\vec{r}=0} \right) \int x_i x_j x_k x_l \rho(\vec{r}) d^3 r \\ &= \frac{1}{4!} \sum_{i,j,k,l=1}^3 (V_{ijkl} + f_{ijkl}^V) \frac{1}{105} (Q_{ijkl} + f_{ijkl}^Q). \end{aligned} \quad (\text{D.1})$$

The function f_{ijkl}^Q is given by Eq. (A.2) and

$$V_{ijkl} = \partial_i \partial_j \partial_k \partial_l v(0) - f_{ijkl}^V \Delta v(0) \quad (\text{D.2})$$

$$\begin{aligned} f_{ijkl}^V &= \left[\partial_i \partial_j \delta_{kl} + \partial_i \partial_k \delta_{jl} + \partial_i \partial_l \delta_{kj} + \partial_j \partial_k \delta_{il} + \partial_j \partial_l \delta_{ik} + \partial_k \partial_l \delta_{ij} \right] \\ &\quad - \frac{\Delta}{5} \left[\delta_{ij} \delta_{kl} + \delta_{ik} \delta_{jl} + \delta_{il} \delta_{jk} \right] \end{aligned} \quad (\text{D.3})$$

The Cartesian hexadecapole moment tensor Q_{ijkl} contains $3 \cdot 3 \cdot 3 \cdot 3 = 81$ elements. Due to symmetry (Q_{ijkl} is invariant against permutation of its indices i, j, k and l) 66 and due to tracelessness conditions ($\sum_i Q_{iijk} = 0$ for all j, k combinations) six of these 81 elements are identical leaving this tensor, like the spherical Q_{4m} with only nine degrees of freedom.

One can try to imagine the Cartesian hexadecapole tensor as a 3×3 matrix, where each element is a traceless 3×3 matrix. Using the abbreviation $\{x_i x_j x_k x_l\} = \int \rho(\vec{r}) x_i x_j x_k x_l d^3 r$ the xx element (the matrix Q_{ijxx}) looks like this

$$3 \cdot 5 \cdot \begin{pmatrix} \{7xxxx - 6x^2r^2 + \frac{3}{5}r^4\} & \{xyxx - 3xyr^2\} & \{7xzx - 3xzr^2\} \\ \{7yxxx - 3xyr^2\} & \{7yyxx - (x^2 + y^2)r^2 + \frac{1}{5}r^4\} & \{7yzxx - yzr^2\} \\ \{7zxxx - 3xzr^2\} & \{7zyxx - yzr^2\} & \{7zzxx - (x^2 + z^2)r^2 + \frac{1}{5}r^4\} \end{pmatrix}$$

with zero trace: $\sum_i Q_{iixx} = Q_{xxxx} + Q_{yyxx} + Q_{zzxx} = 0$. Also the tensor f_{ijkl}^Q can be seen as a 3×3 matrix, where each element is a traceless 3×3 matrix. Here the xx elements is

$$f_Q^{ijxx} = 3 \cdot 5 \cdot \begin{pmatrix} \{6x^2r^2 - \frac{3}{5}r^4\} & 3\{xyr^2\} & 3\{xz\} \\ 3\{xyr^2\} & \{(x^2 + y^2)r^2 - \frac{1}{5}r^4\} & \{yzr^2\} \\ 3\{xzr^2\} & \{yzr^2\} & \{(x^2 + z^2)r^2 - \frac{1}{5}r^4\} \end{pmatrix}. \quad (\text{D.4})$$

The same symmetry and traceless-ness conditions are true for the electric hexadecapole field (EHF) tensor V_{ijkl} ¹ and the xx element (the matrix V_{ijxx}) looks like this

$$\begin{pmatrix} v_{xxxx} - \frac{6}{7}\Delta v_{xx} + \frac{3}{35}\Delta^2 v & v_{xyxx} - \frac{3}{7}\Delta v_{xy} & v_{xzx} - \frac{3}{7}\Delta v_{xz} \\ v_{yxxx} - \frac{3}{7}\Delta v_{xy} & v_{yyxx} - \frac{1}{7}\Delta(v_{xx} + v_{yy}) + \frac{\Delta^2}{35}v & v_{yzxx} - \frac{1}{7}\Delta v_{yz} \\ v_{zxxx} - \frac{3}{7}\Delta v_{xz} & v_{zyxx} - \frac{1}{7}\Delta v_{yz} & v_{zzxx} - \frac{1}{7}\Delta(v_{xx} + v_{zz}) + \frac{\Delta^2}{35}v \end{pmatrix}.$$

The corresponding xx element from the modification is

$$f_{ijxx}^V = \frac{\Delta}{7} \begin{pmatrix} 6\partial_x^2 - \frac{3}{5}\Delta & 3\partial_x\partial_y & 3\partial_x\partial_z \\ 3\partial_x\partial_y & (\partial_x^2 + \partial_y^2) - \frac{\Delta}{5} & \partial_y\partial_z \\ 3\partial_x\partial_z & \partial_y\partial_z & (\partial_x^2 + \partial_z^2) - \frac{\Delta}{5} \end{pmatrix} v. \quad (D.5)$$

The elements yy , zz , $xy = yx$, $xz = zx$ and $yz = zy$ look similar and can easily be obtained from Eq. (D.4) and Eq. (D.5). Now, we evaluate Eq. (D.1). First, we have to check whether the dot product of the hexadecapole tensors V_{ijkl} and Q_{ijkl} respectively with its modification f_{ijkl}^Q and f_{ijkl}^V respectively is zero. There are no mixed terms if (from now on the Einstein sum convention is used):

$$V_{ijxx} f_{ijxx}^Q + V_{ijyy} f_{ijyy}^Q + V_{ijzz} f_{ijzz}^Q + 2(V_{ijxy} f_{ijxy}^Q + V_{ijyz} f_{ijyz}^Q + V_{ijxz} f_{ijxz}^Q) \stackrel{!}{=} 0. \quad (D.6)$$

We obtain for the two sums

$$\begin{aligned} \frac{1}{15} \left(V_{ijxx} f_{ijxx}^Q + V_{ijyy} f_{ijyy}^Q + V_{ijzz} f_{ijzz}^Q \right) &= -4[\{xyr^2\}V_{xyzz} + \{x zr^2\}V_{xzyy} + \{yzr^2\}V_{yzxx}] \\ &\quad - \frac{2}{5}\{r^4\}[V_{xxxx} + V_{yyyy} + V_{zzzz}] \\ &\quad + 4[\{x^2r^2\}V_{xxxx} + \{y^2r^2\}V_{yyyy} + \{z^2r^2\}V_{zzzz}] \\ \frac{2}{15} \left(V_{ijxy} f_{ijxy}^Q + V_{ijyz} f_{ijyz}^Q + V_{ijxz} f_{ijxz}^Q \right) &= 4[\{xyr^2\}V_{xyzz} + \{x zr^2\}V_{xzyy} + \{yzr^2\}V_{yzxx}] \\ &\quad - 2\frac{2}{5}\{r^4\}[V_{xxyy} + V_{xxzz} + V_{yyzz}] \\ &\quad - 4[\{x^2r^2\}V_{xxxx} + \{y^2r^2\}V_{yyyy} + \{z^2r^2\}V_{zzzz}]. \end{aligned}$$

Using $\sum_j V_{iijj} = 0$ these expressions indeed cancel and Eq. (D.6) is true. The same is true for Q_{ijkl} with f_{ijkl}^V . Like in the second order also here only two contributions survive:

$$\begin{aligned} E^{(4)} &= \frac{1}{4!} \sum_{i,j,k,l=1}^3 \left(V_{ijkl} + f_{ijkl}^V \right) \frac{1}{105} \left(Q_{ijkl} + f_{ijkl}^Q \right) \\ &= \frac{1}{4!} \frac{1}{105} \sum_{i,j,k,l=1}^3 \left(V_{ijkl} Q_{ijkl} + f_{ijkl}^V f_{ijkl}^Q \right). \end{aligned} \quad (D.7)$$

The first term is the hexadecapole interaction and the second term are corrections to lower orders, which we will calculate now. We need to evaluate:

$$f_{ijxx}^V f_{ijxx}^Q + f_{ijyy}^V f_{ijyy}^Q + f_{ijzz}^V f_{ijzz}^Q + 2(f_{ijxy}^V f_{ijxy}^Q + f_{ijyz}^V f_{ijyz}^Q + f_{ijxz}^V f_{ijxz}^Q).$$

¹If one extends the calculation from Appendix B to the fourth order, one finds similar to the EFG tensor (f_{2m} and c_{00} “dirt” from the zeroth order) not only components f_{4m} but also e_{00} and e_{2m} “dirt” from lower orders - in this case from the zeroth and second order. The traceless-ness conditions cancel this contributions leaving the the Cartesian EHF tensor with only nine degrees of freedom: f_{4m} .

We obtain

$$\begin{aligned}
 \frac{1}{15} \left(f_{ijxx}^V f_{ijxx}^Q + f_{ijyy}^V f_{ijyy}^Q + f_{ijzz}^V f_{ijzz}^Q \right) &= \frac{38}{7} [\{x^2 r^2\} \partial_x^2 + \{y^2 r^2\} \partial_y^2 + \{z^2 r^2\} \partial_z^2] \Delta v(0) \\
 &+ \frac{38}{7} [\{xy r^2\} \partial_x \partial_y + \{yz r^2\} \partial_y \partial_z + \{xz r^2\} \partial_x \partial_z] \Delta v(0) \\
 &- \frac{137}{7 \cdot 25} \{r^4\} \Delta \Delta v(0) \\
 \\
 \frac{1}{15} \left(f_{ijxy}^V f_{ijxy}^Q + f_{ijyz}^V f_{ijyz}^Q + f_{ijxz}^V f_{ijxz}^Q \right) &= \frac{2}{7} [\{x^2 r^2\} \partial_x^2 + \{y^2 r^2\} \partial_y^2 + \{z^2 r^2\} \partial_z^2] \Delta v(0) \\
 &+ \frac{23}{7} [\{xy r^2\} \partial_x \partial_y + \{yz r^2\} \partial_y \partial_z + \{xz r^2\} \partial_x \partial_z] \Delta v(0) \\
 &+ \frac{16}{7 \cdot 25} \{r^4\} \Delta \Delta v(0).
 \end{aligned}$$

Taking in account the factor two we obtain for the correction:

$$\begin{aligned}
 \Delta E &= \frac{1}{4!} \frac{15}{105} \left(\frac{42}{7} [\{x^2 r^2\} \partial_x^2 + \{y^2 r^2\} \partial_y^2 + \{z^2 r^2\} \partial_z^2] \right. \\
 &\quad \left. + \frac{84}{7} [\{xy r^2\} \partial_x \partial_y + \{yz r^2\} \partial_y \partial_z + \{xz r^2\} \partial_x \partial_z] - \frac{105}{7 \cdot 25} \{r^4\} \Delta \right) \Delta v(0) \\
 &= \frac{1}{28} \sum_{ij} \{x_i x_j r^2\} \partial_i \partial_j \Delta v(0) - \frac{1}{280} \{r^4\} \Delta^2 v(0). \tag{D.8}
 \end{aligned}$$

We modify Eq. (D.8) by forcing the tensors to be traceless

$$\{x_i x_j r^2\} \partial_i \partial_j \Delta v(0) = \left\{ \left(x_i x_j - \frac{1}{3} \delta_{ij} r^2 \right) r^2 \right\} (\partial_i \partial_j - \frac{1}{3} \delta_{ij} \Delta) \Delta v(0) + \frac{1}{9} \{r^4\} \Delta^2 v(0) \delta_{ij}.$$

There are no mixed terms here, since the dot product of a traceless matrix with a unit matrix is zero. Inserting this in Eq. (D.8) we obtain for the correction energy

$$\Delta E = \frac{1}{28} \sum_{ij} \left\{ \left(x_i x_j - \frac{1}{3} \delta_{ij} r^2 \right) r^2 \right\} (\partial_i \partial_j - \frac{1}{3} \delta_{ij} \Delta) \Delta v(0) + \frac{1}{120} \{r^4\} \Delta^2 v(0). \tag{D.9}$$

With $\{x_i x_j r^2\} = \int \rho(\vec{r}) x_i x_j r^2 d^3 r \equiv eZ \langle x_i x_j r^2 \rangle$, the nuclear part can be translated in spherical notation by translating the $x_i x_j$ in real spherical harmonics (see page 112):

$$\begin{aligned}
 &\begin{pmatrix} \langle x x r^2 - \frac{1}{3} r^4 \rangle & \langle x y r^2 \rangle & \langle x z r^2 \rangle \\ \langle y x r^2 \rangle & \langle y y r^2 - \frac{1}{3} r^4 \rangle & \langle y z r^2 \rangle \\ \langle z x r^2 \rangle & \langle z y r^2 \rangle & \langle z z r^2 - \frac{1}{3} r^4 \rangle \end{pmatrix} \\
 &= \sqrt{\frac{4\pi}{15}} \begin{pmatrix} \langle r^4 (Y_{22} - \frac{1}{\sqrt{3}} Y_{20}) \rangle & \langle r^4 Y_{2,-2} \rangle & \langle r^4 Y_{21} \rangle \\ \langle r^4 Y_{2,-2} \rangle & \langle -r^4 (Y_{22} + \frac{1}{\sqrt{3}} Y_{20}) \rangle & \langle r^4 Y_{2,-1} \rangle \\ \langle r^4 Y_{21} \rangle & \langle r^4 Y_{2,-1} \rangle & \langle r^4 \frac{2}{\sqrt{3}} Y_{20} \rangle \end{pmatrix}. \tag{D.10}
 \end{aligned}$$

Using the Poisson equation $\Delta v(0) = -c_0 n(0)$ (with $c_0 = \frac{1}{\epsilon_0}$ in SI units and $c_0 = \frac{4\pi a_0 Ha}{e^2}$ in atomic units), we obtain for the so called kinetic energy tensor (second partial derivatives of the electronic charge density) in spherical notation (see Appendix B)

$$\begin{pmatrix} n_{xx} - \frac{1}{3} \Delta n & n_{xy} & n_{xz} \\ n_{yx} & n_{yy} - \frac{1}{3} \Delta n & n_{yz} \\ n_{zx} & n_{zy} & n_{zz} - \frac{1}{3} \Delta n \end{pmatrix} =$$

D Contributions to the interaction energy from the 4th order Taylor expansion

$$= \sqrt{\frac{15}{4\pi}} \lim_{r \rightarrow 0} \frac{1}{r^2} \begin{pmatrix} n_{22}(r) - \frac{1}{\sqrt{3}}n_{20}(r) & n_{2,-2}(r) & n_{21}(r) \\ n_{2,-2}(r) & -n_{22}(r) - \frac{1}{\sqrt{3}}n_{20}(r) & n_{2,-1}(r) \\ n_{21}(r) & n_{2,-1}(r) & \frac{2}{\sqrt{3}}n_{20}(r) \end{pmatrix}. \quad (\text{D.11})$$

Inserting Eq. (D.11) and Eq. (D.10) back in Eq. (D.9) gives finally the corrections

$$\Delta E = -c_0 \frac{eZ}{14} \sum_{m=-2}^2 \left[\lim_{r \rightarrow 0} \frac{1}{r^2} n_{2m} \cdot \langle r^4 Y_{2m} \rangle \right] - c_0 \frac{eZ}{120} \langle r^4 \rangle n(0).$$

This can be written as another correction to the zeroth order and a correction to the second order. In spherical notation these are

$$\Delta E^{(0)} = -c_0 \frac{eZ}{120} \langle r^4 \rangle \Delta n(0) \quad (\text{D.12})$$

$$\Delta E_m^{(2)} = -c_0 \frac{eZ}{14} \left[\lim_{r \rightarrow 0} \frac{1}{r^2} n_{2m} \cdot \langle r^4 Y_{2m} \rangle \right]. \quad (\text{D.13})$$

E Derivation of the quadrupole shift Hamiltonian

In this appendix, the derivation of the quadrupole shift Hamiltonian is presented. This derivation is very similar to the derivation of the quadrupole Hamiltonian, demonstrated in Appendix C.

We start with the the correction to the energy to the second order in spherical notation Eq. (D.13):

$$\Delta E_m^{(2)} = \frac{1}{14} \left[-c_0 \sqrt{\frac{15}{4\pi}} \lim_{r \rightarrow 0} \frac{1}{r^2} n_{2m}(r) \right] \cdot \left[\sqrt{\frac{4\pi}{15}} eZ \langle r^4 Y_{2m} \rangle \right].$$

Replacing the classical functions by its quantum mechanical operators provides the Hamiltonian for this correction energy $\Delta E_m^{(2)}$

$$\hat{H}_m^{(2)} = \frac{1}{14} \underbrace{\left[-c_0 \sqrt{\frac{15}{4\pi}} \lim_{\hat{r} \rightarrow 0} \frac{1}{\hat{r}^2} \hat{n}_{2m}(\hat{r}) \right]}_{\hat{E}_{2m}} \cdot \underbrace{\left[\sqrt{\frac{4\pi}{15}} eZ \langle \hat{r}^4 \hat{Y}_{2m} \rangle \right]}_{\hat{N}_{2m}}.$$

The operator containing the electronic part we call \hat{E}_{2m} and the operator containing the nuclear part \hat{N}_{2m} . Just like in Appendix C, the eigenvalues are obtained from the matrix elements

$$E_m^{(2)} = \frac{1}{14} \langle \psi_e^{(0)} | \hat{E}_{2m} | \psi_e^{(0)} \rangle \cdot \langle I | \hat{N}_{2m} | I \rangle. \quad (\text{E.1})$$

Also here, the electron part can be obtained from DFT codes and we are left with transforming the nuclear operator \hat{N}_{2m} into eigenfunctions of $|I\rangle$. We need an expression for $\hat{r}^4 \hat{Y}_{2m}$ in terms of \hat{I} . We start with multiplying Eq. (C.5) with \hat{r}^2 :

$$\hat{r}^4 \hat{Y}_{20}(\hat{r}) = \frac{1}{2} \sqrt{\frac{5}{4\pi}} (3\hat{z}^2 - \hat{r}^2) \hat{r}^2 \quad \text{and} \quad \hat{I}^4 Y_{20}(\hat{I}) = \frac{1}{2} \sqrt{\frac{5}{4\pi}} (3\hat{I}_z^2 - \hat{I}^2) \hat{I}^2. \quad (\text{E.2})$$

Since \hat{I}_z and \hat{I}^2 commute, $[\hat{I}^2, \hat{I}_z] = 0$, the order does not matter. In order to get a connection between $\hat{r}^4 \hat{Y}_{20}$ and $\hat{I}^4 \hat{Y}_{20}$, we have to apply the Wigner-Eckart-theorem Eq. (C.3), which states that all tensors of rank l are proportional. $\hat{r}^4 \hat{Y}_{20}$ is also a tensor of rank 2 because \hat{r}^4 is just a scalar. We continue the procedure of Appendix C and calculate the constant C , connecting the two tensors given in Eq. (E.2):

$$\frac{\langle I', m'_I | r^4 Y_{20} | I, m_I \rangle}{\langle I', m'_I | \hat{I}^4 Y_{20} | I, m_I \rangle} \stackrel{\text{Eq. (C.3)}}{=} \frac{\langle I' | r^4 Y_{20} | I \rangle}{\langle I' | \hat{I}^4 Y_{20} | I \rangle} = C. \quad (\text{E.3})$$

Analog to Q we define \tilde{Q} (which is \tilde{Q}_{zz}):

$$\tilde{Q} \equiv Z \langle I, m_I = I | (3\hat{z}^2 - \hat{r}^2) \hat{r}^2 | I, m_I = I \rangle = 2 \sqrt{\frac{4\pi}{5}} Z \langle I, I | \hat{r}^4 \hat{Y}_{20} | I, I \rangle. \quad (\text{E.4})$$

First we apply the Wigner-Eckart-theorem on Eq. (E.4)

$$\langle I | \hat{r}^4 \hat{Y}_{20} | I \rangle = \frac{\tilde{Q}}{2 \sqrt{\frac{4\pi}{5}} Z \begin{pmatrix} I & 2 & I \\ -I & 0 & I \end{pmatrix}},$$

then we apply the Wigner-Eckart-theorem on

$$\langle I, I | \hat{I}^4 \hat{Y}_{20} | I, I \rangle = \begin{pmatrix} I & 2 & I \\ -I & 0 & I \end{pmatrix} \langle I | \hat{I}^4 \hat{Y}_{20} | I \rangle.$$

Now, we evaluate $\langle I, I | \hat{I}^4 \hat{Y}_{20} | I, I \rangle$ using the eigenvalues of \hat{I}^2 and \hat{I}_z :

$$\begin{aligned} \langle I, I | \hat{I}^4 \hat{Y}_{20} | I, I \rangle &= \frac{1}{2} \sqrt{\frac{5}{4\pi}} \langle I, I | (3\hat{I}_z^2 - \hat{I}^2) \hat{I}^2 | I, I \rangle \\ &= \frac{1}{2} \sqrt{\frac{5}{4\pi}} \hbar^4 (3I^2 - I(I+1))(I(I+1)) \\ &= \frac{1}{2} \sqrt{\frac{5}{4\pi}} \hbar^4 (2I^2 + I - 1) I^2 \\ \Rightarrow \langle I | \hat{I}^4 \hat{Y}_{20} | I \rangle &= \frac{\frac{1}{2} \sqrt{\frac{5}{4\pi}} \hbar^4 (2I^2 + I - 1) I^2}{\begin{pmatrix} I & 2 & I \\ -I & 0 & I \end{pmatrix}}. \end{aligned}$$

Now, we insert these results in Eq. (E.3) and obtain for C

$$C = \frac{\langle I | \hat{r}^4 \hat{Y}_{20} | I \rangle}{\langle I | \hat{I}^4 \hat{Y}_{20} | I \rangle} = \frac{\tilde{Q}}{Z(2I^2 + I - 1)I^2 \hbar^4}.$$

The constant C does not depend on m_I, m'_I and m . So this is also true for the other four components

$$\hat{I}^4 \hat{Y}_{22} = \frac{1}{2} \sqrt{\frac{15}{4\pi}} (\hat{I}_x^2 - \hat{I}_y^2) \hat{I}^2 \quad (\text{E.5})$$

$$\hat{I}^4 \hat{Y}_{21} = \sqrt{\frac{15}{4\pi}} \hat{I}_x \hat{I}_z \hat{I}^2 \quad (\text{E.6})$$

$$\hat{I}^4 \hat{Y}_{2-1} = \sqrt{\frac{15}{4\pi}} \hat{I}_y \hat{I}_z \hat{I}^2 \quad (\text{E.7})$$

$$\hat{I}^4 \hat{Y}_{2-2} = \sqrt{\frac{15}{4\pi}} \hat{I}_x \hat{I}_y \hat{I}^2. \quad (\text{E.8})$$

We know from quantum mechanics that $[\hat{I}^2, \hat{I}_x] = [\hat{I}^2, \hat{I}_y] = [\hat{I}^2, \hat{I}_z] = 0$. And since $[\hat{I}^2, \hat{I}_z \hat{I}_x] = \hat{I}_z [\hat{I}^2, \hat{I}_x] + [\hat{I}^2, \hat{I}_z] \hat{I}_x = 0 + 0 = 0$ (analog the others) the order does not matter.

Now, we have the desired connection between $\hat{r}^4 \hat{Y}_m^2$ and $\hat{I}^4 \hat{Y}_m^2$:

$$\hat{r}^4 \hat{Y}_m^2(\hat{r}) = \frac{\tilde{Q}}{Z(2I^2 + I - 1)I^2 \hbar^4} \hat{I}^4 \hat{Y}_m^2(\hat{I}), \quad (\text{E.9})$$

where $\hat{I}^4 \hat{Y}_m^2(\hat{I})$ is given by Eq. (E.2) and Eq. (E.5) to Eq. (E.8).

To obtain the quadrupole shift Hamiltonian $\hat{\mathcal{H}}_{QS}$ we need to sum up all m components of $\hat{\mathcal{H}}_m$. To make life more simple we choose also here the PAS¹ of the kinetic energy tensor

$$\begin{pmatrix} n_{xx} & 0 & 0 \\ 0 & n_{yy} & 0 \\ 0 & 0 & n_{zz} \end{pmatrix} = \sqrt{\frac{15}{4\pi}} \lim_{r \rightarrow 0} \frac{1}{r^2} \cdot \begin{pmatrix} n_{22}(r) - \frac{1}{\sqrt{3}} n_{20}(r) & 0 & 0 \\ 0 & -n_{22}(r) - \frac{1}{\sqrt{3}} n_{20}(r) & 0 \\ 0 & 0 & \frac{2}{\sqrt{3}} n_{20}(r) \end{pmatrix}.$$

¹Since the V_{2m} components are calculated from the n_{2m} components, this PAS coincides with the PAS of the EFG tensor, if $n_{2m} = 0$ with $m = -2, -1, 1$, *i.e.* both tensors are already in diagonal form, but may be different otherwise.

(These n_{ii} are the “traceless” elements, $\sum_i n_{ii} = 0$.)

In the PAS only 2 components contribute

$$\hat{E}_{20} = -c_0 \sqrt{\frac{15}{4\pi}} \lim_{r \rightarrow 0} \frac{1}{r^2} n_{20}(r) = -c_0 \frac{\sqrt{3}}{2} n_{zz} \quad (\text{E.10})$$

$$\hat{E}_{22} = -c_0 \sqrt{\frac{15}{4\pi}} \lim_{r \rightarrow 0} \frac{1}{r^2} n_{22}(r) = -c_0 \frac{1}{2} \eta_{QS} n_{zz} \quad (\text{E.11})$$

with $\eta_{QS} = (n_{xx} - n_{yy})/n_{zz}$, in general different² from the EFG η (unless $\eta = 0 \Rightarrow \eta_{QS} = 0$).

In order to get the full Hamiltonian we need to add up the single terms

$$\hat{\mathcal{H}}_{QS} = \sum_{m=-2}^2 \mathcal{H}_m = \frac{1}{14} \left(\hat{E}_{20} \hat{N}_{20} + \hat{E}_{22} \hat{N}_{22} \right).$$

Inserting $\hat{N}_{2m} = \sqrt{\frac{4\pi}{15}} eZ r^4 Y_{2m}$ with Eq. (E.9) and Eq. (E.10) and Eq. (E.11) we obtain the Hamiltonian

$$\hat{\mathcal{H}} = -\frac{c_0}{14} \frac{e\tilde{Q}n_{zz}}{4(2I-1)I(I+1)I\hbar^4} \left[\left(3\hat{I}_z^2 - \hat{I}^2 \right) + \eta_{QS} \left(\hat{I}_x^2 - \hat{I}_y^2 \right) \right] \hat{I}^2. \quad (\text{E.12})$$

Compared to the quadrupole Hamiltonian, we see an additional \hat{I}^2 operator here. Furthermore contains the denominator in the prefactor $I(I+1)\hbar^2$ – the eigenvalue of \hat{I}^2 , which results (when applying the Hamiltonian on the nuclear state $|I\rangle$) in a multiplication by 1 (=nothing happened). Therefore, we will write the quadrupole shift Hamiltonian as

$$\hat{\mathcal{H}}_{QS} = -\frac{c_0}{14} \frac{e\tilde{Q}n_{zz}}{4(2I-1)I\hbar^2} \left[\left(3\hat{I}_z^2 - \hat{I}^2 \right) + \eta_{QS} \left(\hat{I}_x^2 - \hat{I}_y^2 \right) \right]. \quad (\text{E.13})$$

Note, in SI notation, $c_0 = 1/\epsilon_0$.

²For axial symmetry, both η are identical (zero), but in general, they must not be the same, since the relation of different n_{2m} must not coincide with the integral over their counterparts, divided by x , as V_{2m} is obtained.

F EFG implementation

In this appendix, we will derive an analytical expression for the off-site contribution \tilde{V}_{ij}^{off} , the second term in Eq. (4.6) from Section 3.5.

We are dealing with the contributions from the other atoms to the EFG of the atom under consideration. We take two atoms: the off-site atom is B and the potential is given by $v(\vec{\rho} - \vec{R})$ and the atom under consideration is A and we are interested in expressing the potential of B in $\vec{\rho}$, meaning how it is experienced by A , see left picture in Figure F.1 for a schematic illustration. Any (analytical) function $v(\vec{\rho})$ can be expanded in radial functions and spherical harmonics:

$$\begin{aligned} v(\vec{\rho}) &= \sum_{lm} v_{lm}(\rho) Y_{lm}(\hat{\rho}) \quad \text{with} \quad v_{lm}(\rho) = \int v(\vec{\rho}) Y_{lm}^*(\hat{\rho}) d\hat{\rho} \\ \Rightarrow v(\vec{\rho}) &= \sum_{lm} \left[\int v(\vec{\rho}) Y_{lm}^*(\hat{\rho}) d\hat{\rho} \right] Y_{lm}(\hat{\rho}). \end{aligned}$$

Since we are dealing with real spherical harmonics, the $*$ will be omitted from now on. Now, we use a “trick” and write $v(\vec{\rho})$ in the integral as $v(\vec{\rho} - \vec{R})$ and expand this again:

$$\begin{aligned} v(\vec{\rho} - \vec{R}) &= \sum_{LM} v_{LM}(|\vec{\rho} - \vec{R}|) Y_{LM}(\widehat{\rho - R}) \\ \Rightarrow v(\vec{\rho}) &= \sum_{lm} \left[\int \sum_{LM} v_{LM}(|\vec{\rho} - \vec{R}|) Y_{LM}(\widehat{\rho - R}) Y_{lm}(\hat{\rho}) d\hat{\rho} \right] Y_{lm}(\hat{\rho}). \end{aligned}$$

In order to calculate the integral we use another trick: we rotate the coordinate system with the operator \hat{D} and the matrix M (with $MM^T = \mathbb{1}$), respectively. Now, in Σ' the vector \vec{R} points along the z' -axis: $\hat{D}\vec{R} = \vec{R}M = (0, 0, R) = (M^T \underline{R})^T$. ($\vec{R} = \underline{R}^T$ is a row vector and \underline{R} is a column vector.) See centre picture in Figure F.1.

Spherical functions are rotated with the Wigner D functions D_{nm}^l :

$$\hat{D}Y_{lm}(\hat{r}) = \sum_n Y_{ln}(\hat{r}) D_{nm}^l = Y_{lm}(\hat{D}^{-1}\hat{r}) = Y_{lm}(\hat{r}M).$$

For $l = 1$ there are three linear independent Y_{lm} functions and for $l = 2$ the sum runs over five.

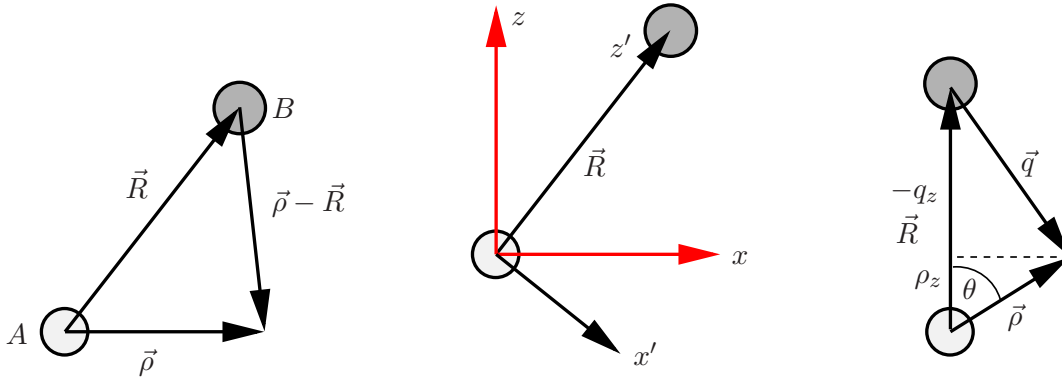


Figure F.1: On-site atom A (white) and off-site atom B (grey), separated by the vector \vec{R} . Illustrative pictures for the derivation of the off-site contributions, see text.

First, we consider only the part with $Y_{LM}(\widehat{\rho-R})Y_{lm}(\hat{\rho})$ and insert 1l:

$$\begin{aligned}
 \int Y_{LM}(\widehat{\rho-R})Y_{lm}(\hat{\rho}) d\hat{\rho} &= \int Y_{LM}((\widehat{\rho-R})MM^T)Y_{lm}(\hat{\rho}MM^T) d\hat{\rho} \\
 &= \int Y_{LM}((\widehat{\rho M-RM})M^T)Y_{lm}((\hat{\rho}M)M^T) d\hat{\rho} \\
 &= \int Y_{LM}((\widehat{\rho-RM})M^T)Y_{lm}(\hat{\rho}M^T) d\hat{\rho} \\
 &= \sum_{nN} \int Y_{LN}(\widehat{\rho-RM})D_{MN}^L Y_{ln}(\hat{\rho})D_{mn}^l d\hat{\rho} \\
 &= \sum_{nN} \int Y_{LN}(\widehat{\rho-RM})Y_{ln}(\hat{\rho}) d\hat{\rho} D_{MN}^L D_{mn}^l.
 \end{aligned}$$

From the second to the third line we used that instead of integrating over $\hat{\rho}$ we can also integrate over $\hat{\rho}M$. This makes no difference since the integral runs over the whole space. Then we can substitute all $\hat{\rho}M$ with $\hat{\rho}$ for simplicity. From the third to fourth line the Wigner D functions were used:

$$Y_{lm}(\hat{\rho}M) = \sum_n Y_{ln}(\hat{\rho})D_{nm}^l \Rightarrow Y_{lm}(\hat{\rho}M^T) = \sum_n Y_{ln}(\hat{\rho})D_{nm}^{Tl} = \sum_n Y_{ln}(\hat{\rho})D_{mn}^l.$$

\vec{R} in $v_{LM}(|\vec{\rho}-\vec{R}|)$ has been rotated as well which yields finally:

$$v(\vec{\rho}) = \left[\sum_{nN} \sum_{lm} \sum_{LM} \int v_{LM}(|\vec{\rho}-(0,0,R)|) Y_{LN}(\widehat{\rho-RM}) Y_{ln}(\hat{\rho}) d\hat{\rho} D_{MN}^L D_{mn}^l \right] Y_{lm}(\hat{\rho}).$$

In order to solve the integral we have to check the different dependencies. Therefore, we chose the following notation, see right picture in Figure F.1:

$$\begin{aligned}
 z &= \cos(\theta), \quad y = \sin(\theta) = \sqrt{1-z^2}, \quad \vec{\rho} = \rho(y \cos \varphi, y \sin \varphi, z), \quad \vec{q} = \vec{\rho} - \vec{R} \\
 \Rightarrow q(\rho, z) &= \sqrt{\rho^2 + R^2 - 2\rho Rz} \quad \text{and} \quad \vec{q} = (\rho y \cos \varphi, \rho y \sin \varphi, \rho z - R).
 \end{aligned}$$

The x and y component of $\vec{\rho}$ and \vec{q} are identical and the (negative) q_z component is obtained by: $q_z = \rho z - R$ with $\rho z = \rho z$.

To be consistent we write $\vec{q} = q((\rho y/q) \cos \varphi, (\rho y/q) \sin \varphi, (\rho z - R)/q)$ and define $z_q = (\rho z - R)/q$. This yields:

$$\begin{aligned}
 v_{LM}(|\vec{\rho}-(0,0,R)|) &= v_{LM}(q) = v_{LM}(\rho, z), \\
 Y_{LN}(\widehat{\rho-RM}) &= Y_{LN}(\hat{q}) = Y_{LN}(\varphi, z_q), \\
 Y_{ln}(\hat{\rho}) &= Y_{ln}(\varphi, y) = Y_{ln}(\varphi, z),
 \end{aligned}$$

and the integral becomes:

$$\int v_{LM}(\rho, z) Y_{LN}(\varphi, z_q) Y_{ln}(\varphi, z) d\varphi dz.$$

The spherical functions are defined as:

$$Y_{lm}(\varphi, z) = c_l^{|m|} P_l^{|m|}(z) \begin{cases} \cos(|m|\varphi), & m > 0 \\ 1, & m = 0 \\ \sin(|m|\varphi), & m < 0 \end{cases} \quad c_l^{|m|} = \sqrt{\frac{2l+1}{2\pi(1+\delta_{m0})} \frac{(l-|m|)!}{(l+|m|)!}}$$

$$P_l^{|m|}(z) = (1-z^2)^{\frac{m}{2}} \frac{d^{|m|}}{dz^{|m|}} P_l(z) \quad P_l(z) = \frac{1}{2^l l!} \frac{d^l}{dz^l} (z^2-1)^l,$$

and inserting these in the integral yields:

$$c_L^{|N|} c_l^{|n|} \int_{-1}^1 v_{LM}(\rho, z) P_L^{|N|}(z_q) P_l^{|n|}(z) dz \int_0^{2\pi} \phi_{|N|} \phi_{|n|} d\varphi.$$

The φ integration can be done immediately:

$$\phi_{|m|} = \begin{cases} \cos(|m|\varphi), & m \geq 0 \\ \sin(|m|\varphi), & m < 0 \end{cases} \Rightarrow \int_0^{2\pi} \phi_{|N|} \phi_{|n|} d\varphi = \pi(1 + \delta_{n0}) d_{nN}.$$

We arrive at

$$v(\vec{\rho}) = \sum_n \sum_{lm} \sum_{LM} \pi(1 + \delta_{n0}) c_L^{|n|} c_l^{|n|} \int_{-1}^1 v_{LM}(\rho, z) P_L^{|n|}(z_q) P_l^{|n|}(z) dz D_{Mn}^L D_{mn}^l Y_{lm}(\hat{\rho}).$$

In order to solve the remaining z integral we have to find expressions for the first two functions $v_{LM}(\rho, z)$ and $P_L^{|n|}(z_q)$. We start with expanding the Legendre polynomial $P_L^{|n|}(z_q)$ into a Taylor series around $\rho = 0$ up to second order. Therefore, we write (keeping in mind that n has to be positive and omitting $|n|$):

$$\begin{aligned} P_L^n(z_q(\rho)) &= y(\rho)^n \cdot H_L^n(z_q(\rho)) \quad \text{with} \quad y(\rho) = \sqrt{1 - z_q^2} = \sqrt{1 - (\rho z - R)^2 / q^2} \\ P_L^n(\rho) &= \sum_{j=0}^{\infty} \frac{\rho^j}{j!} \frac{d^j}{d\rho^j} \left[y(\rho)^n \cdot H_L^n(z_q(\rho)) \right]_{\rho=0}. \end{aligned}$$

First, we will consider necessary $\rho = 0$ terms:

$$\begin{aligned} \bullet \quad q(\rho = 0) &= R, & q'(\rho = 0) &= -z, & q''(\rho = 0) &= \frac{1 - z^2}{R}, \\ \bullet \quad z_q(0) &= -1, & z'_q(\rho = 0) &= 0, & z''_q(\rho = 0) &= \frac{1 - z^2}{R^2}, \\ \bullet \quad y(\rho = 0) &= 0, & y'(\rho = 0) &= \frac{\sqrt{1 - z^2}}{R}, & y''(\rho = 0) &= \frac{2z\sqrt{1 - z^2}}{R^2}. \end{aligned}$$

$H_L^n(z_q(\rho))$ and derivatives of $H_L^n(z_q(\rho))$ at $\rho = 0$ are harmless polynomials and therefore not divergent.

The zeroth order yields only one term:

$$P_L^n(0) = y(0)^n \cdot H_L^n(-1).$$

Since $y(0) = 0$ there is just one contribution for $n = 0$: $H_L^0(-1)$.

The first order yields two terms:

$$P_L^n(0) = ny(0)^{n-1} y'(0) \cdot H_L^n(-1) + y(0)^n \cdot H_L'^n(-1).$$

Since $H_L^0(-1) = 0$ there is only one contribution for $n = 1$: $y'(0) \cdot H_L^1(-1)$. (In all cases ' is the derivative with respect to ρ and after deriving ρ is set to zero.)

The second order yields four terms:

$$\begin{aligned} P_L^n(0) &= n(n-1)y(0)^{n-2} y'(0)^2 \cdot H_L^n(-1) + ny(0)^{n-1} y''(0) \cdot H_L^n(-1) \\ &\quad + 2ny(0)^{n-1} y'(0)^2 \cdot H_L'^n(-1) + y(0)^n \cdot H_L''^n(-1). \end{aligned}$$

Since $H_L^1(-1) = 0$ there is one contribution for $n = 0$: $H_L''^0(-1)$, one for $n = 1$: $y''(0) \cdot H_L^1(-1)$ and one for $n = 2$: $2y'(0)^2 \cdot H_L^2(-1)$.

$H_L^{\prime\prime 0}(-1)$ (derivative with respect to ρ) can be written as $(dH_L^0/d\rho) \cdot z_q^{\prime\prime}(0) = H_L^1(-1) \cdot (1-z^2)/R^2$ (chain rule). So we end up with:

$$\begin{aligned}
 P_L^n(\rho, z) &\simeq \left\{ \begin{aligned}
 &H_L^0(-1) + \frac{1-z^2}{R^2} \cdot H_L^1(-1) \cdot \frac{\rho^2}{2}; & (n=0) \\
 &\frac{\sqrt{1-z^2}}{R} \cdot H_L^1(-1) \cdot \rho + \frac{2z}{R^2} \sqrt{1-z^2} \cdot H_L^1(-1) \cdot \frac{\rho^2}{2}; & (n=1) \\
 &2 \frac{1-z^2}{R^2} \cdot H_L^2(-1) \cdot \frac{\rho^2}{2} & (n=2)
 \end{aligned} \right\}.
 \end{aligned}$$

It is sufficient to consider only contributions up to second order since the EFG is evaluated at the limes for $\rho \rightarrow 0$. The $H_L^n(-1)$ functions are given by:

$$\begin{aligned}
 H_L^0(-1) &= (-1)^L \\
 H_L^1(-1) &= (-1)^{L+1} \frac{L(L+1)}{2} \\
 H_L^2(-1) &= (-1)^L \frac{(L+2)(L+1)L(L-1)}{8}.
 \end{aligned}$$

Now, we expand the potential $v_{lm}(\rho)$ in a Taylor series around $\rho = 0$ ($q = R$) up to second order in ρ :

$$v_{LM}(\rho, z) \simeq v_{LM}(R) - z \frac{d}{dq} v_{LM}(q) \Big|_{q=R} \cdot \rho + \left[z^2 \frac{d^2}{dq^2} + \frac{1-z^2}{R} \frac{d}{dq} \right] v_{LM}(q) \Big|_{q=R} \cdot \frac{\rho^2}{2}$$

Same argument as before, we can stop after the second order because we are only interested in very small ρ .

For the EFG tensor we only have to consider $l = 2$. So for the Legendre function $P_l^n(z)$ there are only three contributions:

$$\begin{aligned}
 P_2^0(z) &= \frac{1}{2}(3z^2 - 1) \\
 P_2^1(z) &= 3z\sqrt{1-z^2} \\
 P_2^2(z) &= 3(1-z^2).
 \end{aligned}$$

Now, we have explicit expressions for all three functions and the z integration can be carried out:

$$\begin{aligned}
 v_{2m}(\rho) &= 2\pi \sum_{LM} \left\{ \right. & (F.1) \\
 &c_L^0 c_2^0 \frac{1}{105} \frac{\rho^2}{R^3} \left[-14RH_L^1 v_{LM} - (14R^2 H_L^0 + 8\rho^2 H_L^1) v'_{LM} + (14R^3 H_L^0 + \rho^2 RH_L^1) v''_{LM} \right] D_{M0}^L D_{m0}^2 \\
 &+ c_L^1 c_2^1 \frac{2}{35} \frac{\rho^2}{R^3} H_L^1 \left[14R v_{LM} + (4\rho^2 - 14R^2) v'_{LM} + 3\rho^2 R v''_{LM} \right] \left(D_{M,-1}^L D_{m,-1}^2 + D_{M1}^L D_{m1}^2 \right) \\
 &\left. + c_L^2 c_2^2 \frac{8}{35} \frac{\rho^2}{R^3} H_L^2 \left[14R v_{LM} + 6\rho^2 v'_{LM} + \rho^2 R v''_{LM} \right] \left(D_{M,-2}^L D_{m,-2}^2 + D_{M2}^L D_{m2}^2 \right) \right\}.
 \end{aligned}$$

Here, $'$ in v'_{LM} and v''_{LM} denotes the derivative with respect to q at $q = R$. This can be evaluated further with the solution of the Poisson equation:

$$v_{LM}(q) = \frac{2\pi}{2L+1} \left(\frac{1}{q^{L+1}} \int_0^q dx x^{L+2} n_{LM}(x) + q^L \int_q^\infty dx x^{-L+1} n_{LM}(x) \right).$$

With the following notation $I_1 = \int_0^R dx x^{L+2} n_{LM}(x)$ and $I_2 = \int_R^\infty dx x^{-L+1} n_{LM}(x)$ we obtain:

$$\begin{aligned} v_{LM}(R) &= \frac{2\pi}{2L+1} \left(\frac{1}{R^{L+1}} \cdot I_1 + R^L \cdot I_2 \right) \\ v'_{LM}(R) &= \frac{2\pi}{2L+1} \left(-\frac{L+1}{R^{L+2}} \cdot I_1 + LR^{L-1} \cdot I_2 \right) \\ v''_{LM}(R) &= \frac{2\pi}{2L+1} \left(\frac{(L+1)(L+2)}{R^{L+3}} \cdot I_1 + L(L-1)R^{L-2} \cdot I_2 - (2L+1)n_{LM}(R) \right). \end{aligned}$$

For the coefficients we have

$$\begin{aligned} c_L^0 c_2^0 &= \frac{1}{2\pi} \sqrt{\frac{3}{5}} \sqrt{\frac{2L+1}{L+1}} \\ c_L^1 c_2^1 &= \frac{1}{4\pi L} \sqrt{\frac{3}{5}} \sqrt{\frac{2L+1}{L+1}} \\ c_L^2 c_2^2 &= \frac{1}{8\pi L} \sqrt{\frac{3}{5}} \sqrt{\frac{2L+1}{(L-1)(L+1)(L+2)}}. \end{aligned}$$

In the EFG tensor, the Cartesian components are obtained by Eq. (3.2). Every compound is divided by ρ^2 and the limes for $\rho \rightarrow 0$ is taken. Therefore, only the terms which are proportional to ρ^2 (or less, but that is not the case) in Eq. (F.1) survive. Higher orders of ρ vanish since the other contributions are constants. The remaining spherical components for the EFG are:

$$\begin{aligned} \sqrt{\frac{15}{4\pi}} \lim_{\rho \rightarrow 0} \left(\frac{1}{\rho^2} \cdot v_{2m}(\rho) \right) &= \sum_{LM} \frac{\sqrt{\pi}(-1)^L}{\sqrt{2L+1}} \left\{ \right. \\ &\left[\frac{1}{\sqrt{L+1}} \left(\frac{(L+1)(L+2)}{R^{L+3}} I_1 + L(L-1)R^{L-2} I_2 - \frac{2}{3}(2L+1)n_{LM}(R) \right) \right] D_{M0}^L D_{m0}^2 \\ &\left[\frac{\sqrt{L+1}}{2} \left(-\frac{L+2}{R^{L+3}} I_1 + (L-1)R^{L-2} I_2 \right) \right] \left(D_{M,-1}^L D_{m,-1}^2 + D_{M1}^L D_{m1}^2 \right) \\ &\left[\frac{\sqrt{(L+2)(L+1)(L-1)}}{2} \left(\frac{1}{R^{L+3}} I_1 + R^{L-2} I_2 \right) \right] \left(D_{M,-2}^L D_{m,-2}^2 + D_{M2}^L D_{m2}^2 \right) \left. \right\}. \end{aligned}$$

G Model Hamiltonian results for perovskites

This appendix contains additional information about the p - d model Hamiltonian physics for perovskites, as applied for SrTiO₃ and BaTiO₃ in Section 5.3.

In order to extract the parameters from the band structure as used in Section 5.3, we need the total Hamiltonian

$$\hat{H} = \sum_m \left[\hat{H}_m + e_m \left(|d, \vec{k}\rangle \langle d, \vec{k}| + |p, \vec{k}\rangle \langle p, \vec{k}| \right) \right]. \quad (\text{G.1})$$

Here, \hat{H}_m is the Hamiltonian given in Eq. (5.2) and e_m is the mean energy of a pair of bands. The energies are therefore obtained from

$$E_{\vec{k}m\nu} + e_m = e_m + \nu \sqrt{\Delta_m^2 + V_m^2 (f_{m\vec{k}})^2}. \quad (\text{G.2})$$

For the three pairs of the π_{ij} bands, $f_{m\vec{k}}$ is given by

$$f_{\pi_{ij}\vec{k}}^2 = 2(2 - C_i - C_j), \quad (\text{G.3})$$

with $C_i \equiv \cos(k_i a)$. The two σ bands are distinguished by the index $\lambda = \pm 1$ and $f_{m\vec{k}}$ is

$$f_{\sigma\lambda\vec{k}}^2 = \left[3 - C_x - C_y - C_z + \lambda \left(C_x^2 + C_y^2 + C_z^2 - C_x C_y - C_x C_z - C_y C_z \right)^{1/2} \right]. \quad (\text{G.4})$$

Inserting these in Eq. (G.2) for the Γ point ($\vec{k}a = 0$), and the X point, ($k_x a = \pi$, $k_y = k_z = 0$) we obtain

$$\Gamma_{25} = e_\pi - \Delta_\pi = e_\sigma - \Delta_\sigma, \quad \text{and} \quad \Gamma_{25} \equiv E_p \approx \varepsilon_p \quad (\text{G.5})$$

$$\Gamma'_{25} = e_\pi + \Delta_\pi, \quad \text{and} \quad \Gamma'_{25} \equiv E_{d_{t2g}} \approx \varepsilon_d \quad (\text{G.6})$$

$$\Gamma_{12} = e_\sigma + \Delta_\sigma, \quad \text{and} \quad \Gamma_{12} \equiv E_{d_{eg}} \quad (\text{G.7})$$

$$X_5 = e_\pi + \sqrt{\Delta_\pi^2 + 4V_\pi^2}, \quad (\text{G.8})$$

$$X_1 = e_\sigma + \sqrt{\Delta_\sigma^2 + 4V_\sigma^2}. \quad (\text{G.9})$$

Here, ε denotes the energy of the atomic level, and E denotes the energy level corrected by a ‘crystal field’ δ_{CF} , see below.

Now it is trivial to find the parameters Δ_m, V_m

$$2\Delta_\pi = \Gamma'_{25} - \Gamma_{25} \equiv E_{d_{t2g}} - E_p, \quad (\text{G.10})$$

$$2\Delta_\sigma = \Gamma_{12} - \Gamma_{25} \equiv E_{d_{eg}} - E_p = \varepsilon_d - \varepsilon_p + \delta_{CF}, \quad (\text{G.11})$$

$$4V_\pi^2 = (X_5 - \Gamma'_{25})(X_5 - \Gamma_{25}), \quad (\text{G.12})$$

$$4V_\sigma^2 = (X_1 - \Gamma_{12})(X_1 - \Gamma_{25}). \quad (\text{G.13})$$

The energy values at the different Γ and X points for SrTiO₃ are given Table G.1.

So far, we have used the WE model, *i.e.* we have taken into account only the oxygen p and the titanium d states. Since this model is not sufficient to explain the observed behaviour of the oxygen p_σ states, we have to expand the model. Harrison’s model [98] includes also the oxygen s states. The s states change the dispersion in the σ bands, so that we have two parameters $V_{pd\sigma}$,

Table G.1: The energies (given in eV) at the Γ and X points for SrTiO₃ for two different lattice parameters a obtained from FPLO. Here, $\Gamma_1 \approx \varepsilon_s$, $\Gamma_{25} \approx \varepsilon_p$, $\Gamma'_{25} = E_{d_{t2g}} \approx \varepsilon_d$ and $\Gamma_{12} = E_{deg}$

a [Å]	Γ_{12}	Γ_1	Γ_{15}	Γ_{25}	Γ_{15}	Γ'_{25}	Γ_{12}	X_5	X_1
3.8996	-17.199	-16.177	-2.891	-1.166	-0.372	1.709	4.319	3.705	6.551
4.009	-16.923	-15.968	-2.828	-1.046	-0.408	1.579	3.800	3.332	5.798

$V_{sd\sigma}$ instead of just one V_σ . Thus, the expressions become more complex, even in the symmetry points. In this model, the Eqs. (G.5), (G.6) and (G.8) remain the same and the parameters ε_p , ε_d and V_π are unchanged. For Γ_{12} Eq. (G.7) and X_1 Eq. (G.9), Harrison obtains

$$\Gamma_{12} = \frac{\varepsilon_d + \varepsilon_s}{2} + \sqrt{\left(\frac{\varepsilon_d - \varepsilon_s}{2}\right)^2 + 6V_{sd\sigma}^2}, \quad (\text{G.14})$$

$$X_1 \approx \frac{\varepsilon_{d\sigma} + \varepsilon_p}{2} + \sqrt{\left(\frac{\varepsilon_{d\sigma} - \varepsilon_p}{2}\right)^2 + 4V_{pd\sigma}^2}, \quad (\text{G.15})$$

where $\varepsilon_{d\sigma} = \varepsilon_d + 2V_{sd\sigma}^2/\Delta_{sd}$. From these equations, the parameters $V_{pd\sigma}$ and $V_{sd\sigma}$ can be obtained. Besides, there is also an additional equation for Γ_1

$$\Gamma_1 = \varepsilon_s. \quad (\text{G.16})$$

Substituting $\Delta_{sd} \equiv \varepsilon_d - \varepsilon_s \gg V_{sd\sigma}$ in Eq. (G.14), we obtain

$$\begin{aligned} \Gamma_{12} &= \frac{\varepsilon_d + \varepsilon_s}{2} + \left(\frac{\Delta_{sd}}{2}\right) \sqrt{1 + \frac{24V_{sd\sigma}^2}{\Delta_{sd}^2}} \\ &\approx \frac{\varepsilon_d + \varepsilon_s}{2} + \left(\frac{\Delta_{sd}}{2}\right) \left[1 + \frac{12V_{sd\sigma}^2}{\Delta_{sd}^2}\right] \\ &= \varepsilon_d + 6\frac{V_{sd\sigma}^2}{\Delta_{sd}}. \end{aligned}$$

Hence,

$$E_{deg} \equiv \Gamma_{12} \approx \varepsilon_d + \frac{6V_{sd\sigma}^2}{\Delta_{sd}}. \quad (\text{G.17})$$

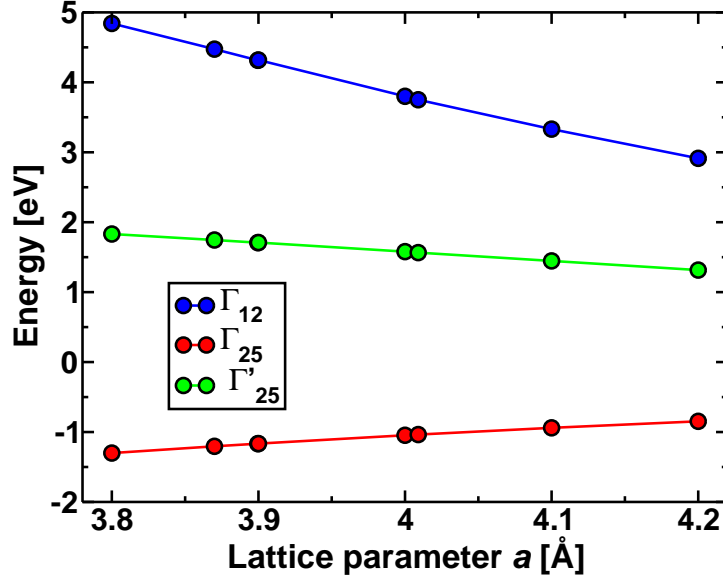
For the main text, we need an expression for Δ_σ :

$$\begin{aligned} \Delta_\sigma &= (\Gamma_{12} - \Gamma_{25})/2 \\ &= (\Gamma_{12} - \varepsilon_p)/2 \\ &\approx \frac{1}{2} \left(\varepsilon_d + \frac{6V_{sd\sigma}^2}{\Delta_{sd}} - \varepsilon_p \right) \\ &= \Delta_\pi + 3V_{sd\sigma}^2/\Delta_{sd}. \end{aligned} \quad (\text{G.18})$$

Finally the hopping parameters of both models are given in the Table G.2

Table G.2: Transfer integrals V_m for SrTiO₃ for two different lattice parameters a obtained from FPLO.

a	$V_{sd\sigma}$	$V_{pd\sigma}$	V_σ	$V_{pd\pi} = V_\pi$
3.9	2.9855	2.7237	2.0754	1.5590
4.0	2.7054	2.4064	1.8486	1.3854


 Figure G.1: Energies at the Γ point, Γ_{12} , Γ_{25} and Γ'_{25} for SrTiO₃ in dependence of the lattice parameter a , obtained from FPLO.

Remark I:

In the derivative Eq. (5.15), we have assumed that $\Delta'_\pi = 0$ and $\Delta'_{sd} = 0$. Since $\Delta_\pi = (\Gamma'_{25} - \Gamma_{25})/2$ and $\Delta_{sd} = \Gamma'_{25} - \Gamma_1$ this would only be correct, if Γ_1 , Γ_{25} and Γ'_{25} would be constant under lattice expansion. However, in Figure G.1 we see, that for Γ_{25} and Γ'_{25} this is not the case. Nevertheless, for $\Delta_\sigma = (\Gamma_{12} - \Gamma_{25})/2$, where the derivative is calculated for, Eq. (5.15), the dependence of Γ_{12} on a is much more pronounced.

Remark II:

In the WE model, we use E_m as model parameter, hence $\Gamma \approx \varepsilon$, and in the Harrison model, we use ε_m as model parameter, hence $\Gamma = \varepsilon$. However, there is some contribution of the CF acting on the *e.g.*, p states at the Γ point: the interactions with Sr states, with core states, with Madelung potentials etc. Therefore, ε_p is rather a model parameter than the true atomic energy, E_p , of a $2p$ state. If we speak about the model only, we may drop E_p and E_{t2g} , and retain only ε_p , ε_d and E_{eg} .

H Data sets and elaborated results for the quadrupole shift

This appendix reports tabulated and more elaborated results for the trends in the electronic part (n_{zz}) and the nuclear part (\tilde{Q}) of the quadrupole shift, of which the underlying physics was discussed in Chapter 6.

H.1 Trends in n_{zz}

In order to get a feeling for the size of the quadrupole shift, we have reported the ratio of the quadrupole shift and the regular quadrupole interaction for a set of elements in simple crystal structures (Figure 6.3). Those elements are identified here in the periodic table, Figure H.1. The quadrupole shift information in Figure 6.3 was obtained by a calculation of $n_{zz} = \sqrt{\frac{5}{\pi}} \lim_{r \rightarrow 0} n_{20}(r)/r^2$. We will give n_{zz}/ϵ_0 in SI units, meaning the obtained values from the band structure calculation, given in atomic units (e/a_0^5), will be multiplied with $c_0 = 4\pi a_0 Ha/e^2$.

1	2	3	4	5	6	7	8	9	10	11	12	13	14	15	16	17	18	
hydrogen 1 H 1.0079																	helium 2 He 4.0026	
lithium 3 Li 6.941	beryllium 4 Be 9.0122											boron 5 B 10.811	carbon 6 C 12.011	nitrogen 7 N 14.007	oxygen 8 O 15.999	fluorine 9 F 18.998	neon 10 Ne 20.180	
sodium 11 Na 22.990	magnesium 12 Mg 24.305											aluminum 13 Al 26.982	silicon 14 Si 28.086	phosphorus 15 P 30.974	sulfur 16 S 32.065	chlorine 17 Cl 35.453	argon 18 Ar 39.948	
potassium 19 K 39.098	calcium 20 Ca 40.078																	
		scandium 21 Sc 44.956	titanium 22 Ti 47.887	vanadium 23 V 50.942	chromium 24 Cr 51.996	manganese 25 Mn 54.938	iron 26 Fe 55.845	cobalt 27 Co 58.933	nickel 28 Ni 58.693	copper 29 Cu 63.546	zinc 30 Zn 65.38	gallium 31 Ga 69.723	germanium 32 Ge 72.61	arsenic 33 As 74.922	selenium 34 Se 78.96	bromine 35 Br 79.904	krypton 36 Kr 83.80	
rubidium 37 Rb 85.468	strontium 38 Sr 87.62	yttrium 39 Y 88.906	zirconium 40 Zr 91.224	niobium 41 Nb 92.906	molybdenum 42 Mo 95.96	technetium 43 Tc [98]	ruthenium 44 Ru 101.07	rhodium 45 Rh 102.91	palladium 46 Pd 106.42	silver 47 Ag 107.87	cadmium 48 Cd 112.41	indium 49 In 114.82	tin 50 Sn 118.71	antimony 51 Sb 121.76	tellurium 52 Te 127.60	iodine 53 I 126.90	xenon 54 Xe 131.29	
cesium 55 Cs 132.91	barium 56 Ba 137.33	* 57-70	lutetium 71 Lu 174.97	hafnium 72 Hf 178.49	tantalum 73 Ta 180.95	tungsten 74 W 183.84	rhenium 75 Re 186.21	osmium 76 Os 190.23	iridium 77 Ir 192.22	platinum 78 Pt 195.08	gold 79 Au 196.97	mercury 80 Hg 200.59	thallium 81 Tl 204.38	lead 82 Pb 207.2	bismuth 83 Bi 208.98	polonium 84 Po [209]	astatine 85 At [210]	radon 86 Rn [222]
francium 87 Fr [223]	radium 88 Ra [226]	** 89-102	lawrencium 103 Lr [262]	rutherfordium 104 Rf [267]	dubnium 105 Db [268]	seaborgium 106 Sg [271]	bohrium 107 Bh [272]	hassium 108 Hs [279]	meitnerium 109 Mt [279]	darmstadtium 110 Ds [281]	roentgenium 111 Rg [281]	unbinilium 112 Uub [285]	untrium 113 Uut [284]	unquadrium 114 Uuq [284]	unpentium 115 Uup [289]	unhexium 116 Uuh [289]	unseptium 117 Uus [294]	unoctium 118 Uuo [294]

Figure H.1: The periodic table of the elements. The studied elements are shaded in grey.

We investigate three series: hcp with ideal c/a ratio (1.633), bct with a ratio of $c/a = 1.2$ and bct with a ratio of $c/a = 0.8$. In order to keep the computational effort limited, we use experimental lattice parameters as they can be found on www.webelements.com. For At, we used the experimental lattice parameters of Po since there are none for At available. The elements, which are naturally not in hcp are transformed in hcp structure with the same volume per element as in the elemental solids. From these volumes also the bct with the two different ratios was calculated. This means for all three series the volume was kept constant.

In the Tables H.1 and H.2 the elements are ordered in the following groups, which will allow us to distinguish some periodic trends: (1) second main group (alkaline earth), s elements (2) $n = 3$, $3p$ elements (3) $n = 5$, $4d$ elements (4a) $n = 6$, $5d$ elements (4b) $n = 6$, $6p$ elements (5) fourth main group (carbon group), p elements (6) sixth main group (halogen elements), p elements

V_{zz} is given in 10^{21}V/m^2 and n_{zz}/ϵ_0 is given in 10^{42}V/m^4 . When talking about trends of n_{zz}/ϵ_0 or the EFG, only the magnitude is compared – not the absolute value.

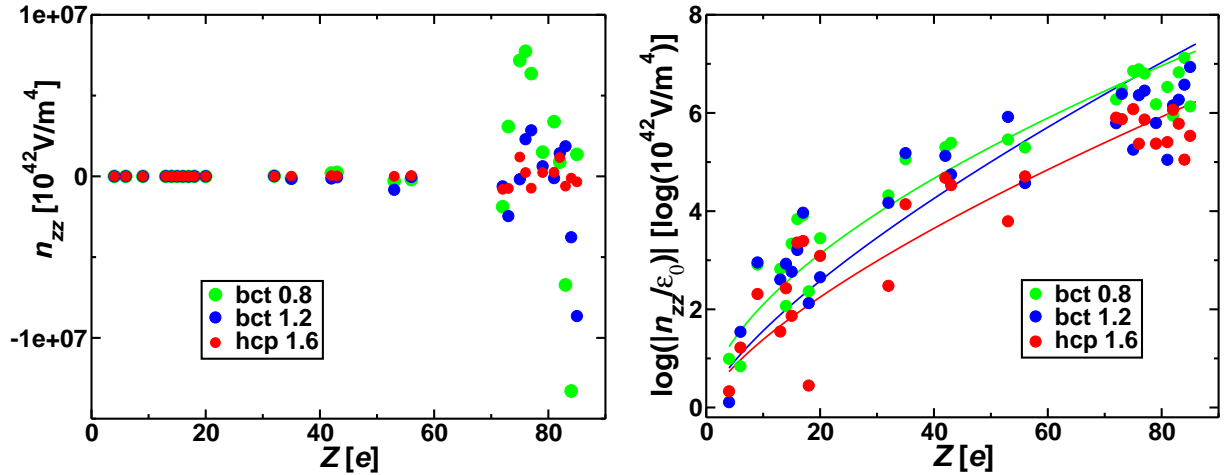


Figure H.2: The quantity n_{zz}/ϵ_0 (left graph) and $\log(|n_{zz}/\epsilon_0|)$ (right graph) as a function of the nuclear charge Z for hcp with $c/a = 1.6$ (red), bct with $c/a = 1.2$ (blue) and bct with $c/a = 0.8$ (green).

hcp elements

We start comparing V_{zz} and n_{zz}/ϵ_0 for the hcp structure. We compare these quantities for the two convergent cases: non-relativistic (NREL) with a point nucleus and full relativistic (FREL) with finite nucleus, see Tab H.1.

For the influence of the FREL with finite nucleus we observe, that in most cases V_{zz} does not change much when going from the NREL to the FREL version. But for some of the heavy elements (Re, Bi, Po, At, Br, I) it makes quite a difference if the NREL or the more realistic FREL version is used in the calculation. n_{zz}/ϵ_0 , on the other hand, is always larger for finite nucleus in the FREL versions than for the point nucleus with NREL version (except for I). For the lighter elements ((1), (2), (3), (5) except Pb and (6)) the combination of relativity and a finite nucleus increase n_{zz}/ϵ_0 by a factor 2 to 9. For the heavier elements (4a) and (4b) the factor is larger. In (4a) the factor increases from 15 (Hf) to 70 (Au) except for Os with a factor of 7. In (4b) the factor is around 40, except for Po and At - here the factor is only 2 and 6, respectively.

For the tendency of n_{zz}/ϵ_0 we observe, that it increases in both cases when going down a group (see (1), (5), (6) and (2) vs. (4b)). In both cases n_{zz}/ϵ_0 increases for p elements when going from left to right (see (2), (4b) and (5) vs (6)) and decreases for d elements (see (3) and (4a)). (Except for the noble gas Ar - which has a full shell and should therefore decrease.) In both cases n_{zz}/ϵ_0 is larger for p elements, than for d elements preceding them (see (4a) and (4b)).

The comparison of n_{zz}/ϵ_0 and V_{zz} shows, that the former quantity is much more sensitive to the main quantum number. n_{zz}/ϵ_0 varies between eight (six) orders of magnitude in FREL (NREL) treatment, whereas V_{zz} varies only between three orders of magnitude.

bct elements

In order to exclude that the observations in the previous section are too closely related to the hcp structure, we repeat the discussion for two bct structures with the ratios $c/a = 1.2$ and $c/a = 0.8$. Both cases are calculated for the FREL version with a finite nucleus. We observe for the tendency of n_{zz}/ϵ_0 that like in the hcp case, in both ratio cases n_{zz}/ϵ_0 increases when going down a group (see (1), (5), (6) and (2) vs. (4b)) Also here, for both ratio cases n_{zz}/ϵ_0 increases for p elements when going from left to right (see (2), (4b) and (5) vs (6)). (Again, except for Ar.) For the d elements it is different here: n_{zz}/ϵ_0 increases from Hf to Re (1.2)/Os(0.8) and then decreases up

to Au. Also (3) is different here, decreasing for 1.2 and increasing for 0.8 - but two values maybe too little to get this trend. Unlike the hcp case, n_{zz}/ϵ_0 is of similar magnitude for p elements and d elements preceding them (see (4a) and (4b)), in both ratio cases. But p elements have the largest value for n_{zz}/ϵ_0 (At in 1.2 and Po in 0.8).

Table H.1: n_{zz}/ϵ_0 in 10^{42} V/m⁴ and V_{zz} in 10^{21} V/m² for the hcp comparison, see text. The first two columns are calculated non-relativistic with a point nucleus and the second two columns full relativistic with a finite nucleus.

Element		n_{zz}/ϵ_0	V_{zz}	n_{zz}/ϵ_0	V_{zz}
Be	(1)	$6.57 \cdot 10^{-1}$	0.004	$2.14 \cdot 10^{\pm 0}$	0.004
Ca		$-2.48 \cdot 10^{+2}$	-0.401	$-1.23 \cdot 10^{+3}$	-0.401
Ba		$-5.74 \cdot 10^{+3}$	-0.703	$-5.10 \cdot 10^{+4}$	-0.821
Al	(2)	$-1.02 \cdot 10^{+1}$	-0.054	$-3.54 \cdot 10^{+1}$	-0.052
Si		$-7.84 \cdot 10^{+1}$	-0.263	$-2.69 \cdot 10^{+2}$	-0.267
P		$1.70 \cdot 10^{+1}$	0.062	$7.38 \cdot 10^{+1}$	0.054
S		$6.29 \cdot 10^{+2}$	1.575	$2.30 \cdot 10^{+3}$	1.579
Cl		$-6.81 \cdot 10^{+2}$	-1.488	$-2.46 \cdot 10^{+3}$	-1.388
Ar		$7.10 \cdot 10^{-1}$	0.001	$2.80 \cdot 10^{\pm 0}$	0.001
Mo	(3)	$-6.65 \cdot 10^{+3}$	-1.198	$-4.77 \cdot 10^{+4}$	-1.778
Tc		$-5.57 \cdot 10^{+3}$	-0.531	$-3.39 \cdot 10^{+4}$	-0.824
Hf	(4a)	$5.26 \cdot 10^{+4}$	5.193	$8.02 \cdot 10^{+5}$	5.156
Ta		$2.96 \cdot 10^{+4}$	1.073	$7.47 \cdot 10^{+5}$	1.247
Re		$-4.14 \cdot 10^{+4}$	-1.531	$-1.20 \cdot 10^{+6}$	-3.568
Os		$-3.57 \cdot 10^{+4}$	-0.736	$-2.37 \cdot 10^{+5}$	-0.554
Ir		$-2.16 \cdot 10^{+2}$	1.220	$7.34 \cdot 10^{+5}$	1.633
Au		$-3.36 \cdot 10^{+3}$	-0.070	$-2.37 \cdot 10^{+5}$	-0.161
Tl	(4b)	$-6.22 \cdot 10^{+3}$	-0.371	$-2.54 \cdot 10^{+5}$	-0.416
Pb		$-6.17 \cdot 10^{+2}$	-2.150	$-1.16 \cdot 10^{+6}$	-2.445
Bi		$1.19 \cdot 10^{+4}$	1.212	$6.05 \cdot 10^{+5}$	0.385
Po		$7.87 \cdot 10^{+4}$	5.533	$1.12 \cdot 10^{+5}$	2.586
At		$-8.99 \cdot 10^{+4}$	-6.330	$3.41 \cdot 10^{+6}$	1.141
C	(5)	$-7.89 \cdot 10^{\pm 0}$	-0.182	$-1.66 \cdot 10^{+1}$	-0.181
Si		$-7.80 \cdot 10^{+1}$	-0.263	$-2.69 \cdot 10^{+2}$	-0.267
Ge		$-1.11 \cdot 10^{+2}$	-0.068	$3.01 \cdot 10^{+2}$	0.016
Pb		$-3.39 \cdot 10^{+4}$	-2.150	$-1.16 \cdot 10^{+6}$	-2.445
F	(6)	$-8.30 \cdot 10^{+1}$	-0.782	$-2.05 \cdot 10^{+2}$	-0.735
Cl		$-6.81 \cdot 10^{+2}$	-1.488	$-2.46 \cdot 10^{+3}$	-1.388
Br		$-6.38 \cdot 10^{+3}$	-2.887	$-1.38 \cdot 10^{+3}$	-1.090
I		$-2.16 \cdot 10^{+4}$	-4.047	$-6.21 \cdot 10^{+4}$	-0.342
At		$-8.99 \cdot 10^{+4}$	-6.330	$3.41 \cdot 10^{+5}$	1.141

For the influence of the c/a change we observe: for 15 of the 27 elements V_{zz} is larger for $c/a = 0.8$ than for 1.2. For Hf, Re, Os Bi and Po the EFG is between 10 and 31. For 17 of the 27 elements n_{zz}/ϵ_0 is larger for $c/a = 0.8$ than for 1.2 all s and d elements ((1),(3)(4) and some p elements (not (6))). The largest n_{zz}/ϵ_0 (order of 10^{+5}) is obtained for At for $c/a = 1.2$ and for Po, Os, Re, Bi and Ir for $c/a = 0.8$.

The graphs in Figure H.2 show n_{zz}/ϵ_0 and $\log(n_{zz}/\epsilon_0)$ as a function of the nuclear charge Z . We see, that there is a difference between these structures, but the trend is very similar. A large value for n_{zz}/ϵ_0 will be obtained from very heavy elements.

H.2 Models for the nuclear charge density, Q and \tilde{Q}

In this section, we will make explicit calculations of Q and \tilde{Q} for two phenomenological nuclear models. From this, we will get insight how the nuclear quantities Q and \tilde{Q} are affected by which features of the nuclear shape, and for which kind of nuclei we can expect them to be large. We start by restating the expressions for Q Eq. (6.28) and \tilde{Q} Eq. (6.29)

$$eQ = \int \rho(\vec{r})(3z^2 - r^2)d^3r \quad (\text{H.1})$$

$$e\tilde{Q} = \int \rho(\vec{r})(3z^2 - r^2)r^2d^3r. \quad (\text{H.2})$$

H.2.1 Axially symmetric ellipsoid

First, we consider a quite simple example for the charge density of the nucleus, where the nucleus has the form of an axially symmetric¹ ellipsoid: $\frac{x^2}{a^2} + \frac{y^2}{a^2} + \frac{z^2}{c^2} = 1$. Inside this ellipsoid with the parameters a and c , the density is assumed to be constant $\rho(\vec{r}) = \rho_0$ and outside the ellipsoid the density is zero.

Therefore, we can write the charge density as:

$$\rho(\vec{r}) = \rho_0 [\theta(x+a) - \theta(x-a)] [\theta(y+\tilde{b}) - \theta(y-\tilde{b})] [\theta(z+\tilde{c}) - \theta(z-\tilde{c})] \quad (\text{H.3})$$

with $\tilde{b} = \sqrt{a^2 - x^2}$ and $\tilde{c} = \sqrt{a^2 - x^2 - y^2} \frac{a}{c}$.

For the total charge we obtain

$$eZ = \int \rho(\vec{r})d^3r = \rho_0 \cdot V_{\text{ellipsoid}} = \rho_0 \frac{4\pi}{3} a^2 c \quad \Leftrightarrow \quad \rho_0 = \frac{3eZ}{4\pi a^2 c}.$$

The quadrupole moment is calculated by inserting the density Eq. (H.3) in Eq. (H.1) and taking the constant density out of the integral and restricting the integration limits to the ellipsoid borders

$$\begin{aligned} eQ &= \rho_0 \int_{\text{ellipsoid}} (3z^2 - r^2)d^3r \\ &= \rho_0 \int_{-a}^a dx \int_{-\sqrt{a^2-x^2}}^{\sqrt{a^2-x^2}} dy \int_{-\sqrt{a^2-x^2-y^2}\frac{a}{c}}^{\sqrt{a^2-x^2-y^2}\frac{a}{c}} dz \left(2z^2 - (x^2 + y^2) \right) \\ &= \rho_0 \frac{8\pi}{5} a^4 c \left[\left(\frac{c}{a} \right)^2 - 1 \right]. \end{aligned}$$

Inserting the charge density yields

$$Q = \frac{2}{5} Z a^2 \left[\left(\frac{c}{a} \right)^2 - 1 \right]. \quad (\text{H.4})$$

In case of a sphere ($a = c$), the quadrupole moment vanishes $Q = 0$, for a rugby ball ($c > a$) the quadrupole moment is positive $Q > 0$ and for a pancake ($c < a$) the quadrupole moment is negative $Q < 0$.

¹A general ellipsoid: $\frac{x^2}{a^2} + \frac{y^2}{b^2} + \frac{z^2}{c^2} = 1$ with $a \neq b \neq c$ has no axially symmetry.

The same calculation for \tilde{Q} yields

$$\begin{aligned} e\tilde{Q} &= \int_{\text{ellipsoid}} \rho(\vec{r})(3z^2 - r^2)r^2 d^3r \\ &= \rho_0 \frac{8\pi}{105} a^6 c \left[3 \left(\frac{c}{a} \right)^4 + \left(\frac{c}{a} \right)^2 - 4 \right]. \end{aligned}$$

Inserting the charge density yields:

$$\tilde{Q} = \frac{2}{35} Z a^4 \left[3 \left(\frac{c}{a} \right)^4 + \left(\frac{c}{a} \right)^2 - 4 \right]. \quad (\text{H.5})$$

We obtain the same behaviour as above: in case of a sphere ($a = c$) \tilde{Q} vanishes. For a rugby ball ($c > a$) \tilde{Q} is positive and for a pancake ($c < a$) \tilde{Q} is negative. \tilde{Q} follows the sign of Q . This quantity has the unit of $b^2 = 10^{-56} m^4$.

Since there is no new variable in \tilde{Q} , the measurement of Q and \tilde{Q} can determine both a and c . Since each quantity itself has two parameters, knowing only Q or only \tilde{Q} one can not determine the ellipsoid: there are many possibilities to vary a and c to obtain the measured quantity. But measuring both, Q and \tilde{Q} , one can get shape ($\frac{c}{a}$) and size (a) of the ellipsoid, which is describing the nucleus in this model.

It is possible to rewrite \tilde{Q} as a function of a , c and Q :

$$\tilde{Q} = \frac{a^2}{7} \left(4 + 3 \left(\frac{c}{a} \right)^2 \right) \cdot Q. \quad (\text{H.6})$$

We are interested in a large value for \tilde{Q} , since these will give large correction energies. This is the case for a large a and a large value for $\frac{c}{a}$ (which means a large Q). This means a large nucleus, which deviates much from a sphere, will give a large \tilde{Q} . Be aware that $\frac{c}{a}$ in the first place influences Q and only as a secondary effect influences \tilde{Q} itself. The term with only a^2 is dominating in Eq. (H.6).

Evaluating a ratio of $\left(\frac{c}{a}\right)^2 = 0.9$ and $\left(\frac{c}{a}\right)^2 = 1.1$ respectively yields nearly the same value for absolute value of Q , but the magnitude of \tilde{Q} will be larger for the rugby ball $\left(\frac{c}{a}\right)^2 = 1.1$ than for the pancake $\left(\frac{c}{a}\right)^2 = 0.9$. Hence a positive Q will give a larger \tilde{Q} than a negative Q for this model.

H.2.2 Nuclear model

Now, we will consider a more realistic model, where the nucleus is phenomenological described by a deformed sphere, where the radius $R(\theta)$ is given by:

$$R(\theta) = a(1 + \beta_2 Y_{20}(\theta) + \beta_4 Y_{40}(\theta) + \dots). \quad (\text{H.7})$$

a is the monopole radius and β_i are the deformation parameters. To get a feeling for this model, we plot

$$\begin{aligned} x &= R(\theta) \cos(\varphi) \sin(\theta) \\ y &= R(\theta) \sin(\varphi) \sin(\theta) \\ z &= R(\theta) \cos(\theta) \end{aligned}$$

with $a = 2$ fm for different values of β_2 and β_4 : in Figure H.3, β_4 is zero and only β_2 deviates from zero. The nucleus looks very similar to an axially symmetric ellipsoid, but it is none (in general), because the condition $\frac{x^2}{a^2} + \frac{y^2}{a^2} + \frac{z^2}{c^2} = 1$ does not hold. For $\beta_2 = 0$ the nucleus is a

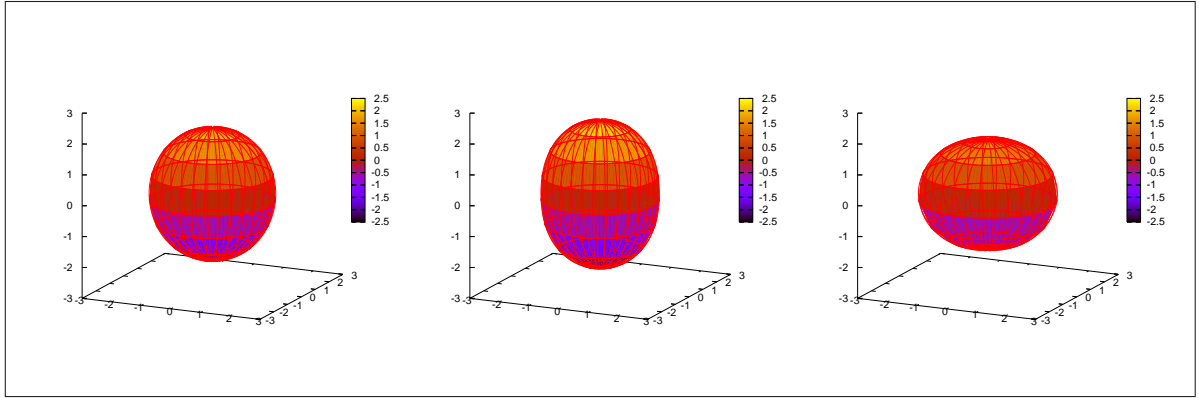


Figure H.3: Schematic pictures of a nucleus, using the nuclear model Eq. (H.7) for the radius of the nucleus. Left: $\beta_2 = 0.1$, $\beta_4 = 0.0$, middle: $\beta_2 = 0.3$, $\beta_4 = 0.0$, right: $\beta_2 = -0.2$, $\beta_4 = 0.0$.

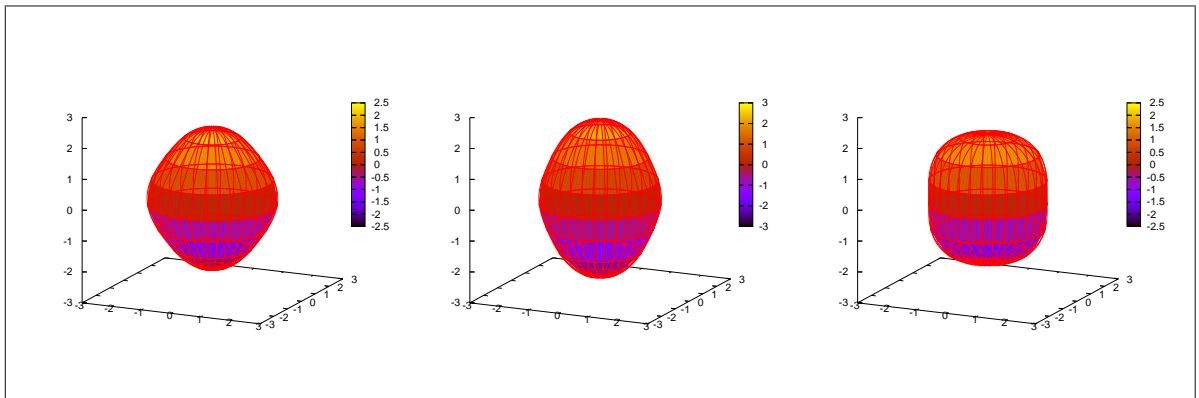


Figure H.4: Schematic pictures of a nucleus, using the nuclear model Eq. (H.7) for the radius of the nucleus. Left: $\beta_2 = 0.1$, $\beta_4 = 0.1$, middle: $\beta_2 = 0.3$, $\beta_4 = 0.1$, right: $\beta_2 = 0.2$, $\beta_4 = -0.1$.

sphere. For $\beta_2 > 0$ the nucleus takes the form of a rugby ball, deviating more and more from the sphere the larger β_2 gets. For $\beta_2 < 0$ the nucleus takes the form of a pancake, getting more flat for increasing β_2 .

In Figure H.4, β_4 is nonzero. It is responsible for deviation from the apparently axially symmetric looking ellipsoid: for $\beta_4 > 0$ the nucleus gets pointier at the equator and the poles (taking really the form of a rugby ball) and for $\beta_4 < 0$ the nucleus takes the form of the yellow plastic part of the “Kinder Surprise” egg². The larger β_4 , the larger the deviation.

Case $\beta_4 = 0$

We consider a nucleus with $\beta_4 = 0$ and $\beta_2 = \beta$. The volume of this nucleus is:

$$\begin{aligned} V &= \int_0^{2\pi} d\varphi \int_0^{R(\theta)} dr \int_0^\pi d\theta r^2 \sin(\theta) \quad \text{with} \quad R(\theta) = a(1 + \beta Y_{20}(\theta)) \\ &= \frac{4\pi}{3} a^3 \left[1 + \frac{12}{5} \alpha^2 + \frac{16}{35} \alpha^3 \right] \quad \text{with} \quad \alpha = \frac{1}{2} \sqrt{\frac{5}{4\pi}} \beta. \end{aligned}$$

²http://en.wikipedia.org/wiki/Kinder_Surprise

It can easily be seen, that this deformed nucleus is a sphere for $\alpha = \beta = 0$ and an axially symmetric ellipsoid, if this volume is identical to the volume of the ellipsoid ($\frac{4\pi}{3}a^2c$), which gives the condition:

$$\left[1 + \frac{12}{5}\alpha^2 + \frac{16}{35}\alpha^3\right] \stackrel{!}{=} \frac{c}{a}.$$

Therefore, the axially symmetric ellipsoid is just a special case of this more general deformation.

For the quadrupole moment Q_{20} we obtain:

$$\begin{aligned} Q_{20} &= \sqrt{\frac{4\pi}{15}}\rho_0 \int_0^{2\pi} d\varphi \int_0^{R(\theta)} dr \int_0^\pi d\theta r^2 \sin(\theta)r^2 Y_{20}(\theta) \\ &= \sqrt{\frac{4\pi}{15}}\beta\rho_0 a^5 \left[1 + \frac{1144}{1001}\alpha + \frac{3432}{1001}\alpha^2 + \frac{2080}{1001}\alpha^3 + \frac{848}{1001}\alpha^4\right]. \end{aligned}$$

For \tilde{Q}_{20} we obtain:

$$\begin{aligned} \tilde{Q}_{20} &= \sqrt{\frac{4\pi}{15}}\rho_0 \int_0^{2\pi} d\varphi \int_0^{R(\theta)} dr \int_0^\pi d\theta r^4 \sin(\theta)r^2 Y_{20}(\theta) \\ &= \sqrt{\frac{4\pi}{15}}\frac{5}{7}\beta\rho_0 a^7 \frac{1}{12155} [17017 + 29172\alpha + 145860\alpha^2 + 176800\alpha^3 \\ &\quad + 216240\alpha^4 + 114240\alpha^5 + 30400\alpha^6]. \end{aligned}$$

β is a very small number, *e.g.*, $\beta = 0.2$. This means α will be even smaller $\alpha = 0.063$ and the higher powers of α will be even smaller, *e.g.*, $\alpha^2 = 0.004$. Hence each term in the brackets in Q_{20} is one order of magnitude smaller than the preceding one. The same is true for the \tilde{Q}_{20} . The main contributions are linear in $\alpha \propto \beta$ (with the volume of a sphere)

$$eQ = Q_{zz} = 3\frac{2}{\sqrt{3}}Q_{20} = 2\sqrt{\frac{4\pi}{5}}\beta\rho_0 a^5 = 3\sqrt{\frac{4\pi}{5}}\frac{eZ}{2\pi}\beta a^2 \quad (\text{H.8})$$

$$e\tilde{Q} = \tilde{Q}_{zz} = 3\frac{2}{\sqrt{3}}\tilde{Q}_{20} = 2\sqrt{\frac{4\pi}{5}}\beta\rho_0 a^7 = a^2 \cdot eQ. \quad (\text{H.9})$$

Taking into account also the α^2 contribution we get (now the volume is more complicated)

$$eQ = Q_{zz} = 3\frac{2}{\sqrt{3}}Q_{20} = 2\sqrt{\frac{4\pi}{5}}\beta\rho_0 a^5 \left(1 + \frac{4}{7}\sqrt{\frac{5}{4\pi}}\beta\right) = 3\sqrt{\frac{4\pi}{5}}\frac{eZ}{2\pi}\beta a^2 \frac{\left(1 + \frac{8}{7}\alpha\right)}{\left(1 + \frac{12}{5}\alpha^2\right)} \quad (\text{H.10})$$

$$e\tilde{Q} = \tilde{Q}_{zz} = 3\frac{2}{\sqrt{3}}\tilde{Q}_{20} = 2\sqrt{\frac{4\pi}{5}}\beta\rho_0 a^7 \left(1 + \frac{6}{7}\sqrt{\frac{5}{4\pi}}\beta\right) = a^2 \cdot eQ + \frac{4}{7}\beta^2\rho_0 a^7. \quad (\text{H.11})$$

Here, we have to make a case study for the centre of the equations Eq. (H.10) and Eq. (H.11): for positive β (meaning positive Q) the term quadratic in β has the same sign and increases Q and \tilde{Q} . But if β (and therefore Q) is negative, the term quadratic in β is still positive and therefore decreases Q and \tilde{Q} . In both cases this effect is not large, since the term quadratic in β is about one magnitude smaller than the term linear in β . But it means, that like in the case of the ellipsoid, a positive quadrupole moment will give a larger correction \tilde{Q} .

And like in the other three examples: \tilde{Q} is large when the quadrupole moment Q (the deformation β) is large and the nucleus is large.

Case $\beta_4 \neq 0$

Now, we use two β parameters:

$$\begin{aligned} R(\theta) &= a(1 + \beta_2 Y_{20}(\theta) + \beta_4 Y_{40}(\theta)) \\ &= a(1 + \alpha_2(3 \cos^2(\theta) - 1) + \alpha_4(35 \cos^4(\theta) - 30 \cos^2(\theta) + 3)) \end{aligned}$$

with $\alpha_2 = \frac{1}{2} \sqrt{\frac{5}{4\pi}} \beta_2$ and $\alpha_4 = \frac{1}{8} \sqrt{\frac{9}{4\pi}} \beta_4$.

The volume of this nucleus is

$$\begin{aligned} V &= \int_0^{2\pi} d\varphi \int_0^{R(\theta)} dr \int_0^\pi d\theta r^2 \sin(\theta) \\ &= \frac{4\pi}{3} a^3 \left[1 + \frac{20}{7} \alpha_2^2 + \frac{64}{3} \alpha_4^2 + \frac{2560}{231} \alpha_2 \alpha_4^2 + \frac{192}{35} \alpha_2^2 \alpha_4 + \frac{9216}{1001} \alpha_4^3 \right]. \end{aligned}$$

Again, the nucleus has the volume of a sphere plus correction terms in higher orders (quadratic or cubic) of the deformation parameters β_2 and β_4 .

The quadrupole moment of this nucleus is:

$$\begin{aligned} Q_{20} &= \sqrt{\frac{4\pi}{15}} \rho_0 \int_0^{2\pi} d\varphi \int_0^{R(\theta)} dr \int_0^\pi d\theta r^2 \sin(\theta) r^2 Y_{20}(\theta) \\ &= \sqrt{\frac{4\pi}{15}} \beta_2 \rho_0 a^5 \left(1 + \frac{8}{7} \alpha_2 \right) + \sqrt{\frac{4\pi}{15}} \sqrt{\frac{9}{5}} \beta_4 \rho_0 a^5 \left(\frac{16}{7} \alpha_2 + \frac{1600}{693} \alpha_4 \right) + \mathcal{O}(\alpha_i^3). \end{aligned} \quad (\text{H.12})$$

The first part of this Q_{20} (order α_2 and α_2^2) is identical to Eq. (H.10) as it should be, since here α_4 is not involved yet. The lowest orders of α_4 are given in the second part of Eq. (H.12): $\alpha_4 \alpha_2$ and α_4^2 . Unfortunately there is no term linear in α_4 , which means we have to consider these expressions up to the quadratic order to get information about β_4 .

For \tilde{Q}_{20} we obtain for both β parameters:

$$\begin{aligned} \tilde{Q}_{20} &= \sqrt{\frac{4\pi}{15}} \rho_0 \int_0^{2\pi} d\varphi \int_0^{R(\theta)} dr \int_0^\pi d\theta r^4 \sin(\theta) r^2 Y_{20}(\theta) \\ &= \sqrt{\frac{4\pi}{15}} \beta_2 \rho_0 a^7 \left(1 + \frac{12}{7} \alpha_2 \right) + \sqrt{\frac{4\pi}{15}} \sqrt{\frac{9}{5}} \beta_4 \rho_0 a^7 \left(\frac{24}{7} \alpha_2 + \frac{1056}{693} \alpha_4 \right) + \mathcal{O}(\alpha_i^3). \end{aligned} \quad (\text{H.13})$$

Also here, the first part of this \tilde{Q}_{20} (order α_2 and α_2^2) is identical to Eq. (H.11) as it should be, since here α_4 is not involved yet. The lowest orders of α_4 are $\alpha_4 \alpha_2$ and α_4^2 .

We can rewrite $e\tilde{Q} = \tilde{Q}_{zz} = \frac{2}{\sqrt{3}} \tilde{Q}_{20}$ as a function of $eQ = Q_{zz} = 3 \frac{2}{\sqrt{3}} Q_{20}$ (neglecting cubic and higher orders of α_i):

$$eQ = 2\sqrt{\frac{4\pi}{5}} \beta_2 \rho_0 a^5 \left(1 + \frac{8}{7} \alpha_2 \right) + 2\sqrt{\frac{4\pi}{5}} \sqrt{\frac{9}{5}} \beta_4 \rho_0 a^5 \left(\frac{16}{7} \alpha_2 + \frac{1600}{693} \alpha_4 \right) \quad (\text{H.14})$$

$$\begin{aligned} e\tilde{Q} &= a^2 \cdot eQ + 2\sqrt{\frac{4\pi}{5}} \beta_2 \rho_0 a^7 \frac{4}{7} \alpha_2 + 2\sqrt{\frac{4\pi}{5}} \sqrt{\frac{9}{5}} \beta_4 \rho_0 a^7 \left(\frac{8}{7} \alpha_2 - \frac{544}{693} \alpha_4 \right) \\ &= a^2 \cdot eQ + 2a^7 \rho_0 \left[\underbrace{\frac{2}{7}}_{0.29} \beta_2^2 + \underbrace{\sqrt{\frac{9}{5}} \frac{4}{7}}_{0.77} \beta_2 \beta_4 - \underbrace{\frac{68}{338}}_{0.20} \beta_4^2 \right]. \end{aligned} \quad (\text{H.15})$$

We have to distinguish between three different cases:

$-\beta_2, \beta_4 > 0$: Q is positive because each term in Eq. (H.14) is positive. Since both β_i fulfil $0 < \beta_i < 1$, \tilde{Q} Eq. (H.15) is also positive, the term with the minus is never dominating. Hence \tilde{Q}

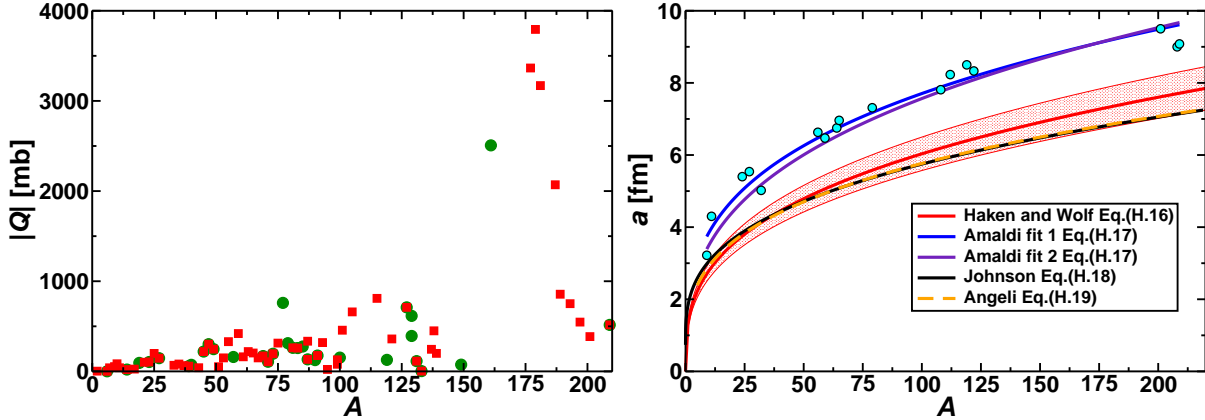


Figure H.5: **Left:** the absolute value of the quadrupole moment Q in dependence of the mass number A . The values are taken from the literature: Pyykkö [58] (green circles) and Harris *et al.* [42] (red squares). **Right:** nuclear radius a in dependence of A obtained by different measurements, see text.

is large, when Q is large and a is large. \tilde{Q} larger for $\beta_2 > \beta_4$ than for $\beta_2 = \beta_4$ or $\beta_2 < \beta_4$ because of the minus sign in Eq. (H.15).

$-\beta_2, \beta_4 < 0$: Q is negative because the dominating term in Eq. (H.14) is the one linear in β_2 . All the other terms will give positive contributions! From this model it can be seen, that a nucleus with both $\beta_i < 0$ will give a smaller magnitude of the quadrupole moment than a nucleus with both $\beta_i > 0$. In Eq. (H.15) the first two terms of the $[\]$ expression will be positive and the last one negative. But the main contribution to \tilde{Q} is a^2Q , so \tilde{Q} is also negative. The magnitude of \tilde{Q} is smaller for both $\beta_i < 0$ than both $\beta_i > 0$.

-Both β_i have a different sign: the sign of β_2 determines the sign of Q and therefore the sign of \tilde{Q} . It depends on their ratio, how the higher order terms increase or decrease Q resp. \tilde{Q} .

We conclude, that the largest values for Q and therefore also \tilde{Q} are obtained for both β_i being positive (preferably $\beta_2 > \beta_4$ to increase \tilde{Q}). Furthermore a large nucleus a and a large deformation increases Q as well as \tilde{Q} .

H.2.3 Trends for Q and R

Evaluating both the axially symmetric ellipsoid Appendix H.2.1 and the nuclear model Appendix H.2.2 showed us, that there are two conditions to get a large \tilde{Q} : first, we need a nucleus with a large deformation factor ($\frac{c}{a}$ or β_i , respectively), which is proportional to a large quadrupole moment Q , where a positive quadrupole moment will be preferred. Second, we need a large nucleus (large a).

Now, we will inspect these two quantities Q and a for real nuclei. We start with the quadrupole moment Q in dependence of the mass number A . In the literature there are (among others) two papers listing values for Q for various elements and isotopes, one was compiled by Pyykkö in 2001 [58] and the other one by Harris *et al.* in 2002 [42]. The quadrupole moments in dependence of the mass number A are shown in the left graph in Figure H.5. We see that for the heavy nuclei ($A > 150$) the quadrupole moments are much larger than for the light and medium nuclei.

Next, we will enquire the size of the nucleus. In the textbook of Haken and Wolf from 2003 [221], the nuclear radius is defined as the distance, where the repulsive coulomb force and the attractive nuclear force are of similar strength. Empirically studies yield for the nuclear radius a

in dependence of the mass number A

$$a(A) = (1.3 \pm 0.1) A^{\frac{1}{3}} \text{ fm.} \quad (\text{H.16})$$

We will compare this with other data found in the literature. In 1947, a table with several nuclear radii was published by Amaldi *et al.* [228]. These can be fitted to

$$a(A) = (1.94 \cdot A^{0.3}) \text{ fm} \quad \text{or} \quad a(A) = (1.63 \cdot A^{\frac{1}{3}}) \text{ fm.} \quad (\text{H.17})$$

In 1985, Johnson *et al.* [229] obtained a function for the nuclear radius in dependence of A

$$a(A) = (1.079 A^{\frac{1}{3}} + 0.736) \text{ fm.} \quad (\text{H.18})$$

In 2004, Angeli [171] found

$$a(A) = 1.489 A^{0.294} \text{ fm.} \quad (\text{H.19})$$

Contrary to Johnson, Angeli's data set is consistent: values from different measurement methods are brought into agreement with each other as much as possible (*e.g.*, by taking into account that one method is known to systematically overestimate the radii). Furthermore, Angeli applied correlation checks to verify that there weren't spurious wrong data points in the set. Hence, his data set is much cleaner, which improves the value of even a simple fit function.

A plot of all four functions for the radius is shown in the right graph in Figure H.5.

We see, that the radii obtained by these four estimations agree reasonable with each other, especially the radii obtained from the newest measurements: there is almost no change between 1985 and 2004.

We conclude from these dependencies, that heavy elements will have larger quadrupole moments Q and larger nuclear radii R and will therefore yield larger values for the correction \tilde{Q} .

This is in cooperation with the electronic investigation, where heavier elements will also have a larger n_{zz} .

Remark: In the paper of Johnson *et al.* [229] and Angeli [171], the root-mean-square of the nuclear radius (RMS) $\sqrt{\langle r^2 \rangle}$ is given. The connection between the RMS and the radius of a sphere a , in which the nuclear charge is uniformly distributed is given by Ref. [230]

$$a = \sqrt{\frac{5}{3}} \sqrt{\langle r^2 \rangle}. \quad (\text{H.20})$$

Table H.2: n_{zz}/ϵ_0 in 10^{42} V/m⁴ and V_{zz} in 10^{21} V/m² for the bct comparison, see text. All quantities are calculated full relativistic with a finite nucleus. The first two columns are calculated for a ratio of $c/a = 1.2$, and the second two columns for a ratio of $c/a = 0.8$.

Element		n_{zz}/ϵ_0	V_{zz}	n_{zz}/ϵ_0	V_{zz}
Be	(1)	$7.79 \cdot 10^{-1}$	0.042	$-9.81 \cdot 10^{\pm 0}$	-0.371
Ca		$-4.50 \cdot 10^{+2}$	-0.185	$2.81 \cdot 10^{+3}$	0.974
Ba		$3.74 \cdot 10^{+4}$	0.356	$1.98 \cdot 10^{+5}$	2.883
Al	(2)	$-4.05 \cdot 10^{+2}$	-0.474	$-6.65 \cdot 10^{+2}$	-0.816
Si		$-8.47 \cdot 10^{+2}$	-0.836	$1.17 \cdot 10^{+2}$	0.119
P		$-5.84 \cdot 10^{+2}$	-0.483	$2.18 \cdot 10^{+3}$	1.744
S		$1.62 \cdot 10^{+3}$	1.110	$6.89 \cdot 10^{+3}$	4.391
Cl		$9.29 \cdot 10^{+3}$	5.119	$8.30 \cdot 10^{+3}$	4.673
Ar		$-1.34 \cdot 10^{+2}$	-0.063	$-2.32 \cdot 10^{+2}$	-0.109
Mo	(3)	$1.34 \cdot 10^{+5}$	4.156	$-2.01 \cdot 10^{+5}$	-8.302
Tc		$5.57 \cdot 10^{+4}$	3.524	$-2.46 \cdot 10^{+5}$	-11.838
Hf	(4a)	$6.18 \cdot 10^{+5}$	1.134	$1.88 \cdot 10^{+6}$	12.889
Ta		$2.46 \cdot 10^{+6}$	8.503	$-3.08 \cdot 10^{+6}$	-6.911
Re		$1.79 \cdot 10^{+5}$	5.737	$-7.17 \cdot 10^{+6}$	-30.978
Os		$-2.30 \cdot 10^{+6}$	-1.649	$-7.74 \cdot 10^{+6}$	-22.387
Ir		$-2.85 \cdot 10^{+6}$	-8.891	$-6.36 \cdot 10^{+6}$	-3.775
Au		$-6.24 \cdot 10^{+5}$	-0.795	$-1.50 \cdot 10^{+6}$	-6.483
Tl	(4b)	$1.11 \cdot 10^{+5}$	-0.180	$-3.39 \cdot 10^{+6}$	-7.581
Pb		$-1.42 \cdot 10^{+6}$	-3.069	$-8.82 \cdot 10^{+5}$	-1.897
Bi		$-1.86 \cdot 10^{+6}$	-5.012	$6.72 \cdot 10^{+6}$	10.886
Po		$3.77 \cdot 10^{+6}$	9.195	$1.33 \cdot 10^{+7}$	17.566
At		$8.65 \cdot 10^{+6}$	13.732	$-1.36 \cdot 10^{+6}$	5.561
C	(5)	$-3.48 \cdot 10^{+1}$	-0.374	$-6.94 \cdot 10^{\pm 0}$	-0.096
Si		$-8.47 \cdot 10^{+2}$	-0.836	$1.17 \cdot 10^{+2}$	0.119
Ge		$-1.48 \cdot 10^{+4}$	-1.207	$-2.10 \cdot 10^{+4}$	-1.718
Pb		$-1.42 \cdot 10^{+6}$	-3.069	$-8.82 \cdot 10^{+5}$	-1.897
F	(6)	$9.02 \cdot 10^{+2}$	3.166	$8.15 \cdot 10^{+2}$	2.939
Cl		$9.29 \cdot 10^{+3}$	5.119	$8.30 \cdot 10^{+3}$	4.673
Br		$1.52 \cdot 10^{+5}$	9.170	$1.14 \cdot 10^{+5}$	7.830
I		$8.31 \cdot 10^{+5}$	11.361	$2.88 \cdot 10^{+5}$	7.233
At		$8.65 \cdot 10^{+6}$	13.732	$-1.36 \cdot 10^{+6}$	5.561

Bibliography

- [1] P. Blaha, K. Schwarz, G. Madsen, D. Kvasnicka, and J. Luitz. *An Augmented Plane Wave + Local Orbitals Program for Calculating Crystal Properties*. ISBN 3-9501031-1-2, Technische Universität Wien (2001).
- [2] K. Koepernik and H. Eschrig. *Phys. Rev. B* **59**, 1743 (1999).
- [3] J. M. B. Kellogg, I. I. Rabi, N. F. Ramsey, and J. R. Zacharias. *Phys. Rev.* **55**, 318 (1939).
- [4] P. Blaha, K. Schwarz, and P. Herzig. *Phys. Rev. Lett.* **54**, 1192 (1985).
- [5] O. C. Kistner and A. W. Sunyar. *Phys. Rev. Lett.* **4**, 412 (1960).
- [6] N. D. Mermin. *Phys. Rev.* **137**, A1441 (1965).
- [7] M. Born and R. Oppenheimer. *Annalen der Physik* **84**, 457 (1927).
- [8] P. Hohenberg and W. Kohn. *Phys. Rev.* **136**, B864 (1964).
- [9] H. Eschrig. *The Fundamentals of Density Functional Theory*. Eagle Leipzig (2003).
- [10] W. Kohn and L. J. Sham. *Phys. Rev.* **140**, A1133 (1965).
- [11] D. M. Ceperley and B. J. Alder. *Phys. Rev. Lett.* **45**, 566 (1980).
- [12] S. D. Kenny, G. Rajagopal, R. J. Needs, W.-K. Leung, M. J. Godfrey, A. J. Williamson, and W. M. C. Foulkes. *Phys. Rev. Lett.* **77**, 1099 (1996).
- [13] U. von Bart and L. Hedin. *J. Phys. C* **5**, 1629 (1972).
- [14] J. P. Perdew and A. Zunger. *Phys. Rev. B* **23**, 5048 (1981).
- [15] J. P. Perdew and Y. Wang. *Phys. Rev. B* **45**, 13244 (1992).
- [16] J. P. Perdew, K. Burke, and M. Ernzerhof. *Phys. Rev. Lett.* 3865 (1996).
- [17] C. Krellner, N. S. Kini, E. M. Brüning, K. Koch, H. Rosner, M. Nicklas, M. Baenitz, and C. Geibel. *Phys. Rev. B* **76**, 104418 (2007).
- [18] A. Georges, G. Kotliar, W. Krauth, and M. J. Rozenberg. *Rev. Mod. Phys.* **68**, 13 (1996).
- [19] G. Kotliar, S. Y. Savrasov, K. Haule, V. S. Oudovenko, O. Parcollet, and C. A. Marianetti. *Rev. Mod. Phys.* **78**, 865 (2006).
- [20] G. Madsen and P. Novák. *Notes about constraint LDA calculations to determine U* (2007). www.wien2k.at/reg_user/textbooks/.
- [21] M. T. Czyżyk and G. A. Sawatzky. *Phys. Rev. B* **49**, 14211 (1994).
- [22] H. Eschrig, K. Koepernik, and I. Chaplygin. *J. Sol. State Chem.* **176**, 482 (2003).
- [23] S. Goedecker. *Rev. Mod. Phys.* **71**, 1085 (1999).

- [24] S. Cottenier (2009). Private communication.
- [25] S. Cottenier. *DFT and the Family of (L)APW-methods: a step-by-step Introduction* (2002). www.wien2k.at/reg_user/textbooks/, ISBN 90-807215-1-4.
- [26] K. Koepnik, H. Eschrig, I. Opahle, U. Nitzsche, I. Chaplygin, and M. Richter. *psi-k-newsletter* (2002).
- [27] H. Rosner, J. M. An, W. E. Pickett, and S.-L. Drechsler. *Phys. Rev. B* **66**, 024521 (2002).
- [28] H. Rosner, M. Divis, K. Koepnik, S.-L. Drechsler, and H. Eschrig. *J. Phys.: Condens. Matter* **12**, 5809 (2000).
- [29] H. Rosner, A. Kitaigorodsky, and W. E. Pickett. *Phys. Rev. Lett.* **88**, 127001 (2002).
- [30] K. Koepnik. *Full Potential Local Orbital Minimal Basis Bandstructure Scheme* (2005). Unpublished documentation.
- [31] K. Koepnik. *Talk at the FPLO workshop* (2008).
- [32] F. Haarmann, K. Koch, D. Zahn, and H. Rosner. *manuscript in preparation* .
- [33] S. Lany, P. Blaha, J. Hamann, V. Ostheimer, H. Wolf, and T. Wichert. *Phys. Rev. B* **62**, R2259 (2000).
- [34] S. Cottenier, V. Bellini, M. Çakmak, F. Manghi, and M. Rots. *Phys. Rev. B* **70**, 155418 (2004).
- [35] S. J. Asadabadi, S. Cottenier, H. Akbarzadeh, R. Saki, and M. Rots. *Phys. Rev. B* **66**, 195103 (2002).
- [36] P. Herzog. *Theoret. Chim. Acta* **67**, 323 (1985).
- [37] A. Abragam. *The Principles of Nuclear Magnetism*. Oxford Univ. Pr. (1996).
- [38] C. P. Slichter. *Principles of Magnetic Resonance*. Springer (1996).
- [39] H. W. Spiess. *Rotation of Molecules and Nuclear Spin Relaxation, NMR-Basic Principles and Progress*, vol. 15. Springer Verlag (1978).
- [40] P. Blaha, K. Schwarz, and P. H. Dederichs. *Phys. Rev. B* **37**, 2792 (1988).
- [41] K. Koch and S. Cottenier. *EFG analysis* (2006). www.wien2k.at/reg_user/textbooks/.
- [42] R. Harris and E. Becker. *J. Magn. Reson.* **156**, 323 (2002).
- [43] P. Pyykkö. *Mol. Phys.* **106**, 1965 (2008).
- [44] F. Haarmann (2008). Private communication.
- [45] M. R. Hansen, G. K. H. Madsen, H. J. Jakobsen, and J. Skibsted. *J. Phys. Chem. B* **110**, 5975 (2006).
- [46] M. Iglesias, K. Schwarz, P. Blaha, and D. Baldomir. *Phys. Chem. Minerals* **28**, 67 (2001).
- [47] K. Koepnik (2008). Private communication.
- [48] P. Blaha (2007). Private communication.

- [49] P. Blaha, K. Schwarz, W. Faber, and J. Luitz. *Hyperfine Int.* **126**, 389 (2000).
- [50] M. Ogura and H. Akai. *J. Phys.: Condens. Matter* **17**, 5741 (2005).
- [51] A. Ormeci, H. Rosner, F. Wagner, M. Kohout, and Yu Grin. *J. Phys. Chem. A* **110**, 1100 (2006).
- [52] F. Haarmann, K. Koch, D. Grüner, W. Schnelle, O. Pecher, R. Cardoso-Gil, H. Borrmann, H. Rosner, and Yu. Grin. *Chem. Eur. J.* **15**, 1673 (2009).
- [53] G. Bruzzone. *Estratto Boll. Sci. Fac. Chim. Ind. Bologna* **24**, 113 (1966).
- [54] G. Bruzzone, M. L. Fornasini, and F. Merlo. *J. Less-Common Met.* **154**, 67 (1989).
- [55] G. Bruzzone, M. L. Fornasini, and F. Merlo. *J. Less-Common Met.* **154**, 67 (1989).
- [56] W. Harms, M. Wendorff, and C. Rohr. *Z. Naturforsch.* **62**, 177 (2007).
- [57] F. Haarmann, K. Koch, P. Jeglič, H. Rosner, and Yu. Grin. *manuscript in preparation* .
- [58] P. Pyykkö. *Mol. Phys.* **99**, 1617 (2001).
- [59] G. Bruzzone. *Acta Cryst.* **18**, 1081 (1965).
- [60] U. Frank-Cordier, G. Cordier, and H. Schaefer. *Z. Naturforsch. b* **37**, 119 (1982).
- [61] P. H. Tobash, Y. Yamasaki, and S. Bobev. *Acta Cryst. E* **61**, 174 (2005).
- [62] J. Nagamatsu, N. Nakagawa, T. Muranaka, Y. Zenitani, and J. Akimitsu. *Nature* **410**, 63 (2001).
- [63] A. Ivanovskii, I. Shein, and N. Medvedeva. *USPEKHI KHIMII* **77**, 491 (2008).
- [64] G. H. Funk. *Z. Anorg. Allg. Chem.* **142**, 269 (1925).
- [65] W. Hofmann and W. Jäniche. *Z. Physik. Chem.* **31B**, 214 (1936).
- [66] V. I. Matkovich, J. Economy, and R. F. Griese Jr.. *J. Am. Chem. Soc.* **84**, 2337 (1964).
- [67] I. Loa, K. Kunc, K. Syassen, and P. Bouvier. *Phys. Rev. B* **66**, 134101 (2002).
- [68] J. Nakamura, M. Watanabe, T. Oguchi, S. Nasubida, E. Kabasawa, N. Yamada, K. Kuroki, S. Yamazaki, H. Shin, Y. Umeda, S. Minakawa, N. Kimura, and H. Aoki. *J. Phys. Soc. Jpn.* **71**, 408 (2002).
- [69] U. Burkhardt, V. Gurin, F. Haarmann, H. Borrmann, W. Schnelle, A. Yaresko, and Yu. Grin. *J. Sol. State Chem.* **177**, 389 (2004).
- [70] J. J. van Laar. *Z. Physik. Chem.* **63**, 216 (1908).
- [71] J. J. van Laar. *Z. Physik. Chem.* **64**, 257 (1908).
- [72] Y. A. Chang, S. Chen, F. Zhang, X. Yanc, F. Xieb, R. Schmid-Fetzerd, and W. A. Oates. *Progress in Material Science* **49**, 313 (2004).
- [73] K. Koepernik, B. Velický, R. Hayn, and H. Eschrig. *Phys. Rev. B* **55**, 5717 (1997).
- [74] K. Koepernik, B. Velický, R. Hayn, and H. Eschrig. *Phys. Rev. B* **58**, 6944 (1998).

- [75] E. J. Felten. *J. Am. Chem. Soc.* **78**, 59725977 (1956).
- [76] A. J. C. Wilson. *Proc. Phys. Soc.* **54**, 487 (1942).
- [77] H. E. Sostmann. *Isotech Journal of Thermometry* **4**, 59 (1993).
- [78] V. Petzhold. *Electronic structure and related superconducting properties of conventional superconductors*. Master's thesis, TU Dresden (2007).
- [79] A. Leithe-Jasper (2009). Private communication.
- [80] N. W. Ashcroft and N. D. Mermin. *Solid State Physics*. Harcourt, Inc. (1976).
- [81] C. Kittel. *Introduction to Solid State Physics*. John Wiley & Sons, Inc. (1996).
- [82] H. G. F. Winkler. *Struktur und Eigenschaften der Kristalle*. Springer Verlag (1955).
- [83] M. E. Lines and A. M. Glass. *Principles and Applications of Ferroelectrics and Related Materials*. Oxford: Clarendon (1977).
- [84] L. F. Mattheiss, E. M. Gyorgy, and D. W. Johnson. *Phys. Rev. B* **37**, 3745 (1988).
- [85] Y. Moritomo, A. Asamitsu, H. Kuwahara, and Y. Tokura. *Nature* **380**, 6570 (1996).
- [86] S. Ishihara, T. Hatakeyama, and S. Maekawa. *Phys. Rev. B* **65**, 064442 (2002).
- [87] R. Cohen. *Nature* **358**, 136 (1992).
- [88] Y. A. Abramov, V. G. Tsirelson, V. E. Zavodnik, S. A. Ivanov, and I. D. Brown. *Acta Crystallogr. B* **51**, 942 (1995).
- [89] N. Sai and D. Vanderbilt. *Phys. Rev. B* **62**, 13942 (2000).
- [90] R. Blinc, V. V. Laguta, B. Zalar, M. Itoh, and H. Krakauer. *J. Phys.: Condens. Matter* **20**, 085204 (2008).
- [91] L. F. Mattheiss. *Phys. Rev.* **181**, 987 (1969).
- [92] L. F. Mattheiss. *Phys. Rev. B* **2**, 3918 (1970).
- [93] L. F. Mattheiss. *Phys. Rev. B* **6**, 4718 (1972).
- [94] T. Wolfram. *Phys. Rev. Lett.* **29**, 1383 (1972).
- [95] T. Wolfram and S. Ellialtioglu. *Phys. Rev. B* **25**, 2697 (1982).
- [96] T. Wolfram, E. A. Kraut, and F. J. Morin. *Phys. Rev. B* **7**, 1677 (1973).
- [97] S. A. Prosandeev, A. V. Fisenko, and N. M. Nebogatikov. *Sov. Phys. Solid State* **29**, 2600 (1987).
- [98] W. A. Harrison. *Electronic Structure and the Properties of Solids*. Freeman (San Francisco) (1980).
- [99] M. D. Kuzmin, A. I. Popov, and A. K. Zvezdin. *Phys. Stat. Sol. (B)* **168**, 201 (1991).
- [100] J. C. Slater. *Phys. Rev.* **78**, 748 (1950).
- [101] J. G. Bednorz and K. A. Müller. *Z. Phys. B* **64**, 189 (1986).

- [102] M. Schmitt. *Elektronische Struktur und magnetische Eigenschaften niedrigdimensionaler Übergangsmetalle*. Master's thesis, TU Dresden (2007).
- [103] U. Nitzsche and H. Rosner. *manuscript in preparation* .
- [104] S. L. Chaplot, W. Reichardt, L. Pintschovius, and N. Pyka. *J. Phys. Chem. Sol.* **53**, 761 (1992).
- [105] M. Braden, B. Büchner, S. Klotz, W. G. Marshall, M. Behruzi, and G. Heger. *Phys. Rev. B* **60**, 9616 (1999).
- [106] M. T. Weller and D. R. Lines. *J. Sol. State Chem.* **82**, 21 (1989).
- [107] A. Podlesnyak, A. Mirmelstein, V. Bobrovskii, V. Voronin, A. Karkin, I. Zhdakhin, B. Goshchitskii, E. Midberg, V. Zubkov, T. D'yachkova, E. Khlybov, J. Genoud, S. Rosenkranz, F. Fauth, W. Henggeler, and A. Furrer. *Physica C* **258**, 159 (1996).
- [108] A. A. Gippius, M. Schmitt, K. S. Okhotnikov, W. Schnelle, K. Koch, O. Janson, W. Liu, Y.-H. Huang, F. Weikert, M. Baenitz, and H. Rosner. *submitted to Phys. Rev. B* .
- [109] S. M. Hayden, G. Aeppli, H. A. Mook, S.-W. Cheong, and Z. Fisk. *Phys. Rev. B* **42**, 10220 (1990).
- [110] T. Tsuda, T. Shimizu, H. Yasuoka, K. Kishio, and K. Kitazawa. *J. Phys. Soc. Jpn.* **57**, 2908 (1988).
- [111] P. E. Sulewski, P. A. Fleury, K. B. Lyons, S.-W. Cheong, and Z. Fisk. *Phys. Rev. B* **41**, 225 (1990).
- [112] S. M. Hayden, G. Aeppli, H. A. Mook, S.-W. Cheong, and Z. Fisk. *Phys. Rev. B* **42**, 10220 (1990).
- [113] P. Blaha, K. Schwarz, and P. Novák. *Int. J. Quant. Chem.* **101**, 550 (2005).
- [114] H. Rosner, S.-L. Drechsler, K. Koepernik, R. Hayn, and H. Eschrig. *Phys. Rev. B* **63**, 073104 (2001).
- [115] M. Itoh, M. Sugahara, T. Yamauchi, and Y. Ueda. *Phys. Rev. B* **53**, 11606 (1996).
- [116] H. Rosner. *Electronic Structure and Exchange Integrals of Low-Dimensional Cuprates*. Ph.D. thesis, TU Dresden (1999).
- [117] L. P. Regnault, M. Aïn, B. Hennion, G. Dhahlenne, and A. Revcolevschi. *Phys. Rev. B* **53**, 5579 (1996).
- [118] H. Kuroe, J. Sasaki, T. Sekine, N. Koide, Y. Sasago, K. Uchinokura, and M. Hase. *Phys. Rev. B* **55**, 409 (1997).
- [119] M. Takigawa (2008). Private communication.
- [120] R. Neudert, S.-L. Drechsler, J. Málek, H. Rosner, M. Kielwein, Z. Hu, M. Knupfer, M. S. Golden, J. Fink, N. Nücker, M. Merz, S. Schuppler, N. Motoyama, H. Eisaki, S. Uchida, M. Domke, and G. Kaindl. *Phys. Rev. B* **62**, 10752 (2000).
- [121] H. Rosner, M. Divis, K. Koepernik, S.-L. Drechsler, and H. Eschrig. *Comment on: J. Phys.-Condes. Matter* **12**, 5809 (2000).

- [122] D. Kasinathan (2009). Private communication.
- [123] Y. Kamihara, T. Watanabe, M. Hirano, and H. Hosono. *J. Am. Chem. Soc.* **130**, 3296 (2008).
- [124] G. F. Chen, Z. Li, D. Wu, G. Li, W. Z. Hu, J. Dong, P. Zheng, J. L. Luo, and N. L. Wang. *Phys. Rev. Lett.* **100**, 247002 (2008).
- [125] Z.-A. Ren, J. Yang, W. Lu, W. Yi, G.-C. Che, L.-L. Dong, X.-L. Sun, and Z.-X. Zhao. *Mater. Res. Innovations* **12**, 105 (2008).
- [126] Z.-A. Ren, J. Yang, W. Lu, W. Yi, X.-L. Shen, Z.-C. Li, G.-C. Che, X.-L. Dong, L.-L. Sun, F. Zhou, and Z.-X. Zhao. *Europhys. Lett.* **82**, 57002 (2008).
- [127] Z. Ren, W. Lu, J. Yang, W. Yi, X. Shen, Z. Li, G. Che, X. Dong, L. Sun, F. Zhou, and Z. Zhao. *Chin. Phys. Lett.* **25**, 2215 (2008).
- [128] H. Takahashi, K. Igawa, K. Arii, Y. Kamihara, M. Hirano, and H. Hosono. *Nature* **453**, 376 (2008).
- [129] M. Rotter, M. Tegel, and D. Johrendt. *Phys. Rev. Lett.* **101**, 107006 (2008).
- [130] K. Sasmal, B. Lv, B. Lorenz, A. Guloy, F. Chen, Y. Xue, and C. W. Chu. *Phys. Rev. Lett.* **101**, 107007 (2008).
- [131] G. Wu, H. Chen, T. Wu, Y. L. Xie, Y. J. Yan, R. H. Liu, X. F. Wang, J. J. Ying, and X. H. Chen. *J. Phys.: Condens. Matter* **20**, 422201 (2008).
- [132] A. Leithe-Jasper, W. Schnelle, C. Geibel, and H. Rosner. *Phys. Rev. Lett.* **101**, 207004 (2008).
- [133] M. Kumar, M. Nicklas, A. Jesche, N. Caroca-Canales, M. Schmitt, M. Hanfland, D. Kasinathan, U. Schwarz, H. Rosner, and C. Geibel. *Phys. Rev. B* **78**, 184516 (2008).
- [134] S. Milton, S. Torikachvili, N. Bud'ko, and P. Canfield. *Phys. Rev. Lett.* **101**, 057006 (2008).
- [135] W. Yu, A. A. Aczel, T. J. Williams, S. L. Budko, N. Ni, P. C. Canfield, and G. M. Luke. *Phys. Rev. B* **79**, 020511 (2009).
- [136] X. C. Wang, Q. Q. Liu, Y. X. Lv, W. B. Gao, L. X. Yang, R. C. Yu, F. Li, and C. Q. Jin. *arXiv:0806.4688v3* (2008).
- [137] Y. Mizuguchi, F. Tomioka, S. Tsuda, T. Yamaguchi, and Y. Takano. *Appl. Phys. Lett.* **94**, 012503 (2009).
- [138] F. Hunte, J. Jaroszynski, A. Gurevich, D. C. Larbalestier, R. Jin, A. S. Sefat, M. A. McGuire, B. C. Sales, D. K. Christen, and D. Mandrus. *Nature* **453**, 903 (2008).
- [139] D. Kasinathan, A. Ormeci, K. Koch, U. Burkhardt, W. Schnelle, A. Leithe-Jasper, and H. Rosner. *New J. Phys.* **11**, 025023 (2009).
- [140] I. Mazin, M. Johannes, L. Boeri, K. Koepf, and D. Singh. *Phys. Rev. B* **78**, 085104 (2008).
- [141] T. Yildirim. *Phys. Rev. Lett.* **102**, 037003 (2009).
- [142] I. Mazin and M. Johannes. *arXiv:0807.3737v1* (2008).

- [143] F. Ronning, T. Klimczuk, E. Bauer, H. Volz, and J. Thompson. *J. Phys. Cond. Mat.* **20**, 322201 (2008).
- [144] C. Krellner, N. Caroca-Canales, A. Jesche, H. Rosner, A. Ormeci, and C. Geibel. *Phys. Rev. B* **78**, 100504 (2008).
- [145] M. Rotter, M. Tegel, and D. Johrendt. *Phys. Rev. B* **78**, 020503 (2008).
- [146] A. Kreyssig, M. A. Green, Y. Lee, G. Samolyuk, P. Zajdel, J. W. Lynn, S. L. Bud'ko, M. S. Torikachvili, N. Ni, S. Nandi, J. B. Leo, S. J. Poulton, D. N. Argyriou, B. N. Harmon, R. J. McQueeney, P. C. Canfield, and A. I. Goldman. *Phys. Rev. B* **78**, 184517 (2008).
- [147] A. Jesche, N. Caroca-Canales, H. Rosner, H. Borrmann, A. Ormeci, D. Kasinathan, H. H. Klauss, H. Luetkens, R. Khasanov, A. Amato, A. Hoser, K. Kaneko, C. Krellner, and C. Geibel. *Phys. Rev. B* **78**, 180504(R) (2008).
- [148] M. Tegel, M. Rotter, V. Weiss, F. Schappacher, R. Pöttgen, and D. Johrendt. *J. Phys.: Condens. Matter* **20**, 452201 (2008).
- [149] S. H. Baek, N. J. Curro, T. Klimczuk, E. D. Bauer, F. Ronning, and J. D. Thompson. *Phys. Rev. B* **79**, 052504 (2009).
- [150] K. Kitagawa, N. Katayama, K. Ohgushi, M. Yoshida, and M. Takigawa. *J. Phys. Soc. Jpn.* **77**, 114709 (2008).
- [151] P. Jeglič (2008). Private communication.
- [152] C. de la Cruz, Q. Huang, J. W. Lynn, J. Li, W. Ratcliff II, J. L. Zarestky, H. A. Mook, G. F. Chen, J. L. Luo, N. L. Wang, and P. Dai. *Nature* **453**, 899 (2008).
- [153] P. Jeglič, J.-W. G. Bos, A. Zorko, M. Brunelli, K. Koch, H. Rosner, S. Margadonna, and D. Arčon. *Phys. Rev. B* **79**, 094515 (2009).
- [154] H.-J. Grafe, D. Paar, G. Lang, N. J. Curro, G. Behr, J. Werner, J. Hamann-Borrero, C. Hess, N. Leps, R. Klingeler, and B. Büchner. *Phys. Rev. Lett.* **101**, 047003 (2008).
- [155] H.-J. Grafe, G. Lang, F. Hammerath, D. Paar, K. Manthey, K. Koch, H. Rosner, N. J. Curro, G. Behr, J. Werner, N. Leps, R. Klingeler, and B. Büchner. *New J. Phys.* **11**, 035002 (2009).
- [156] T. Nomura, S. W. Kim, Y. Kamihara, P. V. Hirano, M. Sushko, K. Kato, M. Takata, A. L. Shluger, and H. Hosono. *Supercond. Sci. Technol.* **21**, 125028 (2008).
- [157] S. Lebègue, Z. P. Yin, and W. E. Pickett. *New J. Phys.* **11**, 025004 (2009).
- [158] J. Cederberg, D. Olson, A. Nelson, D. Laine, P. Zimmer, M. Welge, M. Feig, T. Höft, and N. London. *J. Chem. Phys.* **110**, 2431 (1999).
- [159] M.-Y. Liao and G. S. Harbison. *J. Chem. Phys.* **100**, 1895 (1994).
- [160] P. Pyykkö. *Chem. Phys. Lett.* **6**, 479 (1970).
- [161] J. Thyssen, P. Schwerdtfeger, M. Bender, W. Nazarewicz, and P. B. Semmes. *Phys. Rev. A* **63**, 022505 (2001).
- [162] R. M. Steffen. *Hyperfine Int.* **9**, 39 (1981).

- [163] R. M. Steffen. *Hyperfine Int* **24**, 223 (1985).
- [164] S. Cottenier and M. Rots. *Hyperfine Interactions and their Application in Nuclear Condensed Matter Physics: a microscopic Introduction*. unpublished lecture notes Katholieke Universiteit Leuven (2005).
- [165] T.-C. Wang. *Phys. Rev.* **99**, 566 (1955).
- [166] V. Kellö and A. J. Sadlej. *Int. J. Quant. Chem.* **68**, 159 (1998).
- [167] V. Kellö and A. J. Sadlej. *J. Chem. Phys.* **112**, 522 (2000).
- [168] M. Pernpointner, M. Seth, and P. Schwerdtfeger. *J. Chem. Phys.* **108**, 6722 (1998).
- [169] J. N. P. Van Stralen and L. Visscher. *Mol. Phys.* **101**, 2115 (2003).
- [170] P. Ring and P. Schuck. *The Nuclear Many Body Problem*. Springer-Verlag, New York (1980).
- [171] I. Agnelli. *Atomic Data and Nuclear Data Tables* **87**, 185 (2004).
- [172] N. J. Stone. *Atomic Data and Nuclear Data Tables* **90**, 75 (2005).
- [173] R. K. Harris and E. D. Becker. *J. of Magn. Reson.* **156**, 323 (2002).
- [174] W. H. Zachariasen. *Acta Crystallographica* **12**, 698 (1959).
- [175] K. Koch, K. Koepernik, D. Van Neck, H. Rosner, and S. Cottenier. *submitted to Phys. Rev. A*.
- [176] P. Pyykkö and J. Linderberg. *Chem. Phys. Lett.* **5**, 34 (1970).
- [177] K. J. D. MacKenzie and M. E. Smith. *Multinuclear solid-state NMR of inorganic materials*. Elsevier (2002).
- [178] E. N. Kaufmann and R. J. Vianden. *Rev. Mod. Phys.* **51**, 161 (1979).
- [179] R. J. Vianden. *Hyperfine Int.* **35**, 1079 (1987).
- [180] J. Christiansen, P. Heubes, R. Keitel, W. Klinger, W. Loeffler, W. Sandner, and W. Withuhn. *Z. Phys. B* **24**, 177 (1976).
- [181] M. Forker and L. Freise. *Hyperfine Int.* **34**, 329 (1987).
- [182] H. C. Verma. *Hyperfine Int.* **15/16**, 207 (1983).
- [183] J. Cederberg, J. Randolph, B. McDonald, B. Paulson, and C. McEachern. *J. Mol. Spec.* **250**, 114 (2008).
- [184] N. F. Ramsey. In: *Experimental Nuclear Physics*. John Wiley and Sons: New York (1953). Part III, Volume 1.
- [185] N. F. Ramsey. *Molecular Beams*. Oxford University Press: London (1956).
- [186] J. C. Zorn and T. C. English. In: *Advances in Atomic and Molecular Physics*. Academic Press: New York (1973). Volume 9, pp 243.
- [187] J. Cederberg, E. Frodermann, H. Tollerud, K. Huber, M. Bongard, J. Randolph, and D. Nitz. *J. Chem. Phys.* **124**, 244304 (2006).

- [188] J. Cederberg, S. Fortman, B. Porter, M. Etten, M. Feig, M. Bongard, and L. Langer. *J. Chem. Phys.* **124**, 244305 (2006).
- [189] J. Cederberg, J. Nichol, E. Frodermann, H. Tollerud, G. Hilk, J. Buysman, W. Kleiber, M. Bongard, J. Ward, K. Huber, T. Khanna, J. Randolph, and D. Nitz. *J. Chem. Phys.* **123**, 134321 (2005).
- [190] J. Cederberg, D. Olson, J. Larson, G. Rakness, K. Jarausch, J. Schmidt, B. Borovsky, P. Larson, and B. Nelson. *Phys. Rev. A* **57**, 2539 (1998).
- [191] K. P. Huber and G. Herzberg. *Molecular Spectra and Molecular Structure*, vol. VI. van Nostrand Reinhold Comp. (1979).
- [192] E. van Lethe and E. Baerends. *J. Chem. Phys.* **112**, 8279 (2000).
- [193] F. Corà, M. Alfredsson, G. Mallia, D. S. Middlemiss, W. C. Mackrodt, R. Dovesi, and R. Orlando. *Struct. Bonding (Berlin)* **113**, 171 (2004).
- [194] J. Heyd, G. Scuseria, and M. Ernzerhof. *J. Chem. Phys.* **118**, 8207 (2003).
- [195] K. N. Kudin, G. E. Scuseria, and R. L. Martin. *Phys. Rev. Lett.* **89**, 266402 (2002).
- [196] F. Tran, P. Blaha, K. Schwarz, and P. Novák. *Phys. Rev. B* **74**, 155108 (2006).
- [197] F. Tran, J. Shweifer, P. Blaha, K. Schwarz, and P. Novák. *Phys. Rev. B* **77**, 085123 (2008).
- [198] H. M. Petrilli, P. E. Blochl, P. Blaha, and K. Schwarz. *Phys. Rev. B* **57**, 14690 (1998).
- [199] A. Svane, N. E. Christensen, C. O. Rodriguez, and M. Methfessel. *Phys. Rev. B* **55**, 12572 (1997).
- [200] D. Torumba, K. Parlinski, M. Rots, and S. Cottenier. *Phys. Rev. B* **74**, 144304 (2006).
- [201] T. Crawford and H. Schaefer. *Rev. comput. Chem.* **14**, 33 (2000).
- [202] V. Kellö, P. Pyykkö, A. J. Sadlej, P. Schwerdtfeger, and J. Thyssen. *Chem. Phys. Lett.* **318**, 222 (2000).
- [203] V. Kellö and A. J. Sadlej. *Chem. Phys. Lett.* **292**, 403 (1998).
- [204] V. Kellö and A. J. Sadlej. *Mol. Phys.* **96**, 275 (1998).
- [205] V. Kellö and A. J. Sadlej. *Phys. Rev. A* **60**, 3575 (1999).
- [206] V. Kellö, A. J. Sadlej, P. Pyykkö, D. Sundholm, and M. Tokman. *Chem. Phys. Lett.* **302**, 414 (0999).
- [207] M. Pernpointner, P. Schwerdtfeger, and B. A. Hess. *Int. J. Quant. Chem.* **76**, 371 (2000).
- [208] V. Kellö and A. J. Sadlej. *Collect. Czech. Chem. Commun.* **72**, 64 (2007).
- [209] C. Thierfelder, P. Schwerdtfeger, and T. Saue. *Phys. Rev. A* **76**, 034502 (2007).
- [210] J. L. Dunham. *Phys. Rev.* **41**, 721 (1932).
- [211] C. Schlier. *Fortschr. Phys.* **9**, 455 (1961).
- [212] H. M. Foley. *Phys. Rev.* **72**, 504 (1947).

- [213] J. M. B. Kellogg, I. I. Rabi, N. F. Ramsey Jr., and J. R. Zacharias. *Phys. Rev.* **57**, 677 (1940).
- [214] N. F. Ramsey. *Phys. Rev.* **89**, 527 (1953).
- [215] G. Barone, R. Mastalerz, M. Reiher, and L. Roland. *J. Phys. Chem. A* **112**, 1666 (2009).
- [216] P. Dufek, P. Blaha, and K. Schwarz. *Phys. Rev. Lett.* **75**, 3545 (1995).
- [217] L. Errico, G. Darriba, M. Renteria, Z. Tang, H. Emmerich, and S. Cottenier. *Phys. Rev. B* **77**, 195118 (2008).
- [218] V. Kellö, A. J. Sadlej, and P. Pyykkö. *Chem. Phys. Lett.* **329**, 112 (2000).
- [219] S. Büttgenbach. *Hyperfine Int.* **20**, 1 (1984).
- [220] J. R. Crespo López-Urrutia, P. Beiersdorfer, K. Widmann, B. B. Birkett, A.-M. Mårtensson-Pendrill, and M. G. H. Gustavsson. *Phys. Rev. A* **57**, 879 (1998).
- [221] H. Haken and H. C. Wolf. *Atom- und Quantenphysik*. Springer (2003).
- [222] L. A. Paquette. *J. Mol. Struct.* **190**, 143 (1988).
- [223] S. J. Clark, M. D. Segall, C. J. Pickard, P. J. Hasnip, M. J. Probert, K. Refson, and M. C. Payne. *Z. Kristallogr.* **220**, 567 (2005).
- [224] J. R. Yates, C. J. Pickard, and F. Mauri. *Phys. Rev. B* **76**, 024401 (2007).
- [225] N. d’Avezac, M. Marzari and F. Mauri. *Phys. Rev. B* **76**, 165122 (2007).
- [226] J. D. Jackson. *Classical Electrodynamics*. Wiley (1999).
- [227] A. J. Freeman and R. B. Frankel. In: *Recoil Absorption of Gamma Rays and Studies of Nuclear Hyperfine Interactions in Solids*, 497. Academy Press (1967). Volume 11, pp 497.
- [228] E. Amaldi and B. N. Cacciapuoti. *Phys. Rev.* **71**, 739 (1947).
- [229] W. R. Johnson and G. Soff. *Atomic Data and Nuclear Data Tables* **33**, 405 (1985).
- [230] L. Visscher and K. G. Dyall. *Atomic Data and Nuclear Data Tables* **67**, 207 (1997).

List of scientific contributions

Publications discussed in this thesis:

1. **Section 5.1:** F. Haarmann, **K. Koch**, D. Grüner, W. Schnelle, O. Pecher, R. Cardoso-Gil, H. Borrmann, H. Rosner, and Yu. Grin. *Electronic Structure, Chemical Bonding, and Solid-State NMR Spectroscopy of the Digallides of Ca, Sr, and Ba*, Chem. Eur. J. **15**, 1673 (2009).
2. **Section 5.1:** F. Haarmann, **K. Koch**, P. Jeglič, H. Rosner, and Yu. Grin. *NMR spectroscopy on intermetallic compounds: An experimental and theoretical approach to gallides*, (manuscript in preparation).
3. **Section 5.2:** H. Rosner, **K. Koch**, and Yu. Grin. *The intrinsic Al-defect structure of $Al_{1-x}B_2$* , submitted to Angew. Chem..
4. **Section 5.3:** **K. Koch**, R. Kuzian, K. Koepernik, I. V. Kondakova, and H. Rosner. *Analysis of the Electric Field Gradient in the Perovskites $SrTiO_3$ and $BaTiO_3$: Density Functional and Model Calculations*, submitted to Phys. Rev. B.
5. **Section 5.4:** A. A. Gippius, M. Schmitt, K. S. Okhotnikov, W. Schnelle, **K. Koch**, O. Janson, W. Liu, Y.-H. Huang, F. Weikert, M. Baenitz, and H. Rosner. *Electronic and magnetic properties of the spin gap compound $Cu_2(PO_3)_2CH_2$: magnetic versus structural dimers*, submitted to Phys. Rev. B.
6. **Section 5.5.4:** D. Kasinathan, A. Ormeci, **K. Koch**, U. Burkhardt, W. Schnelle, A. Leithe-Jasper, and H. Rosner. *AFe_2As_2 ($A = Ca, Sr, Ba, Eu$) and $SrFe_{2-x}TM_xAs_2$ ($TM = Mn, Co, Ni$): crystal structure, charge doping, magnetism and superconductivity*, New J. Phys. **11**, 025023 (2009).
7. **Section 5.5.5:** H.-J. Grafe, G. Lang, F. Hammerath, D. Paar, K. Manthey, **K. Koch**, H. Rosner, N. J. Curro, G. Behr, J. Werner, N. Leps, R. Klingeler, and B. Büchner. *Electronic properties of $LaO_{1-x}F_xFeAs$ in the normal state probed by NMR/NQR*, New J. Phys. **11**, 035002 (2009).
8. **Section 5.5.5:** P. Jeglič, J.-W. G. Bos, A. Zorko, M. Brunelli, **K. Koch**, H. Rosner, S. Margadonna, and D. Arçon. *Influence of the Nd 4f States on the Magnetic Behavior and the Electric Field Gradient of the Oxypnictides superconductors $NdFeAsO_{1-x}F_x$* , Phys. Rev. B **79**, 094515 (2009).
9. **Chapter 6:** **K. Koch**, K. Koepernik, D. Van Neck, H. Rosner, and S. Cottenier. *Electron penetration in the nucleus: its effect on the quadrupole interaction*, submitted to Phys. Rev. A.

Other publications:

10. **K. Koch** and S. Cottenier. *EFG analysis*, www.wien2k.at/reg_user/textbooks/ (2006).
11. C. Krellner, N. S. Kini, E. M. Brüning, **K. Koch**, H. Rosner, M. Nicklas, M. Baenitz, and C. Geibel. *CeRuPO: A rare example of a ferromagnetic Kondo lattice*, Phys. Rev. B **76**, 104418 (2007).

12. F. Haarmann, **K. Koch**, D. Zahn, and H. Rosner. *Local ordering in the intermetallic compound $Cu_{1-x}Al_2$ – an experimental and theoretical study*, (manuscript in preparation).
13. F. Haarmann, **K. Koch**, H. Rosner, and Yu. Grin. *Local ordering in the intermetallic compound $Sr_{1-x}Ga_{2+3x}$ – an experimental and theoretical study*, (manuscript in preparation).

Talks at conferences/workshops and during work visits

date	conference	title of the talk
03.2006	DPG ¹ Spring Meeting Dresden	<i>Theoretical investigation of the vacancies in AlB_2</i>
05.2006	Baltic Boat Conference Sweden/Finland	<i>Theoretical investigation of the vacancies in AlB_2</i>
05.2006	FPLO workshop Dresden	<i>Theoretical investigation of the vacancies in AlB_2</i>
09.2006	IMPRS ² seminar Sächsische Schweiz	<i>NMR measurement and EFG calculation of MGa_4</i>
09.2006	IMPRS seminar Sächsische Schweiz	<i>The Electric Field Gradient: EFG - Implementation in FPLO</i>
11.2007	FPLO workshop La Plata, Argentina	<i>The Electric Field Gradient: EFG - Implementation in FPLO</i>
01.2008	IMPRS seminar Dresden	<i>The Electric Field Gradient: EFG - Implementation in FPLO</i>
03.2008	DPG Spring Meeting Berlin	<i>Electric field gradients in low dimensional cuprates</i>
08.2008	FPLO workshop Dresden	<i>Electronic structure of $RFeAsO$ and AFe_2As_2 - a comparative study</i>
11.2008	Katholieke Universiteit Leuven Universiteit Gent Leuven and Gent, Belgium	<i>Electron penetration into the nucleus - its effect on the quadrupole interaction</i>
03.2009	DPG Spring Meeting Dresden	<i>Analysis of the electric field gradient in the perovskites $SrTiO_3$ and $BaTiO_3$: density functional and model calculations</i>
03.2009	NMR workshop Dresden	<i>Electric field gradients in perovskites - the ‘intuitive picture’ vs reality: why do simple models fail?</i>

¹Deutsche Physikalische Gesellschaft

²International Max Planck Research School

Posters at conferences

date	conference	title of the poster
01.2006	ECDM ³ conference Brandenburg	<i>Electron charge density and the influence of vacancies in metal diborides</i>
03.2007	DPG Spring Meeting Regensburg	<i>Electric field gradient and chemical bonding in intermetallic gallides</i>
03.2008	WIEN2k workshop Wien, Austria	<i>Electron penetration in the nucleus: its effect on the EFG</i>
07.2008	SCTE ⁴ conference Dresden	<i>Local ordering in the intermetallic compound $Cu_{1-x}Al_2$ - an experimental and theoretical study</i>
10.2008	FeAs workshop Dresden	<i>Electronic structure of $RFeAsO$ and AFe_2As_2 - a comparative study</i>
09.2009	HRMS ⁵ conference Italy	<i>A new challenge to molecular spectroscopy: the influence of electron penetration on the quadrupole interaction</i>

³European Charge Density Meeting

⁴International Conference on Solid Compounds of Transition Elements

⁵High-Resolution Molecular Spectroscopy International Conference

Acknowledgements

At this point I would like to thank the people mentioned below for their emotional and scientific support, help and advice. Without them, this work would not have been possible.

First of all, I would like to thank Prof. Juri Grin, who gave me the opportunity to work in this interesting research field at the Max Planck Institute for Chemical Physics of Solids. I am especially grateful for his support during this time.

A large “thank you” goes to my supervisor Dr. Helge Rosner for his patient coaching. He taught me a lot about solid state physics and about how scientific results are presented, regardless if for a poster, a talk, a paper or simply within conversation. Furthermore, I am especially grateful that he gave me the opportunity to join the FPLO workshop in La Plata (Argentina) in 2007.

I thank Prof. Dr. Helmut Eschrig (IFW, Dresden) and Prof. Dr. Peter Blaha (TU Wien, Austria) for many interesting discussions.

I am indebted to Klaus Koepernik (IFW, Dresden) for the supervision concerning the implementation of the EFG in the FPLO code and the long analytical calculations prior to that. In addition, I am very grateful for his and Alim Ormeci’s support concerning programming questions/problems in the FPLO code and the very helpful discussions.

I thank Frank Haarmann for helping me to understand the method of NMR and the interesting collaboration of NMR experiments with EFG calculations, especially concerning the di- and tetragallides reported in this thesis. Besides, I want to thank him for giving me the opportunity to participate in the exciting NMR workshop he has organised in 2009.

Stefaan Cottenier (Ghent University, Belgium) was an inexhaustible source of answers to my questions concerning WIEN2k and the EFG in the beginning of my PhD work. Furthermore, I would like to thank him for our good collaboration tackling the challenging question about the quadrupole shift, which took “only” 1000 emails back and forth. In addition, I would like to thank him for inviting me for a scientific stay in Ghent/Leuven (Belgium) in 2008.

I would like to thank Roman Kuzian (Institute for Problems of Materials Science, Ukraine) for bringing the perovskites to my attention and solving their EFG “puzzle”. He taught me a lot about p - d model Hamiltonian physics.

I thank Peter Jeglič and Denis Arčon (Institute Jozef Stefan, Slovenia) and Hans-Joachim Grafe (IFW, Dresden) for the cooperative work on the new high T_c superconductors NdFeAsO and LaFeAsO.

Further thanks go to all the past and present members of the Emmy-Noether-group: Alexander Tsirlin, Alim Ormeci, Claire Loison, Deepa Kasinathan, Fabian Seifert, Helge Rosner, Johannes Steinmetz, Julia Wildeboer, Luis Craco, Miriam Schmitt, Oleg Janson and Vivien Petzold; and also to Carsten Neise, Helmut Eschrig, Manuel Richter, Mathias Bayer, Michael Kuzmin, Stephan Schönecker and Ulrike Nitzsche from the Theoretical Solid State Physics Group at the IWF for helpful and cooperative discussions, not only about physics.

I would like to acknowledge Horst Borrmann for fruitful cooperation of charge densities within the SPP 1178 (Experimental Charge Density as the Key to Understand Chemical Interactions) and the SPP 1178 for financial support.

I would like to thank Frank Wagner for arranging the access to the computer cluster in Garching.

The International Max Planck Research School is acknowledged for financial support and organising interesting seminars, especially the ones in the Sächsische Schweiz. Special thanks go to the coordinator Ulf Saalman and all IMPRS students, especially Orkidia Bilani and Aroon O'Brien. Last but not least I would like to thank all colleagues at the MPI CPfS for a nice working atmosphere.

Finally I thank my friends and family, especially Marcus, Edgar and Anja for their infinite patience, emotional support and friendship and everybody I might have forgotten in this list.

Versicherung

Hiermit versichere ich, dass ich die vorliegende Arbeit ohne unzulässige Hilfe Dritter und ohne Benutzung anderer als der angegebenen Hilfsmittel angefertigt habe; die aus fremden Quellen direkt oder indirekt übernommenen Gedanken sind als solche kenntlich gemacht. Die Arbeit wurde bisher weder im Inland noch im Ausland in gleicher oder ähnlicher Form einer anderen Prüfungsbehörde vorgelegt.

Die vorliegende Dissertation wurde unter der Betreuung von Prof. Juri Grin in der Arbeitsgruppe chemische Metallkunde im Max-Planck-Institut für chemische Physik fester Stoffe im Rahmen der International Max Planck Research School in Dresden angefertigt.

Dresden, den

(Katrin Koch)